

Tuning the ground state of pyrochlore oxides using chemical pressure

A thesis

Submitted in partial fulfillment of the requirements of the degree of

Doctor of Philosophy

by:

Prachi Telang

Registration ID 20122034



Department of Physics

INDIAN INSTITUTE OF SCIENCE EDUCATION AND RESEARCH


PUNE-411008, India

There are no accidents!
Master Oogway (Kung Fu Panda)

Certificate

Certified that the work incorporated in the thesis entitled **“Tuning the ground state of pyrochlore oxides using chemical pressure”** submitted by **Prachi Telang** was carried out by the candidate, under my supervision. The work presented here or any part of it has not been included in any other thesis submitted previously for the award of any degree or diploma from any other university or institution.

Date: August 12, 2020


17/8/20
Surjeet Singh(Supervisor)

Declaration

I declare that this written submission entitled “**Tuning the ground state of pyrochlore oxides using chemical pressure**” represents my ideas in my own words and where others’ ideas have been included, I have adequately cited and referenced the original sources. I also declare that I have adhered to all principles of academic honesty and integrity and have not misrepresented or fabricated or falsified any idea/data/fact/source in my submission. I understand that violation of the above will be cause for disciplinary action by the Institute and can also evoke penal action from the sources which have thus not been properly cited or from whom proper permission has not been taken when needed.

Date: August 12, 2020

A handwritten signature in black ink that reads "P. Telang". The signature is written in a cursive style and is enclosed within a simple rectangular box.

(Prachi Telang)

Acknowledgments

The last several years at IISER have been quite eventful. Though it all sums up with a degree, the years spent in getting it will always be cherished. I am immensely thankful to everyone I met during this period, as I always learnt something from everyone.

The first and foremost thanks go to my supervisor Dr Surjeet Singh who taught me how to approach a scientific problem and then tackle it with the means available. I learnt many things from him such as paying attention to the details, finding nuances in the data and presentation skills. I would not have been able to do even half of what I did without his support and guidance.

A due thanks to my research advisory committee members Dr Arijit Bhattacharayay and Dr Angshuman Nag for their valuable suggestions and continued support in this academic endeavour.

This work would not have been complete without scientific collaboration with Dr. Giacomo Prando (Uni. Pavia, Italy) who led the *mu*SR experiments at PSI, Switzerland. He was kind and patient enough to guide me through my first experience at a beamline and later with the data analysis. It was great to collaborate with Prof. Ajay Sood and Dr. Victor Muthu from IISc for the high-pressure experiments at Elettra synchrotron, Italy. Sincere thanks to Dr. Muthu who joined us at the beamline and taught us handling of the pressure cell. It was rather courageous of him to trust two novice and sleep-deprived students with the very expensive pressure cell. Continuing on this thread, I was lucky to visit several synchrotron facilities during my PhD. This was made possible because of the fantastic funding programs managed by DST which allows Indian research community to access world class research facilities. The work in this thesis benefited immensely from these programs and I hope they continue in future. I would like to take this opportunity to thank all the beam-scientists at various facilities. They were patient, helpful and played a crucial role in ensuring the success of every experiment.

I am sincerely thankful to IISER Pune for providing the best possible infrastructure and an encouraging environment to foster research. The uninterrupted access to various in-house research facilities and support from technical staff was pivotal for sustaining the research work. I would like to thank all the non-academic staff, especially Tushar, Prabhakar and Prabhas for their cooperation and help. I am grateful to all the funding

agencies, IISER Pune, SERB, Infosys, Newton-Bhabha and DST for financial support in the form of salary, experimental visits as well as for supporting conference travels.

My pillars of strength in this journey were my friends and labmates. Each of them supported me and inspired me to do better. It was great learning things from Koushik, who had an amazing knack of teaching various things in the lab. Rabindra always made the lab experience a lot of fun. I started working on the main thesis work with Kshiti and our discussions on science and everything under the sky will forever be treasured. Shanu had a very rare gift of listening capacity and I exploited it often in the Bamboo garden. My abstract dream of assassins that we thought of turning into a novel or a movie remains my plan B. Panja, with his dedication to everything he learns, was a role model for hard work. Company of Luminita ma'am was a delight. Her skill of effortlessly juggling multiple roles is enlivening. I want to thank her for all the delicious and savory snacks that she often treated us with. All the juniors who joined the lab made it merrier. Their help in grinding the never ending synthesis saved me from depression. A special thanks to Saurabh, Prakash, Navita and Anupam for hearty laughs, no-sugar coffees and for being a great lab-member.

Now is the turn to acknowledge the core group which was no less than a shield to any difficulty I ever faced. I never realized when Hridya silently walked into my life. Anjusha and Chetan were the first ones to befriend me in the whole campus. I am thankful to Giri for all the afternoon lunches beneath the bamboo tree for as long as he was around. Anjusha's time management skills still amuse me. I was lucky to personally experience the personality transformation in Ajith. His self-control is inhumane and I have immense respect for him. I owe him a big thank you for being the gadget guru whenever anything tech went wrong and I hope this (free) support will continue in future. Dibyata accompanied me and toiled through the sleepless night during the beamtimes. I will always cherish the bond shared by us at different levels. Krithika is very patient and one of the kindest souls I have ever met. Krithika and Dibyata set couple goals with their nonchalant love for one another.

Lastly, and most importantly, a wholehearted thanks to my family for their constant love, patience, and encouragement. It wasn't easy to pretend to be a hosteller when home was just minutes away. The credit of not feeling guilty of missing many things back home goes to the unconditional support of my parents. The company of my nieces,

Aarya and Ira was always a delight and the much-needed sunshine on gloomy days. A special thanks to my sister for bringing clarity through all the doubts and confusion. I am thankful to Sumit for stepping in my life at the right time that made all the difference.

Ultimately, this acknowledgement cannot be exhaustive as there are too many people who contributed in a number of ways to this journey. I will finish by thanking the almighty for making everything fall in its place.

Date: August 12, 2020

(Prachi Telang)

Abstract

$A_2B_2O_7$ oxides (where A^{3+} is a rare-earth and B^{4+} a transition-metal ion) crystallizing with the cubic pyrochlore structure are well-known three-dimensional spin frustrated systems. The source of frustration in these systems originate from the interpenetrating corner-linked tetrahedral frameworks of A^{3+} and B^{4+} ions.

Recently, some of these pyrochlores with 5d transition metal ions occupying the B-sublattice have gained considerable attention due to their novel topological properties emerging from the interplay of three fundamental energy scales: the onsite Coulomb repulsion (U), crystal field energy (Δ), and, the spin-orbit coupling (λ). In the pyrochlores with $B = \text{Ir}$, these three energies are of the order of 1 eV, which places them at the crossroads leading to strongly correlated systems in large U limit, and topological insulators in the strong λ limit. The energy scale Δ , on the other hand, splits the spin-orbit coupled lowest J-multiplet in Ir^{4+} (d^5), reducing the moment in the ground state to an effective $J = 1/2$. Consequently, the pyrochlore iridates exhibit interesting and unexpected properties, including a spin-liquid ground state in $\text{Pr}_2\text{Ir}_2\text{O}_7$ (PIO), temperature-induced metal-to-insulator transition concomitant with the onset of antiferromagnetic ordering in $R = \text{Nd}, \text{Sm}, \text{Eu}$ and Gd members, and an insulating behaviour in the members consisting of heavier rare-earths. Some of these iridates, namely the ones with $R = \text{Sm}, \text{Eu}, \text{Gd}$ (and Y), are predicted to be in the close proximity of a Weyl semimetallic ground state, which motivated the present research.

In order to realise a possible Weyl semimetallic ground state, we synthesized a series of $(\text{Eu}_{1-x}\text{Bi}_x)_2\text{Ir}_2\text{O}_7$ samples. We chose $\text{Eu}_2\text{Ir}_2\text{O}_7$ (EIO) due to its proximity to the Weyl semimetallic ground state. The other end member $\text{Bi}_2\text{Ir}_2\text{O}_7$ (BIO) (which also crystallize with the cubic pyrochlore structure) is a strongly correlated metal. The crucial point is that both Eu and Bi form their respective compounds, which implies that a solid-solution between them will not affect the valence of Ir , and hence the $J = 1/2$ on the pyrochlore lattice is expected to remain unperturbed throughout the $(\text{Eu}_{1-x}\text{Bi}_x)_2\text{Ir}_2\text{O}_7$ series. Additional advantage of doping with Bi is that the A-site remains magnetically inactive.

We discovered a rather counter-intuitive result in this solid solution series. We found that even though the ionic radius of Bi^{3+} is considerably bigger than Eu^{3+} , dilute Bi doping at the Eu site results in a lattice volume collapse without any apparent structural

change or the valence of the constituents. The lattice contraction was confirmed using high-resolution synchrotron x-ray diffraction. The ground state of EIO was found to be robust for compositions in the anomalous volume contraction region and is strongly suppressed for higher doping concentration. In the anomalous region, we find that dilute Bi-doping tunes the ground state closer to the Weyl point, inferred from the behaviour of ρ vs. T , which is theoretically shown to follow a $1/T$ dependence by Hosur et al. At the metal-insulator boundary at $x = 0.1$, we observed absence of any magnetic ordering confirmed using μ SR down to 20 mK. Further, from the transport behaviour, we conjectured a Quadratic Band Touching (QBT), another novel ground state from which other non-trivial topological phases can be derived, for this composition. We, therefore, conclude that the composition $(\text{Eu}_{1.8}\text{Bi}_{0.2})\text{Ir}_2\text{O}_7$ is the parent phase hosting a QBT from which the WSM phase is derived through breaking of the time reversal symmetry in a narrow composition range around $x = 0.02$ where the index 'n' in the $1/T^n$ fit approaches $n = 1$ over a broad temperature range.

We further extended this study to other members of the pyrochlore iridate series $\text{A}_2\text{Ir}_2\text{O}_7$ ($\text{A} = \text{Sm}, \text{Gd}$ and Dy) series. Though the anomalous lattice contraction was observed at dilute Bi doping in all the members, it was found to be the highest for the Bi substituted $\text{Sm}_2\text{Ir}_2\text{O}_7$ (SIO). As BIO and SIO have the same lattice constant value, this established the electronic origin of the anomalous lattice contraction phenomena. Bi doping affected the physical properties for all the pyrochlore iridates. As the difference between the A-site ionic radius and Bi decreased, rapid suppression of the insulating and magnetic ground state of the pyrochlore compounds was observed.

We carried out photoelectron spectroscopy to understand the mechanism of the metal-insulator transition in the $(\text{Eu}_{1-x}\text{Bi}_x)_2\text{Ir}_2\text{O}_7$ series. The core-level spectra along with the valence band spectra indicated hybridisation between Bi 6p and Ir 5d orbitals as a possible mechanism for the emergence of metallic behaviour with increasing Bi doping. Additionally, we confirmed that the valence state of Eu, Bi and Ir remains unchanged over the whole range of x values.

Our study suggests that Bi-doping in pyrochlore iridates is a unique way to realise novel ground states in this system. This is achieved as the isovalent Bi doping preserves the Ir^{4+} sublattice, which is a key to obtaining various non-trivial topological phases. In particular, we show that dilute Bi doping is a possible route to realizing the Weyl

semimetallic ground state in $A = \text{Eu}$, and Sm . Our findings are expected to motivate further research in exploring new quantum phases in the $U - \lambda$ phase space of $5d$ transition metal oxides.

List of publications

- **Anomalous lattice contraction and emergent electronic phases in Bi-doped $\text{Eu}_2\text{Ir}_2\text{O}_7$; Prachi Telang**, Kshiti Mishra, Giacomo Prando, A. K. Sood, Surjeet Singh *Phys. Rev. B* 99, 201112(R) (2019)
- **Dilute stuffing in the pyrochlore iridate $\text{Eu}_2\text{Ir}_2\text{O}_7$; Prachi Telang**, Kshiti Mishra, A. K. Sood, Surjeet Singh *Phys. Rev. B* 97, 235118 (2018).
- **Monopole-limited nucleation of magnetism in $\text{Eu}_2\text{Ir}_2\text{O}_7$; Giacomo Prando, Prachi Telang**, Stephen D. Wilson, Michael J. Graf, Surjeet Singh *Phys. Rev. B* 101, 174435 (2020).
- **On the effect of isovalent Bi substitution at the Eu site in the pyrochlore $\text{Eu}_2\text{Ir}_2\text{O}_7$; Prachi Telang**, Kshiti Mishra, Surjeet Singh *AIP Conference Proceedings* 1942, 110051 (2018).
- **One-shot wet chemical synthesis and properties of pyrochlore iridates $\text{A}_2\text{Ir}_2\text{O}_7$; Haritha Rajeev, Prachi Telang** and Surjeet Singh *Solid state communications* 312, 113863 (2020)
- **Metal-insulator transition in $(\text{Eu}_{1-x}\text{Bi}_x)_2\text{Ir}_2\text{O}_7$ - HAXPS study; Prachi Telang** and Surjeet Singh (to be submitted)
- **Laser-diode-heated floating-zone crystal growth of ErVO_3 ; Prachi Telang**, Andrey Maljuk, Dibyata Rout, Rongwei Hu, Markos Skoulatos, Koushik Karmakar, Silvia Seiro, Bertrand Roessli, Uwe Stuhr, Bernd Büchner, Sang-Wook Cheong, Surjeet Singh *Journal of crystal growth* 507, 406 (2019).
- **Magnetic properties of high-pressure optical floating-zone grown LaNiO_3 single crystals; Kaustav Dey, Waldemar Hergett, Prachi Telang**, Mahmoud M. Abdel-Hafiez and Rüdiger Klingeler *Journal of crystal growth* 524, 125157 (2019)
- **Imaging the coherent propagation of collective modes in the excitonic insulator candidate Ta_2NiSe_5 at room temperature; Paolo Andrich, Hope M.**

Bretscher, Yuta Murakami, Denis Golez, Benjamin Remez, **Prachi Telang**, Anupam Singh, Luminita Harnagea, Nigel R. Cooper, Andrew J. Millis, Philipp Werner, A. K. Sood, Akshay Rao *arXiv:2003.10799*

List of Figures

1.1	Hubbard model for the half filling case. W , E_F and U are the bandwidth, the Fermi energy and the electron correlation energy respectively. LHB and UHB here refers to the lower and upper Hubbard bands, respectively.	3
1.2	Crystal field splitting of the d orbitals in a transition metal ion in an octahedral coordination	5
1.3	Crystal field splitting of Ir^{4+} in an octahedral environment. (Adapted from Ref [1])	7
1.4	Various electronic phases that could be realised by tuning the interction strength in condensed matter systems. (Adapted from Ref [2])	8
1.5	Schematic of the formation of topological surface states (a) normal band structure, (b)band inversion due to strong spin-orbit coupling, (c) band renormalization, and (d) formation of the topological surface states. (Adapted from Ref [3])	9
1.6	A sphere has genus=0 and the torus has genus= 1 whereas the third shape with two holes has genus=2.	10
1.7	Bulk states represented by Weyl nodes and their surface projection depicted by Fermi arcs.	13
1.8	Conventional unit cell of the pyrochlore $\text{A}_2\text{B}_2\text{O}_7$ structure with (a) only A^{3+} and B^{4+} sublattices shown, and (b) B-O_6 octahedra and $\text{A-O}_6\text{-O}'_2$ scalenhedron are shown in the unit cell.	15
1.9	Geometric frustration arising due to triangular arrangement of the spins interacting antiferromagnetically.	16

1.10	a) All-in spin arrangement b) 2-in-2-out spin ice arrangement c) 3-in-1-out spin arrangement	17
1.11	Phase diagram of transport properties of pyrochlore oxide series plotted against the rare-earth radius.(Adapted from Ref [4])	20
1.12	a)Schematic mean-field phase diagram of the Hubbard model on the pyrochlore lattice showing the narrow range of stability of WSM ground state in pyrochlore iridates b) Evolution of the electronic spectrum along the three points (stars) highlighted on the vertical dashed line in panel a. The red circle shows one Weyl point at the Fermi level (horizontal dashed line). The spectrum is plotted along high symmetry lines in the Brillouin zone.(Adapted from Krempa et al [2])	21
2.1	Bruker D8 advance diffractometer at IISER Pune. The photograph shows the brag-brentano geometry of the instrument with the rotating x-ray source and detector as well as the fixed sample holder.	27
2.2	SEM instrument (Zeiss Ultra Plus) at IISER Pune that was used for EDS and imaging purpose in this thesis.	28
2.3	Experimental setup at the MCX (material characterization beamline), Elettra-synchrotron, Italy. a) Glass capillary filled with sample and mounted on a goniometer which can be adjusted to align the capillary with the incoming x-ray beam b) The transmission geometry of the experiment where the synchrotron x-ray beam comes from a stationary outlet and falls on the capillary which rotates about itself. The stopper stops any undiffracted x-rays. The detector (not shown here) rotates to spans the 2θ range.	30
2.4	A schematic showing the four probe method of measuring the electrical resistivity. I^+ and I^- are the current probes and V^+ and V^- are the corresponding voltage probes.	36
2.5	Samples mounted with four probe geometry on a PPMS resistivity probe	36

2.6	Schematic of a typical four terminal thermal transport measurement assembly (adopted from PPMS, Quantum design manual) and image of a pyrochlore sample mounted for thermopower measurement. The shoe with red dot and blue dot correspond to hot thermometer and cold thermometer respectively.	38
2.7	Top panel: Time trace of hot and cold thermometers during an idealized heat pulse where the base temperature is slowly ramped. Middle panel: Corresponding temperature ΔT and voltage ΔV differentials across the sample, indicating thermal time constants τ_1 and τ_2 and the estimate of the asymptotic differential ΔT_∞ (adopted from TTO manual).	39
2.8	Schematic depicting the sample holder for specific heat arrangement. . .	42
2.9	Angular distribution of positron from μ^+ decay. The asymmetry $a = 1/3$ when all positrons energies are detected with equal probability.	47
2.10	Detector geometry for general purpose spectrometer at PSI (adapted from PSI website)	48
2.11	Schematic of hemispherical analyser. The electrons from the sample pass through lens (electron optics) before entering the analyser through entrance slit S. The electrons exit after passing through the analyser where they are captured by the detector.	52
2.12	HAXPES setup at P22 beamline, Petra III, DESY, Germany.	53
2.13	Schematic of different energy levels involved in a photoemission experiment. E_B is the binding energy of electrons and $\hbar\omega$ is the kinetic energy of the electrons knocked off from the sample. E_{vac} (sample/analyser) is the vacuum energy with respect to sample and analyser respectively. Φ represents the work function.	54
3.1	High-resolution synchrotron powder x-ray diffraction data of various $\text{Eu}_2\text{Ir}_2\text{O}_7$ samples A, B1, B2, C2, C1 and D (see Table 3.1 for details) in the 2θ range covering the Bragg peak (6 2 2), chosen as representative to demonstrate a slight rightward shift of the pattern from C1 to A0 (dashed line is a guide to eye).	59

3.2	Rietveld refinement of composition A and B1. Inset compares precursor impurities with pyrochlore phase, e: Eu_2O_3 ; i: IrO_2 ; p:pyrochlore phase and * marks unidentified phase.	62
3.3	Rietveld refinement of composition B2 and C1. Inset compares precursor impurities with pyrochlore phase, e: Eu_2O_3 ; i: IrO_2 ; p:pyrochlore phase and * marks unidentified phase.	63
3.4	Rietveld refinement of composition C2 and D. Inset compares precursor impurities with pyrochlore phase, e: Eu_2O_3 ; i: IrO_2 ; p:pyrochlore phase and * marks unidentified phase.	64
3.5	(a) to (e) Temperature (T) variation of specific heat (C_p) plotted as C_p/T Vs. T^2 for samples: A0, B1, B2, C2 & C1 shown over a narrow temperature range around the AFM/MI transition. The vertical dashed lines are guide to eye to show the onset of transition and transition width; (f) C_p/T Vs. T^2 shown over the whole measurement temperature range for sample B2. (g) C_p/T Vs. T^2 for all the samples at low-temperatures. The dashed lines are straight-line fits to the data (see text for details) . . .	68
3.6	(a-f) Zero-Field-Cooled (ZFC) and Field-cooled (FC) susceptibility of all the $\text{Eu}_2\text{Ir}_2\text{O}_7$ samples is shown as a function of temperature in a small temperature range around the magnetic ordering temperature; (g) The ZFC and FC susceptibilities over the whole temperature range are shown for sample A as representative. χ_{VV} is Van Vleck susceptibility of Eu^{3+} ion (see text for details).	70
3.7	(a) $\rho(T)/\rho(300K)$ plotted as a function of temperature (T) for various $\text{Eu}_2\text{Ir}_2\text{O}_7$ samples (A, B1, B2, C2, C1 & D); (b) first derivative $\rho' = d\rho/dT$ of the resistivity plots as a function of temperature around the metal-insulator transition. In the inset ρ' is shown for samples B2 and D over a wider temperature range to demonstrate the change of sign of $d\rho/dT$	72
3.8	Thermoelectric power (S) plotted as a function of temperature for various $\text{Eu}_2\text{Ir}_2\text{O}_7$ samples: B1, B2 & C1. The dotted lines are a guide to the eye.	74

4.1	(a) X-ray diffractograms collected at MCX beamline, Elettra-Synchrotron, Italy showing the formation of pyrochlore phase for the entire series $(\text{Eu}_{1-x}\text{Bi}_x)_2\text{Ir}_2\text{O}_7$. Panel (b) and (c) show shift in peak 400 and 440 across the series.	84
4.2	x dependence of the parameter δ . The inset shows the variation of $a(x)$ in the range $0 \leq x \leq 0.1$ for $(\text{Eu}_{1-x}\text{Bi}_x)_2\text{Ir}_2\text{O}_7$ (Ir) and $(\text{Eu}_{1-x}\text{Bi}_x)_2\text{Sn}_2\text{O}_7$ (Sn).	85
4.3	Rietveld refinement of the samples in the series $(\text{Eu}_{1-x}\text{Bi}_x)_2\text{Ir}_2\text{O}_7$ for $x = 0, 0.02, 0.035$ and 0.05	86
4.4	Rietveld refinement of the samples in the series $(\text{Eu}_{1-x}\text{Bi}_x)_2\text{Ir}_2\text{O}_7$ for $x = 0.1, 0.25, 0.5$ and 1	87
4.5	Evolution of structural parameters in the series $(\text{Eu}_{1-x}\text{Bi}_x)_2\text{Ir}_2\text{O}_7$	88
4.6	FESEM images of samples in the series $\text{Eu}_{2-2x}\text{Bi}_{2x}\text{Ir}_2\text{O}_7$. The grain size increases with increasing Bi concentration.	91
4.7	(Left panel) The susceptibility (χ) for $x \leq 0.1$ is shown as a function of temperature. Thermomagnetic hysteresis is seen only for $x = 0, 0.02, 0.035$ and 0.05 sample; the upper (lower) branch represents FC (ZFC) data. (Right Panel) (χ) for $x \geq 0.25$ is shown as a function of temperature	93
4.8	Representative zero-field depolarization curves for the μ^+ spins in the time domain for four $(\text{Eu}_{1-x}\text{Bi}_x)_2\text{Ir}_2\text{O}_7$ samples in the limit $x \leq 0.1$. We obtain the continuous lines after fitting the data to Eq. (4.1). The temperature values are rounded to the closest integer.	94
4.9	(a) The temperature variation of normalized resistivity ρ/ρ_{300} for various x . The inset in (a) shows the power law fit at low-temperatures for $x = 0, 0.02$ and 0.035 . (b), (c) and (d) show the temperature variation of ρ for $x = 0.1, 0.25$ and 1 samples, respectively. The straight line highlights T (b), T^2 (c) and $T^{3/2}$ (d) variation for $x = 0.1, 0.25$ and 1 , respectively. The inset in (b) shows the low-temperature resistivity minimum. The straight line showing a $-\ln T$ increase is a guide to eye.	96
4.10	Power law fit at low-temperatures for $x = 0, 0.02$ and 0.035	97
4.11	The temperature variation of thermopower S for $x = 0, 0.02, 0.035, 0.05, 0.1$ and 1	99

4.12	(a) the specific heat is plotted as C_p/T versus T^2 for $0 \leq x \leq 0.25$. The straight lines through the data points are linear fits $\gamma + \beta T^2$ (b) the variation of γ is shown as a function of x for the whole series.	100
4.13	Pictorial representation of tuning of the Fermi level with Bi concentration. Fermi level is closest to the Weyl crossing for $x = 0.02$ and the ground state is reminiscent of quadratic band touching for $x = 0.1$	101
5.1	3d core level spectra of Europium. The spectra consist of the standard $3d_{3/2}$ and $3d_{5/2}$ peaks along with three satellite peaks denoted by S1, S2, and S3.	107
5.2	4f core level spectra of Iridium.	110
5.3	4f core level spectra of Bismuth.	113
5.4	(a)Valence band spectra of different compositions in the series $(\text{Eu}_{1-x}\text{Bi}_x)_2\text{Ir}_2\text{O}_7$, (b) The region around 12 eV depicting Bi $6s^2$ spectra.	114
5.5	(a)Valence band spectra showing the increasing spectral weight near E_F with Bi doping. (b) Formation of new shoulder peak near E_F for $x \geq 0.1$. 114	
6.1	(a) Evolution of [444] powder x-ray diffraction peak (b) Lattice parameter evolution across the series $\text{Sm}_{1-x}\text{Bi}_x)_2\text{Ir}_2\text{O}_7$	117
6.2	Refinement plots for $x = 0, 0.02, 0.1$ and 0.5 in $(\text{Sm}_{1-x}\text{Bi}_x)_2\text{Ir}_2\text{O}_7$. A mixed phase refinement was carried out for all the samples with the main pyrochlore phase and Si; Panel (a) highlights all the prominent Si peaks with the star sign.	119
6.3	(a) Peak evolution across the $(\text{Gd}_{1-x}\text{Bi}_x)_2\text{Ir}_2\text{O}_7$ series (data collected from Argonne National Laboratory) (b) Lattice parameter evolution across the series.	122
6.4	Representative refinement plot for $x = 0.035$ and 0.25 . For the compositions in the range $x \leq 0.1$, mixed phase refinement consisting the pyrochlore phase and the precursor phases were carried out. For $x = 0.25$, single phase refinement was carried out.	122
6.5	(a) Peak evolution across the $\text{Dy}_{1-x}\text{Bi}_x)_2\text{Ir}_2\text{O}_7$ series (b) Evolution of lattice parameters extracted from unit cell.	123

6.6	(a) The temperature variation of absolute resistivity for various x . The resistivity shows a sudden decrease in the magnitude for $x = 0.035$ which is apparent from the scaling on the y-axis.(b) The susceptibility (χ) for $x \leq 0.1$ is shown as a function of temperature. Thermomagnetic hysteresis is seen only for $x = 0, 0.02$ and 0.035 sample; the upper (lower) branch represents FC (ZFC) data. The kink in the $x = 0.05$ data around 50 K corresponds to the ordering of trapped oxygen.	124
6.7	Low temperature fitting of ρ for $x = 0$ and 0.02	125
6.8	Thermopower plotted as a function of temperature for $x = 0, 0.02, 0.035, 0.05$ and 1 .126	
6.9	Transport plotted as a function of temperature for (a) $(\text{Dy}_{1-x}\text{Bi}_x)_2\text{Ir}_2\text{O}_7$ and (b) $(\text{Gd}_{1-x}\text{Bi}_x)_2\text{Ir}_2\text{O}_7$	127
6.10	(a) χ vs. T plotted for the members of the series $(\text{Gd}_{1-x}\text{Bi}_x)_2\text{Ir}_2\text{O}_7$. (b) $1/\chi$ plotted vs T for $x = 0.035$; the red line shows the Curie-Weiss fit to the data in the range 200 - 300 K. The inset panel shows the bifurcation between ZFC and FC susceptibility marking the transition temperature. .	128
6.11	S plotted as a function of temperature for selected compositions in the series (a) $(\text{Dy}_{1-x}\text{Bi}_x)_2\text{Ir}_2\text{O}_7$ and (b) $(\text{Gd}_{1-x}\text{Bi}_x)_2\text{Ir}_2\text{O}_7$	130
7.1	Phase diagram of the pyrochlore iridates.	135
A.1	Rietveld refinement of powder x-ray diffraction data of $\text{Yb}_{2-x}\text{Sn}_{2+x}\text{O}_7$ samples for $x = 0.1$. In this sample, due to the presence of SnO_2 peaks, a multi-phase refinement was carried out. Inset shows the fitting for a SnO_2 (S) as well as pyrochlore(P) peak.	140
A.2	Rietveld refinement of the powder x-ray diffraction data of $\text{Yb}_{2-x}\text{Sn}_{2+x}\text{O}_7$ samples for $x = 0, 0.04, -0.04, -0.1$. Inset panel for $y = 0.04$ shows absence of any SnO_2 impurity peak.	141

A.3	Rietveld refinement of neutron diffraction data of $\text{Yb}_{1.96}\text{Sn}_{2.04}\text{O}_7$ sample. The inset panels highlight two different angular ranges. It can be seen that at smaller angle (inset a), the calculated profile is right shifted compared to the experimental data whereas at higher angles (inset b), exactly opposite trend was observed. This issue was a consequence of time lag while integrating the data from different detectors. The lattice parameters extracted by refining this data could not be trusted as lattice parameter value depended on the angular range selected for the refinement.	142
A.4	Lattice parameters of $\text{Yb}_{2-x}\text{Sn}_{2+x}\text{O}_7$ samples plotted against x.	142
A.5	Left Panel: Heat capacity of $\text{Yb}_{2-x}\text{Sn}_{2+x}\text{O}_7$ for $x = 0, -0.1, 0.1$. Right panel: Field dependence of heat capacity of $\text{Yb}_2\text{Sn}_2\text{O}_7$	143
B.1	Evolution of the x-ray diffraction pattern in the pressure range of 0-19 GPa for $x = 0$	146
B.2	Evolution of the x-ray diffraction pattern in the pressure range of 0-21 GPa for $x = 0.035$	147
B.3	Evolution of the x-ray diffraction pattern in the pressure range of 0-20 GPa for $x = 0.1$	148
B.4	Evolution of the x-ray diffraction pattern in the pressure range of 0-21 GPa for $x = 0.75$	149
B.5	The change in volume ΔV with respect to ambient pressure lattice volume V_0 plotted against the applied pressure for all the samples studied here.	150
B.6	Fitting of the Birch-Murnaghan equation to the lattice volume change plotted as a function of pressure.	150
B.7	(a) Evolution of lattice parameter with temperature for $x = 0, 0.02, 0.1$ and 1 in the series $(\text{Eu}_{1-x}\text{Bi}_x)_2\text{Ir}_2\text{O}_7$ (a_0 denotes the lattice constant at room temperature). (b) Comparison of lattice contraction at room temperature vs at 90 K.	151

B.8 844 peak in the pyrochlore xrd pattern for different compositions showing the evolution of FWHM with lowering of the temperature. The samples with magnetic transition (left panel) show increase in the FWHM in addition to the peaks shifting to higher two theta values with lowering of temperature; whereas only right-shift of the peak position with decreasing the temperature can be observed for the non-magnetic samples (right panel). 152

List of Tables

3.1	Structural parameters for various $\text{Eu}_2\text{Ir}_2\text{O}_7$ samples, labeled A, B1, B2, C1, C2 & D, obtained using Rietveld refinement of the high-resolution synchrotron powder x-ray diffraction data. Parameters characterizing the quality of fit are also included	65
4.1	Goodness of fit parameters for different values of x in $(\text{Eu}_{1-x}\text{Bi}_x)_2\text{Ir}_2\text{O}_7$ samples, obtained using Rietveld refinement of the high-resolution synchrotron powder X-ray diffraction data.* All the occupancies carry an error bar of 0.015	89
4.2	Eu:Bi ratio calculated from EDX measurements	92
4.3	Resistivity value at 2 K and 300 K for different values of x in $\text{Eu}_{2-2x}\text{Bi}_{2x}\text{Ir}_2\text{O}_7$	98
5.1	Eu 3d core level peaks for various compositions of the series $\text{Eu}_{2-2x}\text{Bi}_{2x}\text{Ir}_2\text{O}_7$. In addition to the core shell lines, there are three satellite peaks corresponding to S1, S2, and S3.	106
5.2	Ir 4f core level peaks for all the measured compositions in the series $\text{Eu}_{2-2x}\text{Bi}_{2x}\text{Ir}_2\text{O}_7$. In addition to the core shell lines corresponding to $4f_{5/2}(\text{I/II})$ and $4f_{7/2}(\text{I,II})$, there are additional satellite peaks named as S1, S2, and S3. S2 and S3 peaks were required during the fitting of samples deep in the metallic regime i.e. $x \geq 0.25$ and could be a result of final state effect.	111

5.3	Bi 4f core level peaks for all the measured compositions in the series $\text{Eu}_{2-2x}\text{Bi}_{2x}\text{Ir}_2\text{O}_7$. E represents the extraneous feature in the spectra which was held fixed at a given value while fitting the spectra for all the compositions.	112
6.1	Goodness of fit parameters for different values of x in $(\text{Sm}_{1-x}\text{Bi}_x)_2\text{Ir}_2\text{O}_7$ samples, obtained using Rietveld refinement of the high-resolution synchrotron powder X-ray diffraction data.	120
6.2	Goodness of fit parameters for different values of x in $(\text{Gd}_{1-x}\text{Bi}_x)_2\text{Ir}_2\text{O}_7$ samples, obtained using Rietveld refinement of the high-resolution synchrotron powder x-ray diffraction data in the case of Gd. The last column represents lattice parameters extracted using unit cell from the lab based x-ray data in the case of $(\text{Dy}_{1-x}\text{Bi}_x)_2\text{Ir}_2\text{O}_7$	121
6.3	Parameters obtained from fitting of the magnetization data using Curie-Weiss expression $\chi = C/(T - \theta_P)$ for $(\text{Gd}_{1-x}\text{Bi}_x)_2\text{Ir}_2\text{O}_7$. μ_{eff}/Ir is calculated assuming Gd moments to be $7.9 \mu_B$ and the lande-g factor for Ir to be 2. But the Gd ordering moment can range between $7.9 - 8.1 \mu_B$ and value of g_J for Ir can differ from 2 in the strong SOC limit, hence the μ_{eff}/Ir carries a considerable error bar.	129
A.1	Goodness of fit parameters for different values of x in $\text{Yb}_{2-x}\text{Sn}_{2+x}\text{O}_7$ samples, obtained using Rietveld refinement of powder X-ray diffraction data.	139

Contents

Declaration	vii
Acknowledgments	ix
Abstract	xiii
List of publications	xvii
List of figures	xix
List of tables	xxix
1 Introduction	1
1.1 Electronic interactions in transition metal oxides	2
1.1.1 Electron-electron correlations (U)	2
1.1.2 Crystal Field	4
1.1.3 Spin-orbit coupling	4
1.2 Topology in condensed matter physics	7
1.2.1 Weyl Semimetal	10
1.2.2 Magnetism in pyrochlore oxides	15
1.2.3 Spin Ice	18
1.2.4 Previous studies on pyrochlore iridates	19

2	Experimental Methods	23
2.1	Synthesis	23
2.2	Structural and composition characterization	25
2.2.1	Powder x-ray diffraction	25
2.2.2	Scanning electron microscopy	27
2.2.3	Synchrotron x-ray diffraction	29
2.2.4	Neutron powder diffraction	31
2.2.5	Rietveld refinement	32
2.3	Physical properties	34
2.3.1	Electrical transport	35
2.3.2	Thermal and thermoelectric transport	37
2.3.3	Specific Heat	41
2.3.4	dc susceptibility	44
2.4	Muon spin spectroscopy	45
2.5	Hard x-ray photoelectron spectroscopy	48
2.5.1	Spin-orbit coupling	50
2.5.2	Chemical Shifts	50
2.5.3	Satellite peaks	51
2.5.4	Hard x-ray photoemission spectroscopy	51
2.5.5	Working principle of instrumental setup	51
3	Effect of stuffing in pyrochlores	55
3.1	Stuffing in pyrochlore oxides	55
3.2	Motivation for stuffing in pyrochlore iridate $\text{Eu}_2\text{Ir}_2\text{O}_7$	56
3.2.1	Synthesis Protocol	57
3.2.2	Effect of stuffing on the structure	58
3.3	Effect of stuffing on the physical properties	66
3.3.1	Specific Heat	66
3.3.2	Magnetic susceptibility	69
3.3.3	Electric transport	71
3.3.4	Thermopower	74
3.4	Discussion on the sign of $d\rho/dT$	76
3.5	Summary	79

4	Effect of Bi substitution on $\text{Eu}_2\text{Ir}_2\text{O}_7$	81
4.1	Ground state of $\text{Eu}_2\text{Ir}_2\text{O}_7$ and $\text{Bi}_2\text{Ir}_2\text{O}_7$	81
4.2	Synthesis and structural characterization	82
4.3	Effect of Bi substitution on physical properties	92
4.3.1	Magnetic susceptibility and Muon Spin spectroscopy	92
4.3.2	Electrical transport	95
4.3.3	Thermoelectric properties	98
4.3.4	Heat capacity	99
4.4	Discussion	100
4.5	Summary	103
5	X-ray photoemission studies of $(\text{Eu}_{1-x}\text{Bi}_x)_2\text{Ir}_2\text{O}_7$	105
5.1	Europium core shell spectra	106
5.2	Ir core level spectra	108
5.3	Bi core level spectra	109
5.4	Valence Band Spectra	112
5.5	Discussion	115
5.6	Summary	115
6	Effect of Bi substitution in some other members of the pyrochlore iridate series	116
6.1	Synthesis and structural characterization	117
6.1.1	Lattice parameter variation in $(\text{Sm}_{1-x}\text{Bi}_x)_2\text{Ir}_2\text{O}_7$	117
6.1.2	Lattice parameter variation in $(\text{Gd}/\text{Dy}_{1-x}\text{Bi}_x)_2\text{Ir}_2\text{O}_7$	118
6.2	Physical properties	124
6.2.1	Physical properties of the series $(\text{Sm}_{1-x}\text{Bi}_x)_2\text{Ir}_2\text{O}_7$	124
6.2.2	Physical properties of the series $(\text{Gd}/\text{Dy}_{1-x}\text{Bi}_x)_2\text{Ir}_2\text{O}_7$	127
6.3	Discussion and Summary	130
7	Summary and Outlook	133
Appendix A	Stuffing studies in pyrochlore stannate $\text{Yb}_2\text{Sn}_2\text{O}_7$	137
A.1	137
A.1.1	Synthesis and structural characterization	138

A.1.2	Specific heat of $\text{Yb}_{2-x}\text{Sn}_{2+x}\text{O}_7$	140
A.2	Summary	143
Appendix B	Some additional measurements on the $(\text{Eu}_{1-x}\text{Bi}_x)_2\text{Ir}_2\text{O}_7$ series	145
B.1	High-pressure x-ray diffraction measurements	145
B.2	Low temperature x-ray diffraction	148
B.3	Summary	151
Bibliography		153

Chapter 1

Introduction

Phase transitions and new phases of matter have continued to challenge our understanding of the quantum condensed matter systems. For decades, phase transitions were thought to be facilitated by the breaking of some symmetry. For example, magnetic ordering emerges due to breaking of the time-reversal symmetry; the crystallization of water into ice, on the other hand, involves broken translational symmetry. This paradigm, however, was challenged with the discovery of topological order in some condensed matter systems in the year 1982 [5]. Since then many electronic phases with novel topologies have been predicted theoretically and few have also been realized experimentally. Examples of these electronic phases, across the research frontier, span from graphene to the topological insulators and beyond. Still, several theoretical predictions of various novel topological phases are yet to be realized experimentally. Due to this reason, significant efforts are concentrated around materials with strong spin-orbit interaction, which provide a fertile ground for experimental realization of novel topological phases as will be discussed in detail in some of the subsequent sections of this chapter.

Until recently, systems investigated for their topological features were predominantly s- and p- electron systems, such as Bi_2Se_3 [6]. However, recently, oxides of 5d transition metals have garnered attention due to the presence of strong spin-orbit interaction. Oxides of Rhenium, Osmium, Iridium and neighbouring metals constitute the family of 5d transition metal oxides (TMOs). In 5d TMOs, the electron correlation energy is less when compared to their 3d counterparts due to the spatially extended nature of 5d orbitals. On the other hand, due to the large atomic number of 5d elements, the

spin-orbit interaction in their compounds is significant enough that it cannot be treated as a perturbation anymore. Thus, 5d TMOs sit at the crossroads where both the electronic correlation and spin-orbit coupling determines the ground state. In this chapter, we will give an introduction to important interactions in 5d TMOs and how the interplay of these interactions gives rise to novel topological states such as axion insulator, Weyl semimetal, etc. Then we would narrow down our discussion to oxides of Iridium crystallizing with the pyrochlore structure, also known as pyrochlore iridates, where we would learn about their structure and physical properties.

1.1 Electronic interactions in transition metal oxides

Much of condensed matter is about how different kinds of order emerge from interactions between many simple constituents. An ideal example of this is the family of transition metal oxides (TMOs) where a plethora of novel phenomena such as high- T_C superconductivity, colossal magnetoresistance, and metal-insulator transitions could be observed as a result of the complex interplay of various electronic interactions such as electron correlations (U), crystal field splitting (Δ) and spin-orbit coupling (λ) [7]. The magnitude of these interactions depends on a number of factors like the atomic number of the transition metal, underlying crystal geometry, ligand environment around the transition metal, etc. Understanding the interplay of these interactions which ultimately decides the ground state is one of the fundamental problems in condensed matter physics. In this chapter, we will look at the three most dominant and relevant interactions that are responsible for governing the ground state of 5d TMOs.

1.1.1 Electron-electron correlations (U)

Failure of band theory to explain the insulating ground state in TMOs highlighted the importance of electron-electron interactions. In TMOs, the conduction is driven by d-orbitals which are spatially compact when compared to the s- or p-orbitals in simple metals. This results in strong Coulomb repulsion between the d electrons of TMOs. The transition from metallic to insulating state due to strong electron correlations was successfully modeled theoretically via Hubbard model given by John Hubbard [8]. It is given as follows:

$$\hat{H} = -t \sum_{i,\sigma} \left(\hat{c}_{i,\sigma}^\dagger \hat{c}_{i+1,\sigma} + \hat{c}_{i+1,\sigma}^\dagger \hat{c}_{i,\sigma} \right) + U \sum_i \hat{n}_{i\uparrow} \hat{n}_{i\downarrow} \quad (1.1)$$

The first term of the above equation, when considered alone, is just the tight-binding model for a single orbital. It represents the electron hopping from site i to its nearest neighbor, where $\hat{c}_{i,\sigma}^\dagger$ is the creation operator of an electron with spin σ at site i . The second term represents the interaction between two electrons on the same site. It predicts a transition from metal to insulator as the ratio of interaction to hopping $\frac{U}{t}$, is varied. This ratio can be modified by increasing the inter-atomic spacing, which would decrease the magnitude of t without affecting U . In the limit where $\frac{U}{t} \gg 1$, we end up with a set of isolated magnetic moments. If $\frac{U}{t}$ is not too large, then the overlap integral facilitates superexchange interaction between neighboring magnetic moments, which may lead to a variety of interesting magnetic correlations, such as ferromagnetic, antiferromagnetic, etc. depending on the parameters of the model.

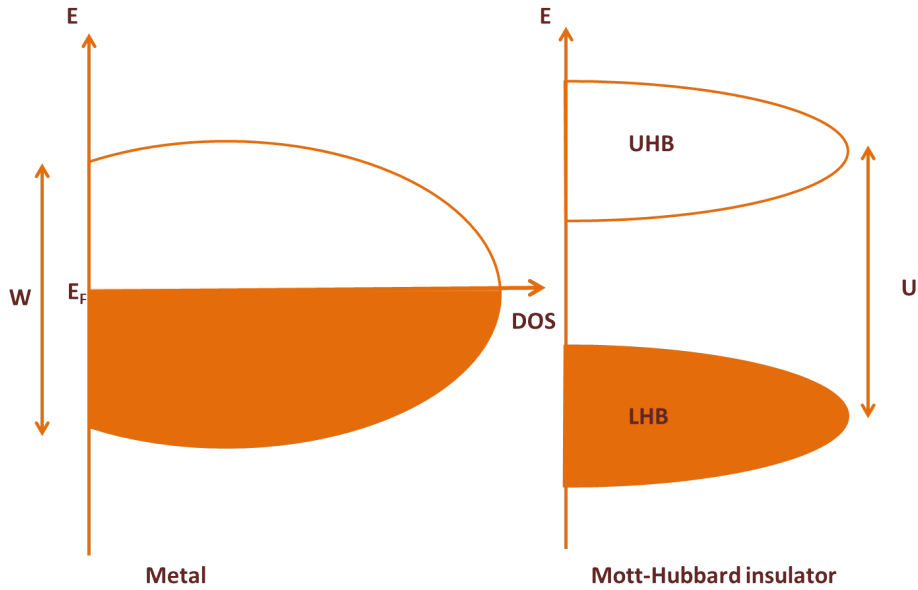


Figure 1.1: Hubbard model for the half filling case. W , E_F and U are the bandwidth, the Fermi energy and the electron correlation energy respectively. LHB and UHB here refers to the lower and upper Hubbard bands, respectively.

The effect of Coulomb repulsion in the single band model is shown schematically in Fig. 1.1. In the limiting case of $U = 0$, the system is just the free-electron model, and we find a simple metallic band with an effective bandwidth $\sim W$. When $U \gg W$ the

electrons become localized and the system splits into two subbands with a gap of size $\sim U$. In the case of half-filling, the lower band is completely filled, forming an insulating state, known as a Mott insulator [9]. Looking at this another way, the system now has a single electron localized to each site such that each site has a magnetic moment; this is why, in light of virtual transitions in second-order perturbation theory, this state is often coincident with an antiferromagnetic ground state. In the intermediate regime where U and W have comparable strengths, a cross-over from metallic to insulating behavior is expected which may depend sensitively on details of the band structure, filling fraction and other perturbations to the Hubbard model. Interesting physics could originate when other interactions such as spin-orbit coupling and crystal field of comparable strength are also present.

1.1.2 Crystal Field

Crystal field effect refers to the lifting of the degeneracy of electron orbitals of the metal ion due to the steric electric field arising from a specific geometry of the surrounding ligand charge distribution. In the context of TMOs, the electrons in the d-orbitals closer to the ligand ions experience maximum repulsion and thus are lifted to higher energy whereas orbitals pointing away from the ligands are pushed to lower energy which results in breaking of the orbital degeneracy. This splitting depends on the factors such as oxidation state of cation, ligand coordination, metal-ligand distance and so on.

For example, if we consider a transition metal ion surrounded by oxygen ions in the octahedral arrangement. The octahedral crystalline field splits the metal d-orbitals into two groups: the doubly degenerate e_g , and triply degenerate t_{2g} separated by an energy gap Δ . Because e_g states have lobes pointing along the coordinate axis, they are higher in energy compared to the t_{2g} states that have lobes pointing along the diagonals.

1.1.3 Spin-orbit coupling

Spin-orbit coupling (SOC), as the name suggests, refers to the entanglement of spin degrees of freedom with the orbital degrees of freedom. The spin-orbit interaction is a relativistic effect which is obtained from the solution of Dirac equation [10]. In the rest frame of an electron moving with relativistic velocity (v) in the electric field (E) of the nucleus, the electric field transforms into a magnetic field B_{eff} by the Lorentz transformation.

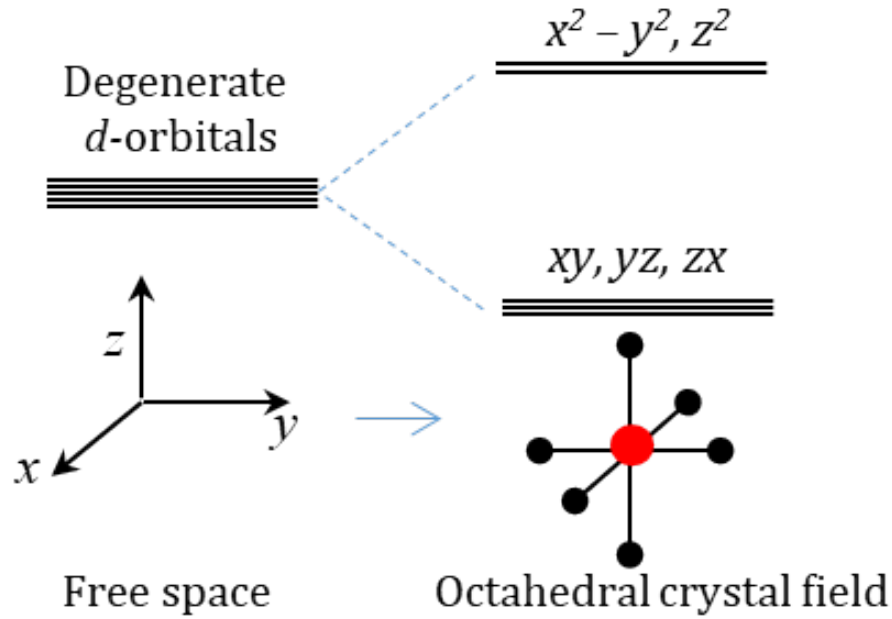


Figure 1.2: Crystal field splitting of the d orbitals in a transition metal ion in an octahedral coordination

$$B_{eff} = (v \times E) / c \quad (1.2)$$

This magnetic field experienced by the electron in its rest frame affects the energy and spin dynamics of the electron. This interaction is termed as the spin-orbit interaction. The Hamiltonian of the spin-orbit interaction can be obtained by either considering the coupling between electron spin with the magnetic field from the orbiting nucleus or by solving the Dirac Hamiltonian for an electron in the electrostatic field. Using either of the methods, the spin-orbit Hamiltonian for a Hydrogen like atom is given by

$$H = \frac{1}{2m^2c^2} \left(\frac{1}{4\epsilon_0\pi} \right) \left(\frac{Ze^2}{r^3} \right) L.S \quad (1.3)$$

Here, m is the mass of the electron, c is the speed of light, r is the orbital radius and, Z is the atomic number. As this term does not commute with L_z or S_z , it is imperative to switch to total angular momentum, where the total angular momentum J can be written as,

$$\hat{J} = \hat{L} + \hat{S} \quad (1.4)$$

$$\hat{J}^2 = \hat{L}^2 + \hat{S}^2 + 2\hat{L}\cdot\hat{S} \quad (1.5)$$

$$\hat{L}\cdot\hat{S} = \frac{1}{2}(\hat{J}^2 - \hat{L}^2 - \hat{S}^2) \quad (1.6)$$

Combining spin 1/2 with angular momentum l , total angular momentum can take values $j = l \pm \frac{1}{2}$. Corresponding basis states $|j = l \pm \frac{1}{2}, m_j, l\rangle$ diagonalize operator,

$$\hat{L}\cdot\hat{S} |j = l \pm \frac{1}{2}, m_j, l\rangle = \frac{\hbar^2}{2} \begin{pmatrix} l \\ -l - 1 \end{pmatrix} |l \pm \frac{1}{2}, m_j, l\rangle \quad (1.7)$$

When this is incorporated in the Hamiltonian, we get,

$$\langle H \rangle_{n,j=l\pm 1/2,m_j,l} = \frac{1}{2m^2c^2} \frac{\hbar^2}{2} \begin{pmatrix} l \\ -l - 1 \end{pmatrix} \frac{Ze^2}{4\pi\epsilon_0} \left\langle \frac{1}{r^3} \right\rangle \quad (1.8)$$

Using the identity, for atoms other than Hydrogen,

$$\left\langle \frac{1}{r^3} \right\rangle = \left(\frac{mc\alpha Z}{\hbar n} \right)^3 \frac{1}{l(l+1/2)(l+1)} \quad (1.9)$$

We thus obtain Z^4 dependence of spin-orbit coupling. This shows that spin-orbit coupling increases dramatically with the atomic number. In atomic systems, the spin-orbit term acts as a first-order perturbative correction whereas for crystalline structures it breaks the spin-degeneracy of the bands formed from these orbitals.

Now that we have introduced all the significant interactions in 5d TMOs, we will proceed to discuss how their complex interplay affects the ground state in iridates. Iridium has electronic configuration of $[\text{Xe}] 4f^{14} 5d^7 6s^2$. In the case of Ir^{4+} , there are five electrons in the 5d manifold. In the presence of an octahedral crystal electric field, these degenerate orbitals get split into low-lying triplet t_{2g} and higher energy doublet e_g . As the e_g orbitals are well separated from the t_{2g} , all the electrons now occupy the t_{2g} orbitals. The t_{2g} orbitals would have remained degenerate but for iridates this is not the case due to the strong SOC. At this point, the spin-orbit interaction acts on t_{2g} orbitals to further lift the degeneracy by splitting it into a low-lying $j = \frac{3}{2}$ quartet and a higher energy $j = \frac{1}{2}$ doublet. The quartet being lower in energy by the value of $\lambda/2$. The quartet is then filled with four electrons, leaving a single electron to half-fill the doublet

with $j = \frac{1}{2}$ effective spin.

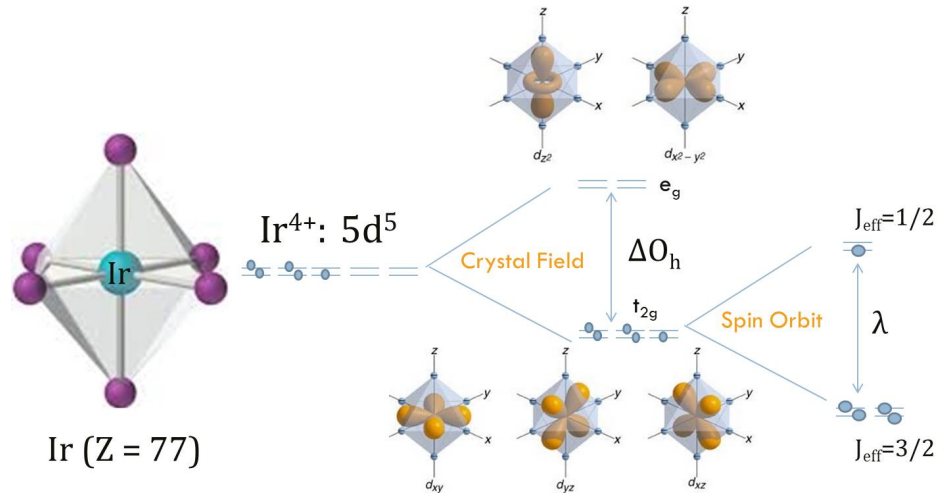


Figure 1.3: Crystal field splitting of Ir^{4+} in an octahedral environment. (Adapted from Ref [1])

The first experimental manifestation of the $j = \frac{1}{2}$ effective spin state in iridates was shown for the compound Sr_2IrO_4 by Kim et al [11]. Sr_2IrO_4 crystallizes in the same tetragonal structure as its 4d counterpart Sr_2RhO_4 . Considering the reduced electron correlation in the 5d orbitals and the odd-number of electrons in the d-orbital, a metallic ground state was expected for this composition. However, in spite of the similarity in lattice parameter of Sr_2IrO_4 with the Fermi-liquid metal Sr_2RhO_4 [12], the ground state for Sr_2IrO_4 was found to be insulating and weakly ferromagnetic. This is called the SOC assisted Mott insulating ground state. The insulating ground state was also observed for other iridates such as pyrochlore iridates, which established the significance of SOC in these systems.

The presence of strong SOC along with moderate electron correlations has opened a multitude of novel electronic phases that were inaccessible by considering Hubbard like hamiltonian. The emergence of the novel electronic ground states due to strong SOC is depicted nicely in this phase diagram of interactions in condensed matter systems (Fig 1.4).

1.2 Topology in condensed matter physics

For decades, the onset of ordering in condensed matter systems was understood by spontaneous symmetry breaking. But around 1980, a new type of ordering that did not

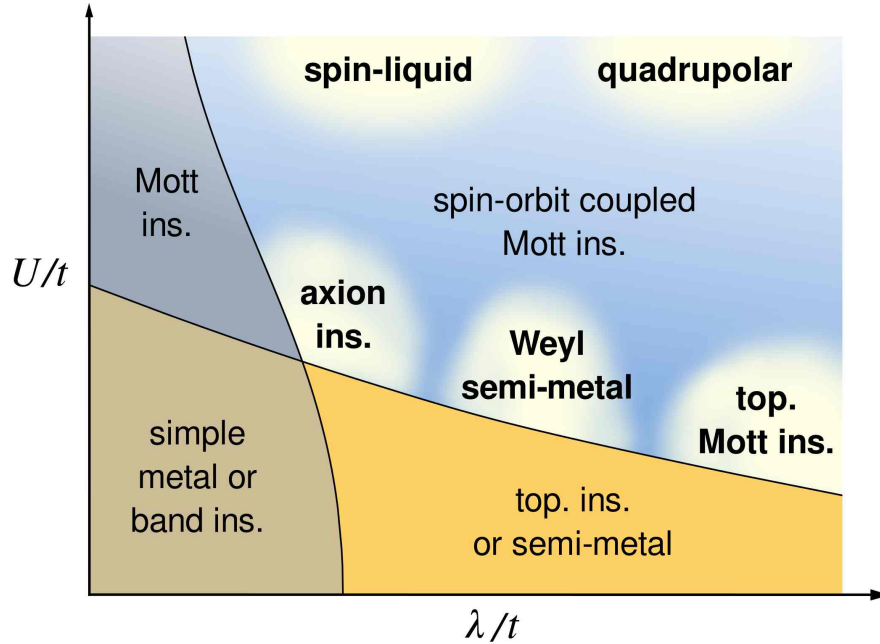


Figure 1.4: Various electronic phases that could be realised by tuning the interaction strength in condensed matter systems. (Adapted from Ref [2])

involve any symmetry-breaking was discovered. Electron quantization was observed in two-dimensional electron gas in the presence of a strong magnetic field perpendicular to the plane at low temperatures [13]. The quantisation was proportional to the magnetic field and formed Hall conductance plateau that increased in an integral number of e^2/h with increasing magnetic field. This phenomenon is an example of what is known as ‘topological order’.

In a topologically ordered phase, the ‘topological invariants’ dictate the behaviour of the physical response functions. In other words, some peculiar global properties emerge from microscopic degrees of freedom. We will first try to understand this in the mathematical context about how the geometry is used to distinguish the topology.

If we consider a torus and a sphere, the fundamental difference between the two is: unlike a torus, the sphere has no hole. Thus, it is not possible to mould the sphere smoothly into a torus without creating a hole. However, a sphere could be deformed continuously into a mug or any arbitrary shape without a hole. Here, the topological protection prevents smooth deformation across interfaces with distinct topologies. This

can be understood using the Gauss-Bonnet theorem. According to the Gauss-Bonnet theorem [14], the area integral of the curvature over the closed surface is quantised and is a “topological invariant”, i.e.,

$$\int K.dS = 2\pi(2 - 2g) \quad (1.10)$$

where K is the local curvature along the surface S ; g is termed as genus number, which is nothing but the number of holes in the surface. If we extend this concept from geometric space to a space defined by the eigenstates of a Hamiltonian described by certain parameters, then the curvature of this space would be known as Berry’s curvature. Similarly, it was shown by Shiing-Shen Chern [15] that the Gauss-Bonnet formula could be applied to the momentum space for a condensed matter system, where, integrating over Berry’s curvature would yield a quantized integer, analogous to genus, known as Chern number. According to the adiabatic theorem, which states that adiabatic changes in a Hamiltonian keep the Chern number constant whereas drastic changes may result in an increase in the Chern number by integer value [16]. The first experimental realization of this was in the quantum Hall state. Laughlin, Hofstadter, and coworkers [17, 18] showed that the integral number jump in the quantum Hall conductance correlated to integer change in the Chern number which occurs when the system fills different Landau levels.

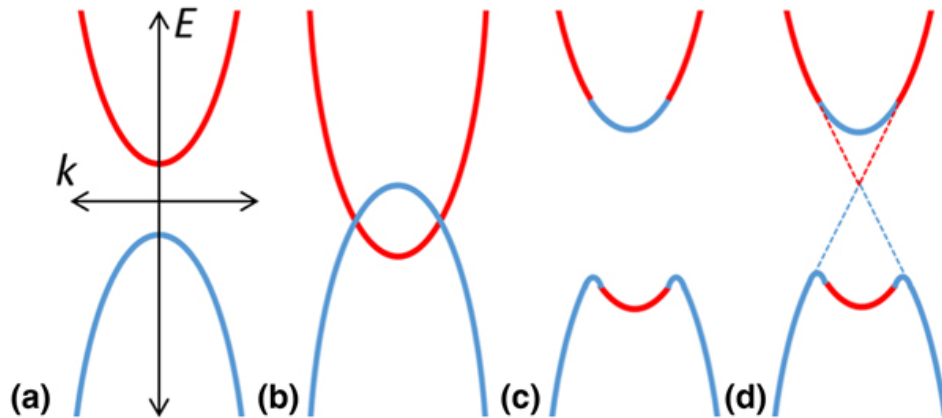


Figure 1.5: Schematic of the formation of topological surface states (a) normal band structure, (b) band inversion due to strong spin-orbit coupling, (c) band renormalization, and (d) formation of the topological surface states. (Adapted from Ref [3])

Another example of a non-trivial topology is that of topological insulators that are

insulating in the bulk but have conducting surface states. In materials with strong SOC, the Rashba effect [10] may induce band inversion between the conduction band and valence bands of the material. At the boundary with the vacuum or a normal insulator, these two bands must be smoothly connected meaning that at least one state (now with definite spin because of the SOC) crosses the bandgap at the surface. Time reversal symmetry is not broken in these systems, so there will actually be a pair of these states with opposite spin and momentum that will cross to form a node inside the bulk bandgap. As such a node must either exist or be absent, there is no way it may be adiabatically removed, i.e. it is topologically distinct from a simple band insulator. The effect of this is that the states corresponding to the node form helical conduction channels around the edges or surfaces which have Dirac-like dispersions and are protected from scattering by the time-reversal symmetry. A trivial band insulator can also have conducting surface states due to dangling bonds, etc. However such surface states are not topologically protected.

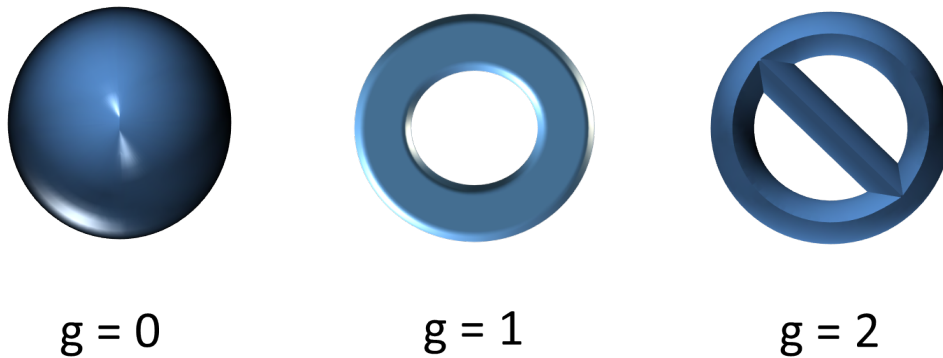


Figure 1.6: A sphere has genus=0 and the torus has genus= 1 whereas the third shape with two holes has genus=2.

After having introduced the concept of topological phases of matter with examples, we will now turn to understand the Weyl semimetal which is of particular interest in this thesis.

1.2.1 Weyl Semimetal

In 1928 P. A. M. Dirac [19] proposed the eponymous Dirac equation, successfully combining special relativity and quantum mechanics for the first time. Dirac's equation consists of a four-component wave function and 4×4 gamma matrices. The four com-

ponents allowed for both positive and negative charge solutions and up and down spin. This was a significant development in theoretical physics which, among other things, predicted the existence of antimatter, and laid the foundation of quantum field theory. Shortly after the Dirac equation, mathematician Herman Weyl proposed a simplified relativistic equation [20] utilizing just the 2×2 complex Pauli matrices σ_n . This simplification demanded the associated fermions to be massless. These are called Weyl fermions. The Weyl fermions have a definitive chirality or handedness, and a pair of opposite chirality Weyl fermions can be combined to obtain a Dirac fermion. For a long time, it was believed that neutrinos might be the Weyl fermions. However, with the discovery of a non-vanishing neutrino mass [21], there are no fundamental particles currently believed to be massless Weyl fermions.

In condensed matter physics, the energy scales of interest are much smaller than the rest mass of the electron; hence, naively, the non-relativistic description is expected to suffice while explaining the electron dynamics without invoking Dirac physics. However, the propagation of even slow electrons through the periodic potential of a crystal leads to a dressing of the electronic states. In certain instances, this results in an effective low-energy description that resembles the Dirac equation. An ideal example of this comes from graphene, where the electron follows a linear energy-momentum dispersion relation and its behavior is captured by the massless two-dimensional Dirac equation. Conditions under which, such band crossing would occur in electronic band structures were investigated by Conyers Herring in 1937 [22]. Herring observed that three-dimensional crystals could host accidental twofold degeneracies of bands, where the dispersion in the vicinity of these band touching points was linear and hence resembled the Weyl equation. This degeneracy was not a result of any particular symmetry but was purely accidental. As particles obeying the Weyl equation are chiral, they exhibit chiral anomaly which is non-conservation of the chiral current. Remarkably, the chiral anomaly, the defining physical property of Weyl fermions, continues to hold true even in the context of condensed matter systems. Adler-Bell and Jackiw [23, 24] demonstrated that a single Weyl fermion when coupled to an electromagnetic field results in the non-conservation of electric charge. However, this has unphysical consequences in a lattice and thus the net chirality of a set of Weyl fermions must vanish, which is facilitated by Fermion doubling theorem. However, even in this setting, it was realized by

Nielsen and Ninimoya [25] that the chiral anomaly can have a nontrivial effect, which cemented the link between band touching in three-dimensional crystals and the chiral or Weyl fermions. These band touchings of Herring were named Weyl nodes by Wan et al. [26]. The name Weyl semimetal (WSM) was introduced to describe a phase where the chemical potential is near the Weyl nodes and a potential realization of such a state in a family of materials, the pyrochlore iridates, was proposed along with the prediction of a special all-in- all-out magnetic ordering pattern [26].

Since then, Weyl semimetals (WSM) have been one of the most sought after research topics in condensed matter physics. So far, few families of compounds have been proposed theoretically to host WSM ground state due to the breaking of time-reversal symmetry. This includes pyrochlore iridates [26] $A_2Ir_2O_7$, half-Heusler alloys APtBi [27] where A is a rare-earth ion and $HgCr_2Se_4$ [28]. Several systems were envisaged to host the WSM ground state by the virtue of breaking of inversion symmetry by Murakami [29] and Halász and Balents [30].

The topological aspect of Weyl fermions is reflected in the fact that they are sources/sinks (monopoles) of the Berry curvature (Chern flux) in the Brillouin zone (BZ). This momentum space topology is associated with several physical phenomena that serve as the finger prints of the WSM ground state. The first manifestation of the topological aspects of Weyl fermions appeared with the realization that Weyl nodes lead to exotic surface states in the form of Fermi arcs [26]. Fermi arcs connect the projections of the nodes onto the surface BZ. Such topological properties are sharply defined as long as one can distinguish band touching associated with opposite Chern flux. The presence of translation symmetry, and hence conserved crystal momenta, is sufficient to protect these defining properties since the nodes are separated in the BZ. Other manifestations of the band topology include an anomalous Hall effect [31, 32] that is tied to the momentum space displacement between nodes, and magnetoresistance arising from the Adler-Bell-Jackiw anomaly [23, 24]. However, it is not possible to detect or measure all the signatures in all the Weyl semimetals. For example, Fermi arcs have been observed in WSM like TaAs, NbP with broken inversion symmetry, although a distinct demonstration of a magnetic WSM remains to be observed [33]. Thus, since the theoretical prediction of WSM in condensed matter systems, there are constant efforts and a large influx of theoretical predictions to point out various signatures of WSM.

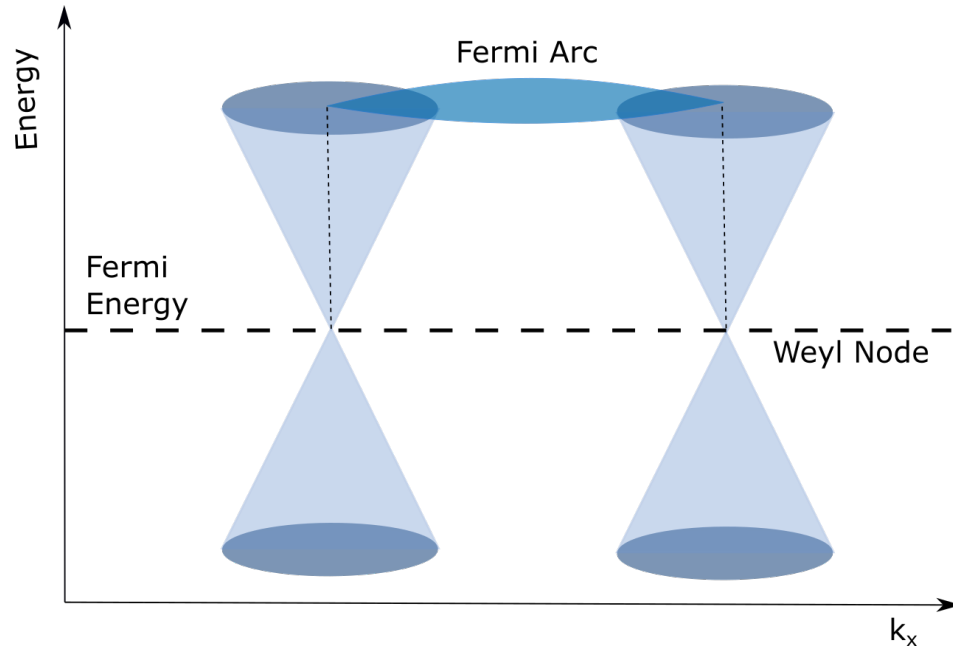


Figure 1.7: Bulk states represented by Weyl nodes and their surface projection depicted by Fermi arcs.

Pyrochlore Structure

In the previous sections, we discussed various interactions that drive the novel physics in iridates. In this section, we would familiarise ourselves with pyrochlore structure and the range of fascinating spin alignments that this structure can host due to its geometrical aspect.

Pyrochlore family derives its name from the iso-structural and eponymous mineral $(\text{Na,Ca})_2\text{Nb}_2\text{O}_6(\text{OH,F})$. The members of this family are predominantly cubic and are represented by a generic formula $\text{A}_2\text{B}_2\text{O}_7$ where B is usually a transition metal ion and A can be a rare-earth or post-transition metal ion. The pyrochlore family spans a broad range of physical properties as a result of a large number of combinations of A and B cations and the variable oxidation states accessible to the transition metal ions [34].

$\text{A}_2\text{B}_2\text{O}_7$ or more suitably $\text{A}_2\text{B}_2\text{O}_6\text{O}'$, which reflects the two inequivalent O-sites, crystallizes with the pyrochlore structure (space group: $Fd-3m$, $Z = 8$) with A, B, O and O' located, respectively, at $16d$ (0.5, 0.5, 0.5), $16c$ (0, 0, 0), $48f$ (u , 0.125, 0.125) and $8b$ (0.375, 0.375, 0.375), positions. The cations A and B form interpenetrating corner-linked tetrahedral networks running parallel to the 111 direction of the cubic unit cell,

as shown in Fig. 1.8. The two sublattices are displaced relative to one another along the unit cell edge by a length $a/2$, where a is the lattice parameter. In the pyrochlore structure, each B-site cation is coordinated to six O ($48f$) ions, forming a BO_6 octahedron (Fig. 1.3). Since the $48f$ position has a variable x -coordinate, the symmetry of BO_6 octahedron depends on the value of u . The perfect octahedral symmetry is achieved for $u = 0.3125$. In interval $0.3125 \leq u \leq 0.375$, which defines the field-of-stability of the pyrochlore structure, the IrO_6 octahedron exhibits a trigonal compression that increase with u . In most known pyrochlores, the value of u lies well within these limits. In the pyrochlore iridates, in particular, the typical value of u is reported to be around 0.333, and the corresponding value of the bond angle $\text{Ir}-\text{O}-\text{Ir}$ varies from $\approx 127^\circ$ to 130° [34].

The A-site ion in the pyrochlore structure forms an axially compressed scalenohedron with six equidistant $48f$ oxygens forming a puckered hexagonal A-O_6 ring; and two axially located $\text{O}(8b)$ that forms a $180^\circ \text{O}'-\text{A}-\text{O}'$ bond oriented perpendicular to the average plane of the A-O_6 ring. The scalenohedron becomes a perfect cube for $u = 0.375$. For smaller values of u than 0.375, the bond length $\text{A}-\text{O}'$ becomes smaller than $\text{A}-\text{O}$, compressing the scalenohedron axially. A sense of the relative orientations of the A- and B-site coordination polyhedrons can be gathered from the fact that bond $\text{O}'-\text{A}-\text{O}'$ always points along the principal diagonal as shown in Fig. 1.8 irrespective of the values that u and a take.

It is possible to visualize pyrochlore structure in multiple ways. As the 16c and 16d sites form layers stacked along the $[111]$ direction, pyrochlore structure could be viewed as stacking of alternating kagome and triangular planar layers [34,35]. From the viewpoint of chemical bonding, the pyrochlore structure could be viewed as a mixing of two frameworks. One formed by the B_2O_6 composition and the other by composition $\text{A}_2\text{O}'$, that forms a zigzag chain through the large channels formed by the B_2O_6 network. The B-O-B angle in this network is restricted to a very narrow range for pyrochlores, from $\approx 127^\circ$ to 134° , with little influence from the A cation. Also there exists a version of pyrochlore structure, called as defect pyrochlore or fluorite structure where the entire $\text{A}_2\text{O}'$ network is missing. This shows that, in the pyrochlore structure, B_2O_6 forms the rigid and essential framework whereas it can sustain significant vacancies at the A site and $\text{O}(8b)$ site.

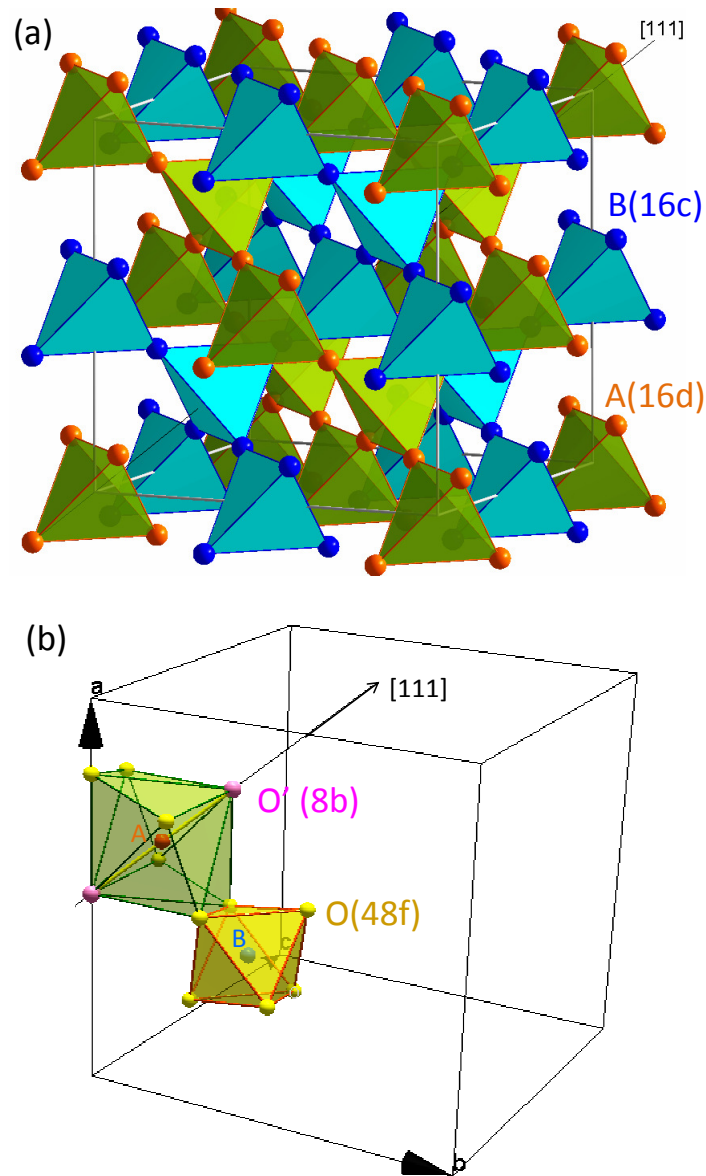


Figure 1.8: Conventional unit cell of the pyrochlore $A_2B_2O_7$ structure with (a) only A^{3+} and B^{4+} sublattices shown, and (b) $B-O_6$ octahedra and $A-O_6-O'_2$ scalenhedron are shown in the unit cell.

1.2.2 Magnetism in pyrochlore oxides

Frustration arises when a system has competing or contradicting constraints, which cannot all be satisfied simultaneously to find a unique ground state. This results either due to the presence of multiple interactions that do not favor the same ground state, or the

crystal symmetry constrains the ability of the individual degrees of freedom to span all the possible configurational space in order to find a unique ground state. For example, as shown in the Fig. 1.9, it is straightforward to arrange the spins on the corners of the square lattice where they satisfy antiferromagnetic correlation with each other. However, in the case of a triangular model, which is the simplest case of geometric frustration it is not possible to arrange the spins at the three corners so as to satisfy antiferromagnetic interaction simultaneously for all the spins.

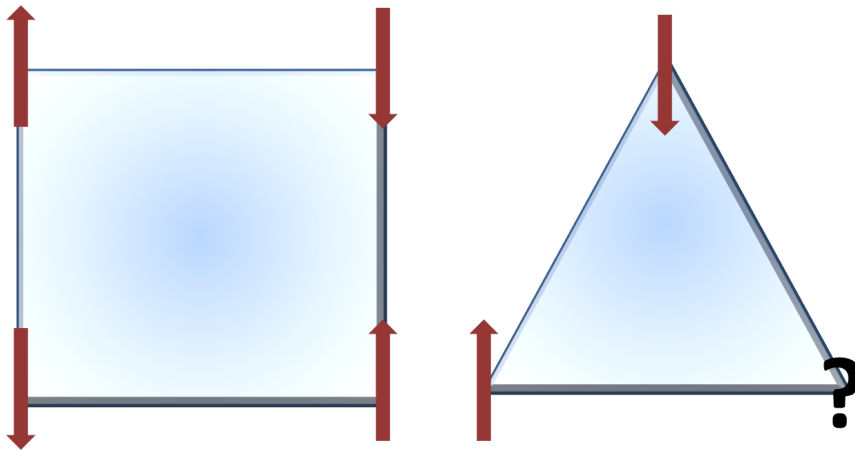


Figure 1.9: Geometric frustration arising due to triangular arrangement of the spins interacting antiferromagnetically.

In pyrochlore oxides, the A and B cations, individually, form a corner shared tetrahedral network which is offset from one another along the $[100]$ or any cubic direction by half the lattice constant [35]. When the cations at A or B site have unpaired spins, the spin-spin interaction and orientation decide magnetism of the system. As the corner shared network is a 3D analog of the triangular model, pyrochlore structure is prone to a high degree of geometric frustration. In addition to the spin-spin interactions, the oxygen atom at the center of each tetrahedra generates an anisotropic crystal field that leads to a strong Ising anisotropy along the $[111]$ direction or pointing from the center of tetrahedra through the corners. However, as cubic crystal symmetry inhibits global Ising axis, as it would artificially break the cubic symmetry, to realize Ising behavior it is necessary to define a local set of directions that are related by symmetry allowed transformations [35]. Such limitations generate magnetic frustration and significantly reduce

the phase space of possible magnetic configurations and thus can induce complex and novel magnetic structures.

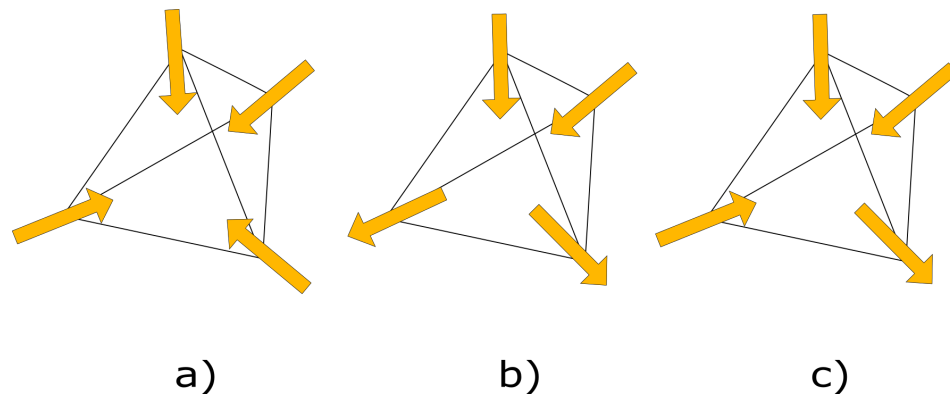


Figure 1.10: a) All-in spin arrangement b) 2-in-2-out spin ice arrangement c) 3-in-1-out spin arrangement

For example, if the ground state of magnetic ions situated at the corner of the tetrahedra had to be arranged in Ising geometry then the magnetic moments at the corner may only point towards or away from the center of the tetrahedra. This results in three distinct spin configurations as depicted in the Fig. 1.10. Panel (a) shows the all-in-all-out (AIAO) arrangement where the spins on the adjacent tetrahedra point respectively towards and away from the center of the tetrahedra alternatively. This arrangement is equivalent of an antiferromagnetic ordering as no resultant moment is generated from this ordering. While in panel (c), the three-in-one-out arrangement is ferromagnetic in nature and would result in a net moment along the 111 direction. On the other hand, there are six ways to arrange the spins in two-in-two-out (2I2O) fashion, one of which is shown in the panel (b). In this case, though locally tetrahedra can have 2I2O configuration, globally a long-range order does not exist. Insulating pyrochlore oxides, like, $\text{Ho}_2\text{Ti}_2\text{O}_7$ are archetypical example of 2I2O order, where neutron scattering measurements have confirmed that the magnetic correlation length is smaller than the unit cell size [36]. This suggests global disorder even in the presence of locally present ordering which originates from the huge degeneracy in the ground state which facilitates plenty of novel physical phenomena.

1.2.3 Spin Ice

This spin arrangement derives its name from the analogous water ice. Historically, the first system to be identified as frustrated was water ice. As water crystallizes, it exhibits bond disorder sustaining down to extremely low temperature, which gives rise to the residual entropy. This entropy was measured in 1933 by Giauque and coworkers [37] and the origin of this entropy was explained by Linus Pauling [38]. He argued that the bonding arrangement in water follows ice rules that demanded two protons to be near to and two farther from each oxide ion. Pauling showed that such bonding arrangement, which could be achieved in six alternate ways, resulted in a macroscopically degenerate ground state of spin ice. The theoretical entropy calculated by Pauling for such a macroscopic degenerate state agreed well with the experimental values. In 1956, Anderson investigated the problem of magnetic ordering in spinels, which are structurally similar to the pyrochlores [39]. To a first approximation, the spin arrangement mapped on to the Pauling's model of spin ice. However, it was only in 1997 that Harris and coworkers could experimentally establish the three-dimensional magnetic analogs of water ice in the pyrochlore oxide $\text{Ho}_2\text{Ti}_2\text{O}_7$, for which the term spin ice was coined to stress the analogy. $\text{Ho}_2\text{Ti}_2\text{O}_7$ is an example of what is known as classical spin ice. Later $\text{Dy}_2\text{Ti}_2\text{O}_7$ was also found to share a similar ground state [40]. In both these compounds, Ti^{4+} is non-magnetic and the magnetism arises from the A-site ion. Ho^{3+} and Dy^{3+} carry a large moment of $\sim 10\mu\text{B}$. Hence long-range dipolar interactions are of significance in these compounds. In addition, under the anisotropic crystal field environment, the rare-earth moments behave as nearly pure two-state Ising spins pointing in or out of the tetrahedra. Owing to the large moment of A-site ions, applied fields of several Teslas are too weak to turn the A-site ions (Ho^{3+} , Dy^{3+}) away from their local quantization axes. Thus, these compounds constitute the classical spin-ice system.

Due to the large moment carried by each magnetic ion, strong quantum effects are absent in the classical spin ice compounds but can be significant in other rare-earth pyrochlores where the magnetic moment of the rare-earth ion is not very large. Compounds like $\text{Yb}_2\text{Ti}_2\text{O}_7$, $\text{Er}_2\text{Ti}_2\text{O}_7$ are of this type, where the effective spin at A site is $1/2, 3/2$, respectively. It has been argued recently that the spins of the aforementioned compounds are controlled by exchange coupling rather than by the long-range dipolar interactions [41]. This makes these materials highly frustrated and prone to quantum

effects. Recently it was shown that $\text{Yb}_2\text{Ti}_2\text{O}_7$ may support quantum spin liquid ground state in a moderate magnetic field and may host an unusual quantum critical point at larger fields [41].

1.2.4 Previous studies on pyrochlore iridates

The comparable strength of electron correlation, spin-orbit coupling, and crystal field splitting, put the pyrochlore iridates at the crossroads of trivial and non-trivial ground states in the U - λ phase diagram (see Fig. 1.4). Tuning the relative strength of these interactions can lead to the realisation of interesting novel ground states. In this section, we would preview the experimental and theoretical work done, that has shaped our understanding of this series.

The first report of the synthesis of pyrochlore iridates was in 1971 by Bouchard and coworkers [42]. However, the physical properties were not reported until much later. In 2001, Taira and coworkers [43] reported Mössbauer and magnetic susceptibility studies of some members of the pyrochlore iridates series. Their study revealed a magnetic transition for $A = \text{Y, Sm, Eu}$ and Lu , which was presumed to be antiferromagnetic or spin-glass based on the bifurcation between zero-field-cooled and field-cooled susceptibility measurements along with the absence of any hysteresis loop. In the same year, Yanagashima and Maeno [44] reported lattice constant and physical characterization of several members of the pyrochlore series. In this study, they observed smaller rare-earth pyrochlore iridates to be insulating whereas members with Eu and bigger sizes were found to be metallic. The samples reported were polycrystalline and the precursors used were rare-earth oxide and Ir-metal. Later, in a detailed study by Matsuhira et al. [4, 45], where oxides of rare-earth and iridium were used for synthesis, it was observed that physical behavior of pyrochlore iridates changed from that of a magnetic insulator for smaller or heavier rare earth (i.e., $A = \text{Gd, Tb, Dy, Ho, Er, and Yb}$, including Y) to a nonmagnetic metal for $\text{Pr}_2\text{Ir}_2\text{O}_7$. The study also revealed that members corresponding to $A = \text{Nd, Sm, and Eu}$ show a thermally induced metal-insulator transition (MI) upon cooling below a temperature (TMI), concomitant with the onset of magnetic ordering. As the ordering was observed in all the compositions irrespective of the magnetism of A-site ion, the magnetism in pyrochlore iridates was attributed to the ordering of Ir^{4+} ($J_{eff} = \frac{1}{2}$) sublattice. A phase diagram for conductive properties of the pyrochlore iridates as a function of A-site radius was given in the same work that shows the strong

dependence of the physical properties on the A-site radius.

To shed light on the nature of the magnetic ordering of Iridium sublattice, Zhao et al. performed zero-field muon spin relaxation measurements on $\text{Eu}_2\text{Ir}_2\text{O}_7$ [46]. Spontaneous muon precession below T_N revealed, a long-range antiferromagnetic ordering of Ir^{4+} sublattice. Further, the nature of ordering was observed to be of all-in-all-out type. Later, μSR studies carried out by other groups on $\text{Sm}_2\text{Ir}_2\text{O}_7$ and $\text{Nd}_2\text{Ir}_2\text{O}_7$ also revealed all-in-all-out nature of magnetic ordering [47,48].

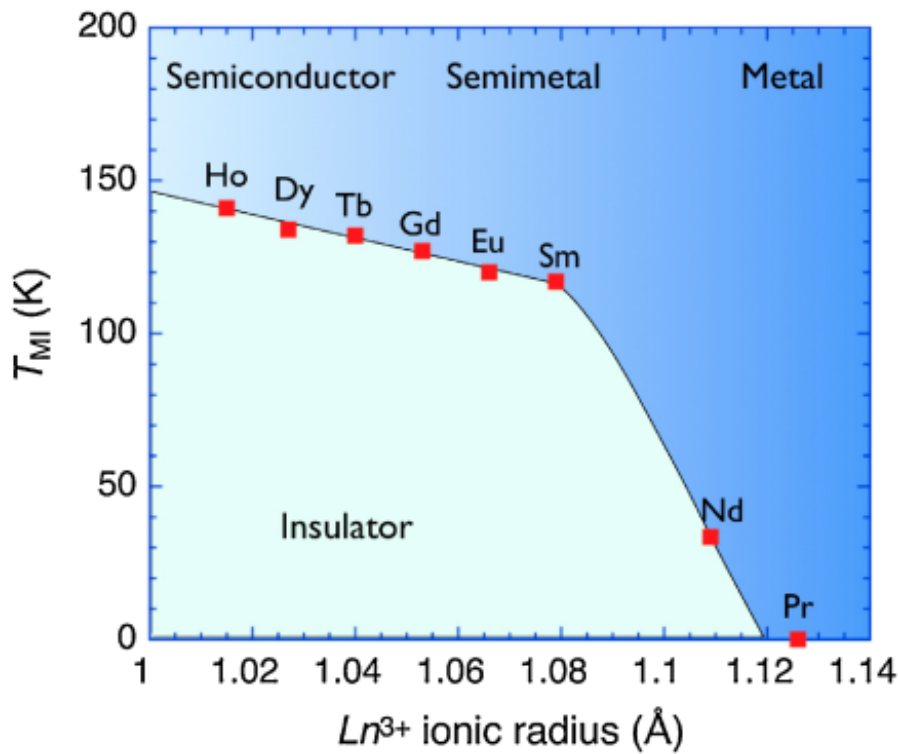


Figure 1.11: Phase diagram of transport properties of pyrochlore oxide series plotted against the rare-earth radius.(Adapted from Ref [4])

As the rare-earth radius reached Pr, the properties changed dramatically and were found to be very different compared to the rest of the series. $\text{Pr}_2\text{Ir}_2\text{O}_7$ was, in fact, the first member amongst pyrochlore iridates to gather research interest for its exceptional properties [49]. This compound was observed to show a lack of long-range magnetic ordering down to 50 mK and was also found to show finite Hall conductance in the absence of an applied magnetic field, suggesting the existence of a chiral spin liquid ground state [49]. Also, the conductance of this composition shows a logarithmic upturn

in the resistivity around 30 K that was thought to originate from the polarisation of conduction electrons due to Pr^{3+} ions. However, recent studies have shown that $\text{Pr}_2\text{Ir}_2\text{O}_7$ in fact, hosts a quadratic degenerate band touching at the Fermi energy which should act as the parent phase for other novel electronic phases predicted for pyrochlore iridates. Another metallic member in the series is $\text{Bi}_2\text{Ir}_2\text{O}_7$. This compound shows a non-trivial $T^{3/2}$ dependence of resistivity with temperature. μSR study on this compound revealed two magnetic transitions at 1.8 K and 0.23 K [50].

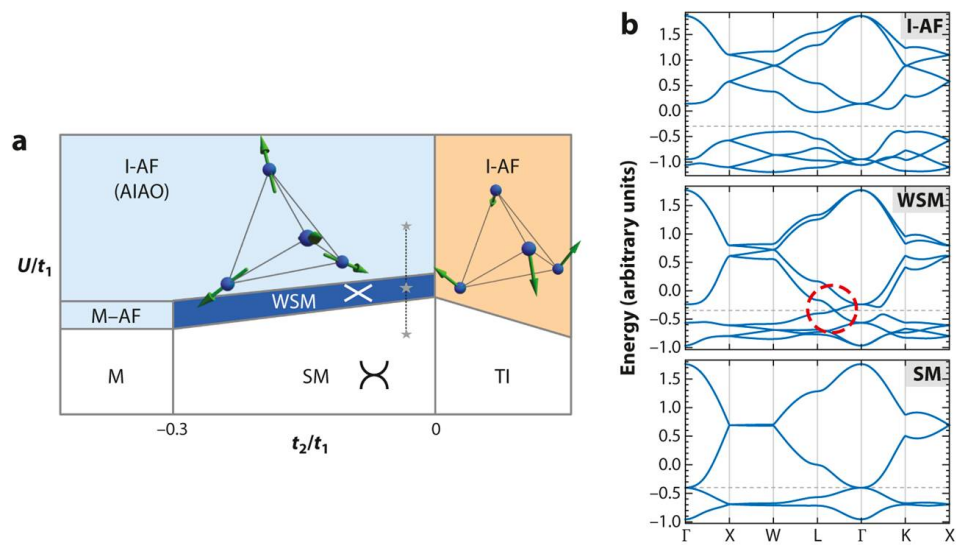


Figure 1.12: a) Schematic mean-field phase diagram of the Hubbard model on the pyrochlore lattice showing the narrow range of stability of WSM ground state in pyrochlore iridates b) Evolution of the electronic spectrum along the three points (stars) highlighted on the vertical dashed line in panel a. The red circle shows one Weyl point at the Fermi level (horizontal dashed line). The spectrum is plotted along high symmetry lines in the Brillouin zone. (Adapted from Ref [2])

On the theoretical front, Pesin and Balents probed pyrochlore iridates theoretically for the first time in 2010, when they searched for possible topological states in pyrochlore iridates originating from the large SOC associated with Ir. They employed the mean-field theory and a slave-rotor approach to determine the ground-state phase diagram over the correlation and SOC energies. In their study, they could show that the family of pyrochlore iridates is capable of supporting a strong topological insulator, as well as magnetically ordered insulating and metallic states. However, pyrochlore iridates amassed significant attention when in 2011, Wan and coworkers, using density functional calculations in the local spin density approximation combined with fi-

nite correlation and spin-orbit coupling, showed the presence of WSM in this family [51, 52]. This work was followed by several other theoretical works, such as the work by Witczak-Krempa et al., where the presence of WSM phase was reiterated using tight-binding model and was shown to be stable over a narrow region between metallic and magnetic insulating phases [2]. Witczak-Krempa also calculated a phase diagram where various electronic phases were realized as a function of the correlation energy U and the indirect hopping strength t . In the Weyl semimetallic state, a linear dispersion was found at a finite number of band touching points in the Brillouin zone which act as a three-dimensional analog of graphene [2]. One important aspect of this state is that it may only exist for a select group of magnetically-ordered configurations that satisfy the inversion symmetry of the crystal such as the AIAO type. Hence the natural candidates to search for Weyl-semimetallic state were the intermediate candidates $\text{Eu}_2\text{Ir}_2\text{O}_7$, $\text{Sm}_2\text{Ir}_2\text{O}_7$, and $\text{Nd}_2\text{Ir}_2\text{O}_7$, which are known to show all-in-all-out magnetic ordering of the Ir^{4+} sublattice. In spite of a lot of experimental efforts, a definitive signature of WSM state is yet to be observed. ARPES measurements were carried out on small single-crystalline samples of $\text{Nd}_2\text{Ir}_2\text{O}_7$, however, that study failed to detect any Fermi arcs. As the theoretical claim by Wan et al. was further supported by multiple other theoretical groups, it is imperative to search for alternate signatures of Weyl semimetal in pyrochlore iridates. Also, one should not overlook the possibility of realising a myriad of other novel ground states that could be realized in the pyrochlore iridate as given by Krempa and coworkers.

Chapter 2

Experimental Methods

Experimental investigation of pyrochlore oxides involves several crucial steps, starting from the synthesis of a single-phase compound to its structural indexing followed by the physical characterization. The last step comprises a combination of several techniques, which is essential to understand the physics and the nature of the ground state. Systematic structural characterization studies that bridge the link between changes in structure with physical properties have been lacking for the pyrochlore iridates. Hence, this work is of substantial importance as high-resolution structural studies along with comprehensive physical characterization are done here to ensure that every conclusion is supported by complementary probes. This brings us to the experimental methods chapter of this thesis where we briefly explain the working principle of all the measurement techniques employed in this thesis for synthesis, structure and physical characterization of the pyrochlore oxides.

2.1 Synthesis

The compounds studied in this thesis are oxides. Due to the high melting points of the oxide precursors, it is not always feasible to simply melt them to react together. Instead, the precursors must be thoroughly mixed and heated to an adequately high temperature and for a long enough duration ranging from several hours to a number of days or even weeks for the reaction to complete. This process is termed as sintering. Sintering involves diffusion and chemical reaction of the precursor materials at high temperatures. As the diffusion also leads to minimization of spaces between particles/grains in the

powder, it also results in densification. The reaction rate can be accelerated by increasing the sintering temperature. The ratio of the precursors is decided based on the final intended stoichiometry.

For pyrochlore iridates, the precursors used were high purity iridium oxide IrO_2 (Sigma Aldrich, 99.99% purity) and rare earth oxides A_2O_3 (either from Sigma Aldrich or Alpha Aesar 99.9% purity) whereas for pyrochlore stannates, tin oxide SnO_2 (Sigma Aldrich, 99.99% purity) was used in the place of iridium oxide. For preparing samples of the composition $\text{A}_{2-x}\text{Bi}_x\text{Ir}_2\text{O}_7$, besides A_2O_3 and IrO_2 as described above, stoichiometric amount of Bi_2O_3 (Sigma Aldrich, 99.9% purity) was also taken in the starting mixture. The precursors were mixed in an approximate molar ratio to yield the required A:Ir proportion. The rare-earth oxides were dried overnight to remove any trace of moisture before weighing it for the reaction. Thorough grinding of the precursors is necessary to achieve a homogeneous mixture of the reactants. To maximize the contact between powder grains and improve diffusion, the powder mixtures were placed in a hydraulic pressure vessel and pressurized to nearly 1500 kg cm^{-2} to form a solid pellet. The pellets are then placed in an alumina crucible and fired in a high-temperature furnace. A typical sintering cycle ranges between 24 to 48 hours. After every cycle, the samples were removed, reground, and checked for their phase purity using x-ray diffraction. If the precursors are found unreacted then the sintering cycle is repeated again. This process is called to an end once a single-phase compound is formed (within the precision of lab-based x-ray diffractometer).

In the case of pyrochlore iridates, the pyrochlore phase forms faster at higher temperatures but at the cost of volatile IrO_2 losses that tend to sublime excessively at temperatures exceeding $\approx 1050 \text{ }^\circ\text{C}$. Hence, it is important to sinter these samples at lower temperatures. This in turn results in longer synthesis duration but simultaneously cutting the risk of significant Ir losses. Hence, for pyrochlore iridates, synthesis protocol is tricky and should be carefully monitored as it can significantly affect the final stoichiometry. On the other hand, the synthesis protocol for analogous pyrochlore stannates is straightforward and a single-phase sample can be easily obtained in 2 to 3 sintering cycles.

2.2 Structural and composition characterization

After the rigorous process of synthesis, it is important to examine the sample for its structural and compositional homogeneity. For this purpose, the samples were examined using the powder x-ray diffraction and scanning electron microscopy. In some cases, the powder neutron diffraction was also carried out. The details of these characterization methods are given in the following section. The data obtained from the diffraction experiments were analyzed using the Rietveld method which is also briefly described towards the end of this section.

2.2.1 Powder x-ray diffraction

Powder x-ray diffraction is one of the most powerful tools for bulk structural analysis. The diffraction process and the subsequent analysis of the data for structure determination were first proposed by the father-son duo William Henry Bragg and William Lawrence Bragg in 1913 [53], for which they were awarded the Nobel prize in Physics in 1915.

Any crystalline material provides arrays of atoms that can act as scatterers of the x-rays which are nothing but electromagnetic radiations. The interaction between an atom and the x-ray is primarily through the electron cloud surrounding the atom and can be modeled via Thompson scattering which describes the interaction between electromagnetic radiation and a free charged particle. Thompson scattering is elastic scattering and can also be viewed as low energy form of Compton scattering where the particle's kinetic energy and photon frequency do not change as a result of the scattering. When the x-rays are scattered by the atoms, the photons add constructively in specific directions determined by the Bragg's law given by:

$$n\lambda = 2d\sin\theta \quad (2.1)$$

Here, d is the spacing between diffracting planes, θ is the incident angle, n is any integer and λ is the wavelength of the beam. The x-rays can produce diffraction patterns because their wavelength is of the same order of magnitude as the spacing d between planes in the crystal.

Form factor gives the measure of the scattering amplitude of a wave by an isolated

atom. It depends on the nature of incident radiation which then determines the scattering mechanism. However, the common feature of all the form factors is that they involve a Fourier transform of a spatial density distribution of the scattering object from real space to momentum space. The generic formula of the form factor for an object with spatial density distribution $\rho(r)$ is given as:

$$f(Q) = \int \rho(r) e^{i\mathbf{Q}\cdot\mathbf{r}} d^3r \quad (2.2)$$

Here, $\rho(r)$ is defined about its center of mass and \mathbf{Q} is the momentum transfer. In the context of x-rays, $\rho(r)$ in the above equation is given by electron charge density about the nucleus, and the form factor is the Fourier transform of this quantity. Hence, x-rays are not sensitive to the lighter elements with a small number of electrons. On a similar note, it is also difficult to distinguish amongst elements with near-by atomic numbers where the electron charge density is nearly same.

The intensity of the diffraction peaks is determined by the arrangement of atoms in the crystalline composition. The intensity of the peaks is related to the intensity by a factor called the structure factor F_{hkl} .

$$F_{hkl} = \sum_{j=1}^m N_j f_j \exp[2\pi i(hx_j + ky_j + lz_j)] \quad (2.3)$$

F_{hkl} sums the result of scattering from all of the atoms in the unit cell to form a diffraction peak from the (hkl) planes of atoms. The amplitude of scattered radiation is determined by the location of the atoms on the atomic planes. The scattering factor f_j quantifies the efficiency of x-ray scattering at any angle by the group of electrons in each atom. This scattering factor is equal to the number of electrons around the atom at 0° , hence the intensity of the Bragg peaks decreases with increasing angle.

With the advancement of science and technology, x-ray diffraction measurements are now capable of rendering significant details about the structure and composition. This includes but is not limited to lattice parameters, atomic position parameters, atomic occupancies and so on.

In this thesis, the information extracted from x-ray diffraction measurements is of significant importance and forms a major part of the thesis. Diffraction experiments were carried out using both lab-based source as well as synchrotron sources.

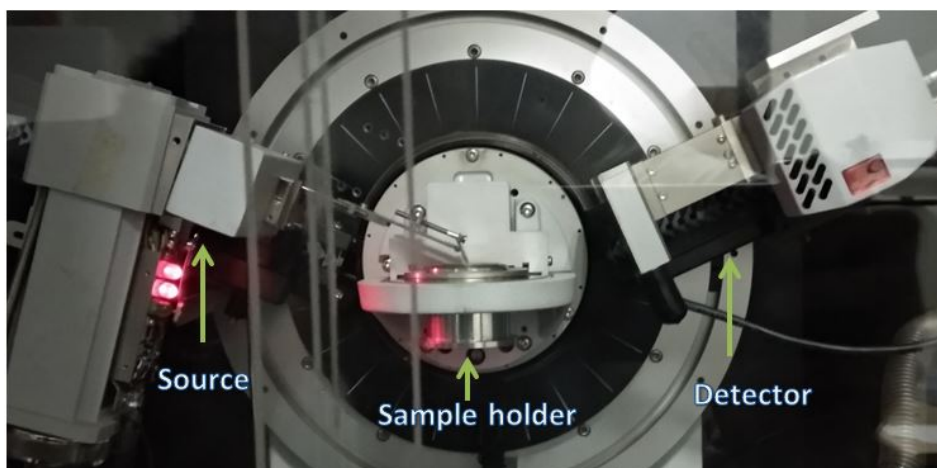


Figure 2.1: Bruker D8 advance diffractometer at IISER Pune. The photograph shows the bragg-brentano geometry of the instrument with the rotating x-ray source and detector as well as the fixed sample holder.

Lab-based x-ray diffraction experiments were carried out to confirm the phase formation as well as for preliminary determination of lattice constants. The experiments were done using a Bruker D8 Advance powder x-ray diffractometer, Germany with Lynxeye detector in Bragg-Brentano geometry. The source was $\text{Cu-K}\alpha$. The measurements were done on finely ground powder that was filled in a sample holder so as to create a flat surface in order to avoid any shift in the patterns arising from height difference. The measured x-ray pattern was matched with the standard data available in the ICDD PDF-2 diffraction database.

2.2.2 Scanning electron microscopy

The structural and compositional homogeneity of the compounds were further characterized using scanning electron microscopy (SEM, Zeiss Ultra Plus, Germany), equipped with an energy dispersive x-ray analysis probe (Oxford, UK). In this method, sintered pellets were examined using a field emission electron beam. A scanning electron microscope focuses a high-energy ($\sim\text{keV}$) electron beam on a small area of the sample. The incident electron beam can interact with the sample in numerous ways, resulting in emissions of different electrons and photons.

In the process of stopping the high-energy electrons, the energy released can knock off some of the electrons of the sample. These are called secondary electrons and they

carry information of the surface. These electrons are useful in determining surface topography of the given sample. Some of the electrons from the incident beam are bounced back from the atomic electron cloud of the sample. The scattering cross-section of these electrons is dependent on the mass density of the atoms and thus, these back-scattered electrons (BSE) carry information of high-resolution surface topography as well as about the structure and the composition. These BSE micrographs were used in this thesis to study the grain morphology.

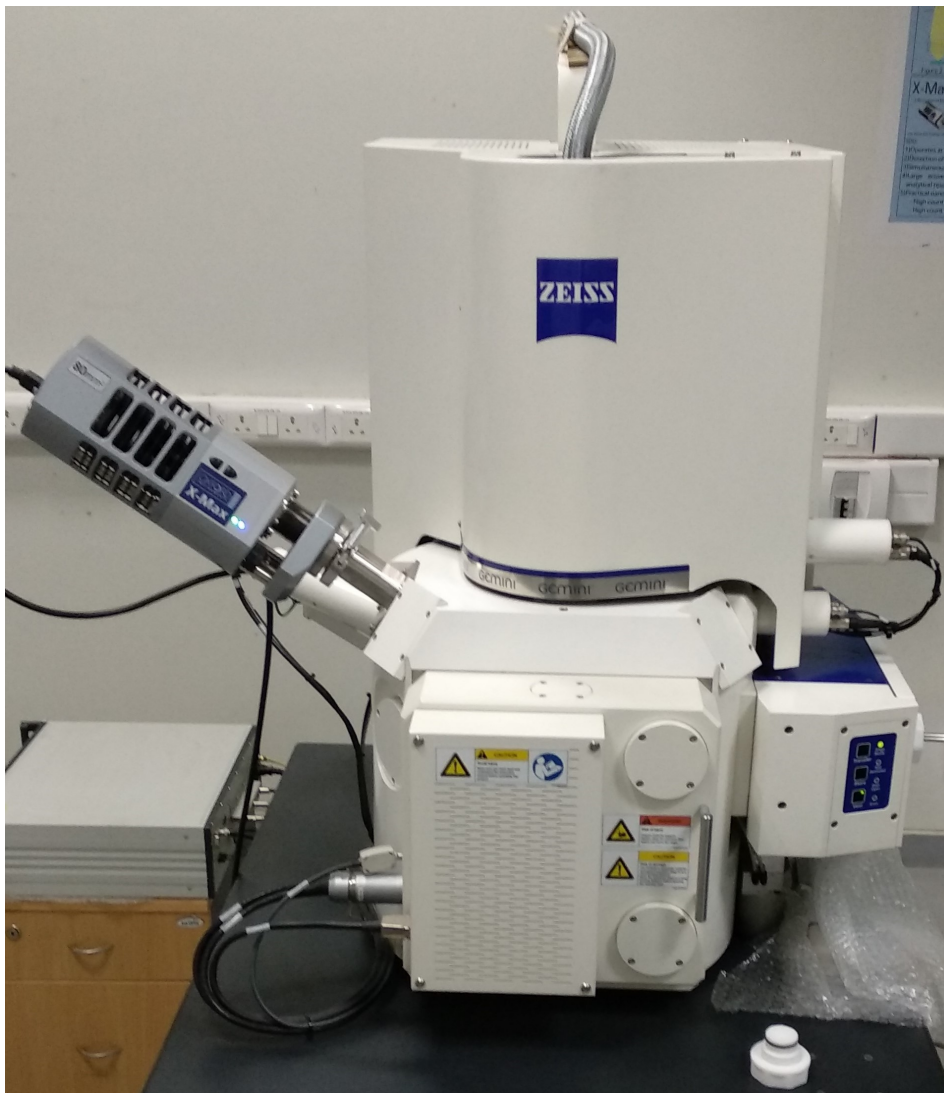


Figure 2.2: SEM instrument (Zeiss Ultra Plus) at IISER Pune that was used for EDS and imaging purpose in this thesis.

When the secondary electrons are emitted from the inner shells, the empty shell are

filled up by the outer shell electrons resulting in the release of x-rays photons. The energy of these x-ray photons is equal to the energy difference between shells involved in the transition and is characteristic of the element. Thus, analysis of these x-rays gives information about the elemental composition of the sample. This technique is known as Energy-dispersive x-ray spectroscopy (EDS) or analysis (EDXA). The FESEM at IISER Pune is equipped with a 20 mm² Oxford Inca EDX detector which enables elemental identification of samples with an energy resolution of 129 eV.

The energy of the incident electron beam is of crucial importance in this process. While the lower-energies (0.02 to 5 keV), due to its low-penetration, are desirable for the determination of the surface topography; for BSE and EDX analysis higher energies are preferred. The optimum value depends on the elements present in the system. An empirical rule is to select the excitation voltage at least twice the corresponding excitation energy of the elements present. In the case of pyrochlore iridates, Ir possesses the highest excitation energy of 9 keV ($K\alpha_1$). Therefore, to estimate the molar ratio of elements present in the compounds, an excitation voltage of 20 - 25 kV has been used in our investigations.

2.2.3 Synchrotron x-ray diffraction

Synchrotron light sources are particle accelerators that use electromagnetic fields to accelerate charged particles (electrons) to very high energies. Once the high-energy electron beam has been generated, it is passed through the storage ring consisting of bending magnets and undulators (periodic structure of dipole magnets). These supply the strong magnetic fields perpendicular to the beam which are needed to convert the high energy electrons into photons of desired energy.

The data obtained from x-ray diffraction experiments carried out at synchrotron sources is high resolution and has many advantages over the conventional lab-based x-ray source. Some of the qualities are listed below.

- X-rays produced at synchrotron sources offer highly monochromatic beam and a wavelength selective monochromator can be employed to choose from a range of values.
- The tunable wavelength enables minimization of background. For examples, lab-based sources can produce significant fluorescence for iron-rich samples.

- The x-ray beam at synchrotron sources is very intense which renders data with superior statistics and improved signal to noise ratio.
- Lab-based x-ray sources use flat-plate geometry for diffraction experiments. This geometry can have focusing issues depending on the angle, as the area illuminated varies for a fixed slit-width and results in broadening of low angle peaks. On the other hand, diffraction experiments are done in transmission geometry at synchrotron sources. The near-parallel beam removes the geometry related issues of a conventional lab-source.

All the above points combined result in high-resolution data for synchrotron x-ray diffraction experiments. Information obtained from the analysis of such high-resolution data offers reliability with a smaller error bar. Hence, it is advantageous to use synchrotron x-ray diffraction experiments while studying systems where subtle changes are expected due to small variation in the stoichiometry, for example, due to small or minor change in the doping level.

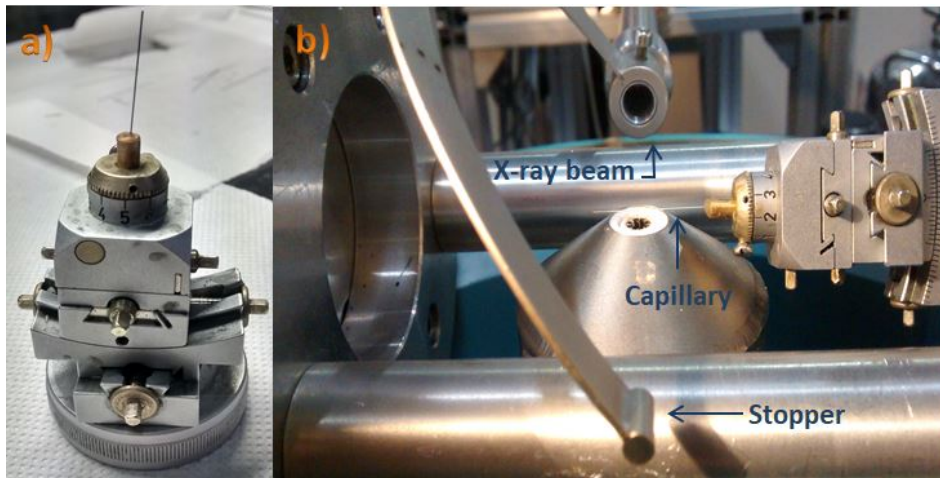


Figure 2.3: Experimental setup at the MCX (material characterization beamline), Elettra-synchrotron, Italy. a) Glass capillary filled with sample and mounted on a goniometer which can be adjusted to align the capillary with the incoming x-ray beam b) The transmission geometry of the experiment where the synchrotron x-ray beam comes from a stationary outlet and falls on the capillary which rotates about itself. The stopper stops any undiffracted x-rays. The detector (not shown here) rotates to spans the 2θ range.

As mentioned earlier, diffraction experiments are done in transmission geometry at synchrotron sources. Absorption can be an issue in transmission geometry for materials

containing a large fraction of high-Z elements. A highly absorbing sample will result in a transmission powder pattern with attenuated diffraction peak intensities, especially at low 2θ angles as the sample absorbs both incoming and diffracted x-rays. This problem can be mitigated by either using high energy x-rays and smaller diameter capillary or by diluting the sample with amorphous powder of silica. Otherwise, absorption correction available in most refinement softwares can also correct this issue to some extent. Typically for $\mu u \geq 5$ (where μ is the x-ray absorption coefficient), the data is not acceptable.

Keeping into consideration the absorption, the finely ground sample is then filled in an appropriately sized glass or kapton capillary and mounted on the sample holder. This sample holder is then aligned parallel to the beam and continuously rotated 360° to avoid preferred orientations. The data range is decided based on the wavelength. The sample holder and the holder after mounting it for the experiment are shown in figures below.

In the present thesis, synchrotron x-ray diffraction experiments were carried at Elettra synchrotron, Trieste, Italy; Petra III, DESY (Deutsches elektronen synkrotronen) Germany and Argonne national laboratory, USA.

2.2.4 Neutron powder diffraction

Neutron diffraction, unlike x-ray diffraction, cannot be performed at laboratory scale as they require a source of neutrons which are usually produced in a nuclear reactor or spallation source. At a research reactor, other components are needed, including a crystal monochromator, as well as filters to select the desired neutron wavelength.

Neutron powder diffraction shares similar principles of operation with x-ray diffraction. However, contrary to x-rays that interact primarily with the electron cloud surrounding each atom, neutrons scattering occurs at the nuclei and provides complementary information not accessible with x-rays. Furthermore, the neutron carries a magnetic moment, which makes it an excellent probe for the determination of magnetic structure.

Scattering of a neutron by the nucleus is mediated by strong nuclear force. The wavelength of thermal neutrons, of the order of several angstroms, is larger by $\sim 4-5$ orders of magnitude than the dimension of the nucleus. Hence, when the plane wave of neutrons is scattered off the nucleus, the nucleus acts as a secondary point source and radiates scattered neutrons as a spherical wave. In this case, $\rho(r)$ is given by the spatial density distribution of the nuclei, which is a delta function (infinitesimal) with

respect to the neutron wavelength. As the Fourier transform of a delta function is unity, the scattering amplitude is independent of Q and hence the measurement angle. Thus, unlike x-rays, the intensity of peaks in a neutron diffraction pattern does not decrease or diminish with increasing angle.

Another difference between x-rays and neutron is that, due to the direct interaction of neutrons with the nucleus, the diffracted intensity depends on each isotope. Hence, neighbouring elements or even hydrogen and deuterium contribute differently to a neutron diffraction pattern. Also, the scattering length varies from isotope to isotope and is not proportional to the atomic number. Hence, the scattering does not follow any standard law and has to be determined empirically.

On the experimental front, neutrons are much preferred over electrons when probing light elements like oxygen. Neutron can provide accurate information about the position and occupancy of oxygen in a compound where x-rays do not provide very reliable information. The downside of neutron diffraction experiments is that they need several grams of compounds for the experiments. This can be taxing while working with expensive oxides, such as iridates. In this thesis, neutron powder diffraction has been carried out on pyrochlore stannates with thermal neutrons at Bhabha atomic research center (BARC), Mumbai, India.

2.2.5 Rietveld refinement

Rietveld refinement method carries the name of its founder, Hugo Rietveld [54]. This method uses a least square approach to simulate a theoretical line profile by refining the measured neutron/x-ray diffraction pattern. This method, first introduced in 1967 for neutron diffraction, brought a revolution in the field of diffraction analysis as, unlike other techniques at that time, it was able to deal reliably with strongly overlapping reflections.

A powder x-ray diffraction pattern is amalgamation of Bragg peaks from the sample with instrumental contributions. With the preliminary input of parameters such as the space group and Wyckoff position of various atoms, the Rietveld refinement is capable of revealing much more details about the structure to great precision. Some of the important steps in the refinement process are listed below.

- Correcting for the zero error. Sample geometry and instrumental configuration

can result in a zero error, which, if not refined, can introduce artifact in the lattice constant values.

- Identifying the correct peak positions: Before the refinement proceeds any further, it is essential to identify the right peak position that can be obtained by refining lattice parameters.
- Peak profile or shape: The peak profile is comprised of contributions from the instrument as well as from the sample in terms of particle size and stress/strain. It is represented by profile functions that determine the FWHM and the peak shape and is angle-dependent. Obtaining a stable peak profile is essential and can be tricky.
- Peak intensity: Intensity depends on composition i.e. structure factor and is also affected by the atomic position and their displacement (the thermal factor).

Agreement between measured and calculated diffraction pattern for all of the above factors along with modeling the background would result in the successful termination of the refinement process. A meaningful refinement depends significantly on the resolution of the data and statistics and is also reflected in the difference curve between theoretical and measured pattern. Nonetheless, the quality of the refinement, to some extent, could be assessed from the goodness of fit parameters. Before defining the goodness of fit parameters, we will first define some relevant terminology. By convention, the intensity values are labeled $y_{O,i}$, where O indicates these are observed values and i indicates the intensity was measured at 2θ value $2\theta_i$. It is necessary to have an uncertainty estimate for $y_{O,i}$, which is labeled as $\sigma[y_{O,i}]$. This is nothing but the standard uncertainty in the data. The meaning of $\sigma[y_{O,i}]$ is that if we had the knowledge of true value of the intensity, labeled as $y_{T,i}$, say, by measuring it an infinite number of times, then on average $y_{O,i}$ will be $\pm\sigma[y_{O,i}]$ of $y_{T,i}$. Hence the expression $\langle (y_{O,i} - \langle y_{O,i} \rangle)^2 \rangle = \sigma^2[y_{O,i}]$ gives expected value where $\langle \rangle$ indicates the expected value.

In Rietveld refinement, we are simulating intensities. The calculated intensity value labeled as $y_{C,i}$ where the subscript C indicates computed intensity. The Rietveld algorithm optimizes the model function to minimize the weighted sum of squared differences between the observed and calculated intensity so as to minimize $\sum_i w_i (y_{C,i} -$

$y_{O,i})^2$ where the weight w_i is $\frac{1}{\sigma^2[y_{O,i}]}$. The first in the list is the weighted profile R-factor (R_{wp}).

$$R_{wp} = \frac{\sum_i w_i (y_{C,i} - y_{O,i})^2}{\sum_i w_i (y_{O,i})^2} \quad (2.4)$$

This factor depends on the uncertainty of each data point. That brings us to the second parameter, described as the best possible weighted profile R-factor or R_{exp} . If N is the total number of data points collected then R_{exp} is defined as,

$$R_{exp} = \frac{N}{\sum_i w_i (y_{O,i})^2} \quad (2.5)$$

A relevant and most commonly used parameter is the goodness of fit parameter or the χ^2 . It is defined by,

$$\chi^2 = \frac{1}{N} \frac{\sum_i w_i (y_{C,i} - y_{O,i})^2}{\sigma^2[y_{O,i}]} \quad (2.6)$$

It can also be expressed as the square of the ratio of R_{wp} and R_{exp} . At the starting of the refinement, χ^2 is typically very large, and as the difference between the calculated and measured profile reduces, the value gradually comes down. The ideal value of χ^2 is unity.

These parameters along with the difference plot between the computed and measured profile can help in assessing the quality of the refinement. The Rietveld refinement, when done successfully on a high quality data, is extremely useful in giving the precise value of multiple structural parameters.

2.3 Physical properties

The samples studied in this thesis were characterized using lab-based instruments, as well as, were probed with advanced measurement techniques at muon, Neutron and Synchrotron sources. First, we would describe the lab-based techniques. All the measurements were done using a physical properties measurement system (PPMS) from Quantum Design, Model 6000, USA. The instrument is equipped with an Ever-cool-II liquid He refrigerator which provides access to measurement temperatures ranging from 1.9 K to 300 K. Inside the sample chamber the magnetic field can be varied between ± 90 kOe using a superconducting magnet submerged in the liquid He bath. Separate probes

were used for different measurements, such as resistivity, specific heat, thermopower, and dc magnetometry. Their details are presented next.

2.3.1 Electrical transport

Measuring the response of itinerant electrons against an applied bias gives crucial information about the band structure and the various scattering mechanism present in the sample. The measurable quantity for electrical transport is the electrical conductivity, σ , defined as the proportionality constant between an applied electrical field and resultant current density $\mathbf{J} = \sigma \mathbf{E}$. The conductivity is inherently a tensor and may contain off-diagonal elements in the presence of a magnetic field. In the literature, typically, resistivity is reported which is simply the inverse of the conductivity. Resistivity is obtained by multiplying the measured resistance (R) of the sample which is cut in the shape of a rectangular bar of cross-sectional area (A) through which a constant current (I) flows and dividing by the length (l) between the voltage probes, as given in the equation below.

$$\rho = \frac{RA}{l} \quad (2.7)$$

The measurement might appear trivial; however, there are several intricacies involved that can dramatically affect the measured values. Hence, care must be taken in order to obtain accurate results. All the resistivity measurements reported in this thesis were done on well-sintered, rectangular-shaped samples using the four-probe method as shown in Fig 2.4. We will now elucidate how this measurement protocol has contributed towards obtaining accurate and noise-free data.

While measuring the resistivity, especially of metallic samples, there can be a significant contact resistance compared to the resistance of the sample. Hence, to get correct values, four-probe measurements are necessary. In a four-probe setup, the current is injected by the outer leads, whereas the inner two leads are used to measure the voltage drop across the sample. As the internal impedance of the voltmeter is in the order of $100 \text{ M}\Omega$, all the current flows through the sample and only sample resistance can be recorded.

Another problem is Joule heating which can be considerable at low temperatures. During the measurement, the sample, the wires, and their junction with the sample, all

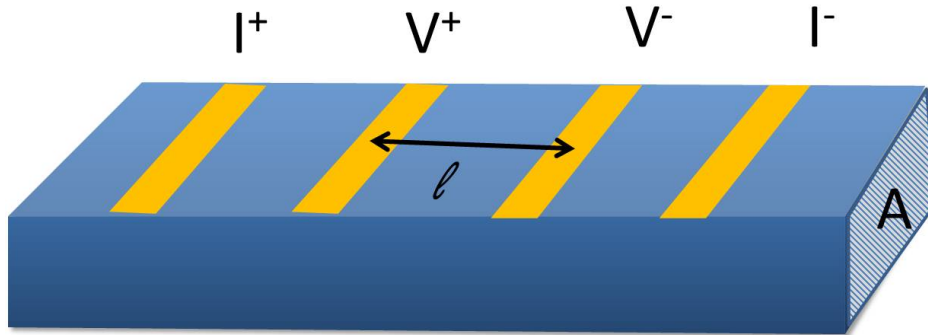


Figure 2.4: A schematic showing the four probe method of measuring the electrical resistivity. I^+ and I^- are the current probes and V^+ and V^- are the corresponding voltage probes.

can contribute to Joule heating and will dissipate the heat at the rate $P=I^2R$. This heat can create local temperature gradient or increase the temperature around the sample. This issue can be mitigated by using low-resistance wires and a small value of the excitation current, in the order of milliamperes. In our experiments, we typically used excitation of 1-5 mA and the contacts were made using 25-micron thick gold wire.

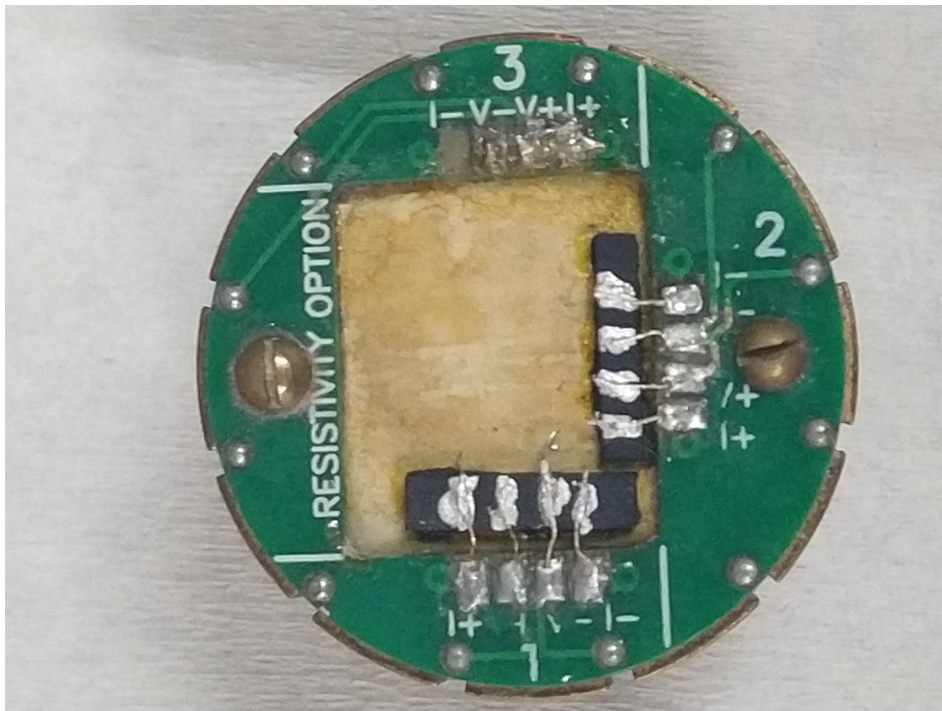


Figure 2.5: Samples mounted with four probe geometry on a PPMS resistivity probe

Finally, the sample must be free from any cracks and should be cut in a regular (rectangular) shape. Resistivity measurements are possible on arbitrarily shaped samples using an alternate method known as the Van-der-paw method. However, in our case, a rectangular geometry ensured smooth translation of the resistance into resistivity using equation 2.7. If there are cracks present in the sample, then as the temperature is ramped down, these cracks can widen and may reflect as arbitrary jumps in the data that is not intrinsic to the sample. This can also lead to different resistivity curves for measurements taken during the heating and cooling of the sample. All the sample measured in this thesis were sintered near their synthesis temperature to ensure crack free dense sample.

2.3.2 Thermal and thermoelectric transport

Thermal transport includes properties like thermal conductivity and thermopower (also called as Seebeck coefficient). Thermal conductivity is a measure of the ability of a material to conduct heat, whereas the thermopower describes the thermal diffusion of free charge carriers (electrons or holes), which creates an electric field inside a material when a temperature gradient is sustained. Thermopower is a complex quantity which is sensitive to changes in the sign and the number of charge carriers and can be a powerful probe in that regard. Measurement of these properties gives considerable information about the electronic structure as well as the electron-phonon interaction in a sample.

In this thesis, both thermal conductivity (κ) and thermopower (α), were measured in the range of 300 K- 2 K using the thermal transport option (TTO) in the physical properties measurement system by Quantum design. The measurement is done in a four-terminal assembly which includes (preferably) a bar-shaped sample to be connected to the heater, hot thermometer, cold thermometer, and a cold finger. The heater and the hot thermometer are wired close to each other at one end of the sample. The heater is used to send a heat pulse to the sample and the cold finger acts as a heat sink and is connected to the thermal bath. This arrangement creates a local temperature gradient across the sample. The hot thermometer is connected near the heater whereas the cold thermometer is connected close to the cold finger. These two thermometers monitor the temperature, and these probes are also used to measure the voltage drop in the case of thermopower measurements. To avoid radiation losses, all the thermal transport measurements are done in high vacuum (10^{-5} Torr) and in addition, the whole measurement assembly is

encapsulated in a copper shield. The schematic of the sample assembly and a mounted sample are shown in Fig. 2.6.

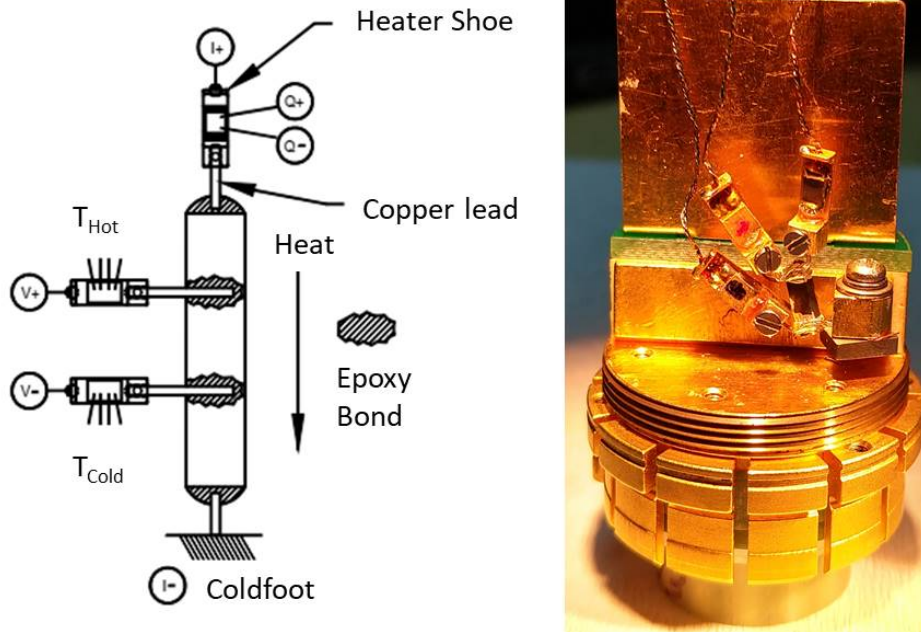


Figure 2.6: Schematic of a typical four terminal thermal transport measurement assembly (adopted from PPMS, Quantum design manual) and image of a pyrochlore sample mounted for thermopower measurement. The shoe with red dot and blue dot correspond to hot thermometer and cold thermometer respectively.

κ is measured by applying heat from the heater shoe in order to create a user-specified temperature differential between the two thermometer shoes. The TTO system dynamically models the thermal response of the sample to the low-frequency, square-wave heat pulse, thus speeding up the data acquisition. The thermal conductivity is then directly calculated from the applied heater power, resulting in ΔT , and sample geometry.

For thermopower, a temperature drop is created across the sample and simultaneously the voltage drop created between the thermometer shoes is also monitored. The additional voltage-sense leads on these thermometer shoes are connected to the ultra-low-noise preamplifier. There are two modes of measurement for thermal properties: continuous mode and single mode. In continuous measurement mode, measurements are being taken continually and the adaptive software is modifying parameters (such as heater power and period) to optimize the measurements. This measurement is relatively fast due to the rapid processing of the data by the curve fitting algorithm which

determines the steady state (equilibrium) thermal properties by extrapolating from the response of a short (around several minutes) heat pulse. In the continuous measurement mode, the base temperature is ramped slowly and the measurements are recorded in parallel.

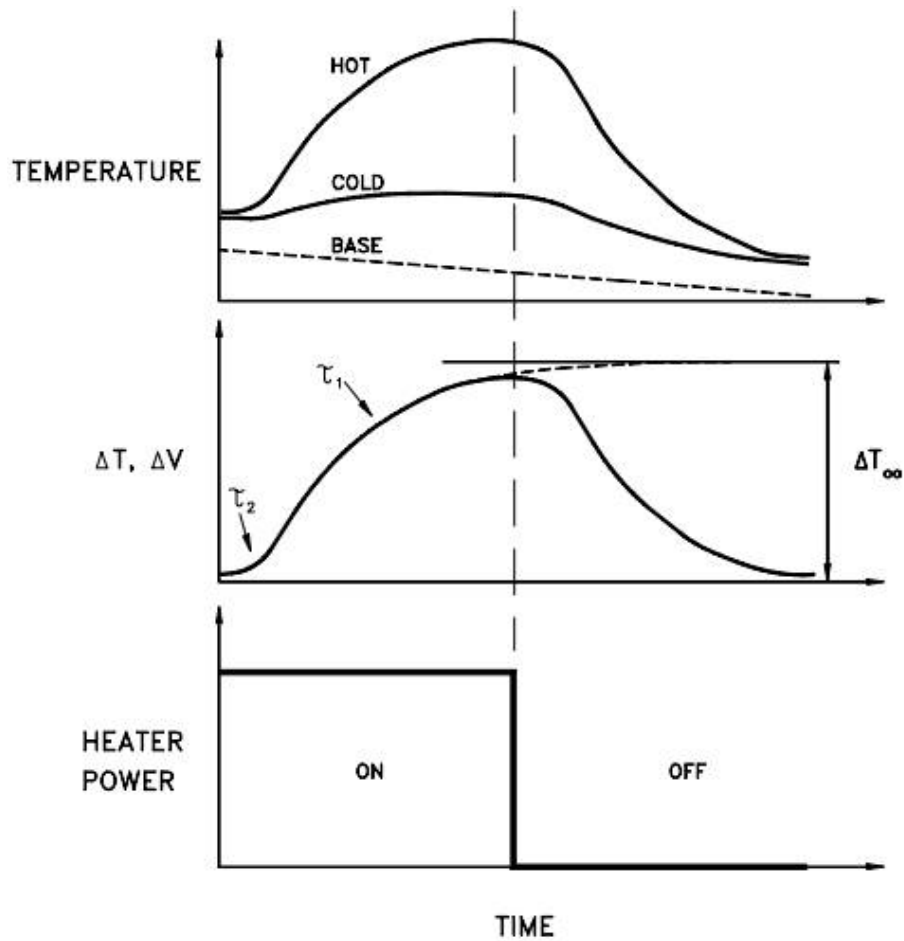


Figure 2.7: Top panel: Time trace of hot and cold thermometers during an idealized heat pulse where the base temperature is slowly ramped. Middle panel: Corresponding temperature ΔT and voltage ΔV differentials across the sample, indicating thermal time constants τ_1 and τ_2 and the estimate of the asymptotic differential ΔT_∞ (adopted from TTO manual).

The single measurement mode, on the other hand, refers to a measurement taken at a given temperature. This mode requires that the system reach a steady state in both the heater “off” and “on” states, which in turn implies that base temperature ramping is not possible. In single measurement mode no curve-fitting is involved, so interpretation of the raw data is more straightforward. The first set of data is taken in the heater “off”

state. After the user-specified heater power is applied, the system waits until the selected equilibrium condition is reached before taking the final measurement in the heater “on” state.

In this thesis, all the measurements are done using the continuous mode, as it offers high data-density across the wide temperature range. We will now see in detail the algorithm employed during continuous measurement mode. In continuous measurement mode, once the ΔT vs. time data over the period of the heat pulse is obtained, a non-linear least-squares fitting routine, which fits the data to the given empirical formula, is triggered

$$\Delta T_{model} = \Delta T_{\infty} \times 1 - [\tau_1 \times \exp\frac{-t}{\tau_1}] - \tau_2 \times \exp\frac{-t}{\tau_2} / (\tau_1 - \tau_2) \quad (2.8)$$

Here ΔT_{∞} represents the asymptotic temperature drop across the sample in the case the heater is left on indefinitely, and τ_1 and τ_2 are long and short empirical time constants, respectively, for the sample. The fitting routine carries out an exhaustive search in these three parameters space, reducing the space with every iteration until the parameter values that yield the minimum residual of the curve fit are identified. The above mentioned equation is employed to the data collected during the heating pulse, while the data collected during the cooling pulse is simultaneously fit essentially by reversing the sign of the model equation: $\Delta T_{model,cooling} = A - \Delta T_{model,heating}$, where A is a constant. Due to prolong thermal diffusion times (τ_1), the thermal history of the sample is crucial and must be considered in the model. This is accomplished by including the remnant effects of the previous two pulses while modeling the current pulse. For thermopower, the ΔV vs. time data is read back towards the end of the measurement, and after the ΔT vs. time data is fit to obtain τ_1 and τ_2 , a linear least-squares routine fits the data to the following equation:

$$\Delta V_{model} = \Delta V_{\infty} \times \frac{(1 - [\tau_1 \times \exp\frac{-t}{\tau_1}] \pm \tau_2' \times \exp\frac{-t}{\tau_2'})}{(\tau_1 - \tau_2')} + bt + c \quad (2.9)$$

where ΔV_{∞} is the asymptotic thermopower voltage drop akin to ΔT_{∞} in equation 2.8, b and c are parameters that describe linear drift and offset voltages, respectively, and $\tau_2' = 0 \dots \tau_1$ is swept so that for each value of τ_2' a linear regression in ΔV_{∞} , b and c is performed. The \pm sign situated in between the exponential terms originates from the

fact that the thermopower of the leads associated with the short time constant τ_2 may be of the opposite sign than that of the sample associated with the long time constant. This is in contrast to the case of thermal conductivity, which is always positive. The parameter for the linear voltage drift b is included here to account for varying thermal voltages in the wiring to the sample and also the slow microvolt-level drift in the preamp electronics.

2.3.3 Specific Heat

The specific heat probe was used to study the long-range magnetic ordering, and electronic and phononic excitations in the pyrochlore iridates, as well as to estimate the electronic coefficient of specific heat. All the measurements were carried out in a calorimeter probe attachment of the PPMS. A schematic diagram of the calorimeter is shown in Fig. 2.8. The calorimeter consists of a sample platform that includes an inbuilt temperature sensor and a heater. The sample platform is suspended by 8 connecting wires (Au-Pd alloy) which provide both electrical connectivity to the sensor and the heater and allow a controlled thermal coupling between the platform and the puck. The puck is in thermal equilibrium with the sample chamber. Any other thermal losses such as radiation loss are minimized by carrying out the measurements under high vacuum ($\sim 10^{-5}$ mbar).

The thermal coupling between the sample and the platform is ensured using the Apiezon grease. For low temperature measurement ($T < 200$ K) Apiezon-N grease is used, whereas, for higher temperature measurements Apiezon-H grease is used. The platform size limits the size of the sample to a maximum value of 3×3 mm², whereas the sample mass can range from 2 mg to 200 mg. The sample is a piece cut from a sintered and dense pellet.

The specific measurement is a two-step measurement. In the first step, specific heat measurements are carried out only for the sample platform and the applied grease. The measurements are done in the temperature range of interest for the sample that is to be measured. The second step involves, measuring the specific heat of the sample which now also has the contribution from the platform and the grease. The background of the platform and the grease can be smoothly removed by subtracting the data obtained in the first step from that of step two. The advantage of this method is that no knowledge of the quantity of grease used is necessary. All the measurements were done following

this protocol.

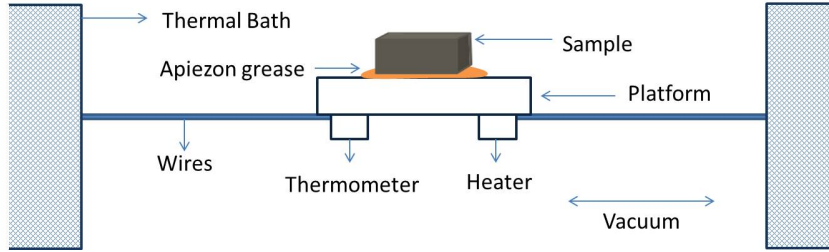


Figure 2.8: Schematic depicting the sample holder for specific heat arrangement.

At the core of the conversion of raw data into the heat capacity of the sample is the mathematical model used to describe the temperature response of the sample platform as a function of time. For this purpose, two models are generally employed. The first one is a simple model, which, as per the name does the most basic processing of the raw data measurement. This model assumes that the sample is in good thermal contact with the sample platform and both of them are at the same temperature during the measurement. In this simple model, the temperature T of the platform as a function of time t obeys the following equation

$$C_{total} \frac{dT}{dt} = -K_w(T - T_b) + P(t) \quad (2.10)$$

where C_{total} is the total heat capacity of the sample along with the sample platform; K_w is the thermal conductance of the supporting wires; T_b is the temperature of the thermal bath (puck frame); and $P(t)$ is the power applied by the heater. The heater power $P(t)$ is equal to P_0 during the heating cycle of the measurement and is equal to zero during the cooling cycle. The solution to this equation is given by exponential functions with a characteristic time constant τ equal to C_{total}/K .

Heat capacity of grease is always measured using the simple model and most of the samples are measured using the same model as well. However, when there is poor thermal contact between the sample and the platform, the software uses the more sophisticated two-tau model to measure the heat capacity.

Two tau model is used when poor thermal contact between the sample and the platform results in a temperature difference between the two. This basically implies two different relaxation time constants for the sample and the stage. The two-tau model simulates the effect of heat flowing between the sample platform and sample, and the

effect of heat flowing between the sample platform and puck. The following equations express the two-tau model:

$$C_{platform} \frac{dT_P}{dt} = P(t) - K_w(T_p(t) - T_b) + K_g(T_s(t) - T_p(t)) \quad (2.11)$$

$$C_{sample} \frac{dT_s}{dt} = K_g(T_s(t) - T_p(t)) \quad (2.12)$$

where $C_{platform}$ is the heat capacity of the sample platform, C_{sample} is the heat capacity of the sample, and K_g is the thermal conductance between the two due to the grease. The respective temperatures of the platform and sample are given by $T_p(t)$ and $T_s(t)$.

For the data fitting purpose, a nonlinear, least-square fitting algorithm is used where the system compares the solution given by the simple model with the actual measurement. The parameter values that give the smallest deviation to the fit determine the heat capacity. The susceptibility of the fit deviation (χ^2) to the minor variations in the fitting parameters is used to estimate the error in the heat capacity. Except while measuring the grease, a fit to the solution of the two-tau model is also carried out. The heat capacity values derived in this manner are used only if it has lesser deviation compared to the simple model. Under certain circumstances, the fit to the two-tau model does not converge, in which case the simple fit is used as default. This type of lack of convergence can occur when the sample is perfectly attached to the platform, and thus the simple model is correct. Difficulties in fitting can occur when the sample has poor contact with the platform and the heat capacity of the sample is not large enough compared to the platform. In such a scenario, the sample coupling is erroneously shown to be 100% and the simple model is employed in non-ideal conditions.

In the case of the simple model, the sample heat capacity is computed from the difference between the total heat capacity of the fit and the addenda heat capacity. In the case of simple model, $\tau_1 = C_{total}/K_w$ and $\tau_2 = 0$ and sample coupling is 100%. When two-tau model is employed, the addenda heat capacity $C_{addenda}$ is retrieved from a previously measured addenda table and $C_{platform}$ is treated as a constant equal to $C_{addenda}$ in the fitting routine. In this case, $\tau_1 = 1/(\alpha - \beta)$ and $\tau_2 = 1/(\alpha + \beta)$ and the sample coupling is computed as $100 \times K_g/(K_g + K_w)$.

The expressions for α and β are given by:

$$\alpha = \frac{K_w}{2C_{platform}} + \frac{K_g}{2C_{platform}} + \frac{K_g}{2C_{sample}} \quad (2.13)$$

$$\beta = \frac{\sqrt{(K_g C_{sample} + K_g C_{platform})^2 + K_w^2 C_{sample}^2 + 2K_w K_g C_{sample}^2 - 2K_w K_g C_{sample} C_{platform}}}{2C_{platform} C_{sample}} \quad (2.14)$$

2.3.4 dc susceptibility

The dc magnetisation measurements were carried out using a vibrating sample magnetometer (VSM) probe inside the PPMS cryostat. The working of VSM is based on the principle of generation of voltage in a coil upon a change in the magnetic flux. In VSM, the induced voltage generated by the sample is translated into equivalent electromagnet units using a standard calibration. This mechanism is described by the following equation.

$$V_{coil} = \frac{d\phi}{dt} = \frac{d\phi}{dz} \frac{dz}{dt} \quad (2.15)$$

Where ϕ represents the magnetic flux through the coils, z is the vertical position of the sample with respect to the coil, and t is the time.

The measurement setup comprises of a linear motor to vibrate the sample inside the pickup coil-set, the first-order gradiometer coil-set consisting of a pair of secondary coils wound around in opposite directions to each other, and the voltmeter to detect the signal from the pickup coil. The sample holder is made up of quartz and the sample is mounted on the holder using a non-magnetic GE varnish. The sample is placed at the center of the coil. The superconducting magnet in the PPMS cryostat is used to generate a uniform dc magnetic field around the sample. As the linear motor vibrates the sample between the coil-set, the magnetic flux due to induced magnetisation on the sample by the dc field varies with the same frequency and thus induces a voltage in the pickup coil. The pick coil offers oscillation amplitude up to 1-3mm in the frequency range of 1-100 Hz, with a resolution of around 10^{-5} emu.

2.4 Muon spin spectroscopy

Muon spin spectroscopy (μ SR) is a technique that tracks the muon spin behaviour as it passes through the sample to probe the magnetism in the given sample. Muons are subatomic particles with a lifetime of $2.2\mu\text{s}$. Muons are spin $\frac{1}{2}$ particles with the same charge as protons and their mass is 207 times that of the electron. Due to their heavy mass, they are not sharply accelerated by electromagnetic fields and do not emit bremsstrahlung radiations. This facilitates their much deeper penetration into the matter compared to the same energy electrons. In addition, the muon has a much smaller (larger) gyromagnetic ratio than the electron (proton) and can be used to study local magnetic fields. Muons are present in the atmosphere and are generated by cosmic rays hitting the atmosphere. However, for measurement purposes, muons with certain energy are necessary and can be produced at neutron sources.

Muon spin rotation/relaxation (μ SR) was first realized in the 1950's when fundamental experiments studying the asymmetry of the muon decay noted the preferential emission of positrons from positive muon decay along the spin orientation could be used as a local probe of interstitial regions in solid materials [55]. For the experiments, muons can be generated in a multi-step process. In the first step, high-energy protons (> 500 MeV) are collided onto a solid target of Carbon or Beryllium. This collision process results in the pion production. The high energy protons interact with the light nuclei resulting in the creation of pions in the following manner:

$$p + p = \pi^+ + p + n \quad (2.16)$$

$$p + n = \pi^+ + n + n \quad (2.17)$$

$$p + n = \pi^- + p + p \quad (2.18)$$

Now the pion is an unstable particle that decays with a lifetime of ~ 26 ns via the weak interaction into a muon and a corresponding neutrino shown as per the following equation.

$$\pi^\pm = \mu^\pm + \nu_\mu \quad (2.19)$$

When the spin zero particle, pion, at rest undergoes decay then in its rest frame

the conservation of linear momentum demands that the resulting muon and antineutrino must be emitted in opposite directions. As the spin and momentum vectors of neutrino must be antiparallel, by conservation of angular momentum, the emitted muon also must have a definite spin with respect to antineutrino. Thus, the muons are also produced in a chiral state having spin and momentum vectors antiparallel. These muons are further filtered into a spin-polarized monochromatic beam. For condensed matter experiments, only positive muons are used with a typical energy of ~ 26 MeV. Positive muons readily lose energy through electrostatic interaction with the lattice and come to rest near the site of lowest electronegativity or near the anion. The polarization of muon is unaffected in this interaction. Once collided, the stopping length of the muon is of the order of 100-300 μm for the solid-state samples; hence, it is more of a bulk probe than being surface sensitive. Thus, the experimental setup with muons do not require ultra-high vacuum environment.

In a typical μSR experiment, the polarised muons are incident on the sample where they get implanted at the interstitial sites and stay there until their decay via weak interaction into a pair of neutrino and positrons.

$$\mu^+ = e^+ + \nu_e + \nu_\mu \quad (2.20)$$

The decayed products are then detected by the detectors, which carry the information about the internal field of the sample at the time of decay. An important principle involved in this decay makes muons an effective probe of magnetism, which concerns the parity violation in this decay process where the positron is emitted preferentially along the direction of its spin. Though a single decay event cannot determine the spin orientation, one can determine the statistical average direction of the spin polarization by measuring the anisotropic distribution of the positrons decayed from muons implanted in identical conditions in the sample. The time evolution of the muon spin polarization depends sensitively on the spatial distribution and dynamical fluctuations of the muon's magnetic environment. The probability of the positron emission at an angle θ relative to the spin \mathbf{S} is shown in Fig. 2.9, and is given by the equation:

$$P \sim [1 + \alpha(\epsilon)\cos\theta] \quad (2.21)$$

Where $\alpha(\epsilon)$ depends on the positron kinetic energy, ϵ . As muons with all the energies are detected, the average over all the possible energies yields an average asymmetry for positron emission of $\alpha = -\frac{1}{3}$. As muons are also emitted in all possible directions, several detectors are employed for the measurement. In the present study, the muon-

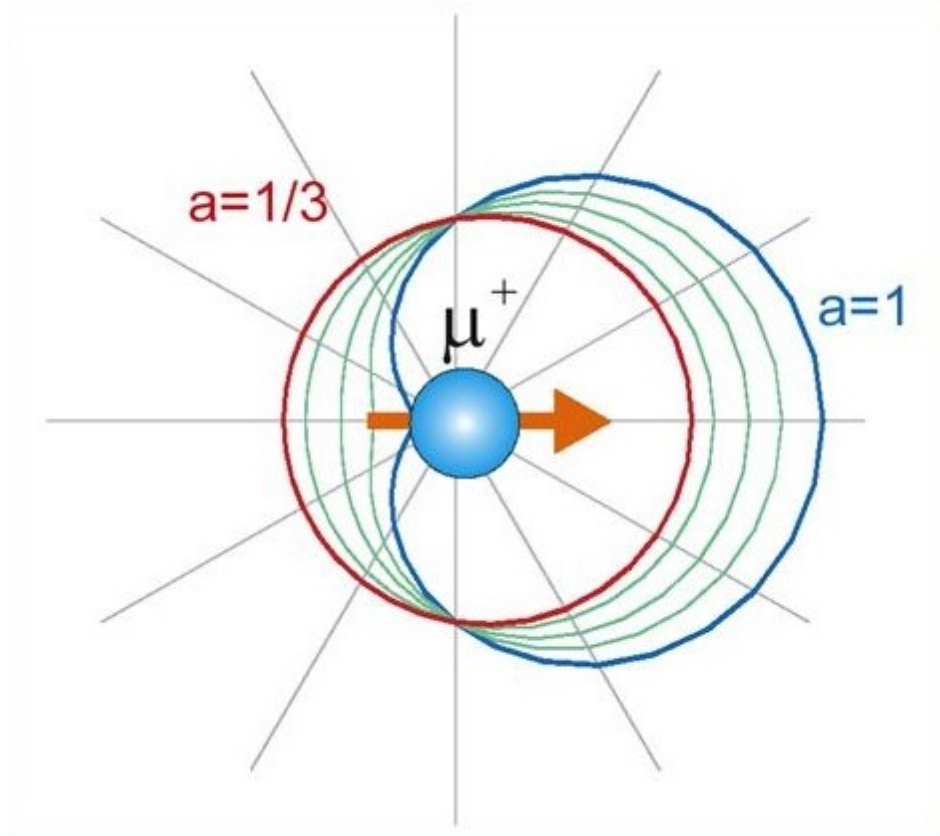


Figure 2.9: Angular distribution of positron from μ^+ decay. The asymmetry $a = 1/3$ when all positrons energies are detected with equal probability.

spin spectroscopy studies were performed at Paul Scherrer institute (PSI) on the GPS (general purpose spectrometer) and LTF (low-temperature facility) spectrometer in conditions of zero-magnetic field (ZF- μ SR). The muon source at PSI is a continuous muons source with the highest flux in the world. A valid measurement is counted only when a single muon is present in the sample at a given time and a continuous supply of such muons facilitates observation of a very fast relaxation rate. The experimental geometry of GPS is given in Fig. 2.10.

The recoiled positrons from the muon decay process are then captured by the detector arrangement consisting of a muon detector (M), 6 positron detectors (Forward,

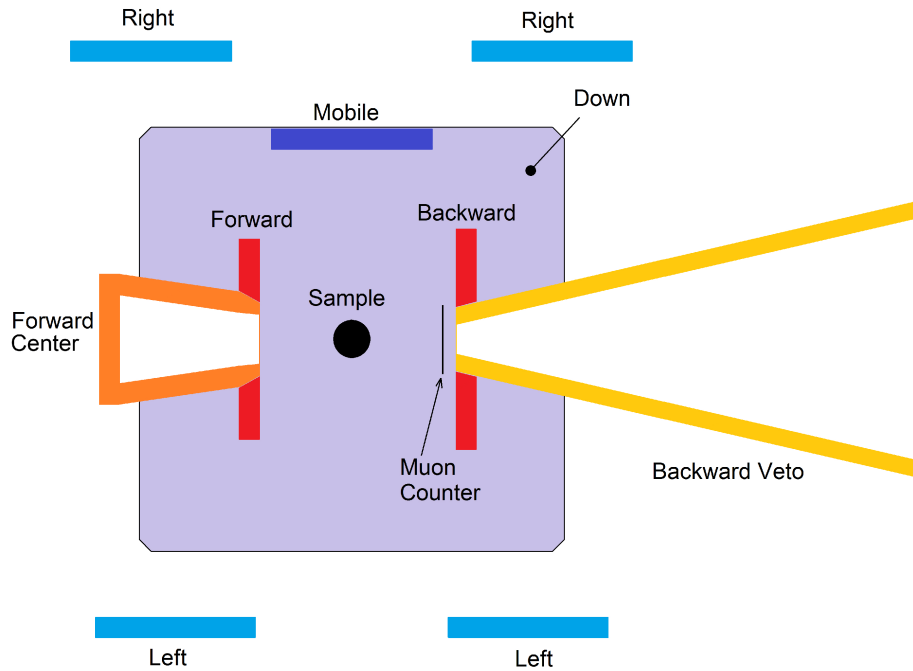


Figure 2.10: Detector geometry for general purpose spectrometer at PSI (adapted from PSI website)

Backward, Up, Down, Right Left, with respect to the direction of the incident beam) and a Backward veto detector, which helps to get rid of the muons passed through the sample and their decayed positrons, by collimating them to a blank spot. By measuring the asymmetry, one gets the frequency of precession of the implanted muons which is related to the magnetic field B via $\omega = \gamma_{\mu} B$ where $\gamma_{\mu} = \frac{g_e}{2m_{\mu}}$ is the gyromagnetic ratio. In a magnetically ordered solid, the implanted muons precess in the internal magnetic field making it possible to not only determine the phase transition temperature but, depending on the form of the asymmetry function, also the nature of magnetic ordering (i.e., long-range ordering versus spin-glass or cluster glass-like inhomogeneous ordering). Due to the large magnetic moment of muon, μ SR is very sensitive to extremely small magnetic fields ($\sim 10^{-5}$ T).

2.5 Hard x-ray photoelectron spectroscopy

Photoelectron spectroscopy is an analysis method first reported by Kai. M. Siegbahn in the 1950's [56]. Photoelectron spectroscopy simply uses the photoelectric effect where

the incident photons can result in the emission of electrons from the solid. With known photon energy and by measuring the kinetic energy of the emitted electrons E_k , the binding energy E_B of the electrons in the solid can be determined using the following equation;

$$E_B = E_{\text{photon}} - \phi - E_k \quad (2.22)$$

Here ϕ is work function specific to that sample. The photoemission spectrum could be obtained by detecting the electron flux as a function of their kinetic energy. Such a photoelectron spectrum is typically plotted against the binding energy and contains various features. The spectral features of the photoelectron spectrum are dependent on the probability of photoexcitation in a given solid. The crude approximation of the probability, P, that given photon energy would excite an electron from its ground state, ψ_i to the excited state ψ_f is given by Fermi's golden rule.

$$\mathbf{P}_{i,f} \propto \langle \psi_f | T | \psi_i \rangle^2 \cdot \delta(E_f - E_i - E_{\text{photon}}) \quad (2.23)$$

Here the transition is assumed to be an electronic dipole transition induced by the dipole operator T. The consequence of the electronic dipole operator T is that only the states satisfying the dipole selection rules can contribute to the spectrum. The dipole selection rules are given by the difference in the quantum numbers,

$$\Delta J = 0, \pm 1 \quad (2.24)$$

$$\Delta M_J = 0, \pm 1 \quad (2.25)$$

$$\Delta S = 0 \quad (2.26)$$

where J, M_J , and S represent the total angular momentum, secondary total angular momentum, and the spin respectively. This energy selectivity rule results in different binding energy for different atoms. But this is not the only factor that impacts the resultant binding energy. The approximation in Fermi's golden rule does not consider any interaction between the electrons in the solid. However, in real experiments, various interactions impact the photoemission spectrum. The most common effects are discussed here.

2.5.1 Spin-orbit coupling

The photoemission process creates a core-hole in the solid. This core hole has a spin $S = 1/2$ moment and the quantum number $L = 0, 1, 2, \dots$ of the excited electron. For a strong spin-orbit interaction this results in a doublet peak to appear for $L > 0$.

$$J_{\pm} = L \pm S = L \pm \frac{1}{2} \quad (2.27)$$

Thus, all the orbital levels with the exception of s levels ($L = 0$) renders a doublet with two possible states with different binding energies. These doublet peaks will have specific area ratios based on the degeneracy of each spin state, which essentially implies the number of different spin combinations that can give rise to the total J. For example, in the case of 2p spectra, where n is 2 and L is 1, J will take the value 1/2 and 3/2. Then the area ratio for the two spin-orbit peaks ($2p_{1/2}2p_{3/2}$) will be 1:2 (corresponding to 2 electrons in the $2p_{1/2}$ level and 4 electrons in the $2p_{3/2}$ level). These ratios are essential when analyzing the spectra of the p, d, and f core levels.

2.5.2 Chemical Shifts

The same element with different valence state has distinct electron configuration. The core-level binding energies of the two different valence states of the given element will be shifted by ΔE_B due to the fact that the core screening of the electrons is different for the two species. This can be modeled as

$$\Delta E_B = K(Q_A - Q_B) + (V_A - V_B) \quad (2.28)$$

where K is an empirical constant describing the extent of the screening as described above, $Q_A - Q_B$ is the charge difference between the two chemical states A and B and $V_A - V_B$ the potential difference between state A and B constituted by the rest of the electron system. In this manner, chemical change of the material can be identified by changes in the electron binding energy and different chemical species with their valence states can be identified.

2.5.3 Satellite peaks

Photoelectron spectra sometimes contain what is known as satellite peaks. The satellite peaks can originate as a result of non-monochromatic excitations or can be a product of the electronic structure of the material. Such peaks are often observed in the vicinity of core-level peak and can originate from the interaction of the excited electrons with its surrounding. However, the presence of such peaks can lead to confusion in the cases where the position of the satellite peak matches with the peak position of another valence state. In such cases, the use of hard x-ray source can give high-resolution photoemission pattern with distinct line shapes and can lead to less ambiguous interpretation of the pattern.

Here, we discuss some of the advantages of using HAXPES over conventional XPS sources.

2.5.4 Hard x-ray photoemission spectroscopy

The conventional definition of hard x-rays photoemission spectroscopy applies to experiments done with photon energy above the Al k_{α} energy of around 1400 eV. However, HAXPES experiments are usually done at synchrotron sources where monochromatic beam with high energy (~ 6 -8 keV) is available. The use of high energy produces photoelectrons with high kinetic energy, thus increasing their inelastic mean free path (the longest distance traveled without an inelastic scattering event). The inelastic mean free path decides the information depth. Thus, using HAXPES, one can probe the bulk of the sample as the information depth of HAXPES can be as high as $d = 15$ nm. However, the disadvantage here is that with increasing photoelectrons energy, the photo-ionization cross-section σ decreases. This implies, that HAXPES experiments can only be performed at beamlines with high photon flux of 1×10^{11} Ph/s.

In this thesis, all the HAXPES experiments are carried out at the P22 beamline, Deutsches Elektronen Synkrotronen, Germany. Now, we will briefly describe the working of HAXPES setup at the P22 beamline.

2.5.5 Working principle of instrumental setup

The P22 HAXPES beamline is specified for photons in the range of 2.7 keV to 15 keV. Significant fluxes of up to 2×10^{13} ph/s at 8 keV can be achieved. This allows for much

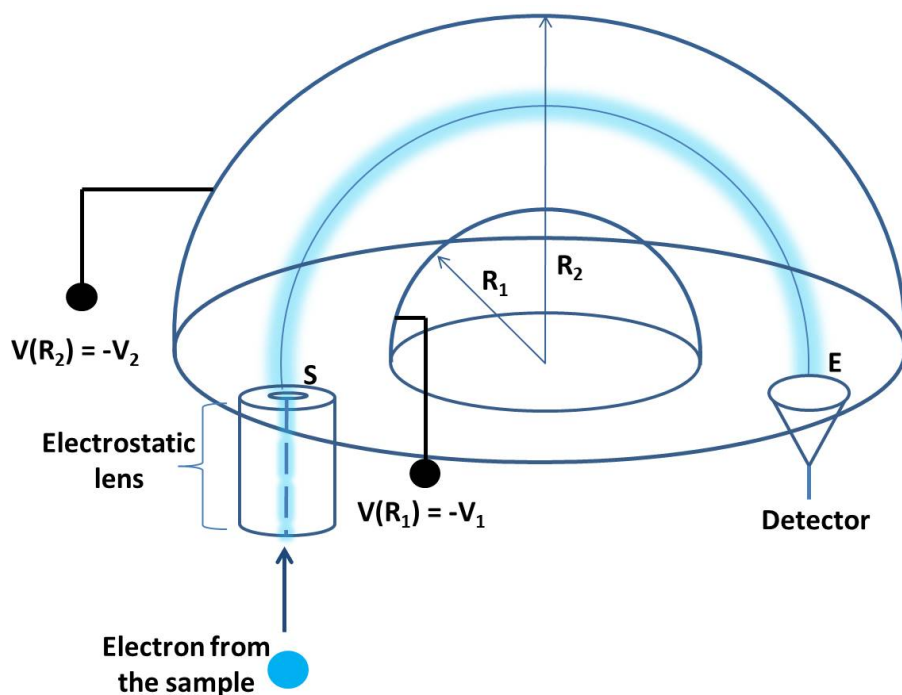


Figure 2.11: Schematic of hemispherical analyser. The electrons from the sample pass through lens (electron optics) before entering the analyser through entrance slit S. The electrons exit after passing through the analyser where they are captured by the detector.

faster scans and compensates for the lower cross-sections at the higher photon energies. Any XPS experiment must be done at high vacuum to permit electron detection without additional scattering between the sample and the detector. An electrostatic 180° hemispherical analyser (HSA) is employed to analyze in energy the electrons expelled from the sample. This electrostatic instrument consists of two concentrically arranged metallic hemispheres and enables to ‘distribute’ the electrons as a function of their kinetic energy. With this intent, a potential difference ΔV is applied between the inner and outer shells of radius R_1 and R_2 , respectively. Both the hemispheres are maintained at a negative potential, with $V(R_2) < V(R_1)$. At a given ΔV , ideally only the electrons with a well-defined kinetic energy E_p are able to complete their path along the medial trajectory of radius $R_0 = (R_1 + R_2)/2$ (R_1 and R_2 radii of the inner and outer hemisphere) and emerge at the exit slit. E_p is called pass energy and its values range between 5 and 50 eV for XPS measurements. Crucially, the pass energy determines the energy resolution of the analyser, which quantifies the ability to separate peaks that differ in energy by

only small amounts.

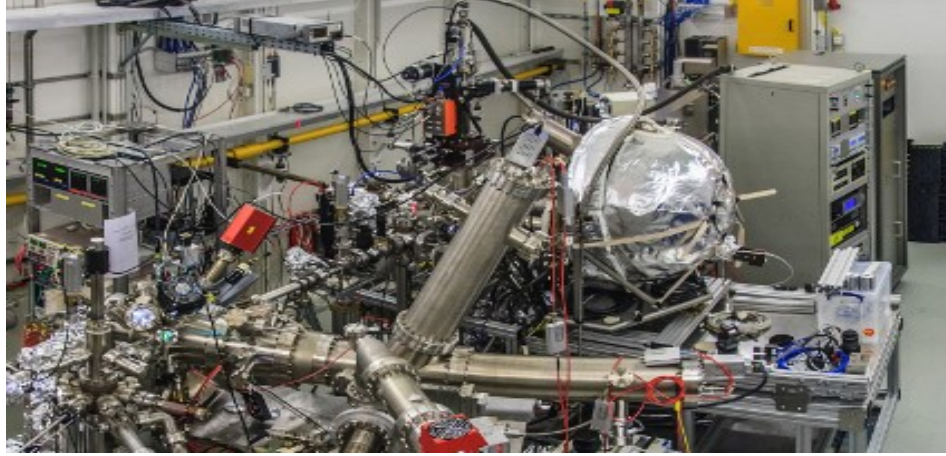


Figure 2.12: HAXPES setup at P22 beamline, Petra III, DESY, Germany.

In order to facilitate scans over arbitrary kinetic energy spectrum, the electrons are decelerated (or accelerated) to the kinetic energy E_p by a potential difference V_R inside the lens system placed between the sample and the entrance slit. The number of electrons is measured by the detector located behind the exit slit of the analyzer. Therefore, by scanning V_R , a spectrum of the photoelectron intensity as a function of the kinetic energy is recorded, the measured kinetic energy being simply $-e \cdot V_R + E_p$. When $V_R = 0$, the Fermi levels of sample and analyzer coincide (in the experimental setup, both the objects are grounded), whereas they are separated by V_R when the retarding voltage is applied. However, due to the different values of the work function, the vacuum levels for the sample and the analyzer do not coincide even for $V_R = 0$. From the energy level diagram illustrated in Fig. 2.13 (adapted from ref 13) it then follows

$$E_b = \hbar\omega - (E_p - \Phi_{analyser} - V_R) = \hbar\omega - E_{vac(analyser)} - \Phi_{analyser} \quad (2.29)$$

This demonstrates that the work function of the analyzer, instead of the work function of the sample, needs to be taken into account. $\Phi_{analyser}$ is included in the equation as in the experiment the kinetic energy scale is referenced to the vacuum level of the analyzer. To keep $\Phi_{analyser}$ constant, all electrodes are covered with a chemically inactive substance (such as gold or graphite).

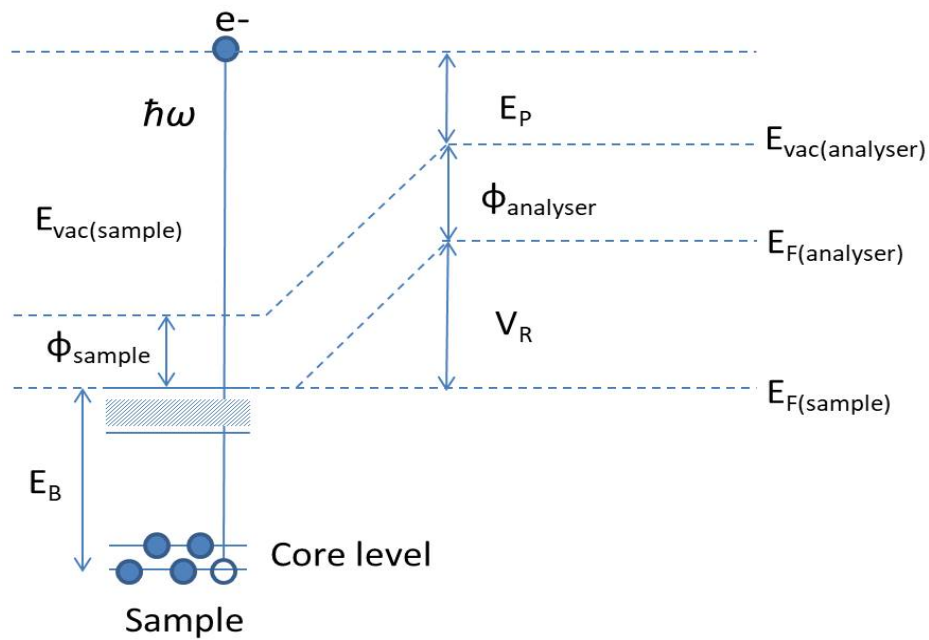


Figure 2.13: Schematic of different energy levels involved in a photoemission experiment. E_B is the binding energy of electrons and $\hbar\omega$ is the kinetic energy of the electrons knocked off from the sample. $E_{\text{vac}(\text{sample/analyser})}$ is the vacuum energy with respect to sample and analyser respectively. Φ represents the work function.

Chapter 3

Effect of stuffing in pyrochlores

We discussed in the introductory chapter about the possibility of realizing a plethora of ground states in pyrochlores $A_2B_2O_7$ depending on the choice of A and B sites. In this chapter, we will study how the dilute substitution of A at the B site or vice-a-versa can affect the ground state properties of the pyrochlore compounds.

3.1 Stuffing in pyrochlore oxides

In pyrochlore oxides, cation anti-site disorder is commonly referred to as ‘stuffing’ (for A-site ion occupying the B-site) or ‘negative stuffing’ (when the reverse happens). Dilute stuffing or anti-stuffing can be done by modifying the stoichiometric proportion of the starting precursors. Stuffing can readily affect the structure due to the difference in the ionic radii of A and B cations. But apart from changing the structural parameters, it can also have a significant effect on the physical properties. For example, the charge imbalance due to different oxidation states of A and B cation would affect the oxygen content and can introduce charge carriers. Also if either A or B cation or both are magnetic, stuffing can have a dramatic effect on the magnetic ground state.

Initially, stuffing in the pyrochlore titanates ($A_2Ti_2O_7$) was reported and systematic studies were performed to understand the variation in physical properties as a consequence of stuffing. In recent years, such studies on the insulating titanate pyrochlores unveiled several interesting aspects of their ground state properties [57–59]. For example, dilute Yb stuffing in the pyrochlore $Yb_2Ti_2O_7$ is reported to have a significant effect on the magnetic ground state as the ferromagnetic T_c is suppressed by nearly 25% by a

mere 2% stuffing, and the shape of the specific heat anomaly also changes considerably signifying a change in the nature of magnetic long-range orderings.

However, similar studies on other families of pyrochlore oxides such as pyrochlore iridates ($A_2Ir_2O_7$) have been lacking. The volatile nature of iridium, and a prolonged sintering period of several weeks required for their synthesis makes the pyrochlore iridates prone to unintentional off-stoichiometry or stuffing during the synthesis. This is reflected in the discrepancy related to structural parameters and physical properties of these pyrochlores as found in the literature (details in the next section). Therefore, it is desirable to investigate and understand the effect of stuffing in the iridate pyrochlores. In this chapter, we address this problem by carrying out a detailed study of the structural variation and consequent changes in the physical properties due to stuffing in the pyrochlore $Eu_2Ir_2O_7$.

For a better understanding of the effect of stuffing on the O-position parameter, it is desirable to have the neutron diffraction data due to the higher sensitivity of neutron to lighter elements. However, due to a large neutron absorption cross-section of both Eu and Ir, it is difficult to carry out neutron studies on $Eu_2Ir_2O_7$. Hence, for this purpose, we also synthesized and studied stuffed samples of the pyrochlore $Yb_2Sn_2O_7$. The details are given in Appendix A.

3.2 Motivation for stuffing in pyrochlore iridate $Eu_2Ir_2O_7$

$Eu_2Ir_2O_7$ (EIO) undergoes a long-range antiferromagnetic ordering concomitant with the metal to insulator transition at 120 K (T_{MI}). Upon cooling below T_{MI} , the resistivity (ρ) of EIO increases sharply, the state below this temperature is therefore dubbed as the 'insulating' state. On the other hand, in the 'metallic' state above T_{MI} , $\rho(T)$ exhibits an anomalous behavior with the slope $d\rho(T)/dT$ negative in some reports [4, 45, 46, 60] and positive in others [61, 62]. However, what causes this stark sample dependence of $d\rho(T)/dT$ in the 'metallic' state has not been properly investigated to the best of our knowledge. In addition, the lack of reports of structural characterizations has made it difficult to corroborate any structural variation with the physical properties. A recent high-pressure investigation by Tafti et al. [63] shows that the sign of $d\rho(T)/dT$ above T_{MI} depends sensitively on the external pressure changing its sign from negative under ambient or low pressures to positive above 6 GPa. Hence, it is natural to speculate that

the structural changes are responsible for such effects. Due to the ionic-size mismatch between Eu^{3+} and Ir^{4+} , a minor Eu-Ir off-stoichiometry in a nominally stoichiometric EIO sample may also induce a small chemical pressure, the question is will this pressure be large enough to explain the sign of $d\rho(T)/dT$ in various EIO samples previously reported? In this chapter, we will discuss our attempt to resolve this discrepancy by investigating the structure and physical properties of six different EIO samples.

3.2.1 Synthesis Protocol

The volatility of IrO_2 and prolonged sintering duration makes it extremely important to follow a certain synthesis protocol for pyrochlore iridates and even more so in a comparative study. We synthesized six different samples and closely tracked the weight loss at each step to understand the various factors that affect the stoichiometry of the final compound.

Six different EIO samples, labeled as A, B1, B2, C1, C2, and D were prepared using the precursors Eu_2O_3 (Sigma Aldrich, 99.9 %) and IrO_2 (Sigma Aldrich, 99.9 %). The ratio Eu/Ir in the starting composition was varied as: $\text{Eu/Ir} = (1-s)/(1+s)$ where $s = 0$ (A), $s = 0.01$ (B1), $s = -0.01$ (B2), $s = 0.02$ (C1), $s = -0.02$ (C2) and $s = 0.015$ (D). As opposed to samples A, B1/B2 and C1/C2 that were synthesized in air, sample D was partly treated under vacuum as described later. The reactants were weighed with a precision of 0.1 mg. After weighing they were thoroughly ground together in an agate mortar and pestle. Subsequently, the mixtures were cold-pressed in a 13 mm stainless steel die under a pressure of 1500 Kg cm^{-2} . The pellets were fired in air at temperatures ranging from 800 up to $1070 \text{ }^\circ\text{C}$ in the following sequence.

Batch 1: Sample A was synthesized by sintering for a total of 374 hrs with almost 20 intermediate grinding/cold-pressing cycles, and by progressively increasing the temperature in subsequent cycles. To prevent loss of volatile IrO_2 , the temperature increment between any two successive firing cycles was never allowed to exceed $10 \text{ }^\circ\text{C}$; and for the same reason only 10 % of total synthesis time was used for sintering at temperatures higher than $1030 \text{ }^\circ\text{C}$.

Batch II: In batch II samples B1 and B2 were synthesized using the same protocol as used for A but in this case the highest sintering temperature employed was reduced to $1000 \text{ }^\circ\text{C}$.

Batch III:: Samples C1 and C2 were synthesized in batch III. In this case, due to

a higher level of off-stoichiometry, the precursor materials took longer to react fully. Altogether, these compositions were sintered for 574 hrs with over 43 intermediate grinding/cold-pressing cycles at temperatures less than 1070 °C.

Batch IV: Sample labeled D was synthesized separately in batch IV with 20 intermediate grinding/cold-pressing cycles for a total of 320 hrs at temperatures less than 1030 °C in air. At this point, the unreacted Eu_2O_3 and IrO_2 peaks were still present. Instead of sintering it further in air at higher temperatures, as done in the case of batch III samples, here an alternate route was employed wherein the sample was annealed at 1100 °C for 60 hrs under high vacuum. This was done to suppress the loss of Ir during sintering to induce negative stuffing as discussed later. The product obtained at the end of this treatment was reground and palletized, and subjected to final sintering at 1000 °C for 12 hrs.

The synthesis process in each case was called to an end only after the powder x-ray diffraction indicated the formation of the pyrochlore phase with minor or no traces of diffraction peaks due to the precursor materials. The pyrochlore phase forms faster at higher temperatures but at the cost of volatile IrO_2 loss from the sample that tends to sublime excessively at temperatures exceeding ≈ 1050 °C owing to its high vapor pressure. Normally, this loss can be quite significant if the sample is not sintered for a long enough duration at lower temperatures to react IrO_2 with Eu_2O_3 .

3.2.2 Effect of stuffing on the structure

During the synthesis process, the phase formation was continuously monitored using a Bruker D8 Advance powder x-ray diffractometer. However, the diffractogram collected towards the end of the synthesis could not capture the difference in the lattice parameters of different samples. Also due to the high neutron absorption cross-section of Eu and Ir, structural determination using neutron scattering data, which would have given more accurate information of the O(48f) positional parameter, was not possible in EIO. Hence minor variations in the unit cell parameters of our variously treated EIO samples were studied using the high-resolution synchrotron powder x-ray diffraction technique. High-resolution data was collected at the powder diffraction beamline (MCX) of the ELETTRA synchrotron radiation facility, Trieste, Italy. For this purpose, a Huber 4-axis x-ray diffractometer equipped with a fast scintillator detector was used [64]. The disadvantage of the x-ray is that it is not very sensitive to the position of lighter

oxygen ion. As a result, the parameter u , which decides the position of $\text{O}(48f)$ ion, remains vaguely defined. However, this problem is partly overcome using the high-resolution synchrotron radiation and a point detector that allows for the determination of the lattice parameter to very high precision. The sample was prepared in the form of a finely grounded powder that was placed in a glass capillary tube of inner diameter 0.1 mm. During the experiment, the capillary was rotated at an angular speed of 180 rpm. Diffractograms were collected in the range $10^\circ \leq 2\theta \leq 46^\circ$ with a step size of either 0.005° (A and D) or 0.01° (B1, B2, C1, and C2), and a counting time of 1s at each step. The incident beam energy was set at 19.7 keV ($\lambda = 0.6294\text{\AA}$).

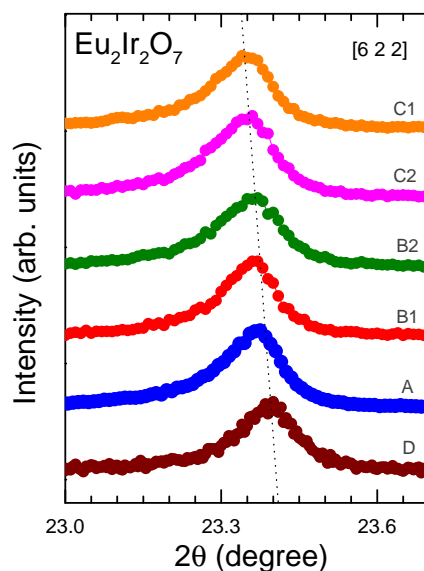


Figure 3.1: High-resolution synchrotron powder x-ray diffraction data of various $\text{Eu}_2\text{Ir}_2\text{O}_7$ samples A, B1, B2, C2, C1 and D (see Table 3.1 for details) in the 2θ range covering the Bragg peak (6 2 2), chosen as representative to demonstrate a slight rightward shift of the pattern from C1 to A0 (dashed line is a guide to eye).

We observed minor unreacted precursor phases in the high-resolution synchrotron x-ray diffraction pattern. The extra phase(s), if any, in all the samples are recorded in the Table 3.1. Direct correspondence of the impurity phases with the starting composition and the sintering method was observed. For example, in sample A, where the starting composition was stoichiometric, some loss of IrO_2 during the synthesis may have resulted in traces of unreacted Eu_2O_3 in the final product. In sample B1, on the other hand, 1 % excess IrO_2 in the starting mixture probably compensated for this loss,

resulting in phase pure diffraction pattern with ratio Eu/Ir closer to the ideal value. Sample D was sintered under vacuum after a preliminary reaction of the precursors in air at $T \leq 1030$ °C. Upon sintering under vacuum for about 60 hrs at 1100 °C, the final product had the desired pyrochlore phase as the main product but along with that minor diffraction peaks revealing the presence of IrO₂ and Ir metal were also detected. This is the only sample where Ir-metal peaks were present, which is perhaps the *main* drawback of sintering under vacuum. The advantage, however, is that by sintering under vacuum iridium losses can be minimized. It has been reported that at high temperatures, IrO₂ absorbs oxygen from its surrounding atmosphere to form a highly volatile oxide of iridium, namely, IrO₃ (Ref. [65]). Thus sintering under inert atmosphere or vacuum prevents Ir losses by suppressing the IrO₃ formation. This is apparently the reason why vacuum sintered samples or those obtained from KF flux tend to show slight Ir excess in their measured stoichiometry [61, 66]. Fig. 3.1 shows the Bragg peak (6 2 2) obtained using the synchrotron data. The shift in position (2θ) of the is apparent from Fig. 3.1 and depicts the variation in lattice parameters in different samples. The immediate conclusion from this graph is that the lattice parameter of sample C1 is the largest and that of D the smallest. To get the precise value of lattice parameters and other relevant structural parameters we performed structural refinement on the data sets of all the samples.

The structure refinement was done by the Rietveld method using the *FullProf* software [67]. In Fig. 3.2-3.4, a match between experimental and calculated pattern is shown for all the six samples. The observed diffraction patterns in each case can be well-fitted to the pyrochlore structure. A mixed-phase refinement was carried out for samples with precursor impurity peaks. The total amount of impurity phases in our samples varied between 1 and 2 %. The data were fitted using the Thompson-cox-Hastings pseudo-Voigt line profile function to account for the slight peak asymmetry. Absorption correction was also taken into account, which is important for the samples with heavier elements [64]. The refinement was considered to have converged when the shifts in the parameters being refined became less than 10% of their estimated standard deviation. The lattice constant (a), variable O-position parameter (u), isotropic thermal parameters (B), and occupancies of Eu and Ir were treated as variables. Several models were employed to refine the occupancies. However, the model where Eu and Ir occu-

pancies were refined by imposing the constraint that sum of occupancies at $16c$ and $16d$ sites to 2, yielded the best fit. Such a constraint is commonly used in structural studies on stuffed pyrochlores [62]. Since oxygen is not very sensitive to x-ray scattering, the occupancies of both the O-sites were fixed as fully occupied. The main results of the Rietveld refinement are collected in Table 3.1. Good quality of the refinement can be inferred from the fitted and the difference plots in Fig. 3.2. A moderately low values of the goodness-of-fit (χ^2), and of the R-factors (R_{wp} , R_p and R_e) reflects a satisfactory fit in each case.

As shown in Table 3.1, the lattice parameter of our samples, obtained for each sample from the Rietveld refinement of the x-ray diffraction data for $2\theta = 10^\circ$ to 46° , vary slightly, which is related to the Eu-stuffing discussed further. The average value of the lattice parameter of our samples is 10.302 \AA , which agrees fairly nicely with the same value reported by Chien and Sleight for their air synthesized sample [68]. This value is, however, bigger than $a = 10.274 \text{ \AA}$, for single crystal specimens grown using KF flux [66]. This difference can be attributed to negative stuffing (i.e., Ir occupying the Eu site), as argued by Ishikawa et al. [61]. In the present study, only sample D, that was treated partly under vacuum is probably negatively stuffed and accordingly, it has the smallest lattice parameter ($a = 10.297 \text{ \AA}$). The u -parameter in our samples lies in the interval between 0.33 and 0.34. The error bar on the value of u , listed in Table 3.1, is taken directly from the output file of our Rietveld refinement; the actual standard deviation is expected to be much larger due to insensitivity of x-ray to the oxygen position. We shall, therefore, content ourselves with the average value of u which is, ~ 0.334 , in a fairly good agreement with similar values previously reported [34]. The actual variations in the value of u of our samples due to stuffing are, at any rate, not expected to be very significant since the overall change in the lattice parameter itself is rather small. The average values of Ir–O($48f$) bond length and Ir–O($48f$)-Ir bond angle for our various EIO samples is around 2.03 \AA , and nearly $\sim 127^\circ$, respectively. Both these values are comparable to the values previously reported for other iridate pyrochlores [69].

We now turn to discuss the changes in lattice parameters which can be readily seen from Fig. 3.1 and is further quantified by the lattice parameters obtained from the structural refinement. We associate the observed variation in the lattice parameter in our various EIO samples with the level of Eu-stuffing at the Ir-site, which appears to be valid

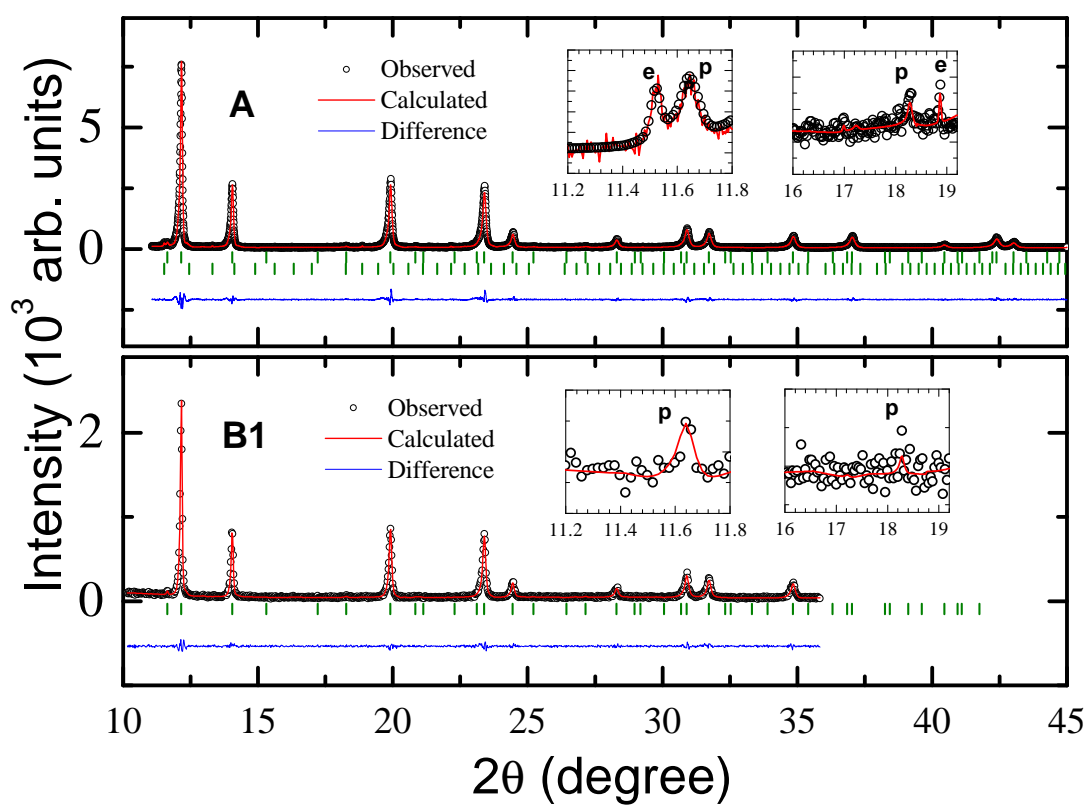


Figure 3.2: Rietveld refinement of composition A and B1. Inset compares precursor impurities with pyrochlore phase, e: Eu_2O_3 ; i: IrO_2 ; p: pyrochlore phase and * marks unidentified phase.

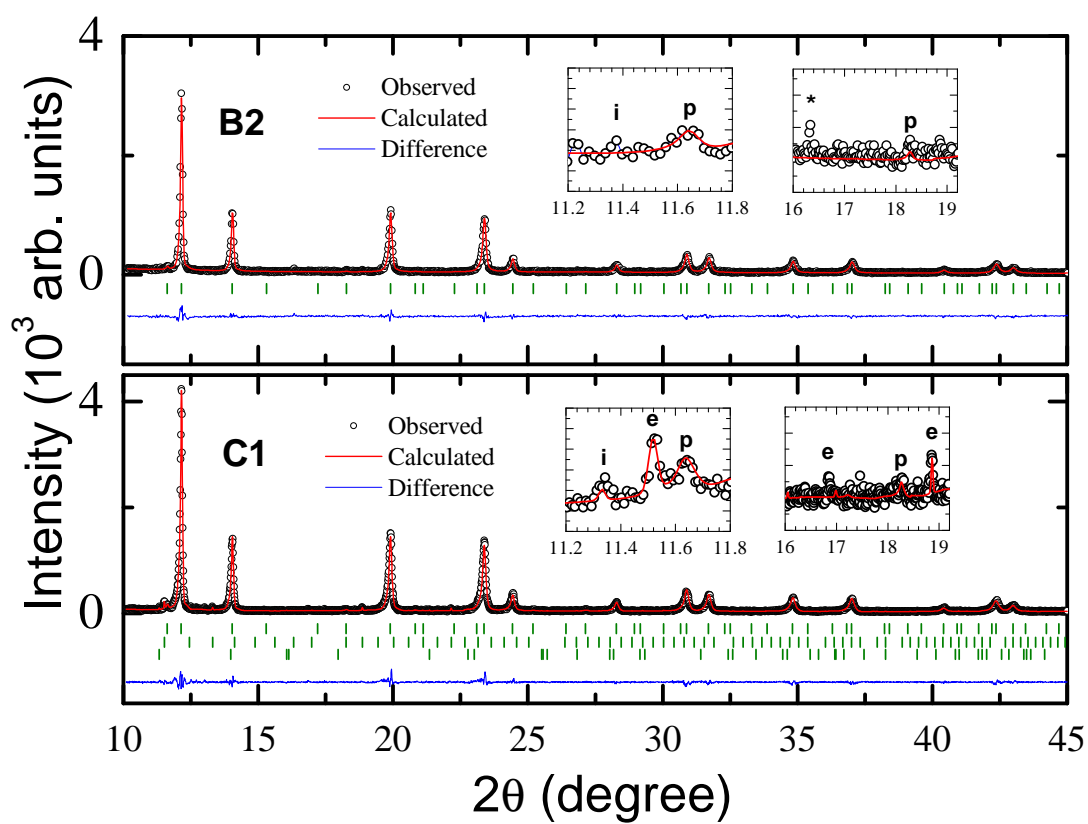


Figure 3.3: Rietveld refinement of composition B2 and C1. Inset compares precursor impurities with pyrochlore phase, e: Eu_2O_3 ; i: IrO_2 ; p: pyrochlore phase and * marks unidentified phase.

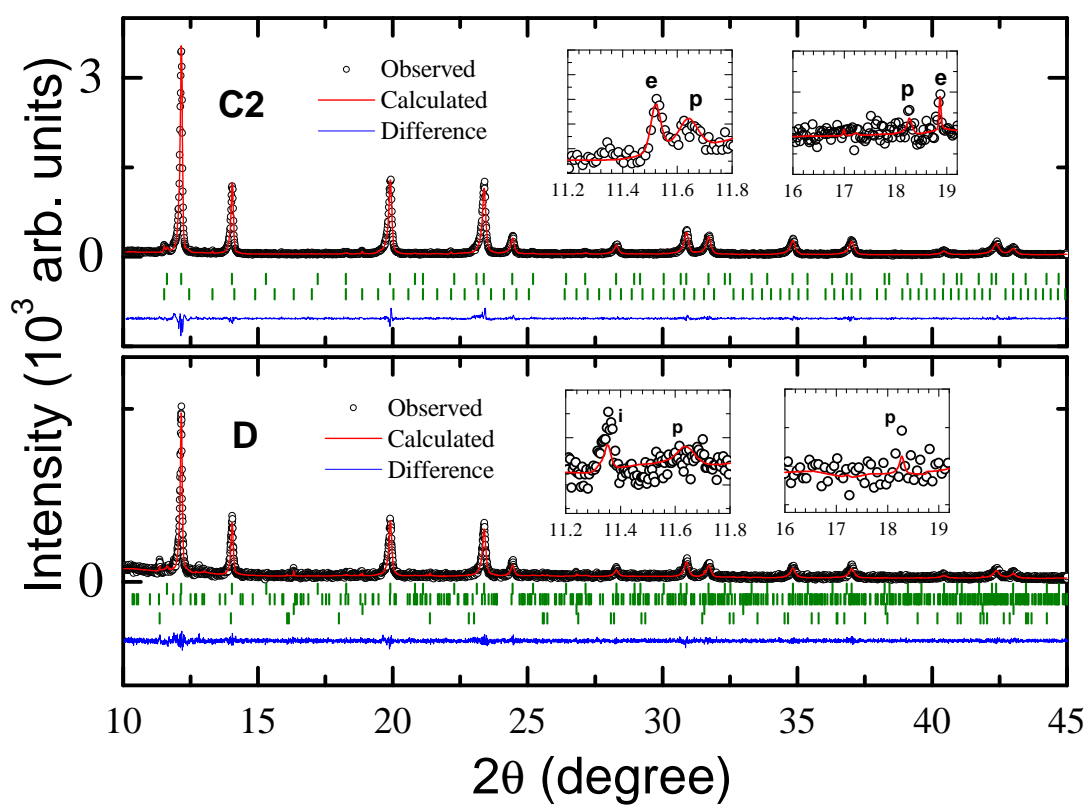


Figure 3.4: Rietveld refinement of composition C2 and D. Inset compares precursor impurities with pyrochlore phase, e: Eu_2O_3 ; i: IrO_2 ; p: pyrochlore phase and * marks unidentified phase.

Table 3.1: Structural parameters for various Eu₂Ir₂O₇ samples, labeled A, B1, B2, C1, C2 & D, obtained using Rietveld refinement of the high-resolution synchrotron powder x-ray diffraction data. Parameters characterizing the quality of fit are also included

Eu ₂ Ir ₂ O ₇ samples	A	B1	B2	C1	C2	D
$a(\text{\AA})$	10.2989	10.2994	10.3034	10.3058	10.3039	10.2965
$u_{O(48f)}$	0.3370(3)	0.3432(4)	0.3399(4)	0.3345(4)	0.3339(4)	0.3371(7)
Eu : Ir	1.001(0.013)	1.002(0.014)	1.011(0.010)	1.049(0.009)	1.002(0.010)	1.009(0.026)
<i>No. of phases refined</i>	2	1	1	3	2	3
<i>Secondary Phase(s)</i>	Eu ₂ O ₃	Nil	Unidentified phase	Eu ₂ O ₃ , IrO ₂	Eu ₂ O ₃	Eu ₂ O ₃ , Ir-metal
χ^2	2.06	1.14	1.23	1.76	1.51	1.16
R_p	8.47	9.03	8.87	9.96	10.02	12.54
R_{wp}	11.2	12	12.1	13.1	13.3	13.4
R_e	7.77	11.1	10.1	10.1	10.2	9.8

given that the Eu:Ir ratio in our samples scales with the lattice parameter as shown in Table 3.1. Our results are also analogous to reports of change in lattice parameter due to minor stuffing in the pyrochlore titanates [57, 70]. Since the ionic radius of Eu^{3+} (1.066 Å) is bigger than that of Ir^{4+} (0.62 Å) (Ref. 71), stuffing of Eu^{3+} at the Ir-site results in an expansion of the lattice. On the other hand, a small level of negative stuffing causes the lattice to contract slightly. In the refined structural data, the extent of Eu-stuffing is shown in Table 3.1. Samples C1 and C2 are Eu-stuffed beyond the measurement errors. On the other hand, in samples A, B1, B2, and D, the level of stuffing, if any, is less than $\pm 1\%$ which could not be any better resolved. However, from the trends in the variation of lattice parameter, and judging from the physical properties presented in the subsequent section, sample A and B1 appear to be closest to the ideal stoichiometry; and sample D appears to be slightly negatively stuffed. The most striking thing to note is that the initial or the starting composition (i.e., Eu/Ir in the starting mixture) is not as important in deciding the final stoichiometry as the details of the synthesis protocol. This statement is further testified by the physical properties that are nearly the same for samples prepared in a given batch, despite differences in their starting compositions.

3.3 Effect of stuffing on the physical properties

Now we turn to discuss the effect of stuffing on the physical properties of different EIO samples. We discussed earlier the existing discrepancy related to its physical properties of EIO in the literature. Ishikawa et al. [61] did study the physical properties of off-stoichiometric single crystalline samples of EIO. However, the lack of quantification of various structural parameters in their work failed to elucidate the relation between stuffing and the physical properties. Our work is a pioneering study in understanding the structure-property correlation in pyrochlore iridates.

3.3.1 Specific Heat

Specific heat of samples A, B1, B2, C1, and C2, over a narrow temperature range near the magnetic transition is plotted as C_p/T Vs. T^2 in Fig. 3.5(a - e). Being very close in compositions, C_p/T of these samples nearly overlap, therefore, specific heat over the full temperature range is shown only for sample B2 as a representative case in panel f. In panels a to e, two vertical dashed lines are shown: the one at a higher temperature

(near 15000 K^2) marks the onset of AFM ordering (T_N). The second line at a lower temperature that passes through the maximum in C_p/T is used to characterize the width of the magnetic transition. In each sample, C_p/T near the maximum is close to $1.1 \pm 0.1 \text{ J mol}^{-1} \text{ K}^{-2}$. This value is in good agreement with previous reports [4, 60]. The value of T_N ($122 \pm 1 \text{ K}$) is nearly the same for all the samples, except A for which it is slightly enhanced to $124 \pm 1 \text{ K}$. The transition width increases with stuffing due to an increase in the structural disorder. For example, in samples C1 and C2, the transition has been considerably smeared out.

The low-temperature specific heat for all the samples are shown in panel g between $T = 2 \text{ K}$ and 5.5 K . At low-temperatures, only the long-wavelength acoustic phonons are excited and their contribution to specific heat varies as T^3 for $T \ll$ the Debye temperature (θ_D). Fitting C_p at low-temperatures to an expression of the form $C_p = \gamma T + \beta T^3$ can, therefore, yield information concerning the electronic correlations. Since the AFM spin-wave contribution to C_p in spin systems with a gapless spin-wave excitation spectrum also varies as T^3 (see Ref. 72), it should not affect the determination of γ . In a spin system with a finite gap in the spin excitation spectrum, the specific heat at low temperatures is expected to decrease exponentially to zero, which is evidently not the case here, suggesting that the excitations are indeed gapless. C_p/T data for each sample is satisfactorily fitted using the equation: $C_p/T = \gamma + \beta T^2$. As expected, β does not vary much between these samples giving a value of nearly $0.77 \pm 0.01 \text{ mJ mol}^{-1} \text{ K}^{-4}$. γ , however, vary from $\sim 10 \text{ mJ mol}^{-1} \text{ K}^{-2}$ for B1 to $\sim 15 \text{ mJ mol}^{-1} \text{ K}^{-2}$ for C1 and C2. The average value is in good agreement with $13 \text{ mJ mol}^{-1} \text{ K}^{-2}$ reported previously [73]. Measurements on B1 were repeated at a later time to confirm that γ for this sample is indeed the lowest. Assuming that only Ir's 5d electrons contribute to the linear term in C_p , the value of γ per Ir-mol ($\sim 6.5 \text{ mJ Ir-mol}^{-1} \text{ K}^{-2}$) is almost an order of magnitude higher than γ of Cu [74] indicating moderately strong electronic correlations as predicted theoretically [51]. The important point to note is that γ has a substantial sample dependence -it tends to increase upon Eu-stuffing. This increase is not necessarily a consequence of further enhancement of the electronic correlations due to stuffing; we believe that it might simply be an effect of the carrier doping as considered by Ishikawa et al. who reported γ values as high as $26 \text{ mJ mol}^{-1} \text{ K}^{-2}$ for their negatively stuffed, most conducting EIO sample [61].

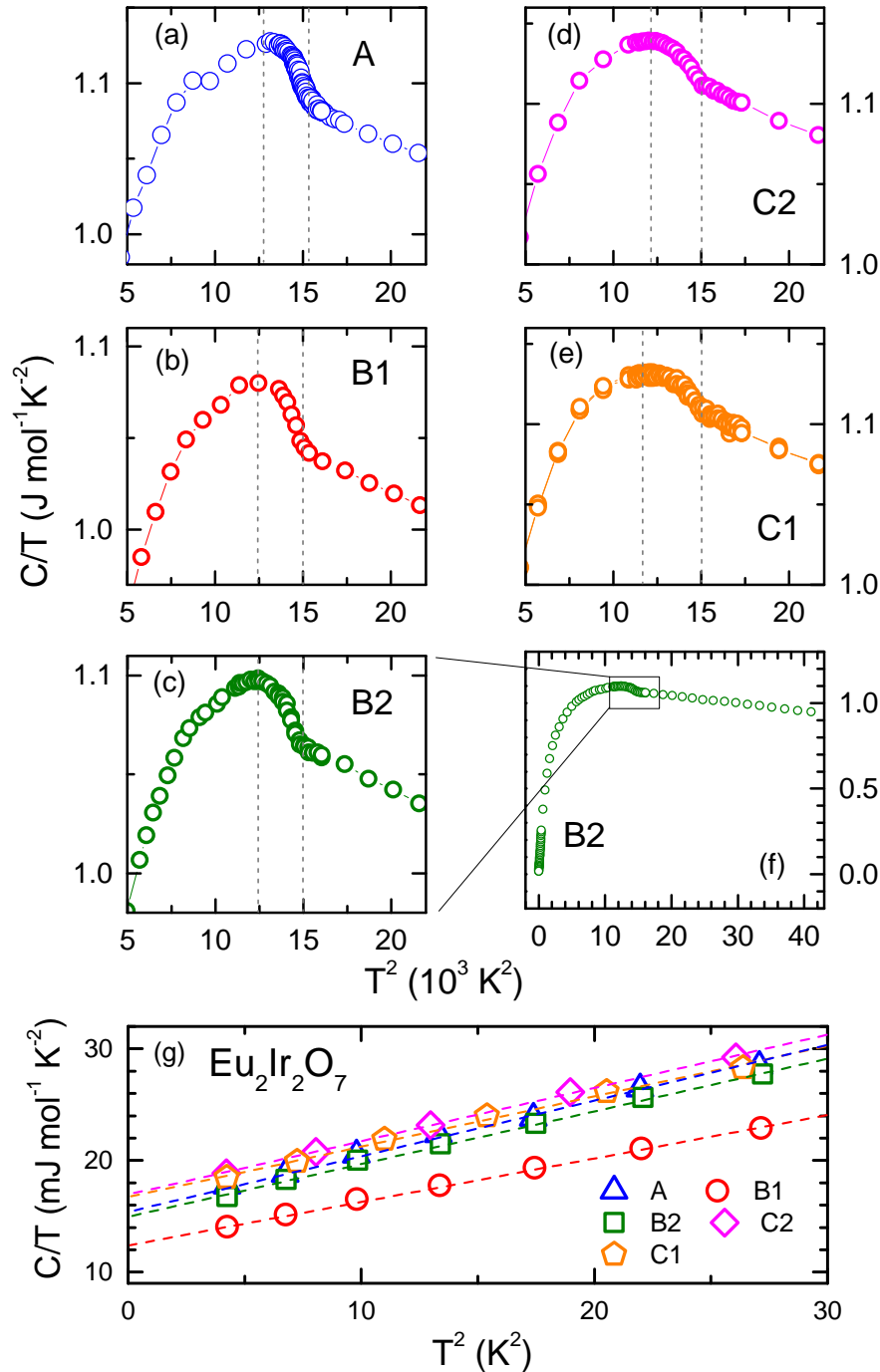


Figure 3.5: (a) to (e) Temperature (T) variation of specific heat (C_p) plotted as C_p/T Vs. T^2 for samples: A0, B1, B2, C2 & C1 shown over a narrow temperature range around the AFM/MI transition. The vertical dashed lines are guide to eye to show the onset of transition and transition width; (f) C_p/T Vs. T^2 shown over the whole measurement temperature range for sample B2. (g) C_p/T Vs. T^2 for all the samples at low-temperatures. The dashed lines are straight-line fits to the data (see text for details)

3.3.2 Magnetic susceptibility

Temperature variation of magnetic susceptibility ($\chi = M/H$) of samples A to D, measured under a static magnetic field of 1 kOe, is shown in Fig. 3.6(a-f). As a representative case, $\chi(T)$ of sample A is shown over the whole temperature range in panel g. When cooled below room temperature, $\chi(T)$ of all the samples increases almost linearly down to $T_N \approx 124$ K, where the Ir moments undergo long-range AFM ordering, which is shown to be of all-in/all-out (AIAO) type, wherein all *four* Ir-moments on a given tetrahedron either point-in towards the center (AI) of the tetrahedron or point-out directly away from the center (AO) [47, 75]. The data below T_N shows large ZFC-FC bifurcation. This bifurcation is believed to be due to a combination of several factors, including the presence of 180° domain walls, anti-site disorder, Ir-vacancies and/or the occurrence of Ir^{5+} (see Ref. 76 for details). The value of magnetic transition temperature in our samples is in good agreement with similar values previously reported [4, 61]. Contribution of Ir moments to $\chi(T)$ can be estimated by subtracting the van Vleck term (χ_{VV}) due to Eu^{3+} . The calculated χ_{VV} (taking the value of SO interaction λ from Ref. 77) is shown in Fig.3.6. Below room temperature χ_{VV} increases with almost the same slope as $\chi(T)$, and below a temperature close to T_N it tends to saturate. Thus, , above T_N , $\chi(T)$ owes its temperature dependence almost entirely to χ_{VV} . In other words, the contribution of Ir moments to $\chi(T)$ appears to be almost temperature-independent above T_N . This behavior suggests that the Ir *5d* electrons are itinerant and undergo a partial localization when cooled below T_N , which qualitatively agrees with the experimental fact that resistivity (next section) also increases sharply below this temperature.

We now examine how the transition temperature in χ is affected due to stuffing in our samples. In A, B1, and B2, the ordering is marked by the presence of a cusp in $\chi(T)$ below which the ZFC and FC bifurcate out. In C1, C2, and D no cusp is seen, the transition has rather smeared out, in agreement with the specific heat. For sample A, T_N (position of the cusp) appears to be slightly higher compared to the other samples.

In short, specific heat and susceptibility data reveal the following information: (i) no significant change in the value of T_N , (ii) broadening of the transition width upon stuffing (or increasing disorder), (iii) the shape of anomaly associated with AFM ordering in both C_p and χ are nearly identical for samples prepared in a given batch, and (iv) a closer look at the magnitude of χ at any fixed temperature (say, at $T = 80$ K) reveals

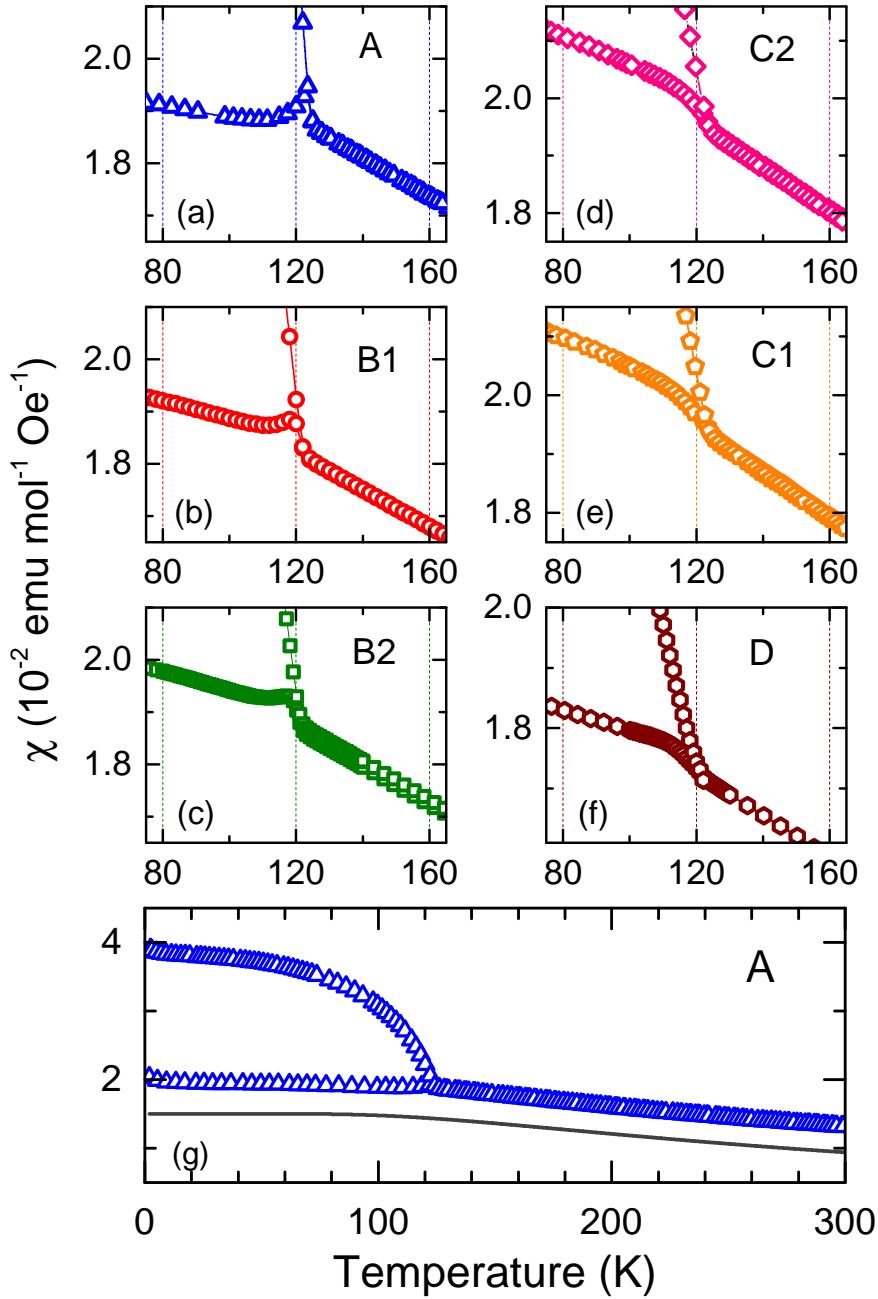


Figure 3.6: (a-f) Zero-Field-Cooled (ZFC) and Field-cooled (FC) susceptibility of all the $\text{Eu}_2\text{Ir}_2\text{O}_7$ samples is shown as a function of temperature in a small temperature range around the magnetic ordering temperature; (g) The ZFC and FC susceptibilities over the whole temperature range are shown for sample A as representative. χ_{VV} is Van Vleck susceptibility of Eu^{3+} ion (see text for details).

that the value of χ scales approximately with the ratio Eu : Ir in our samples. For example, χ of sample D: $\sim 0.00184 \text{ emu mol}^{-1}\text{Oe}^{-1} < \text{A \& B1: } \sim 0.0192 \text{ emu mol}^{-1}\text{Oe}^{-1} < \text{B2: } 0.0198 \text{ emu mol}^{-1}\text{Oe}^{-1} < \text{C1 \& C2: } \sim 0.0212 \text{ emu mol}^{-1}\text{Oe}^{-1}$. This scaling is expected since the concentration of Eu^{3+} determines χ_{VV} which has a significant contribution to the total measured χ as depicted in Fig. 3.6 (lowest panel).

3.3.3 Electric transport

In Fig. 3.7a, normalized resistivity ($\rho_N = \rho(T)/\rho(300\text{K})$) is shown as a function of temperature for all the EIO samples, where $\rho(300\text{K})$ is the value of resistivity at $T = 300 \text{ K}$. ρ_N in each case exhibits a sharp increase upon cooling below $T_{MI} \approx 125 \text{ K}$. The MI transition temperature is estimated from the derivative plots by linearly extrapolating $d\rho/dT$ data above and below the MI transition. The temperature where these lines intersect is taken as T_{MI} . Using this criteria, T_{MI} for samples A, B1, and B2 is nearly 127 K, for samples C1 and C2 it is close to 122 K, and for sample D it is around 120 K. The average value of T_{MI} is 124 K, which shows a good agreement with the previous reports [45, 63], and with the values of T_N obtained from $C_p(T)$ and $\chi(T)$ data presented in the preceding section. However, the temperature T_{MI} suppresses in the stuffed samples while T_N remains nearly constant, which suggests that in a sample with even higher Eu-Ir off-stoichiometry, these temperatures may further separate out, as in the case of $\text{Nd}_2\text{Ir}_2\text{O}_7$, where such a separation has been previously reported [78].

We now focus on the differences in $\rho(T)$ behavior of various EIO samples arising due to off-stoichiometry. An important difference concerns the sign of $\rho' = d\rho/dT$ above T_{MI} . For samples A, B1, and B2, $d\rho/dT$ changes sign from negative to positive upon cooling below a certain temperature T^* that lies above T_{MI} as shown in the inset of Fig. 3.7b. T^* is $\sim 170 \pm 20 \text{ K}$ for A and close to $230 \pm 10 \text{ K}$ for B1 and B2; and for sample D the slope is positive but it is about to become zero as the temperature approaches 300 K, indicating that even for this sample a sign change is expected at higher temperatures above 300 K. On the other hand, for samples C1 and C2, the sign of $d\rho/dT$ remains negative at all temperatures above T_{MI} .

Briefly, two different $d\rho/dT$ behaviors above T_{MI} are observed: samples with larger lattice parameter and higher Eu-stuffing (C1 and C2) exhibit a negative $d\rho/dT$ for all temperatures above T_{MI} ; samples with smaller lattice parameter and Eu/Ir ratio close to 1 (A, B1, B2, and D) exhibit a change of sign of $d\rho/dT$ above T_{MI} . This behavior is

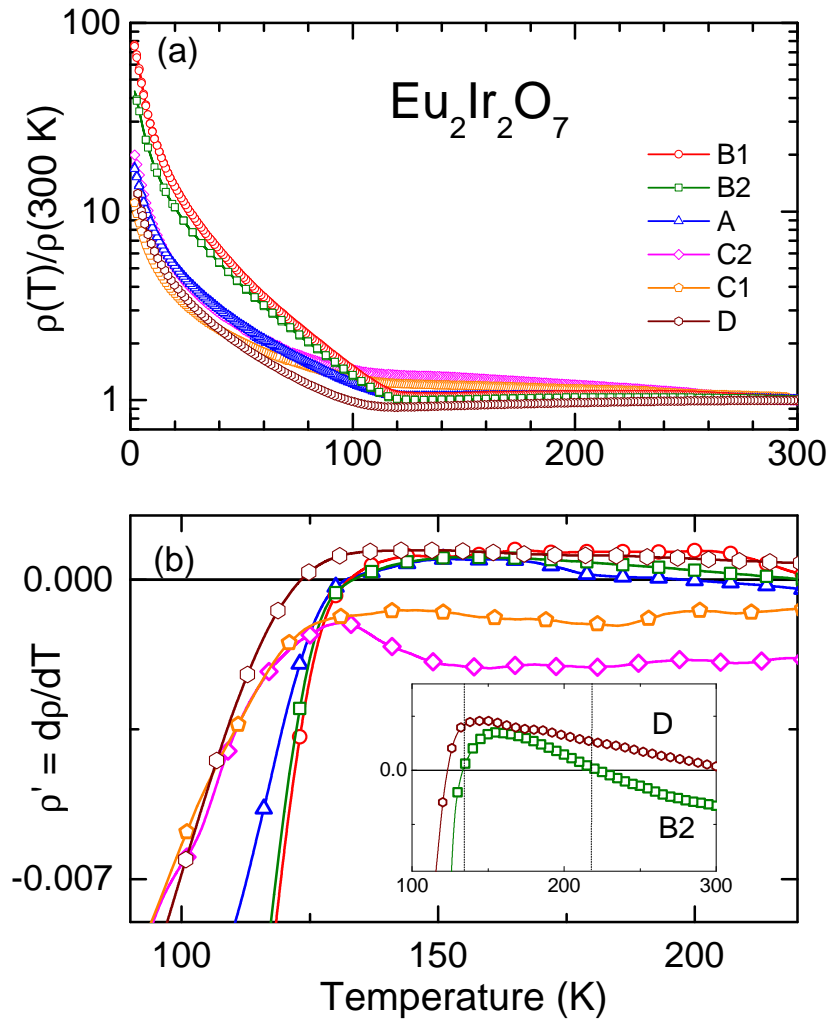


Figure 3.7: (a) $\rho(T)/\rho(300\text{K})$ plotted as a function of temperature (T) for various $\text{Eu}_2\text{Ir}_2\text{O}_7$ samples (A, B1, B2, C2, C1 & D); (b) first derivative $\rho' = d\rho/dT$ of the resistivity plots as a function of temperature around the metal-insulator transition. In the inset ρ' is shown for samples B2 and D over a wider temperature range to demonstrate the change of sign of $d\rho/dT$.

analogous to that under external pressure investigated by Tafti et al. [63]. They show that as the applied pressure increases the sign of $d\rho/dT$ changes from negative to positive, with an intermediate range of pressures where $d\rho/dT$ changes sign at some temperature $T^* > T_{MI}$. This analogy is not surprising since the lattice parameter itself varies with pressure. Thus, in both the studies the lattice parameter variation drives the change of sign of $d\rho/dT$.

While the sign of $d\rho/dT$ in our samples and under applied pressure is in complete agreement, the magnitude of ρ differs in the two cases. In the pressure study, not only the sign of $d\rho/dT$ changed continuously from negative to positive with increasing pressure, the magnitude of ρ also decreased simultaneously. In the present study, on the other hand, ρ of sample C1 (decompressed analog of pressure study) having a negative $d\rho/dT$ is 100 m Ω cm at 2 K which is smaller than the corresponding value for sample A1 (~ 7000 m Ω cm) which has a smaller lattice parameter compared to C1. Sample D, on the other hand, exhibits both a smaller lattice parameter and a smaller resistivity, comparable to that of C1. This, rather uncorrelated variation of ρ in our samples may arise from the fact that the magnitude of resistivity in a sintered pellet, unlike a single crystal specimen under pressure, depends on several factors including, the presence or absence of specific impurity phases that tend to accumulate along the grain boundaries and affect the electrical conduction, carrier doping due to stuffing, the microstructure of the pellets and the oxygen vacancies, if any.

Due to similar conditions used in the preparation of final sintered pellets employed for physical properties measurements in each case, we do not expect either the microstructure or the oxygen vacancies to vary very significantly in our samples. On the other hand, the level of Eu-stuffing, which differs in our samples, and the presence of metallic impurities may have affected the magnitude of ρ . To understand how stuffing leads to carrier doping we need to consider the charge difference between Eu^{3+} and Ir^{4+} . If a sample is synthesized under an inert atmosphere, i.e., if in the surrounding medium there is no oxygen for the sample to absorb then the final product will form with oxygen vacancies. It will, therefore, have a chemical formula of the form: $\text{Eu}_{2+s}\text{Ir}_{2-s}\text{O}_{7-s/2}$, obtained using the charge-neutrality condition. However, when synthesized in air or under an oxygen flow, due to oxygen absorption during the synthesis, the sample is expected to form with fewer oxygen vacancies than before, and its chemical formula will

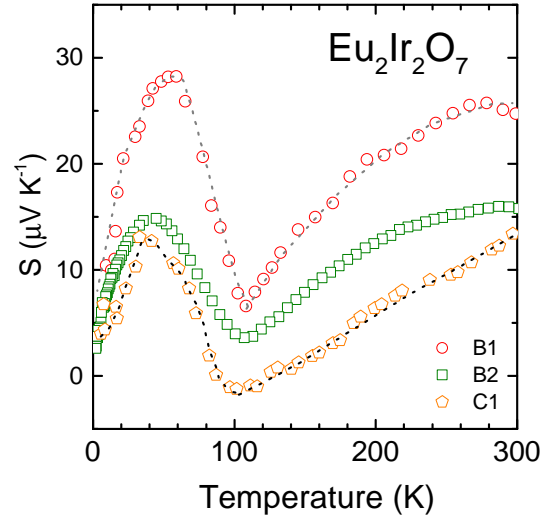


Figure 3.8: Thermoelectric power (S) plotted as a function of temperature for various $\text{Eu}_2\text{Ir}_2\text{O}_7$ samples: B1, B2 & C1. The dotted lines are a guide to the eye.

be: $\text{Eu}_{2+s}\text{Ir}_{2-s}\text{O}_{7+\delta-s/2}$, where δ is a non-negative quantity that corresponds to the hole doping in the sample. In the stuffed samples, therefore, the magnitude of ρ can decrease considerably due to these additional charge carriers.

With this insight, we now compare the resistivity of sample B1 to that of C1. We notice a significant decrease in ρ , approximately $7000 \text{ m}\Omega \text{ cm}$ (B1) to $\sim 100 \text{ m}\Omega \text{ cm}$ (C1), which we believe is mainly because of the carrier doping in C1 as a consequence of stuffing. On the other hand, a comparison of samples prepared in the same batch revealed a much smaller difference (for example, $\sim 100 \text{ m}\Omega \text{ cm}$ at 2 K for C1 and $\sim 750 \text{ m}\Omega \text{ cm}$ at the same temperature for C2), which is probably due to the presence of conducting IrO_2 as a parasitic phase in sample C1, and also a slightly higher Eu stuffing level for this sample. The resistivity of sample D is considerably reduced compared to that of B1 or B2, even though they have only minor differences in their lattice parameter. This could be due to the presence of Ir-metal as a parasitic phase in sample D, and probably the electron doping due to slight negative stuffing is also contributing to it.

3.3.4 Thermopower

To quantify the charge doping in these samples, which is indicated from the change in the magnitude of the resistivity, we tried Hall measurements. However, attempts to

measure the carrier concentration directly using the Hall effect by applying fields up to ± 3 Tesla on the sintered pellets turned out to be unsuccessful. In our Hall measurements, which we did in the five-probe geometry using both positive and negative fields to eliminate the longitudinal voltage drop, we found irreproducible hysteretic behavior.

To mitigate this difficulty to some extent, we carried out thermopower measurements on some of our samples. Thermopower, denoted by S , is a complex physical quantity due to its dependence on various factors [79], including the electronic diffusion under temperature gradient which produces a thermopower proportional to T , and the electron-phonon interaction resulting in the phonon drag contribution. Thermopower of our samples A, B2, and C1 are shown as a function of temperature in Fig.3.8. Upon cooling, S decreases monotonically down to $T \approx 120$ K, which is the expected behavior for metals at high temperatures. Below 120 K, however, it increases rather sharply. This change of behavior near 120 K is most likely related to the metal-insulator transition. Upon further lowering the temperature, S exhibits a peak around $T_{peak} = 50$ K. This peak is likely a manifestation of phonon-drag which increases S as T^3 at low-temperatures and decays as $1/T$ at higher temperatures, resulting in a broad peak in the intermediate temperature range [79]. T_{peak} appears to have a slight sample dependence. The sign of S remains positive over the entire temperature range, which indicates that the majority of carriers in EIO are holes. The overall $S(T)$ behavior of our samples is in a fairly good agreement with the previous reports [4, 45]. A comparison of the thermopower of several EIO samples, including those from the present study, show that the qualitative features in the temperature variation of thermopower are more or less sample independent, but the magnitude of thermopower scales directly with sample's resistivity. For example, B1 which is the most resistive sample in our study exhibits the highest thermopower, and C1 which has the smallest resistivity also has the smallest thermopower. A review of the previous literature revealed a similar trend in the thermopower of EIO samples investigated by various groups. Bouchard et al. [42], for example, reported a thermopower of approximately $10 \mu\text{V/K}$ at 300 K for their air-synthesized sample ($\rho(300 \text{ K}) \approx 20 \text{ m}\Omega \text{ cm}$). The corresponding value for a vacuum synthesized sample, reported by Matsuhira et al. [4] is about $40 \mu\text{V/K}$ ($\rho(300 \text{ K}) \approx 100 \text{ m}\Omega \text{ cm}$) [4]. As a passing remark, we note the presence of a small curvature in the thermopowers of samples B1 and B2 in the temperature range of $120 \text{ K} < T < 300 \text{ K}$; this may be related to the sign change of

$d\rho/dT$ for these samples. In C1 no such curvature is seen.

To summarize, thermopower, which varies as the inverse of the carrier concentration in a simple one-band model [79], also supports the conclusion that stuffing leads to hole doping which simultaneously decreases the thermopower and the resistivity, and increases the coefficient of the linear term in the specific heat.

3.4 Discussion on the sign of $d\rho/dT$

The structural refinements carried out on very high-resolution synchrotron x-ray diffraction data collected for all the EIO samples synthesized in this work led to a precise determination of the lattice parameter, and an estimate of the Eu : Ir stoichiometry of the main pyrochlore phase (Table 3.1). As depicted in Fig. 3.1, where the position of 622 Bragg peak is shown as a reference, the lattice parameter of our samples varies in the following order: $a_{C1} > a_{C2} > a_{B2} > a_{B1} > a_A > a_D$. This variation can be understood on the basis of Eu^{3+} -stuffing at the Ir-site or vice-versa as has been extensively cited for stuffed titanate pyrochlores [58, 70].

All the EIO samples investigated here showed a weakly temperature-dependent resistivity in the metallic state above T_{MI} , which is the hallmark of EIO amongst the entire iridate pyrochlore series. However, the sign of $d\rho/dT$ in the metallic state showed a systematic sample dependence. It changed from negative for samples C1 & C2 having a relatively larger lattice parameter to positive for sample D having the smallest lattice parameter. For samples A, B1 & B2, $d\rho/dT$ changed its sign at an intermediate temperature T^* , such that, between T_{MI} and T^* , $d\rho/dT$ remains positive as it should be for a metal; and for $T > T^*$, it becomes negative. Even for sample D, $d\rho/dT$ approaches zero as T goes to 300 K, indicating that even for this sample a change of sign is expected at higher temperatures. It should be noted that while the sign of $d\rho/dT$ is dependent on the lattice parameter, the temperature T_{MI} does not, which remains nearly unchanged for our samples. The maximum overall change in T_{MI} across our samples remained less than 5 %.

Interestingly, the behavior of $d\rho/dT$ with lattice parameters or equivalently with the chemical pressure induced by stuffing mimics exactly the behavior under externally applied pressure investigated by Tafti et al. [63]. In the pressure study, Tafti et al. used an EIO sample having a negative $d\rho/dT$ in the ‘metallic’ regime analogous to samples

C1 or C2 in our study. They showed that $d\rho/dT$ remained negative under pressures up to about 4.5 GPa, and the sign changed to positive when the pressure exceeded 7 GPa or so. In the intermediate range of pressures, $d\rho/dT$ changed its sign at a temperature $T^* > T_{MI}$ in an exact analogy with our results. In the pressure experiments also, while $d\rho/dT$ changed continuously with increasing pressure, T_{MI} shifted only marginally. Tafti et al. called the ‘metallic’ regime above T_{MI} with negative $d\rho/dT$ as an “incoherent” metal as opposed to the conventional metallic behavior where the sign of $d\rho/dT$ is expected to remain positive.

Our preliminary x-ray diffraction study under high-pressure (Appendix B) at 300 K on sample A at ELETTRA shows that indeed a lattice contraction comparable to the difference between the lattice parameters of samples C1 and D can easily be produced under moderate pressures ($\sim 0.01 \text{ \AA}$, from 4 to 7 GPa—the range over which $d\rho/dT$ changes its sign from negative to positive in the pressure study [63]). From this observation, it can be concluded that the change in lattice parameter due to a minor, and often inadvertent, stuffing resulting from a loss of IrO_2 during sintering, can indeed be comparable to that under moderate pressure.

Since increasing the level of Eu-stuffing enhances the structural disorder, one may argue that the incoherent behavior is likely a consequence of the increased disorder which results in a weak-localization of the charge carriers. However, we note that in the pyrochlore structure, the increase in applied pressure has a tendency to enhance the antisite disorder (see for example, Ref. 80 and references therein). Thus, if disorder-induced weak-localization is indeed leading to the incoherent behavior then we expect $d\rho/dT$ to remain negative under pressure, which is contrary to the experimental observation where the increase in pressure enhances the metallic behavior. It should also be pointed out that in the KF-flux grown Ir-rich EIO single crystals [61], $d\rho/dT$ remains negative up to the highest level of Ir stuffing. Since these samples are structurally disordered due to Ir stuffing, their metal-like resistivity suggests that disorder cannot be the primary reason for the incoherent-metal behavior. In a recent theoretical study, it has been argued that the effect of small disorder in 3D semimetals with intermediate to strong interaction can in general be disregarded due to effective screening of the disorder that raises the critical disorder strength for a disorder-driven diffusive transition to a higher threshold [81]. Thus, we have very little or no reason to believe that the sign of

$d\rho/dT$ is controlled by the level of disorder in the sample.

We now discuss the structural changes taking place upon changing the lattice parameter to understand the anomalous sign of $d\rho/dT$ in the metallic regime. It has been highlighted in several previous studies (see for example, Refs. 82 & 83) that the Ir–O–Ir bond angle is an important parameter that controls the t_{2g} bandwidth, and the strength of the magnetic superexchange interaction between the Ir-moments. Previous pressure studies on some other pyrochlores suggest that u changes only marginally in the presence of moderate pressures [62, 84, 85]. Since the Ir–O–Ir bond angle depends on u , it is also expected to remain almost invariant under pressure. Furthermore, since T_N/T_{MI} in our samples has not changed significantly, we believe that the changes in the Ir–O–Ir bond angle due to stuffing is not expected to be very significant. This suggests that either $d\rho/dT$ in EIO is extremely sensitive to the Ir–O–Ir bond angle, or, perhaps, the direct Ir–Ir hopping, which is expected to be significant due to the extended nature of Iridium’s 5d orbitals, also plays a role here. Unlike the Ir–O–Ir bond angle, the dependence of direct hopping on the lattice parameter is straightforward: as the lattice contracts the Ir–Ir distance decreases, increasing the direct overlap between the 5d orbitals.

The role of direct hopping in the presence of indirect Ir–O–Ir hopping was considered in the theoretical study by Witczak-Krempa et al. [51]. In Fig. 2 of their paper, it is shown that for a fixed Hubbard U , and for a given value of the transfer integral $t_{Ir-O-Ir}$ corresponding to the Ir–O–Ir hopping, various phases, including metal, topological semimetal (TSM), topological insulator (TI), and topologically trivial insulators can be stabilized by tuning the Ir–Ir distance in the proximity of the metal-TSM-insulator phase boundary. In particular, the TSM phase is shown to appear only over a very narrow range of values of t_{Ir-Ir} , i.e., the transfer integral corresponding to the Ir-Ir hopping. Thus, with a small variation of Ir–Ir distance either a metallic or an insulating phase can be stabilized. On the other hand, away from the metal-TSM-insulator phase boundary, direct hopping becomes less relevant, which is probably the reason why in $Nd_2Ir_2O_7$ (NIO), which is located somewhat away from this boundary, the sign of $d\rho/dT$ remains unchanged (positive) under pressure [86].

EIO, on the other hand, is located in a close proximity of the metal-TSM-insulator phase boundary and, therefore, even minor changes in the lattice parameter, either due

to applied pressure or due to stuffing, is expected to have a significant effect on the electrical transport behavior, probably not as much due to the Ir–O–Ir bond angle as to the Ir–Ir bond distance. If this is indeed true then for the physical realization of WSM phase in EIO, which purportedly harbors the Weyl fermions, it is critical to optimize the Eu : Ir ratio to get the optimal Ir–Ir distance and carrier density. This might be the reason why till date there are only few, only one to the best of our knowledge, experimental evidence of the Weyl semimetallic ground state in EIO.

3.5 Summary

Briefly, the work on stuffing aimed at understanding the sample dependence of electrical behavior of the pyrochlore EIO which, along with the neighboring members of this family, has been predicted to show interesting topological phases. In the past literature, two types of resistivity behavior were reported for EIO, one where $d\rho/dT$ remains negative above T_{MI} (type I), and second where it remains positive (type II). Alongside, a pressure study on an EIO sample of type I ($d\rho/dT < 0$) revealed: (i) $d\rho/dT < 0$ for pressures up to 4.6 GPa, (ii) $d\rho/dT$ changing sign at a temperature T^* ($> T_{MI}$) for pressures in the range 4.6 to 7 GPa, and (iii) $d\rho/dT > 0$ for pressures exceeding 7 GPa [63].

In this study, we prepared six different EIO samples with slightly varying compositions to reproduce all the three $d\rho/dT$ behaviors ((i), (ii) and (iii)) listed above at ambient pressure. In order to establish a correspondence between the $d\rho/dT$ behaviors in our various EIO samples with that under pressure in ref. 63, we did high-resolution synchrotron powder x-ray diffraction at the MCX beamline in ELETTRA on all the samples. These experiments successfully revealed minor variations in the unit cell volume of our samples which established that it is the chemical pressure that imitates the external pressure. The Rietveld refinement of the x-ray data further revealed that the observed variation in the unit cell volume is due to Eu-stuffing at the Ir-site. This not only allowed shedding light on the peculiar $d\rho/dT$ behavior under pressure but it also resolved the enigmatic sample dependence of $d\rho/dT$ in the previous reports. Eu-stuffing in EIO results from loss of volatile IrO_2 from the reaction mixture during high-temperature sintering. The experimental results obtained on the various EIO samples suggest that the properties of EIO are not as sensitive to a small variation in the starting composition as they are to the synthesis protocol. This sensitivity is a consequence of the loss of volatile IrO_2 during

the sintering as the temperature exceeds 1050 °C or so. Our results indicate an extreme sensitivity of EIO to pressure: applied, or chemical due to slight Eu-stuffing. We believe this extreme sensitivity is due to the close proximity of EIO to the metal-insulator phase boundary, which makes the Ir-Ir hopping an important parameter in deciding the ground state of EIO. In the future, it will be useful to investigate stuffing in other pyrochlore iridates (e.g., $\text{Sm}_2\text{Ir}_2\text{O}_7$) that also lie close to the metal-insulator phase boundary.

Chapter 4

Effect of Bi substitution on $\text{Eu}_2\text{Ir}_2\text{O}_7$

In the previous chapter, we discussed the effect of antisite defect on the physical properties of pyrochlore iridate $\text{Eu}_2\text{Ir}_2\text{O}_7$ (EIO). In this chapter, we will present the result of the isovalent substitution of Bi^{3+} at the Eu^{3+} in EIO. In the following sections, we present the motivation for the choice of Bi substitution in EIO and further report the effect of Bi substitutions on the structure and physical properties.

4.1 Ground state of $\text{Eu}_2\text{Ir}_2\text{O}_7$ and $\text{Bi}_2\text{Ir}_2\text{O}_7$

The ground state of $A_2\text{Ir}_2\text{O}_7$ is sensitive to the choice of A-cation, varying from insulating for $A = \text{Gd-Lu}$ and Y to metallic for $A = \text{Pr}$ and Bi [4, 44]. The intermediate members $A = \text{Nd, Sm}$ and Eu , on the other hand, show a distinct metal-to-insulator (MI) transition concurrent with the onset of *all-in/all-out* (AIAO) magnetic ordering [47, 48, 75, 87]. Wan et al. used LSDA + U + λ (where LSDA stands for local-spin-density-approximation) to predict the existence of several novel correlated topological phases for these pyrochlores [26]. Subsequently, several other theoretical studies substantiated these predictions [2, 52, 88–91]. It is now believed that the parent phase from which these phases emerge is characterized by the presence of a quadratic band touching (QBT) point at the center Γ of the Brillouin zone [52]. The Weyl semimetallic (WSM) phase, which was predicted by Wan et al., appears when the Kramer’s degeneracy associated with QBT point is lifted due to the breaking of the time-reversal symmetry (TRS) in the AIAO state. This results in pairs of non-degenerate, linearly dispersing modes associated with the Weyl nodes of opposite chirality located on the Fermi energy

(ϵ_F). Though the presence of QBT has been confirmed experimentally for $\text{Pr}_2\text{Ir}_2\text{O}_7$ (PIO) [92], a clear signature of the WSM phase, which appears only over a narrow window in the pyrochlore iridates, has remained elusive till date.

A promising avenue to search for the WSM phase and other correlated topological phases in these pyrochlores is by tuning U or λ close to the MI boundary. In this regard, EIO is a promising candidate as it features not only a non-magnetic A -site, but it is located at the MI phase boundary. In EIO, the pressure experiments by Tafti et al. have revealed close proximity to the WSM phase [63]. Similarly, the optical conductivity of EIO has been shown to exhibit a close correspondence with the theoretically calculated response in the WSM phase [93]. Here, we tune the ground state of EIO by doping with Bi at the Eu site.

EIO, as mentioned earlier, shows a metal to insulator transition concomitant with magnetic ordering at 120 K and has a unit cell length of 10.29 \AA . $\text{Bi}_2\text{Ir}_2\text{O}_7$ (BIO) is a metallic member of the pyrochlore iridate series and has a unit cell length of 10.32 \AA , much larger than EIO. It does not show any magnetic ordering down to 2 K but is reported to undergo two magnetic transitions at 1.8 K and 230 mK respectively [50]. It has an unusual $T^{3/2}$ dependence of resistivity against temperature from 300 K to 2 K. Thin films of this composition are also reported to show linear magnetoresistance. Bi^{3+} (1.17 \AA) has bigger ionic radius than both Pr^{3+} (1.12 \AA) and Nd^{3+} (1.09 \AA). However, the lattice parameters of BIO (10.32 \AA) are smaller than both PIO and $\text{Nd}_2\text{Ir}_2\text{O}_7$ (NIO) which indicates that Bi $6s/6p$ hybridizes with Ir $5d$ orbitals to create shorter bonds. Hence Bi substitution is expected to have a unique effect in addition to tuning the A -site radius.

In past, divalent cation doping in EIO has been tried; however, the issue with divalent doping is that it creates a charge disproportionation ($\text{Ir}^{4+} - \text{Ir}^{5+}$) over the Ir sublattice, which is detrimental to the AIAO state [94, 95]. On the other hand, Bi doping not only preserves the non-magnetic nature of the A -site, but it also dopes charge carriers due to hybridization between Bi ($6s/6p$) and Ir ($5d$) states [96].

4.2 Synthesis and structural characterization

All the samples in the series $\text{Eu}_{2-2x}\text{Bi}_{2x}\text{Ir}_2\text{O}_7$ ($x = 0, 0.02, 0.025, 0.035, 0.05, 0.1, 0.25, 0.50, 0.75, \text{ and } 1$) were synthesized in air via solid-state route using the precur-

sors Eu_2O_3 (Sigma Aldrich, 99.9 %), Bi_2O_3 (Sigma Aldrich, 99.9 %) and IrO_2 (Sigma Aldrich, 99.9 %). The precursors were thoroughly ground together in an agate mortar and pestle. Subsequently, the mixtures were cold-pressed in a 13 mm stainless steel die under a pressure of 1500 Kg cm^{-2} . The pellets were fired in air at an initial temperature of 800°C . Following this the sintering temperatures were increased gradually in steps of $10 - 20^\circ\text{C}$ up to 1030°C . Since Iridium exhibits high vapor pressure above 1000°C , it is necessary to increase the sintering temperature in small steps. Grinding and pelletization were done before each sintering. The synthesis process in each case was called to an end only after the powder X-ray diffraction indicated the formation of the pyrochlore phase with minor or no traces of diffraction peaks due to the precursor materials. The phase formation during the sintering process was monitored using a Bruker D8 Advance powder X-ray diffractometer. It was observed compositions with high Bi concentration required lower sintering temperatures to obtain single-phase. For example, $\text{Bi}_2\text{Ir}_2\text{O}_7$ could be obtained as single-phase around 900°C with a total sintering duration of around 140 hrs, whereas compositions in the range $x \leq 0.25$ required repeated sintering at higher temperatures. The undoped composition required total sintering of 374 hrs; in order to curb the losses of IrO_2 at higher temperatures, only 10% of the total synthesis time was used for sintering at temperatures higher than 1000°C . Compositions with Bi substitution up to $x \leq 0.25$ required similar or marginally less number of sintering cycles to reach single-phase. The ease in the formation of the pyrochlore phase with increasing Bi substitution could be attributed to high diffusivity of Bi_2O_3 , which has a melting temperature of 817°C . For comparison, we also prepared and studied homologous $(\text{Eu}_{1-x}\text{Bi}_x)_2\text{Sn}_2\text{O}_7$ ($0 \leq x \leq 0.1$) samples in manner similar to the Yb-stannates mentioned in previous chapter.

The phase formation of all the samples was monitored through the synthesis process using Bruker D8 diffractometer. After all the compounds were formed, high-resolution x-ray diffraction experiments were carried out on all the samples at MCX Elettra, Italy. The powder x-ray diffraction of the entire $(\text{Eu}_{1-x}\text{Bi}_x)_2\text{Ir}_2\text{O}_7$ series could be indexed based on the pyrochlore structure. In particular, we observe no change of symmetry or phase separation for any of the intermediate members in our high-resolution synchrotron data. With Bi substitution, we expect the lattice parameters to increase gradually as the lattice parameters of BIO are significantly greater than that of EIO. However,

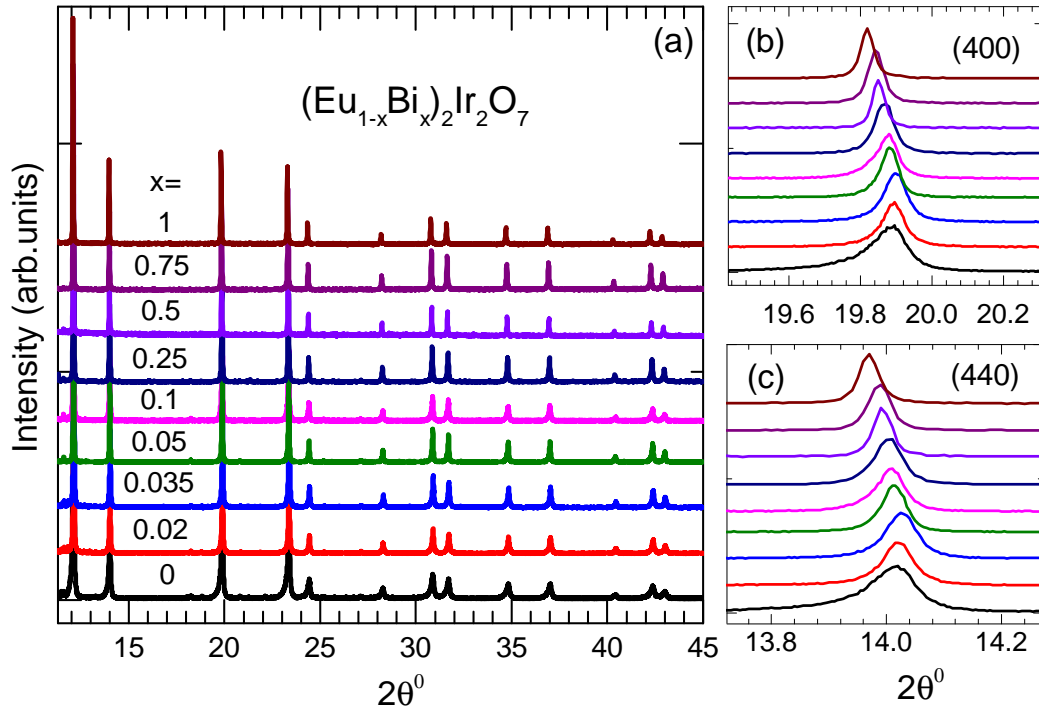


Figure 4.1: (a) X-ray diffractograms collected at MCX beamline, Elettra-Synchrotron, Italy showing the formation of pyrochlore phase for the entire series $(\text{Eu}_{1-x}\text{Bi}_x)_2\text{Ir}_2\text{O}_7$. Panel (b) and (c) show shift in peak 400 and 440 across the series.

we made an unexpected discovery, where we observed that despite the larger size, initial Bi-doping in EIO resulted in an anomalous lattice contraction. Panel (a) of Fig 4.1 shows the high resolution X-ray diffractograms collected at MCX beamline for the series $(\text{Eu}_{1-x}\text{Bi}_x)_2\text{Ir}_2\text{O}_7$. Across the $(\text{Eu}_{1-x}\text{Bi}_x)_2\text{Ir}_2\text{O}_7$ series, the XRD lines clearly shift to higher angles for $x < 0.05$ indicating lattice contraction and this can be seen in panel (b) and (c) which tracks the peak position of 400 and 440 peaks. Above $x > 0.05$, XRD lines shift to a lower angle marking the expansion of the lattice. An analogous stannates series $(\text{Eu}_{1-x}\text{Bi}_x)_2\text{Sn}_2\text{O}_7$ was synthesized to see if Bi creates similar lattice contraction even in pyrochlore stannates. However, we observed a regular behavior of lattice parameters for compositions between $\text{Eu}_2\text{Sn}_2\text{O}_7$ and $\text{Bi}_2\text{Sn}_2\text{O}_7$.

An important point to mention here is that $\text{Bi}_2\text{Sn}_2\text{O}_7$ does not crystallize with pyrochlore structure but in tetragonal structure. It undergoes a structural transition to pyrochlore structure at $\sim 600^\circ\text{C}$. But in the case of $(\text{Eu}_{1-x}\text{Bi}_x)_2\text{Sn}_2\text{O}_7$ series, pyrochlore structure is found to be stable up to 75% of Bi substitution at the Eu site. In Fig. 4.2,

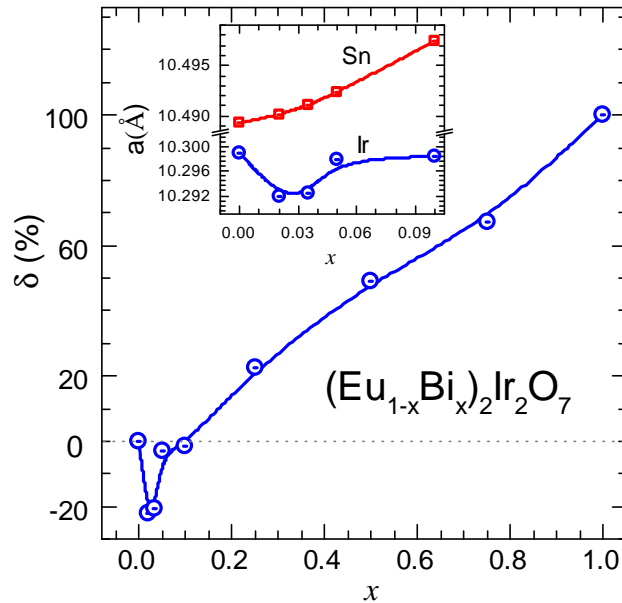


Figure 4.2: x dependence of the parameter δ . The inset shows the variation of $a(x)$ in the range $0 \leq x \leq 0.1$ for $(\text{Eu}_{1-x}\text{Bi}_x)_2\text{Ir}_2\text{O}_7$ (Ir) and $(\text{Eu}_{1-x}\text{Bi}_x)_2\text{Sn}_2\text{O}_7$ (Sn).

we show the variation of lattice parameter a and the deviation δ , which is defined as $\delta(x) = (a - a_0)/(a_1 - a_0)$; where a_0 and a_1 are the lattice parameters of EIO and BIO, respectively. In the range $x \leq 0.035$, a exhibits an anomalous contraction with δ as large as -21% . On the contrary, in the homologous stannate series, doping with Bi leads to a regular lattice expansion as expected from the Vegard's law (see Fig. 4.2 insets). Our results suggest a violation of the Vegard's law in the iridates series.

Very weak diffraction peaks due to unreacted precursors, Eu_2O_3 (indicated by e) for $x = 0, 0.02$ and IrO_2 in case of $x = 0.25$ were observed, in which case, a mixed-phase refinement was carried out. The total amount of the impurity phase was found to be around 1%. The data were fitted using the Thompson-cox-Hastings pseudo-Voigt line profile function to account for the slight peak asymmetry. The asymmetry was highest for $x = 0$ and decreased upon Bi substitution. The peaks were symmetric for $x = 0.1$ and higher doping concentrations. The asymmetric nature of the peak and the peak broadening was found to have intrinsic origin and did not depend on the impurity concentration. This is well established from the several EIO samples studied in Ch. 3, where all the compositions exhibited comparable asymmetry and peak broadening

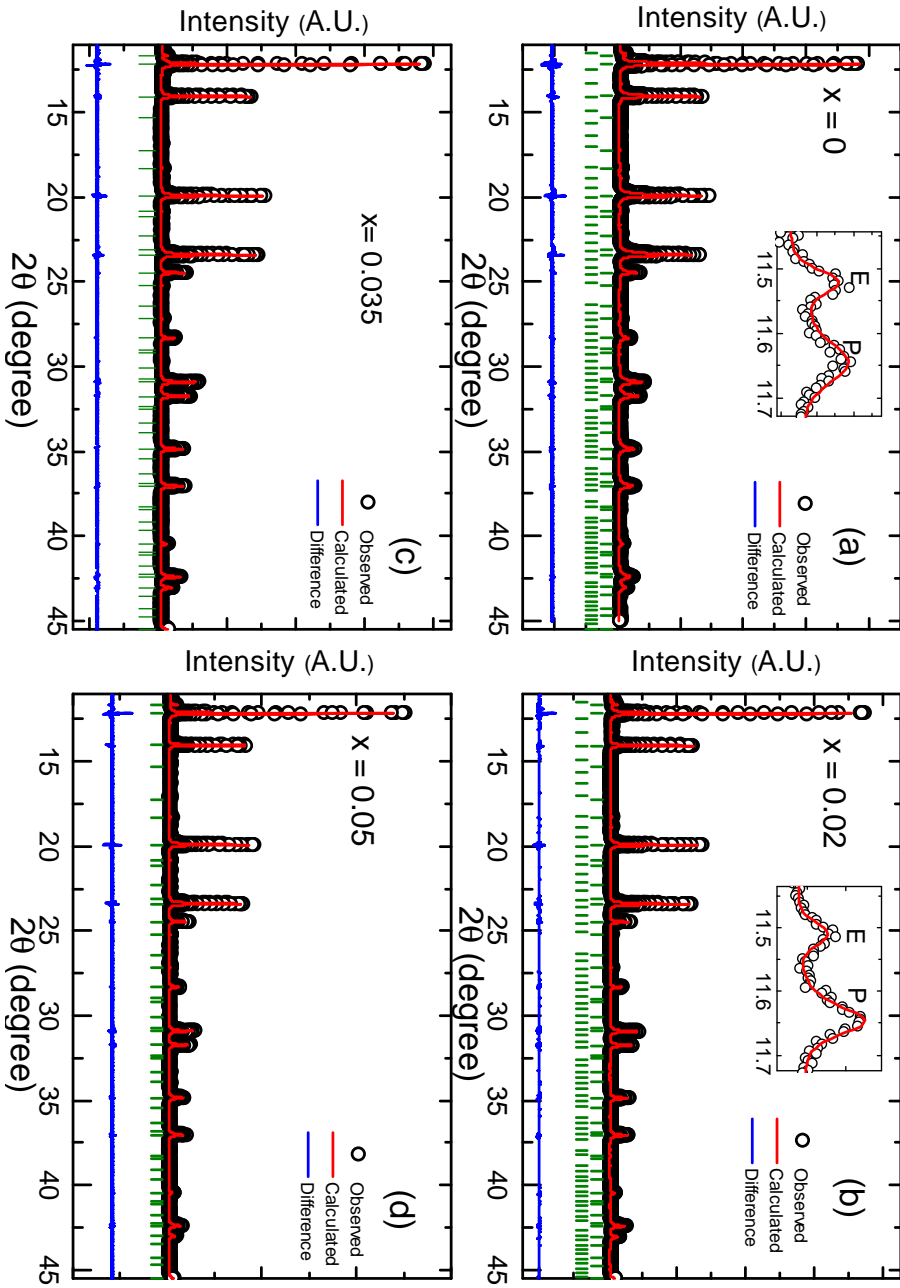


Figure 4.3: Rietveld refinement of the samples in the series $(\text{Eu}_{1-x}\text{Bi}_x)_2\text{Ir}_2\text{O}_7$ for $x = 0, 0.02, 0.035$ and 0.05 .

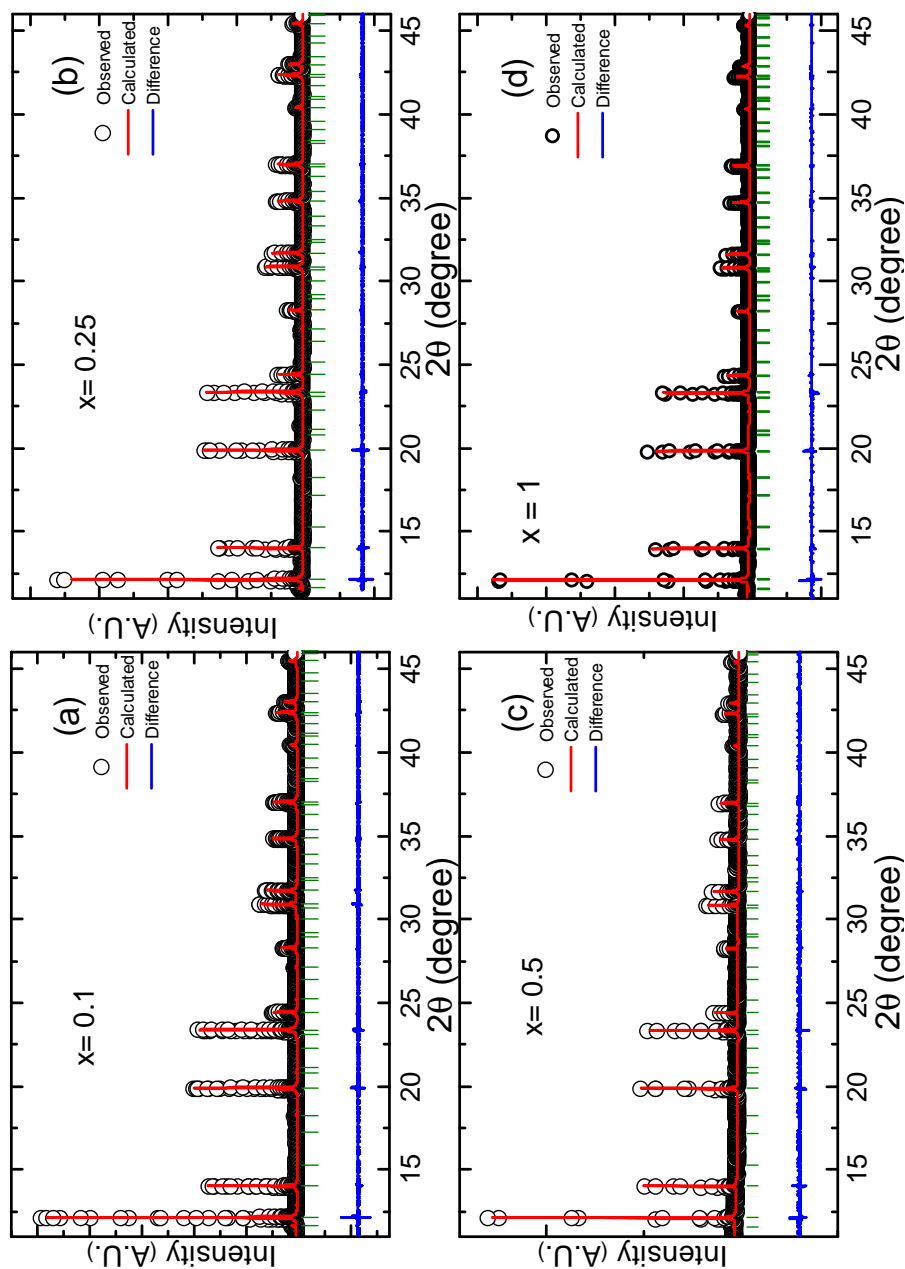


Figure 4.4: Rietveld refinement of the samples in the series $(\text{Eu}_{1-x}\text{Bi}_x)_2\text{Ir}_2\text{O}_7$ for $x = 0.1, 0.25, 0.5$ and 1 .

irrespective of the impurity concentration. Absorption correction was also taken into account, which is important for the samples with heavier elements [64]. The cation occupancies were refined which gave an estimate of Bi in the system. The refinement of the cation occupancies confirmed that Bi is indeed going to the Eu site as an attempt of refining Bi occupation at the Ir site resulted in negative occupancy. The quality of the refinement is reflected in the excellent match between calculated and experimental data in Fig. 4.3 - 4.4. The main results of the Rietveld refinement are collected in Table 1.

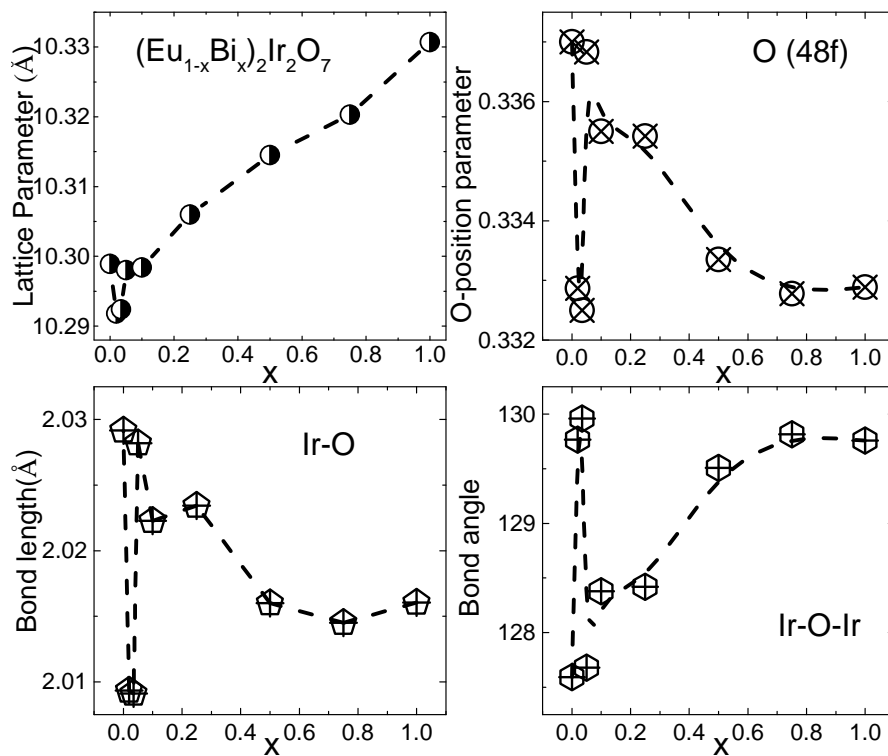


Figure 4.5: Evolution of structural parameters in the series $(\text{Eu}_{1-x}\text{Bi}_x)_2\text{Ir}_2\text{O}_7$.

The lattice contraction was noticeable using the lab-based XRD source as well; however, to get the high precision value of various structural parameters from structural refinement, high-resolution synchrotron X-ray diffraction was performed. The various structural parameters obtained from the Rietveld refinement are plotted in Fig. 4.5. Error bars for all the parameters are the same as the symbol size. The value of $u = 0.337$ for $x = 0$ and $u = 0.3289$ for $x = 1$ agrees with the previously reported values [66, 97]. As the lattice undergoes a contraction, u also exhibit a sudden drop in the value to $u = 0.329$ for $x = 0.02$ and 0.035 . The value of u recovers for $x = 0.05$ and shows a gradual

Table 4.1: Goodness of fit parameters for different values of x in $(\text{Eu}_{1-x}\text{Bi}_x)_2\text{Ir}_2\text{O}_7$ samples, obtained using Rietveld refinement of the high-resolution synchrotron powder X-ray diffraction data. * All the occupancies carry an error bar of 0.015

$\text{Eu}_{2-2x}\text{Bi}_{2x}\text{Ir}_2\text{O}_7$	χ^2	Rp	Rwp	No. of phases refined	Eu occupancy*	Bi occupancy*	Ir occupancy*
$x = 0$	2.05	13.1	15.1	2	1.00768	—	0.99244
$x = 0.02$	1.72	15.5	18.1	2	0.983	0.0169	0.99784
$x = 0.035$	1.62	14.3	16.6	1	0.972	0.0278	0.9892
$x = 0.05$	1.38	18.8	20.4	1	0.955	0.0447	0.9934
$x = 0.1$	1.8	14.7	16.5	1	0.9005	0.0995	0.99796
$x = 0.25$	1.64	14.4	16.2	2	0.7517	0.2483	1.00276
$x = 0.5$	1.1	31.6	32.3	1	0.5104	0.4896	1.00792
$x = 0.75$	1.47	23.8	21.2	1	0.272	0.7272	0.98608
$x = 1$	1.36	24.6	20.7	1	—	0.9699	1.0066

decrease from $u = 0.336$ to $u = 0.338$ for $0.05 \leq x \leq 1$. In pyrochlore oxides, in general, u is expected to decrease with increasing lattice parameters. This trend has been established in pyrochlore ruthenates and stannates but is not thoroughly studied for iridates [69, 87]. However, in the present study, with the exception of the anomalous region, we observe that u decreases as the A-site radius/lattice parameter decreases. The Ir-O-Ir bond angle which is known to show inverse correspondence to u shows a sudden jump in the anomalous region. The angle records nearly 2° change for the anomalous region as well as between the end members. The sudden increase in the bond angle could be understood by noting the overall compression of the IrO_6 octahedra which is reflected by a decrease in the bond length in the anomalous region. Fig. 4.5 shows that, except for the anomalous region, the rest of the series observe a gradual change in various parameters. The anomalous region, on the other hand, exhibits an exactly opposite change from the rest of the series. In pyrochlore structure, increasing the A-site atomic radius increases the Ir-O-Ir bond angle and the lattice parameter in parallel, whereas, hydrostatic pressure increases the former but decreases the latter [63]. This shows the remarkable similarity in the variation of structural parameters on the application of pressure and the anomalous contraction region in our study. In both cases, we observe a decrease in the lattice parameter with an increase in the Ir-O-Ir bond angle.

The morphology of all the samples was examined using SEM. Fig. 4.6 shows the FESEM images for various doping concentrations. A range of grain-size from 10 - 100 nanometer can be seen for EIO (The EIO sample discussed here corresponds to sample A from chapter 3). Similar is the case for $x = 0.02$. With increasing Bi concentration, the grain size gets bigger and more uniform across the sample. For compositions near BIO i.e., $x = 0.75$ and $x = 1$, clear octahedral shaped grains could be observed, similar to that of single-crystal shown by Millican et. al [66]. The crystalline tendency of the grains with increasing Bi substitution is aligned with the fact that Bi inclusion accelerates pyrochlore phase formation. The Eu:Bi ratio was measured using EDX. Pieces of pellets were polished for EDX measurements. On an average 25 - 30 points were collected for each sample to calculate the cation ratio. The ratio calculated from EDX agreed well with the nominal Eu:Bi ratio. The EDX results are summarised in Table 4.2.

Hereafter, we will refer to the negative lattice expansion region $0 \leq x \leq 0.035$ as *anomalous*; the region $0.1 < x \leq 1$ where the lattice expands normally as *normal*, and

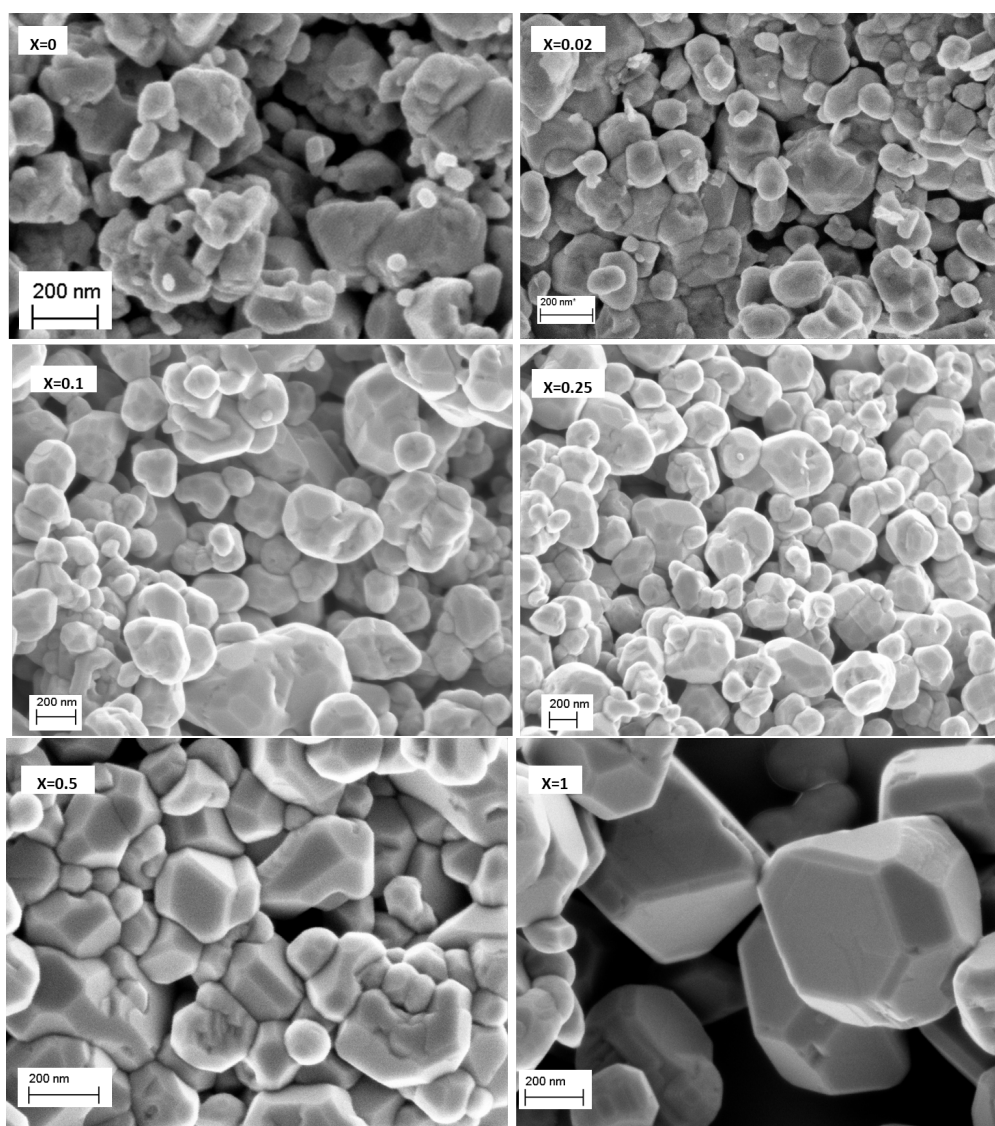


Figure 4.6: FESEM images of samples in the series $\text{Eu}_{2-2x}\text{Bi}_{2x}\text{Ir}_2\text{O}_7$. The grain size increases with increasing Bi concentration.

$\text{Eu}_{2-2x}\text{Bi}_{2x}\text{Ir}_2\text{O}_7$	Bi:Eu(calculated)	Bi:Eu (experimental)	Standard deviation	Number of data points
$x = 0.02$	0.02	0.017	0.0075	29
$x = 0.035$	0.036	0.031	0.0102	28
$x = 0.05$	0.05	0.057	0.0121	24
$x = 0.1$	0.11	0.130	0.0092	25
$x = 0.25$	0.33	0.257	0.0112	19
$x = 0.5$	1	0.856	0.0056	22
$x = 0.75$	3	2.965	0.0112	24

Table 4.2: Eu:Bi ratio calculated from EDX measurements

the intermediate region $0.035 < x < 0.1$ as the *crossover* region.

4.3 Effect of Bi substitution on physical properties

After the interesting trend observed in the lattice parameters, the next obvious step was to study the various physical properties of this series. We performed bulk characterization on all the compositions to track the changes in the ground state going from EIO to BIO. As will be discussed next, we observed that the anomalous lattice contraction is also reflected in the physical properties.

4.3.1 Magnetic susceptibility and Muon Spin spectroscopy

In the left panel of Fig. 4.7, we show the temperature dependence of χ for $0 \leq x \leq 0.1$. The transition to the AIAO state is marked by a cusp in the ZFC data below which the ZFC and FC branches bifurcate in agreement with previous reports [61, 75]. It has been thoroughly investigated that this splitting is not a sign of glassy or inhomogeneous ordering – as is often the case – but it arises in the magnetically ordered state due to a combination of several minor factors, including, the presence of 180° domain walls, antisite disorder, Ir vacancies, and/or the occurrence of Ir^{5+} [76]. We note that in the anomalous doping range, the rate of change of T_N is rather slow ($\Delta T_N/T_N \leq 0.05$) and the qualitative behavior of $\chi(T)$ remains unchanged suggesting that the ground state of EIO is preserved at least up to $x = 0.035$. In the crossover region T_N is suppressed sharply, and for $x = 0.1$ no magnetic ordering is observed down to $T = 2$ K. In particular, a weakly temperature-dependent van-Vleck contribution arises due to the Eu^{3+} ions [77], and it is indeed suppressed upon decreasing the Eu^{3+} concentration. The Van-Vleck susceptibility curve is shown by a dashed line in the left panel of Fig. 4.7. Van-Vleck susceptibility is calculated by taking $\lambda = 400\text{K}$. The same phenomenology is observed for the $x = 0.05$ sample even though the enhancement of the FC branch over

the van-Vleck term is much weaker. Finally, we observe only the van-Vleck-like contribution for the $x = 0.1$ sample, the small upturn for $T \lesssim 10$ K being associated with diluted magnetic impurities [61]. The subtraction of Van-Vleck susceptibility from the total susceptibility results in a nearly temperature-independent susceptibility which cannot be modeled using Curie-Weiss behaviour and is also observed in the literature [44].

The susceptibility of compositions in the paramagnetic region ($x \geq 0.1$) is comprised of Pauli paramagnetism and Van-Vleck contribution. Susceptibility of the higher Bi-doped concentration (Fig 4.7: right panel) shows temperature dependence identical to the Van-Vleck susceptibility. On the other hand, $Bi_2Ir_2O_7$ shows a temperature-independent susceptibility down to 20 K below which it rises sharply. Since the intrinsic susceptibility of this sample is relatively low, this rise could result from small traces of impurities commonly referred to as the impurity driven Curie tail [61].

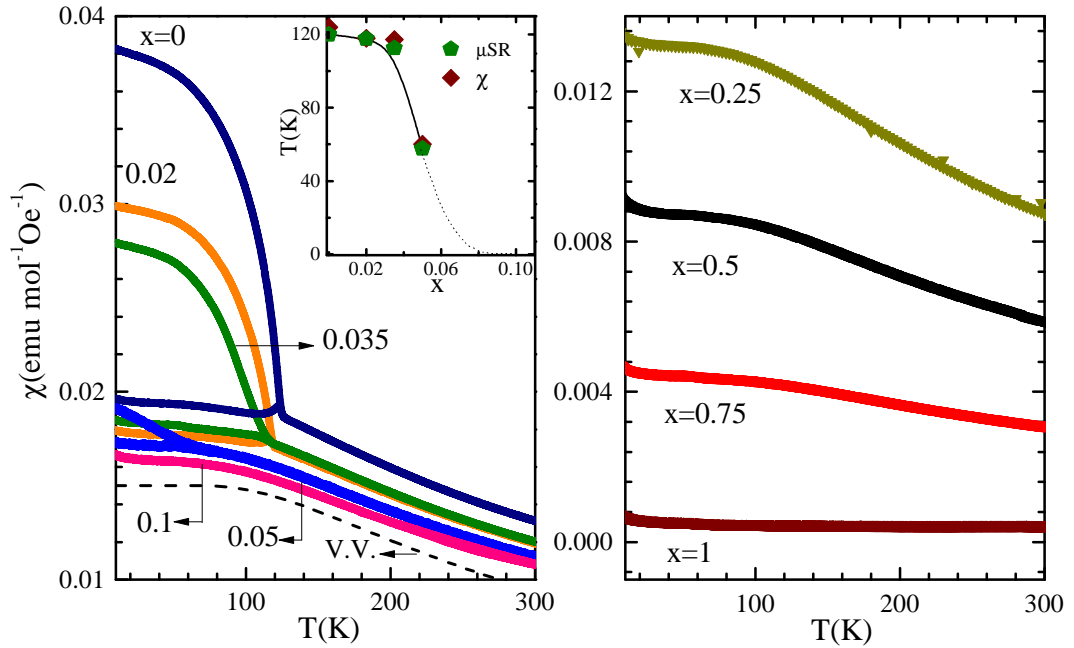


Figure 4.7: (Left panel) The susceptibility (χ) for $x \leq 0.1$ is shown as a function of temperature. Thermomagnetic hysteresis is seen only for $x = 0, 0.02, 0.035$ and 0.05 sample; the upper (lower) branch represents FC (ZFC) data. (Right Panel) (χ) for $x \geq 0.25$ is shown as a function of temperature

We measured $(Eu_{1-x}Bi_x)_2Ir_2O_7$ samples by means of μ^+ SR (muon spin spectroscopy) on the GPS (General Purpose Surface-muon) and LTF (Low Temperature Facility) spectrometers of the Paul Scherrer Institute, Switzerland, for the selected compositions

$x = 0.02, 0.035, 0.05, 0.1$.

In Fig. 4.8 we show the results of μ^+ SR measurements for compositions $0 < x \leq 0.1$ where we plot representative time-depolarization curves for the μ^+ spins in conditions of zero external magnetic field. It is evident that the long-lived coherent oscillations observed at low temperatures for $x = 0.02$ are highly overdamped for $x = 0.05$, which we interpret as the result of a long-range order to short-range order crossover for the magnetic phase [98]. Accordingly, we fit the experimental data to the conventional function used for magnetic materials in poly-crystalline form [99]. The fitting results are shown in Fig. 4.8. From these fits, we estimate the magnetic volume fraction (V_m) as $\sim 90\%$ for $x = 0.02$ and $\sim 70\%$ for $x = 0.05$ at the lowest temperatures. A more dramatic suppression of the AIAO phase is observed for $x = 0.1$ where no sizeable magnetic contribution of electronic origin is observed down to a temperature of 0.02 K. A marginal increase in the overall relaxation at $T = 0.02$ K may point towards the onset of dynamical processes, possibly from extrinsic phases. We define T_N as the highest T value where a transversal relaxation is discernible. The values of T_N based on this criterion agree nicely with those obtained from the ZFC-FC splitting in $\chi(T)$ as shown

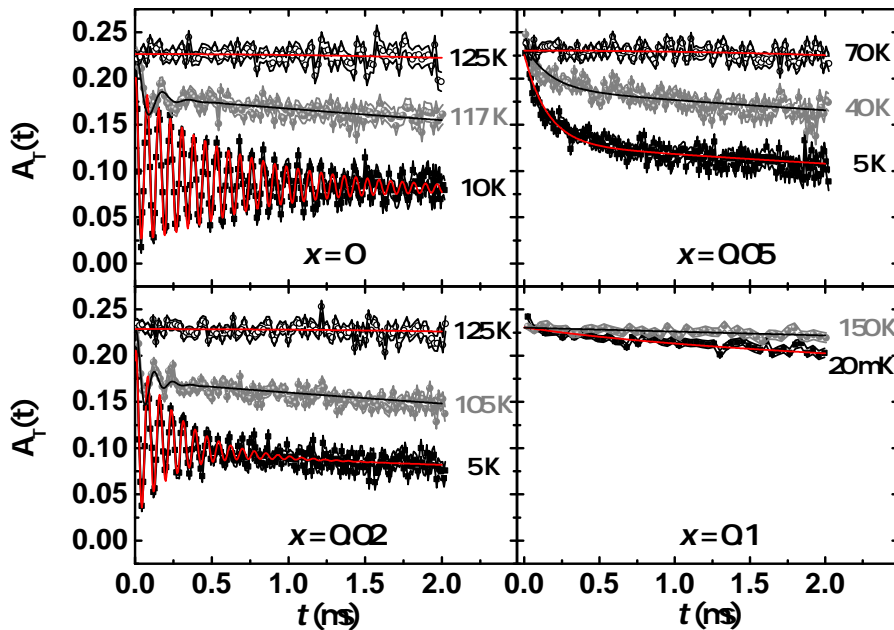


Figure 4.8: Representative zero-field depolarization curves for the μ^+ spins in the time domain for four $(\text{Eu}_{1-x}\text{Bi}_x)_2\text{Ir}_2\text{O}_7$ samples in the limit $x \leq 0.1$. We obtain the continuous lines after fitting the data to Eq. (4.1). The temperature values are rounded to the closest integer.

in Fig. 4.7 (inset).

$$\frac{A_T(t)}{A(0)} = [1 - V_m(T)] e^{-\frac{\sigma_N^2 t^2}{2}} + \left[a_1^\perp(T) F_1(t) e^{-\lambda_1^\perp t} \right. \quad (4.1)$$

$$\left. + a_2^\perp(T) e^{-\lambda_2^\perp t} + a^\parallel(T) e^{-\lambda^\parallel t} \right] \quad (4.2)$$

here, $V_m(T)$ is the magnetic volume fraction of the sample while $a_{1,2}^\perp$ and $a^\parallel(T)$ represent the fractions of muons probing static local magnetic fields perpendicular and parallel to the initial spin polarization, respectively (the subscripts 1 and 2 account for two different crystallographic implantation sites for μ^+). In the \perp component, the spin precession around the local magnetic field is fitted by the function $F_1(t)$, which is a cosine function describing the coherent oscillations in the $x = 0$ and $x = 0.02$ samples, and is set to unity for the $x = 0.05$ and $x = 0.1$ samples. The relaxation times $\lambda_{1,2}^\perp$ and λ^\parallel account for the distribution of static local magnetic fields and dynamical processes, respectively, while σ_N is the relaxation rate due to the nuclear moments in the paramagnetic phase.

4.3.2 Electrical transport

The resistivity of our samples is shown in Fig. 4.9. For $x = 0$, $\rho(T)$ exhibits a behavior similar to that previously reported with a MI transition at $T_{MI} = 120$ K, below which ρ increases sharply upon cooling. In concurrence with χ and μSR , in the anomalous range, T_{MI} decreases very slowly and the qualitative behavior of ρ remains unchanged. One expects a slight broadening of the MI transition due to chemical disorder, but surprisingly this transition is sharpest for the 2% Bi-doped sample. This is analogous to the effect of external pressure previously reported by Tafti et al. [63] who showed that pressure up to 6 GPa tends to sharpen the MI transition. This suggests that any broadening of the MI transition due to chemical disorder is masked by the negative chemical pressure.

We attempted to fit ρ in this doping range to either the Arrhenius or the variable-range-hopping (VRH) models did not yield satisfactory results. The data $\rho(T) = \rho_0 \exp(\Delta/T^\alpha)$ was modeled with $\alpha = 0.25, 0.5,$ and 1 for variable range hopping, variable range hopping with electron correlations, and nearest-neighbor hopping, respec-

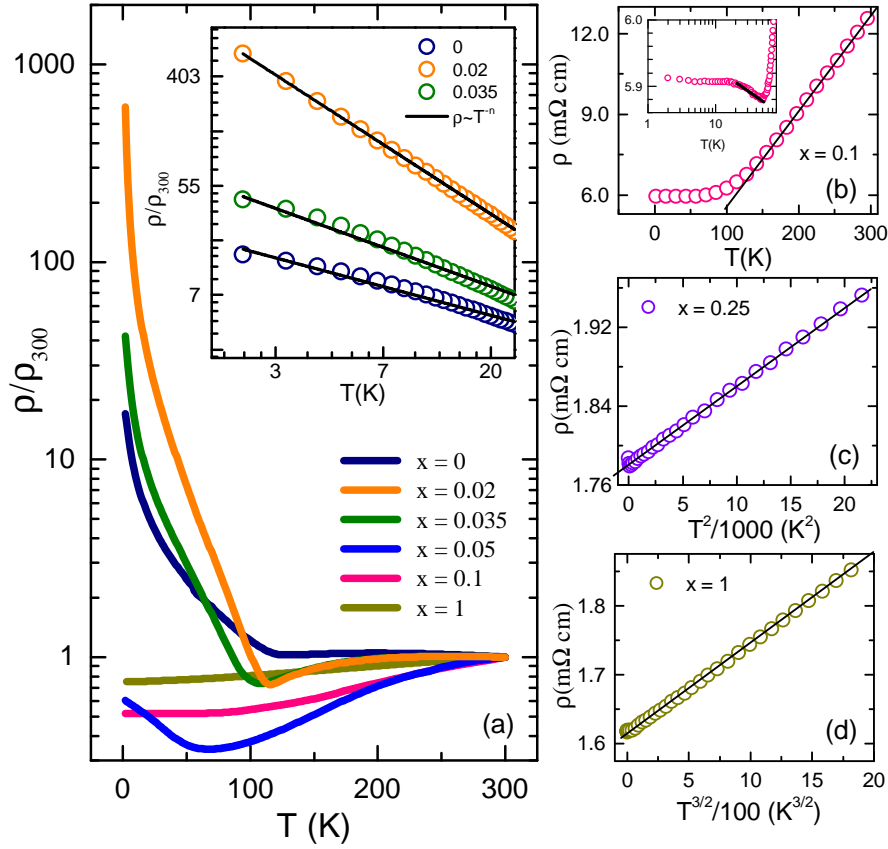


Figure 4.9: (a) The temperature variation of normalized resistivity ρ/ρ_{300} for various x . The inset in (a) shows the power law fit at low-temperatures for $x = 0, 0.02$ and 0.035 . (b), (c) and (d) show the temperature variation of ρ for $x = 0.1, 0.25$ and 1 samples, respectively. The straight line highlights T (b), T^2 (c) and $T^{3/2}$ (d) variation for $x = 0.1, 0.25$ and 1 , respectively. The inset in (b) shows the low-temperature resistivity minimum. The straight line showing a $-\ln T$ increase is a guide to eye.

tively. However, a $1/T^\alpha$ power-law dependence provides a better description of $\rho(T)$ as shown in Fig. 4.9a inset. For $x = 0.02$, this fits the data satisfactorily up to $T = 20$ K, and with $\alpha \approx 1$; but for $x = 0.035$ and 0 , not only the fitting range shrinks, the value of exponent also reduces to $\alpha \approx 0.5$. To verify if the $\alpha \approx 1$ is indeed true only over the narrow doping range, we synthesized another composition in the anomalous region with Bi substitution corresponding to $x = 0.025$ and measured the resistivity of this composition. In Fig. 4.10, we show the fitting for all the different models for composition in the anomalous region, i.e., $0.02 \leq x \leq 0.035$. It can be seen that $\alpha \approx 1$ behavior can also be seen for $x = 0.025$, further confirming that this behavior is unique to the narrow

doping range and is not a measurement or sample artifact.

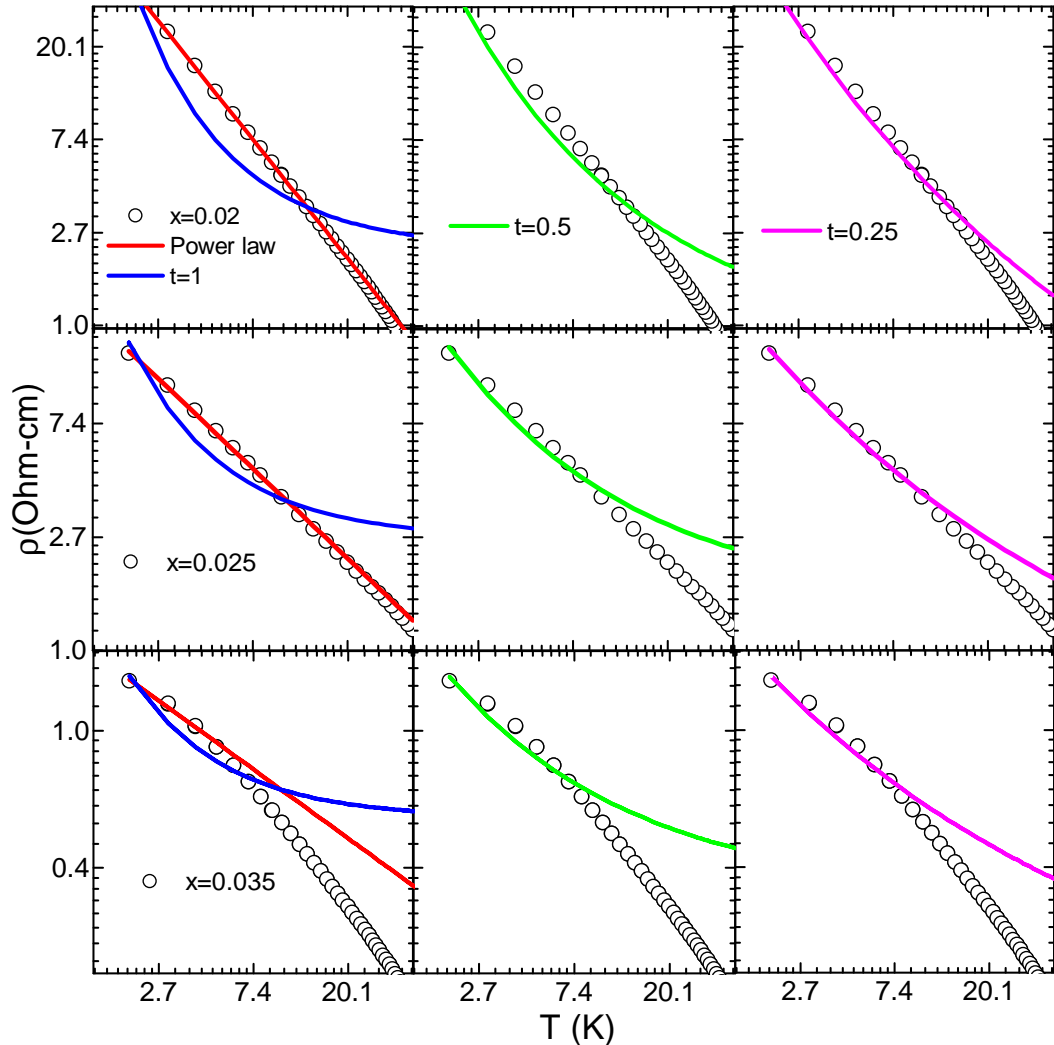


Figure 4.10: Power law fit at low-temperatures for $x = 0, 0.02$ and 0.035 .

In the crossover region, ρ changes dramatically with the MI transition turning broad, centered near $T = 70$ K, consistent with χ or μ_{SR} data. Upon entering the normal region, a metallic behavior with a prominent T^n dependence ensues. Interestingly, for $x = 0.25$, the behavior is that of a Fermi-liquid with T^2 dependence almost over the whole temperature range (Fig. 4.9c); but this changes to $T^{3/2}$ for $x \geq 0.5$. For BIO, a $T^{3/2}$ dependence is found (Fig. 4.9d) in agreement with a previous report [96]. At the boundary $x = 0.1$ where $AIAO \rightarrow 0$, $\rho(T)$ shows a T -linear variation over a broad temperature range (Fig. 4.9b). An expanded view of the low-temperature resistivity of

Table 4.3: Resistivity value at 2 K and 300 K for different values of x in $\text{Eu}_{2-2x}\text{Bi}_{2x}\text{Ir}_2\text{O}_7$

$\text{Eu}_{2-2x}\text{Bi}_{2x}\text{Ir}_2\text{O}_7$	$\rho(\text{m}\Omega \text{ cm})$ at 2 K	$\rho(\text{m}\Omega \text{ cm})$ at 300 K
$x = 0$	1883	110
$x = 0.02$	38998	64
$x = 0.035$	1583	34
$x = 0.05$	9	14
$x = 0.1$	7	13.5
$x = 0.25$	1.8	2.4
$x = 0.5$	1.75	1.92
$x = 0.75$	0.82	0.9
$x = 1$	0.95	1.3

this sample reveals the presence of an upturn with ρ varying as $-\ln T$ down to $T \approx 25$ K below which it tends to saturate (Fig. 4.9b inset).

The absolute value of resistivity at 300 K and 2 K is given for all the compositions in Table 4.3. The resistivity at 300 K decreases gradually with increasing Bi substitution. Ideally, doping should result in increased grain boundary scattering and thus higher resistivity value. But, as ρ at 300 K varies smoothly throughout the series, grain boundary scattering, though present, can be eliminated as a dominant contribution to the overall resistivity.

4.3.3 Thermoelectric properties

From the behavior of χ , μSR and ρ , it is evident that the anomalous lattice contraction preserves the magnetic and insulating ground state which is suppressed as the lattice expands. To understand this peculiar relationship we investigated the thermopower $S(T)$ of our samples. The data for samples $x = 0, 0.02, 0.035, 0.05, 0.1$ and 1 are shown in Fig. 4.11. As shown in Fig. 4.11, in EIO, S remains positive for all temperatures indicating that the dominant charge carriers are hole-like. The qualitative behavior and sign of S are in good agreement with previous reports [4, 100]. In the anomalous doping range, while the qualitative form of S remains unchanged, the entire $S(T)$ curve shifts rigidly downward resulting in negative S for intermediate temperatures. For $x = 0.05$, S is negative for almost entire temperature range. In BIO, S is not only negative, it also shows a typical metal-like behavior: $|S|$ increasing upon increase in T . Finally, for

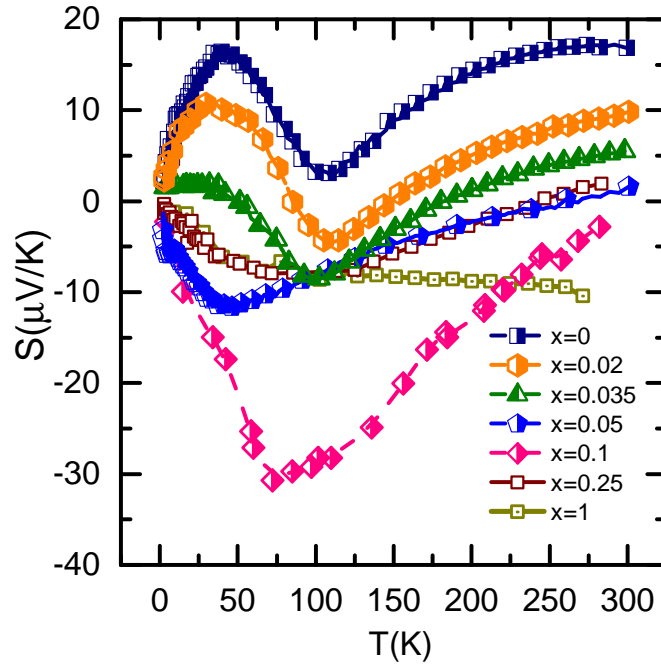


Figure 4.11: The temperature variation of thermopower S for $x = 0, 0.02, 0.035, 0.05, 0.1$ and 1

$x = 0.1$, S is not only negative but it is also qualitatively different, featuring a maximum near $T = 60K$ ($S_{max} = -30\mu VK^{-1}$), which is the highest S for any x in this series. From the variation of S with x we infer that the sign of majority charge carrier changes from hole-like ($x \leq 0.035$) to electron-like ($x \geq 0.05$) as x increases.

4.3.4 Heat capacity

We also performed heat capacity measurements on all the samples. Closely spaced data points were recorded in the low-temperature region to extract the electronic coefficient of specific heat. In Fig. 4.12a, C_p/T is plotted against T^2 for $0 \leq x \leq 0.25$. In the low-temperature range, C_p/T exhibits a good linearity that can be fitted using $C_p = \gamma T + \beta T^3$ where γ and β represents the electronic and phononic contributions, respectively. The spin-wave contribution is expected to be small due to the small size of the ordered Ir moment [48]. Also, this contribution is expected to scales as T^3 and thus will not affect γ . The variation of γ with x is shown in Fig. 4.12a. For EIO, γ of $15 \text{ mJ mol}^{-1}\text{K}^{-2}$ is in good agreement with the previous report [61] and suggests moderately strong electronic correlations as predicted theoretically [52]. Upon Bi doping, γ de-

increases in the anomalous range before increasing again as x enters the crossover range. For $x = 0.1$, γ reaches the highest value of $\sim 25 \text{ mJ mol}^{-1}\text{K}^{-2}$ before declining again with further increase in x . As γ is proportional to the density of states, the variation in the gamma indicates the corresponding variation in the density of states (DOS) at the Fermi level. From the plot, compositions in the anomalous region have smallest DOS in the entire series, whereas the DOS is the highest for $x = 0.1$.

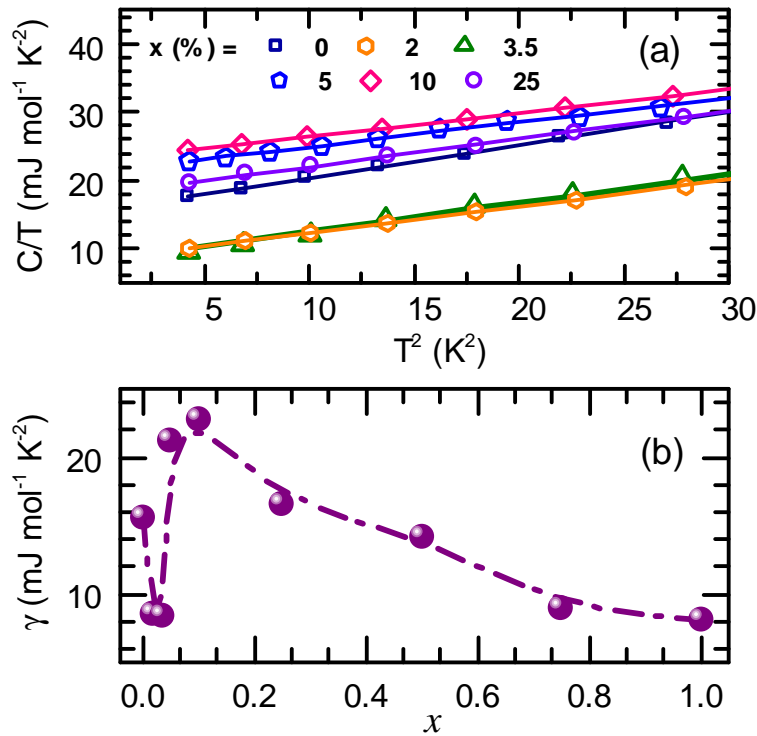


Figure 4.12: (a) the specific heat is plotted as C_p/T versus T^2 for $0 \leq x \leq 0.25$. The straight lines through the data points are linear fits $\gamma + \beta T^2$ (b) the variation of γ is shown as a function of x for the whole series.

4.4 Discussion

We now discuss the anomalous lattice contraction. It is surprising that despite its larger size ($r_{\text{Bi}^{3+}} = 1.17\text{\AA}$) compared to Eu ($r_{\text{Eu}^{3+}} = 1.066\text{\AA}$), initial Bi-doping leads to a lattice contraction. Since BIO has a stable pyrochlore structure with Bi in +3 oxidation state, it is unlikely that Bi-doped in EIO has a valence state different from +3. We nevertheless confirmed this by performing XPS measurements at DESY synchrotron

facility which is described in detail in chapter 5. To put this anomalous behavior into perspective, we should mention here that in the structurally analogous $(Y_{1-x}Bi_x)_2Ru_2O_7$ [101] or $(Eu_{1-x}Sr_x)_2Ir_2O_7$ series [95] no such lattice anomaly has been reported, and the MI transition is also shown to suppress gradually.

Though unusual, the deviation from Vegard's law in TMOs is not completely unknown. For example, La doping in $SrTiO_3$ [102], or in the iridates $Sr_3Ir_2O_7$ and Sr_2IrO_4 [103, 103, 104], has been shown to result in an anomalous lattice expansion. This is believed to be an electronically driven effect arising from carrier doping due to La^{3+} substitution for Sr^{2+} . It is argued that upon carrier doping, in some cases it may be energetically favorable for a system to lower its total energy by shifting the electronic bands through expansion or contraction of the lattice, which is known as the deformation potential effect [105]. In our study, we see that the anomalous lattice contraction is indeed coupled to the electronic properties. However, here a notable exception arises from the isovalent nature of Eu^{3+} and Bi^{3+} , which precludes the conventional carrier doping mechanism. How then are carriers doped when Bi is substituted for Eu? In a recent study, Qi et al. [96] found that in the Bi-doped pyrochlores, the $Ir(5d)-(Bi)6s/6p$ hybridization can be significantly enhanced, which makes the $6s/6p$ electrons of Bi to contribute to the DOS at ϵ_F .

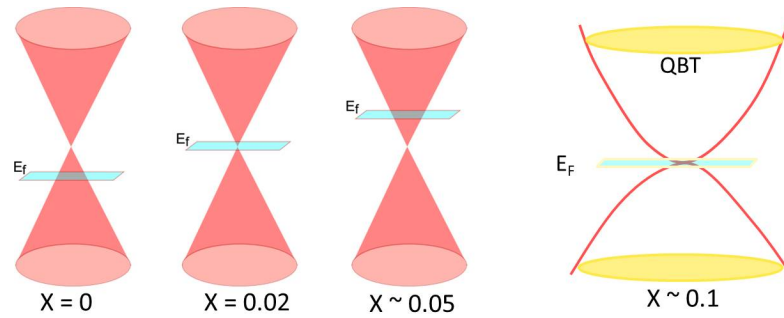


Figure 4.13: Pictorial representation of tuning of the Fermi level with Bi concentration. Fermi level is closest to the Weyl crossing for $x = 0.02$ and the ground state is reminiscent of quadratic band touching for $x = 0.1$.

This brings us to the point concerning the robust ground state of EIO against Bi doping. As shown here, during initial Bi doping not only the AIAO/MI transitions remain preserved they also become sharper (sharpest for $x = 0.02$), and low-temperature ρ approaches a $1/T$ behavior. We suggest that these are manifestations of the WSM

phase that has been concretely established in the theoretical works. We conjecture that ϵ_F at $x = 0$ is located slightly below the Weyl nodes (positive S for $x = 0$); and, upon initial Bi-doping, lattice contracts to shift the bands down (deformation potential effect), which pushes ϵ_F up, closer to the Weyl nodes. This is consistent with the decreasing behavior of γ which is proportional to the DOS at ϵ_F . This also explains why $\rho(T)$ at low-temperatures approaches a $1/T$ behavior. In the WSM phase, the electron-hole symmetry about the Weyl node results in current-carrying states with *zero* total momentum; the electron-electron interaction, therefore, relaxes the current but with zero momentum transfer leading to a $1/T$ dependence [106]. Indeed, as $x \rightarrow 0.02$, the low-temperature $\rho(T)$ is closest to the expected behavior. At higher Bi doping, ϵ_F is gradually tuned away from the Weyl nodes, which explains the changing sign of S . However, this picture breaks down as x increases further leading to the suppression of AIAO state.

We now discuss the sample $x = 0.1$ or $(\text{Eu}_{0.9}\text{Bi}_{0.1})_2\text{Ir}_2\text{O}_7$. For this sample, the lack of magnetic ordering, a large γ value, and a resistivity minimum showing a $-\ln T$ dependence at low-T are all reminiscent of $\text{Pr}_2\text{Ir}_2\text{O}_7$ (PIO), which features a quadratic band touching point protected by the inversion and time-reversal symmetries [49, 92]. Recently, the resistivity minimum in PIO has gathered a renewed interest [92, 107, 108]. In the earlier studies, it was interpreted as arising due to the Kondo effect from Ir($5d$) and localized Pr $4f$ -moments, but it is now believed to be intrinsic to the Ir subsystem, which has the characteristics of a 3D interacting Luttinger semimetal [88, 107]. From this point of view, $(\text{Eu}_{0.9}\text{Bi}_{0.1})_2\text{Ir}_2\text{O}_7$ is interesting as it mitigates the complexity arising due to a magnetic A -site. Based on these similarities, it can be argued that $(\text{Eu}_{0.9}\text{Bi}_{0.1})_2\text{Ir}_2\text{O}_7$ is possibly the mother phase featuring a quadratic band touching point analogous to PIO from which the WSM phase can be derived in the TRS broken regime close to $x = 0$; and other exotic but not necessarily topologically non-trivial electronic phases for $x > 0.1$. In particular, the region from $0.1 < x < 1$ appears to be very fertile as the $\rho(T)$ behavior changes from T -linear ($x = 0.1$) to $T^{3/2}$ ($x \geq 0.5$) with a Fermi-liquid like T^2 dependence at $x = 0.25$. This region should be explored in the future in more detail.

4.5 Summary

To summarize, we show that Bi-doping in EIO provides a unique platform, which, unlike Sr or Ca doping, does not create an $\text{Ir}^{4+} - \text{Ir}^{5+}$ charge disproportionation, and thus keep the Ir^{4+} -sublattice intact, which is a key to obtaining various non-trivial topological phases. We report here three important findings: (i) anomalous lattice contraction strongly tied to the electronic properties; (ii) robust ground state of EIO against initial Bi doping, which we attribute to the topological WSM phase, which can be realized for very small Bi-doping which pushes ϵ_F closer the Weyl node without destroying the linear dispersion; (iii) $(\text{Eu}_{0.9}\text{Bi}_{0.1})_2\text{Ir}_2\text{O}_7$, located at the boundary from which other non-trivial topological phases can be derived. Fig 4.13 shows the pictorial depiction of tuning of the Fermi level with Bi substitution. Our findings are expected to motivate further research in exploring new quantum phases in the $U - \lambda$ phase space of $5d$ transition metal oxides.

Chapter 5

X-ray photoemission studies of $(\text{Eu}_{1-x}\text{Bi}_x)_2\text{Ir}_2\text{O}_7$

In the previous chapter, we showed that an anomalous lattice contraction occurs upon dilute Bi substitution at the Eu site in the pyrochlore $\text{Eu}_2\text{Ir}_2\text{O}_7$ (EIO). We expect the doped Bi ions to assume a +3 oxidation state since $\text{Bi}_2\text{Ir}_2\text{O}_7$ (BIO) exists with a stable pyrochlore structure. However, both Bi and Ir and for that matter even Eu can be stabilized in multiple oxidation states. Thus, the anomalous lattice contraction could originate if Bi assumed +5 oxidation state in the dilute doping region where Bi^{5+} (0.76 Å) is considerably smaller than Eu^{3+} (1.066 Å). Hence, it is important to study the oxidation state of all the cations.

Here, we employ the Hard X-ray Photoemission Spectroscopy (HAXPES) as a non-destructive and element-sensitive probing technique to study the valence state of various cations as well as the valence band spectra. The HAXPES can probe detailed electronic structure of solid materials with significantly higher depth sensitivity than conventional photoelectron spectroscopy. This makes it ideally suited for the investigation of bulk complex correlated materials.

HAXPES measurements were carried out on the P22 beamline of PETRA III (DESY) utilizing Si311 double crystal monochromator. The excitation energy was $E = 5$ keV and the beam size at sample measured 40×20 mm². Spectra were acquired with Specs 225 HV analyzer, the overall energy resolution was set to 0.28 eV. The high-resolution photoemission spectra corresponding to Europium, Iridium, Oxygen and Bismuth as well

as the valence band spectra were collected for the samples corresponding to $x = 0, 0.02, 0.035, 0.05, 0.1, 0.25, 0.75,$ and 1 in the series $(\text{Eu}_{1-x}\text{Bi}_x)_2\text{Ir}_2\text{O}_7$. The data was analyzed using XPSPeak and CASA XPS software [109].

5.1 Europium core shell spectra

We start by presenting the core level spectra for Europium (Eu). Eu is the only rare-earth except Ce, Pr, Sm and Yb which can take variable oxidation states. Europium, apart from the common Eu^{3+} oxidation state, can also be found as Eu^{2+} . Here we probed the Eu 3d core level at the binding energy of $\sim 1100 - 1200$ eV. Fig. 5.1 shows the 3d core-level spectra of Eu for various Bi doping concentrations. The precise values of binding energies for various peaks is given in Table 5.1.

Due to the spin-orbit coupling, the 3d peak is split into two peaks corresponding to $3d_{3/2}$ and $3d_{5/2}$ respectively. The two peaks are separated by 30 eV and are located at ~ 1164.1 eV ($3d_{3/2}$) and ~ 1133.9 eV ($3d_{5/2}$). There are also three satellite peaks located at 1142.4 eV, 1162 eV, and 1127.9 eV. From Fig. 5.1, one can see that the peak shape and peak positions remain unaltered with changing Bi doping concentration within the energy resolution of the detector. Also the value of peak binding energies agrees well with that reported for Eu^{3+} [110]. This shows that Eu oxidation state as well as chemical environment is not affected by Bi substitution, and it remains +3 throughout the series.

$\text{Eu}_{2-2x}\text{Bi}_{2x}\text{Ir}_2\text{O}_7$	$3d_{3/2}$	$3d_{5/2}$	S1	S2	S3
$x = 0$	1164.3	1133.9	1127.9	1142.4	1162.01
$x = 0.02$	1164.4	1133.9	1127.9	1142.3	1162
$x = 0.035$	1164.4	1134	1127.8	1142.5	1162.2
$x = 0.05$	1164.2	1133.9	1127.8	1142.3	1162.1
$x = 0.1$	1164.2	1134	1127.9	1142.4	1162.3
$x = 0.25$	1164.4	1134.1	1127.9	1142.4	1162.2
$x = 0.5$	1164.18	1134	1127.9	1142.3	1162.3

Table 5.1: Eu 3d core level peaks for various compositions of the series $\text{Eu}_{2-2x}\text{Bi}_{2x}\text{Ir}_2\text{O}_7$. In addition to the core shell lines, there are three satellite peaks corresponding to S1, S2, and S3.

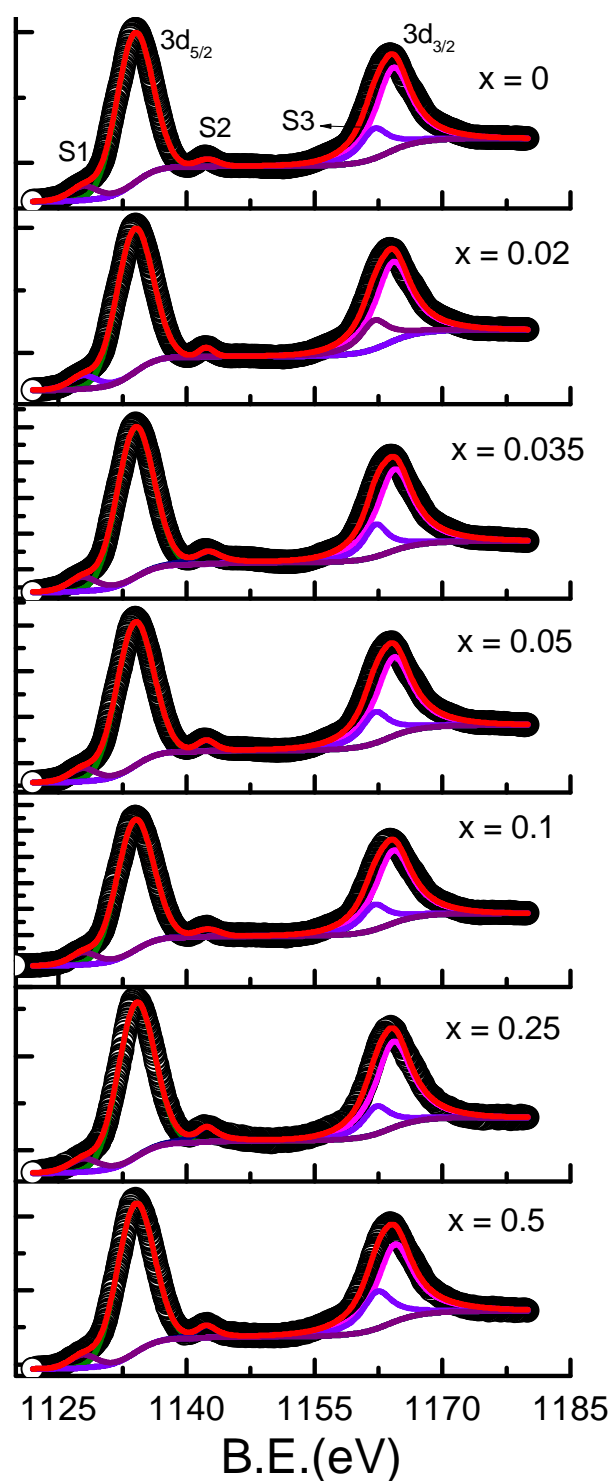


Figure 5.1: 3d core level spectra of Europium. The spectra consist of the standard $3d_{3/2}$ and $3d_{5/2}$ peaks along with three satellite peaks denoted by S1, S2, and S3.

5.2 Ir core level spectra

The photoemission spectra of a large variety of Ir oxides exhibit a distinct asymmetric shape, with satellite peaks associated with the core lines appearing at higher binding energies. In the previous studies, these satellites were often attributed to presence of higher oxidation states of Ir [69]. However, a recent HAXPES study carried out by Kahk et al. [111] et.al on Iridium oxide (IrO_2), reinvestigated this issue and showed that the presence of peaks at higher binding energy do not originate from higher oxidation states. They ascribed these peaks to the final state effect, which we will discuss after showing our results and pointing out the similarities and differences between our data and XPS or HAXPES data published previously for various iridium based oxides.

Fig. 5.2 shows Ir 4f core-level photoelectron spectra for various samples in the series. The spin-orbit coupling results in two peaks corresponding to $4f_{5/2}$ and $4f_{7/2}$. Two satellite peaks neighboring the two 4f spin-orbit split peaks were also present. Altogether, we found that a complete de-convolution of the Ir photoelectron spectra requires five different peaks including an additional satellite peak (S1) at relatively higher binding energy. Appropriate constraints corresponding to FWHM and area ratio were imposed while fitting the spin-orbit split $4f_{5/2}$ and $4f_{7/2}$ peaks. The obtained binding energies across the series for the twin Ir $4f_{5/2}$ peaks were observed in the range 65.6 - 65.8 eV (peak 1) and 64.7 - 64.5 eV (peak 2) whereas the Ir $4f_{7/2}$ peaks ranged as 62.9 - 63 eV (peak 1) and 61.8 - 61.6 eV (peak 2) for all the compositions. The additional satellite peak was observed in the range 67 - 67.4 eV for all the compositions. A plausible explanation for the strong satellite associated with core $4f_{5/2}$ and $4f_{7/2}$ peaks is discussed in the next paragraph after discussing the variation in relative intensity of the peaks upon going from insulating to metallic samples with increasing x .

As shown in Fig. 5.2, we observed a distinct change in the relative intensity of the peaks when traversing from region I ($0 \leq x \leq 0.035$) to region II ($0.05 \leq x \leq 0.1$) to region III ($0.1 < x \leq 1$). The core level spectra remained unchanged for the insulating samples from $x = 0$ to $x = 0.035$, after which it shows a distinct change in the relative intensity of the core level peaks. This however is not accompanied by any measurable shift in the peak position. In the core level spectra for $x \geq 0.1$ (i.e. for the highly metallic samples), the peak shape becomes increasingly asymmetric and the inclusion of additional peaks becomes necessary to achieve a satisfactory fit. In addition to this,

the peaks at lower binding energy in the spin orbit doublet are broad and less intense up to $x = 0.035$. This is not the case for metallic, ($x \geq 0.1$) samples where the core level peaks at the lower binding energy dominates the spectra. The HAXPES data of our $\text{Bi}_2\text{Ir}_2\text{O}_7$ agrees well with that reported previously [97, 112], which rules out any extrinsic origin for these additional satellite peaks that are observed only for the metallic samples.

This shift in the relative intensity is similar to that observed in the study of insulating and metallic ruthenate pyrochlores [113]. When the photoelectron leaves the core level, the core level gets ionized and creates an electrostatic perturbation at the ionized center. If the core-valence Coulomb interaction is greater than the width of the one-electron conduction band, the ionized core will disengage one of the valence orbitals of the ionized atom from the conduction band [114, 115]. The resulting localized atomic state lies below the Fermi energy, and can trap the photoionised electron. Thus, photoelectrons with two different energies are detected, depending on whether the photoelectron was trapped (screened) or not (unscreened) in the localised energy state. This is also in agreement with a comprehensive DMFT study [11] on various ruthenates with varying degree of electronic correlations, where it was shown that the PE spectra exhibits a two peak structure corresponding to the “screened” and “unscreened” components. Further, it was shown that the screened peak disappears in the Mott insulating state, but progressively develops as the band width increases and sample turns metallic.

Similar changes in our Ir 4f core signals suggest for progressive conduction-band widening as the Bi doping concentration increases. In summary, our results find an excellent match with previous XPS studies on pyrochlore iridates [112, 116, 117] and show that throughout the series Iridium retains its +4 oxidation state. The complexity in the measured spectra arises due to “screened” and “unscreened” components rather than to the presence of different oxidation state of Ir.

5.3 Bi core level spectra

We probed the Bi 4f core level to gain knowledge about its valence state. Bi can take valence states ranging from -3 to +5 [118]. The spectra are plotted in Fig. 5.3. The spectra showed very interesting changes with increasing Bi concentration. For all the compositions, the spectra could be deconvoluted using four peaks corresponding to two

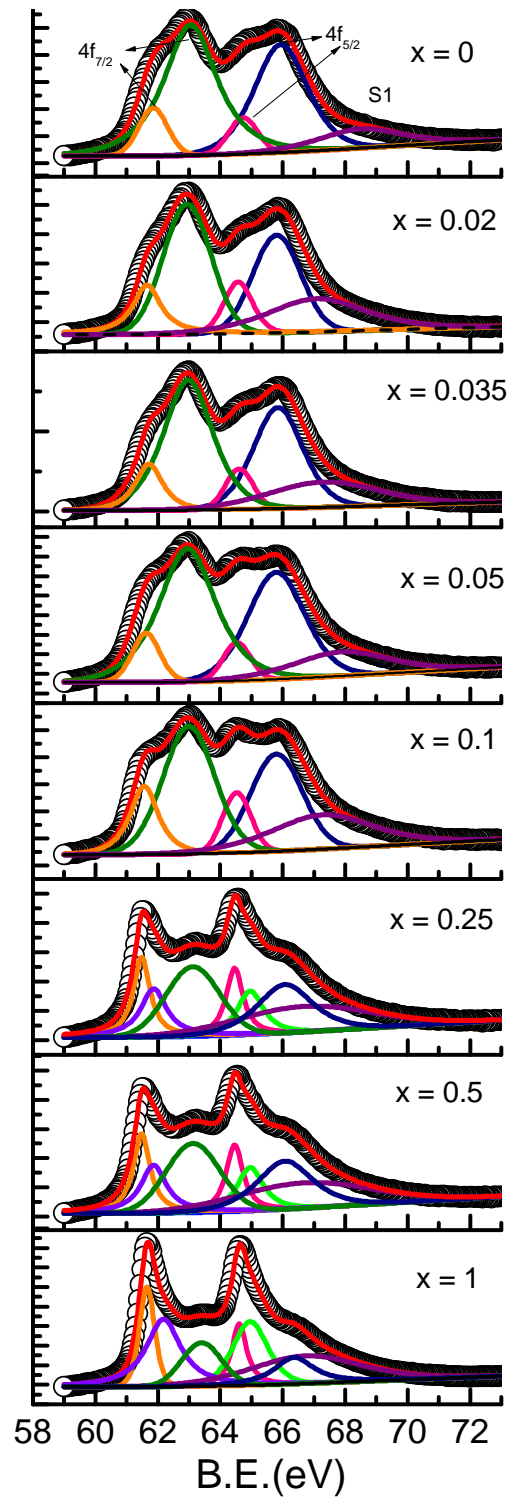


Figure 5.2: 4f core level spectra of Iridium.

$\text{Eu}_{2-2x}\text{Bi}_{2x}\text{Ir}_2\text{O}_7$	$4f_{5/2}(\text{I})$	$4f_{5/2}(\text{II})$	$4f_{7/2}(\text{I})$	$4f_{7/2}(\text{II})$	S(I)	S(II)	S(III)
$x = 0$	65.8	64.6	63	61.8	67.3	-	-
$x = 0.02$	65.8	64.6	62.9	61.6	67.1	-	-
$x = 0.035$	65.8	64.6	63	61.7	67.3	-	-
$x = 0.05$	65.8	64.5	63	61.6	67.3	-	-
$x = 0.1$	65.8	64.5	63	61.6	67.3	-	-
$x = 0.25$	66.1	64.6	63.3	61.6	67.3	65.1	62
$x = 0.5$	66.1	64.5	63.1	61.5	66.7	65	61.9
$x = 1$	66.4	64.6	63.4	61.7	66.7	65	62.2

Table 5.2: Ir 4f core level peaks for all the measured compositions in the series $\text{Eu}_{2-2x}\text{Bi}_{2x}\text{Ir}_2\text{O}_7$. In addition to the core shell lines corresponding to $4f_{5/2}(\text{I/II})$ and $4f_{7/2}(\text{I,II})$, there are additional satellite peaks named as S1, S2, and S3. S2 and S3 peaks were required during the fitting of samples deep in the metallic regime i.e. $x \geq 0.25$ and could be a result of final state effect.

peaks each for the spin-orbit split 4f levels $4f_{5/2}$ and $4f_{7/2}$, similar to the reports of other Bi based pyrochlore iridates. The two peaks are not observed for very insulating samples like Bi_2O_3 , but is a typical feature of conducting samples where Bi hybridisation plays a role [97, 112, 113]. The peak position remained unchanged within the energy resolution throughout the series and matched well with the reports for Bi^{3+} [119]. However, the relative peaks intensity and peak shape changed dramatically on going from the insulating compositions to the metallic ones.

For the insulating composition with $x = 0.02$ and 0.035 , the peak shape is rather symmetric and the intensity of peaks at lower binding energy (designated by $4f_{5/2}(\text{I})$ and $4f_{7/2}(\text{I})$) is small compared to the higher binding energy peaks (designated by $4f_{5/2}(\text{II})$ and $4f_{7/2}(\text{II})$). On the other hand, the peak shape becomes asymmetric and the intensity of peaks at lower binding energy increases significantly upon entering the metallic regime for $x \geq 0.05$, and at the same time the intensity of $4f_{5/2}(\text{II})$ and $4f_{7/2}(\text{II})$ decreases.

Apart from the standard Bi $4f_{5/2}$ and $4f_{7/2}$ peaks, we also observed an additional peak at around 166.3 eV. As this peak is also observed for EIO (not shown here) which does not contain any Bi, we ascribe this feature to some extrinsic contribution. This is further supported by the fact that the intensity of this extra peak is relatively high compared to the Bi 4f spectra for compositions with small Bi doping; for higher Bi-doped samples with higher intensity of the 4f core level peaks, the relative intensity of

$\text{Eu}_{2-2x}\text{Bi}_{2x}\text{Ir}_2\text{O}_7$	$4f_{5/2}(\text{I})$	$4f_{5/2}(\text{II})$	$4f_{7/2}(\text{I})$	$4f_{7/2}(\text{II})$	E
$x = 0.02$	164.5	163.4	159.2	158.4	166.3
$x = 0.035$	164.6	163.4	159.3	158.1	166.3
$x = 0.05$	164.3	163.6	159.2	158.3	166.3
$x = 0.1$	164.2	163.5	159.1	158.2	166.3
$x = 0.25$	164.1	163.5	159.1	158.2	166.3
$x = 0.5$	164.2	163.5	159	158.2	166.3
$x = 1$	164.2	163.5	159.1	158.2	166.3

Table 5.3: Bi 4f core level peaks for all the measured compositions in the series $\text{Eu}_{2-2x}\text{Bi}_{2x}\text{Ir}_2\text{O}_7$. E represents the extraneous feature in the spectra which was held fixed at a given value while fitting the spectra for all the compositions.

the extraneous peak diminishes implying its extraneous origin. The peak position was kept fixed while fitting the spectra for all the compositions.

5.4 Valence Band Spectra

We measured the valence band spectra (VBS) of the samples to gain insight about the metal-to-insulator transition with Bi substitution in EIO. VBS represents all the contributing bands near the Fermi level (E_F) marked by 0 eV in the spectra. The Fermi energy of the spectrometer or the $E_F = 0$ is calibrated by measuring VBS for a standard, which in this case was gold metal foil. The VBS, each plot normalised by dividing the intensity with total area under the curve, is shown in Fig. 5.4(a). VBS spectra were normalized in order to plot them on the same scale for understanding relative changes in various parts of the spectra. Elemental attribution of various features of the spectra was done using two ways: i) Comparing the spectra with the reported data collected at similar energy [111]. ii) Comparing the difference between the spectrum of extreme compositions, for example, $\text{Eu}_2\text{Ir}_2\text{O}_7$ and $\text{Bi}_2\text{Ir}_2\text{O}_7$. The region 0 - 9 eV represents peaks from Ir 5d orbitals which agrees well with the literature [112]. We do not expect any contribution from O (2p) in the measured VBS due to its small photoionization cross-section at 5 keV incident radiation. We also observed contribution from Bi $6s^2$ at ~ 11 eV which is also reported for Bi_2O_3 . The Bi $6s^2$ peak is first detected for $x = 0.05$ and is a prominent feature in the VBS of higher Bi doping concentrations.

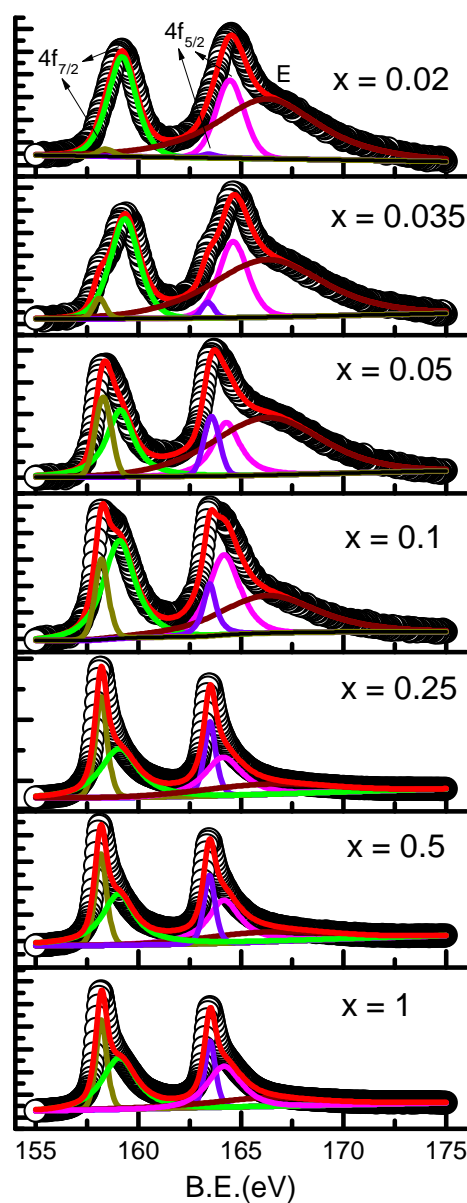


Figure 5.3: 4f core level spectra of Bismuth.

The VBS peaks contributed from Ir 5d shows considerable changes and reconstruction with increasing Bi concentration that suggests possible hybridization between the Ir 5d and Bi 6p bands. On the other hand, the Bi 6s peak only grows in terms of intensity but does not change shape or position across the series. As the Bi 6s peak is located 11 eV away from the Fermi energy and absence of any modification in the peak position indicates that Bi 6s do not hybridize with Ir 5d peaks. This hypothesis also finds a match

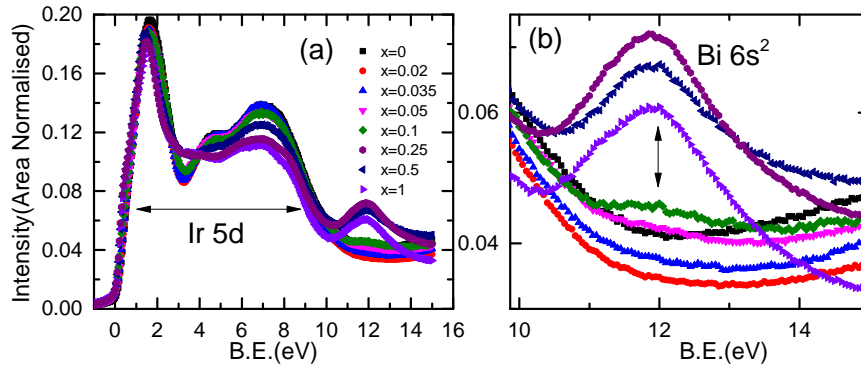


Figure 5.4: (a) Valence band spectra of different compositions in the series $(\text{Eu}_{1-x}\text{Bi}_x)_2\text{Ir}_2\text{O}_7$, (b) The region around 12 eV depicting $\text{Bi } 6s^2$ spectra.

with earlier photoemission and first principle study on Bi-based pyrochlore ruthenate ($\text{Bi}_2\text{Ru}_2\text{O}_7$) [120]. Hence, the Ir 5d hybridization must be with empty Bi p orbitals that are predicted [120] to be positioned near the Fermi energy. A closer look near the Fermi energy (Fig. 5.5(a)) indicates that the spectral weight gradually increases at the Fermi energy with increasing Bi doping, in agreement with the observation that with increasing Bi concentration the electrical conductivity increases i.e., the samples become more and more conducting. Also a shoulder peak appears near the Fermi energy (Fig. 5.5(b)) for $x \geq 0.1$, which also is the Bi concentration value beyond which lattice parameters increases.

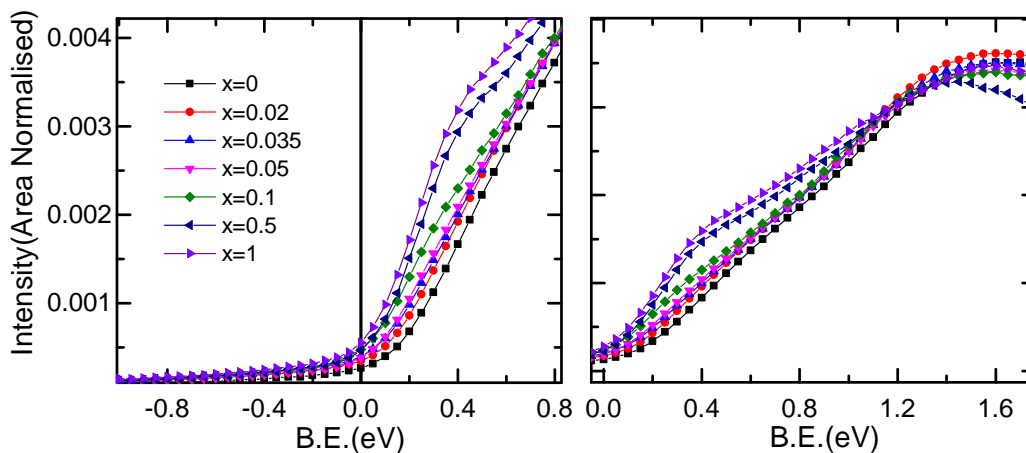


Figure 5.5: (a) Valence band spectra showing the increasing spectral weight near E_F with Bi doping. (b) Formation of new shoulder peak near E_F for $x \geq 0.1$.

5.5 Discussion

From the results presented above, we can see that the peak positions in the core level spectra for all the cations does not vary within the energy resolution of the spectrometer. This shows that all the cation retains their ideal valence state and importantly, the anomalous lattice contraction for $x \leq 0.035$ in the series $(\text{Eu}_{1-x}\text{Bi}_x)_2\text{Ir}_2\text{O}_7$ is not a result of varying oxidation state of any cation. However, the relative peak intensity and the peak shape vary considerably for the core level spectra of both Ir and Bi.

Going from insulating compositions for $0 \leq x \leq 0.035$ to metallic compositions for $x \geq 0.05$, the core level spectra for Ir and Bi shows pronounced asymmetry. Now, the core photoelectron spectra of simple metals are known to display characteristic asymmetry due to electron-hole excitation in the final state [113, 121]. Further, for metallic compounds, it has been shown that the asymmetry of the core peak of a constituting element is proportional to the square of the partial density of states at the Fermi energy provided by the valence orbitals of that element [122]. Thus the asymmetries of the Bi 4f and Ir 4f core signals provide direct evidence of an increasing partial density of states from these two elements at the Fermi energy. In addition to this, the appearance of Bi 6s peak without any shape or peak position change in the valence band spectra further support our conjecture that metallicity in compositions above $x \geq 0.05$ is driven by Bi 6p / Ir 5d orbitals.

5.6 Summary

With the help of HAXPES studies we confirmed that all the cations retain their nominal oxidation state throughout the series. This adds to our hypothesis that the lattice contraction in the series $(\text{Eu}_{1-x}\text{Bi}_x)_2\text{Ir}_2\text{O}_7$ did not result from any change in the oxidation state of any cation. With the help of VBS and the increasing asymmetry of the core level spectra of Ir and Bi, we showed that the Bi 6p - Ir 5d hybridisation drives the metal-insulator transition. The unaltered Bi 6s peak also indicates that Bi 6s level does not contribute to the Fermi level in agreement with previous report [123].

Chapter 6

Effect of Bi substitution in some other members of the pyrochlore iridate series

In the previous chapter, we presented the effect of Bi substitution on the structure and physical properties of $\text{Eu}_2\text{Ir}_2\text{O}_7$ (EIO). We showed that dilute Bi substitution in EIO results in an anomalous lattice contraction which is also reflected in the variation of various physical properties across the anomalous region. Thus, it is of great interest to examine the effect of Bi substitution in some other members of the pyrochlore series.

In this chapter, we study the effect of Bi substitution on the structure and physical properties of insulating and semi-metallic members of the $\text{A}_2\text{Ir}_2\text{O}_7$ series, namely, $\text{A} = \text{Sm}, \text{Gd}, \text{Dy}$ where Sm and Gd samples exhibit a metal-to-insulator transition analogous to EIO, and $\text{Dy}_2\text{Ir}_2\text{O}_7$ is insulating over the whole temperature range. Bi substitution in the pyrochlore iridates generates two effects: i) steric effect due to difference between the lattice parameter of $\text{A}_2\text{Ir}_2\text{O}_7$ and $\text{Bi}_2\text{Ir}_2\text{O}_7$; ii) electronic effect, due to changes in the electronic structure arising from an overlap between Bi 6p and Ir 5d orbitals. Thus, in the pyrochlore iridate series, we expect the electronic effect to be overwhelming in those cases where the difference between the lattice parameters of the end members is small (as, for example, in $\text{A} = \text{Sm}$), and the steric effect to dominate in those cases where this difference is large (as, for example, in $\text{A} = \text{Dy}$). Here, we attempt to get a general understanding of the effect of Bi substitution in these two extreme cases, and correlate

it with our findings on the Weyl candidate EIO reported in the previous chapters.

6.1 Synthesis and structural characterization

All the samples in the series $(A_{1-x}Bi_x)_2Ir_2O_7$ ($A = Sm, Gd, \text{ and } Dy$) were synthesized using the same procedure as detailed in chapter four. Any deviation from the earlier protocol is clearly pointed out where necessary. Amongst the three series, the $(Sm_{1-x}Bi_x)_2Ir_2O_7$ (Sm-Bi) series was characterized in more details and it will be presented first. This will be followed by a report on the effect of Bi substitution on the structure and physical properties of $(Gd/Dy_{1-x}Bi_x)_2Ir_2O_7$ series of compounds.

6.1.1 Lattice parameter variation in $(Sm_{1-x}Bi_x)_2Ir_2O_7$

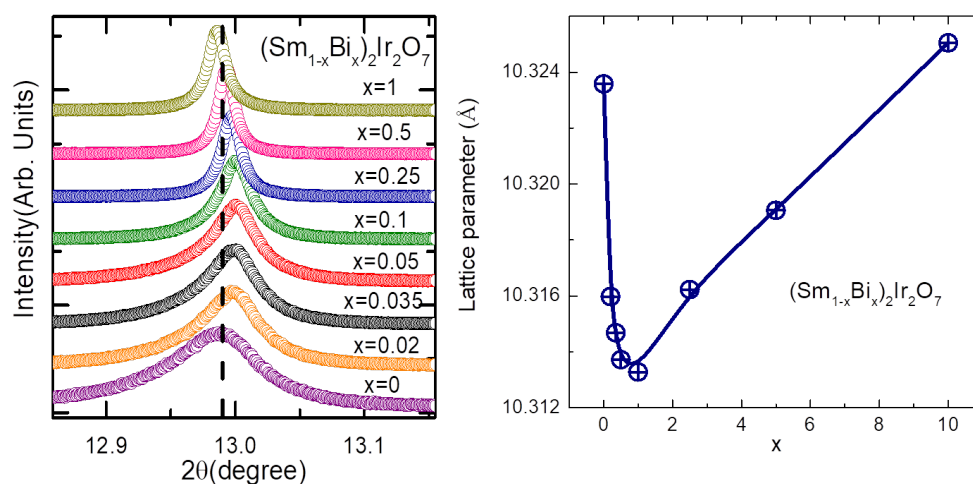


Figure 6.1: (a) Evolution of [444] powder x-ray diffraction peak (b) Lattice parameter evolution across the series $Sm_{1-x}Bi_x)_2Ir_2O_7$.

For the $(Sm_{1-x}Bi_x)_2Ir_2O_7$ series, eight compositions were synthesized with $x = 0, 0.02, 0.035, 0.05, 0.1, 0.25, 0.5$ and 0.75 . The samples were synthesized in air via solid-state reaction route using the precursors Sm_2O_3 (Alfa aesar, 99.9 %), Bi_2O_3 (Sigma Aldrich, 99.9 %) and IrO_2 (Sigma Aldrich, 99.9 %). The sintering procedure is similar to that described in chapter 4. The phase formation during the sintering process was monitored using a Bruker D8 Advance powder X-ray diffractometer. The lattice parameters of the end members of this series are very closely matched. The lattice constant of $Sm_2Ir_2O_7$ is 10.3235 \AA whereas for $Bi_2Ir_2O_7$ it is 10.3250 \AA . Hence, the evolution of lattice parameter in their solid-solution requires careful probing using

high-resolution synchrotron x-ray diffraction to accurately determine the lattice constant for the intermediate composition. Thus, we examined the compositions $x = 0, 0.02, 0.035, 0.05, 0.1, 0.25, 0.5,$ and 1 at 11-BM beamline at the Argonne National Laboratory using the mail-in rapid access facility.

The data collection was performed at a fixed energy of ~ 30 keV. The 11-BM beamline couples an efficient sagittal x-ray beam with a high precision diffractometer circle and perfect Si(111) crystal analyser detection to achieve high sensitivity and resolution. Instrumental resolution at high Q is better than $\Delta Q/Q \approx 2 \times 10^{-4}$, with a typical 2θ resolution of $< 0.01^\circ$ at 30 keV. The transmission measurements were performed with the rotating capillary stage to eliminate the preferred orientation if any. The samples were filled in 0.8 mm diameter Kapton tube. To reduce the sample absorption, the samples were diluted with amorphous silica powder. Further, crushed crystalline Si was added to each sample for greater accountability of the refined lattice constants. All the refined parameters are listed in table 6.1

Fig 6.1(a) shows the evolution of the peak [444] for different compositions. It can be clearly seen from Fig 6.1 that the peaks for all the intermediate compositions are right-shifted compared to the end members of the series. A mixed-phase refinement was carried out for all the samples using the Fullprof suite. The lattice constants were extracted from the Rietveld refinement and are plotted in Fig. 6.1(b). The representative refinement plots are shown in Fig. 6.2. The lattice constant decreases up to $x = 0.1$ and starts recovering for higher doping concentrations. As the electronic effect is expected to prevail in the $(\text{Sm}_{1-x}\text{Bi}_x)_2\text{Ir}_2\text{O}_7$ series, it is seen that the lattice constants for all the intermediate samples are smaller than the end members. The quantity δ (defined earlier for EIO as $\delta(x) = (a - a_0)/(a_1 - a_0)$; where a_0 and a_1 are the lattice parameters of EIO and BIO respectively) for SIO is a gigantic -658% compared to just -21% in the case of EIO. These results further cement our conjecture that the lattice contraction upon Bi substitution in the pyrochlore iridates is of electronic origin.

6.1.2 Lattice parameter variation in $(\text{Gd/Dy}_{1-x}\text{Bi}_x)_2\text{Ir}_2\text{O}_7$

We synthesized compositions with A = Gd and Dy for $x = 0, 0.02, 0.035, 0.05, 0.1, 0.25$ and $x = 0, 0.02, 0.035, 0.05, 0.1, 0.25, 0.5,$ respectively. The precursors for Dy-Bi series were Dy_2O_3 (Alfa aesar, 99.9 %), Bi_2O_3 (Sigma Aldrich, 99.9 %) and IrO_2 (Sigma Aldrich, 99.9 %). For the Gd-Bi series, the precursors used were Gd_2O_3 (Sigma Aldrich,

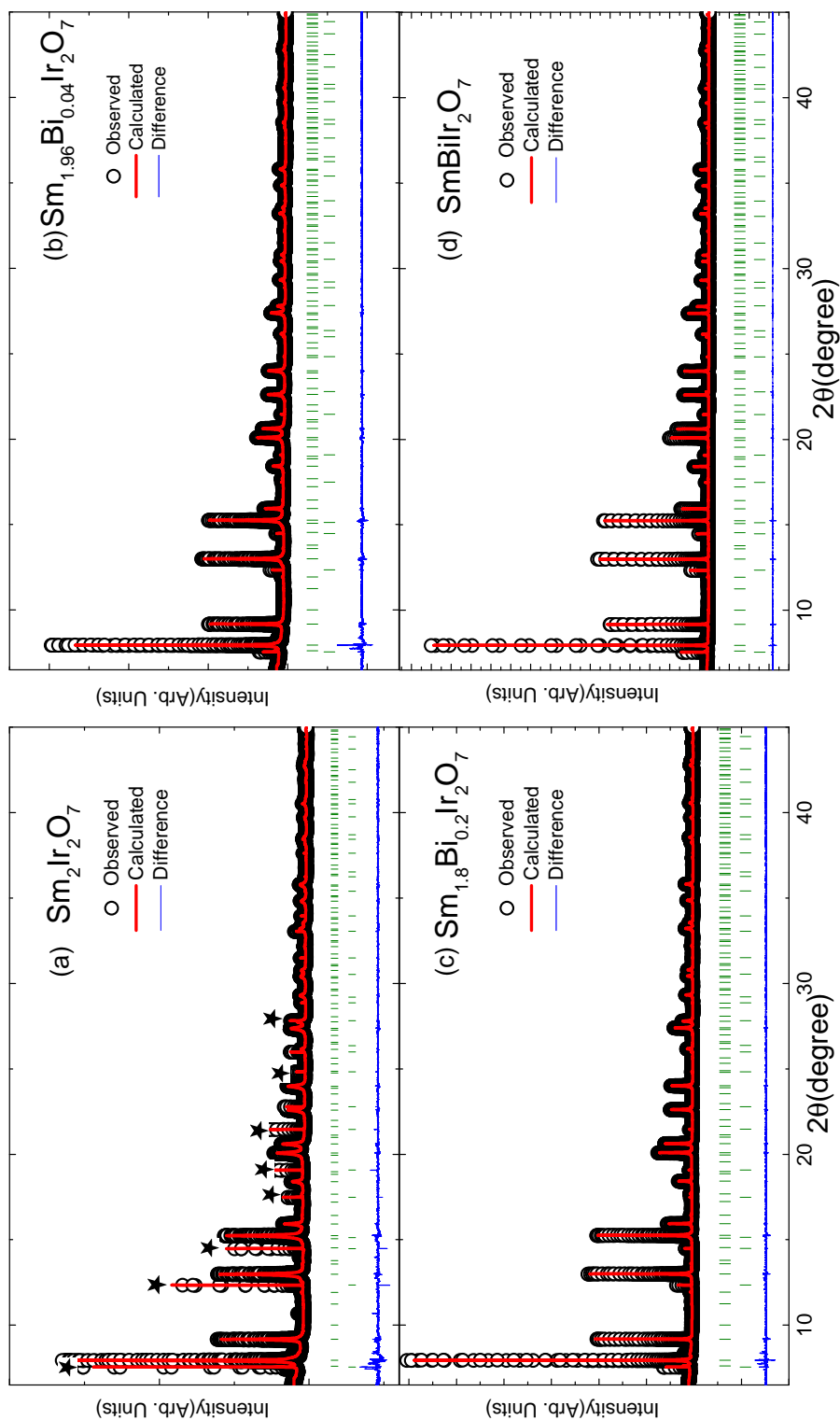


Figure 6.2: Refinement plots for $x = 0, 0.02, 0.1$ and 0.5 in $(\text{Sm}_{1-x}\text{Bi}_x)_2\text{Ir}_2\text{O}_7$. A mixed phase refinement was carried out for all the samples with the main pyrochlore phase and Si; Panel (a) highlights all the prominent Si peaks with the star sign.

Table 6.1: Goodness of fit parameters for different values of x in $(\text{Sm}_{1-x}\text{Bi}_x)_2\text{Ir}_2\text{O}_7$ samples, obtained using Rietveld refinement of the high-resolution synchrotron powder X-ray diffraction data.

$\text{Sm}_{2-2x}\text{Bi}_x\text{Ir}_2\text{O}_7$	χ^2	Rp	Rwp	Lattice parameter	O(48f) parameter
$x = 0$	1.68	5.92	8.37	10.3235	0.337
$x = 0.02$	2.35	6.24	8.82	10.3145	0.333
$x = 0.035$	5.47	9.16	15.1	10.3144	0.325
$x = 0.05$	6.76	10.1	16.1	10.3130	0.324
$x = 0.1$	2.64	6.57	9.6	10.3113	0.333
$x = 0.25$	2.16	5.5	8.06	10.3145	0.333
$x = 0.5$	1.71	4.87	6.99	10.3177	0.332
$x = 1$	1.28	4.71	6.18	10.3232	0.329

Table 6.2: Goodness of fit parameters for different values of x in $(\text{Gd}_{1-x}\text{Bi}_x)_2\text{Ir}_2\text{O}_7$ samples, obtained using Rietveld refinement of the high-resolution synchrotron powder x-ray diffraction data in the case of Gd. The last column represents lattice parameters extracted using unit cell from the lab based x-ray data in the case of $(\text{Dy}_{1-x}\text{Bi}_x)_2\text{Ir}_2\text{O}_7$.

$\text{Gd}_{2-2x}\text{Bi}_{2x}\text{Ir}_2\text{O}_7$	Rp	Rwp	Lattice parameter	O(48f)	$\text{Dy}_{2-2x}\text{Bi}_{2x}\text{Ir}_2\text{O}_7$ a(\AA)
$x = 0$	11.9	17.6	10.2860	0.3296	10.2101
$x = 0.02$	13	17.9	10.2730	0.3324	10.2014
$x = 0.035$	10.9	13.4	10.2710	0.3314	10.2010
$x = 0.05$	12.5	17.5	10.2705	0.3310	10.2020
$x = 0.1$	11.3	15.4	10.2722	0.3354	10.2095
$x = 0.25$	19.1	18.2	10.2870	0.3327	10.2285
$x = 0.5$	-	-	-	-	10.2580

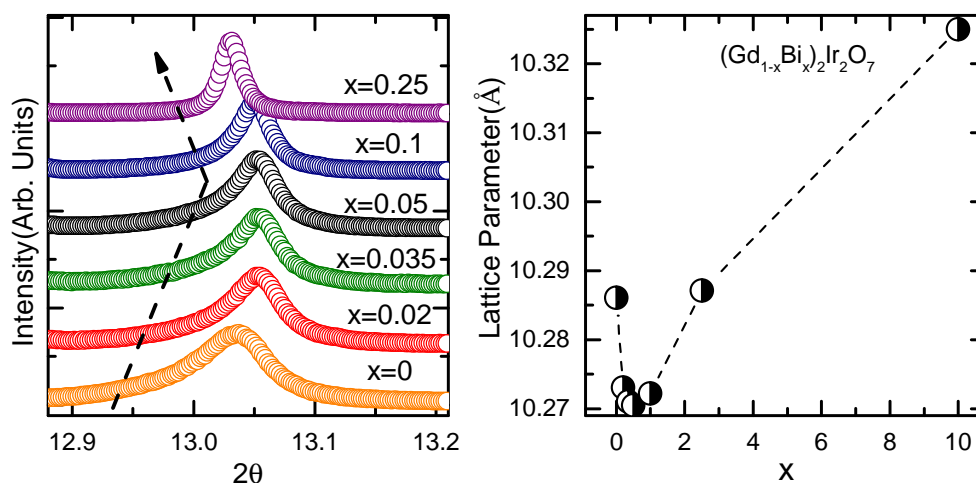


Figure 6.3: (a) Peak evolution across the $(\text{Gd}_{1-x}\text{Bi}_x)_2\text{Ir}_2\text{O}_7$ series (data collected from Argonne National Laboratory) (b) Lattice parameter evolution across the series.

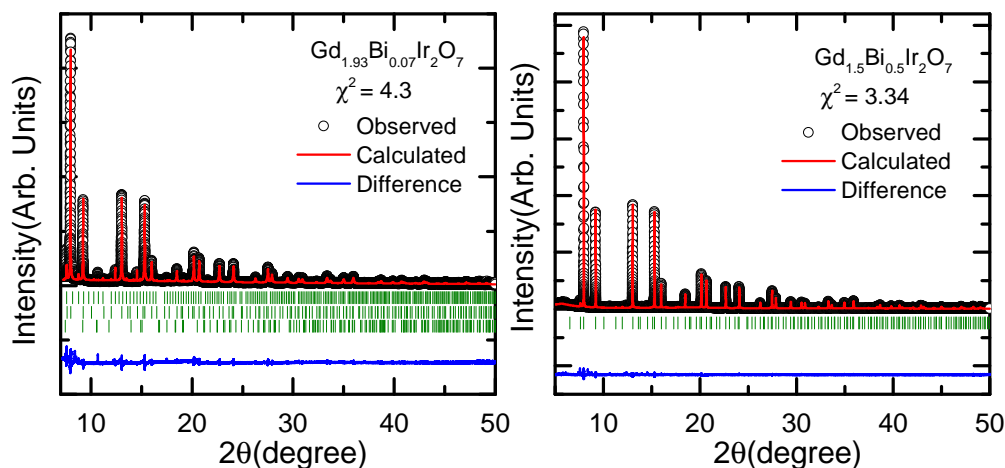


Figure 6.4: Representative refinement plot for $x = 0.035$ and 0.25 . For the compositions in the range $x \leq 0.1$, mixed phase refinement consisting the pyrochlore phase and the precursor phases were carried out. For $x = 0.25$, single phase refinement was carried out.

99.9 %) and Bi_2O_3 (Sigma Aldrich, 99.9 %) and IrO_2 (Alfa aesar, 99.9 %). Similar synthesis protocol as used for the Eu-Bi series was also followed for the synthesis of $(\text{Gd}/\text{Dy}_{1-x}\text{Bi}_x)_2\text{Ir}_2\text{O}_7$ compounds. The phase formation during the sintering process was monitored using a Bruker D8 Advance powder X-ray diffractometer. Ir metal peaks were observed for the Gd-Bi series, which was unusual given the initial moderate sintering temperatures. The x-ray scan of the IrO_2 (Alfa aesar, 99.9 %) precursor revealed the presence of Ir-peaks; hence for all other compositions, IrO_2 procured from Sigma

Aldrich was used. It was found that the IrO_2 obtained from Alfa aesar contained a high proportion of Ir-metal powder. As the precursor weight was calculated assuming the composition to be IrO_2 , the compositions in the Gd-Bi series have excess Iridium. During the sintering process, though most of Ir metal powder did get oxidised to form IrO_2 , small peaks due to traces of residual Ir-metal and IrO_2 were still observed, due to the excess Ir precursors. Additional sintering at higher temperatures $\sim 1080^\circ\text{C}$ were done for the Gd-Bi series to get rid of the excess Ir content. No precursor peaks were observed for $(\text{Gd}_{0.75}\text{Bi}_{0.25})_2\text{Ir}_2\text{O}_7$, where pre-oxidised Ir-metal powder was used.

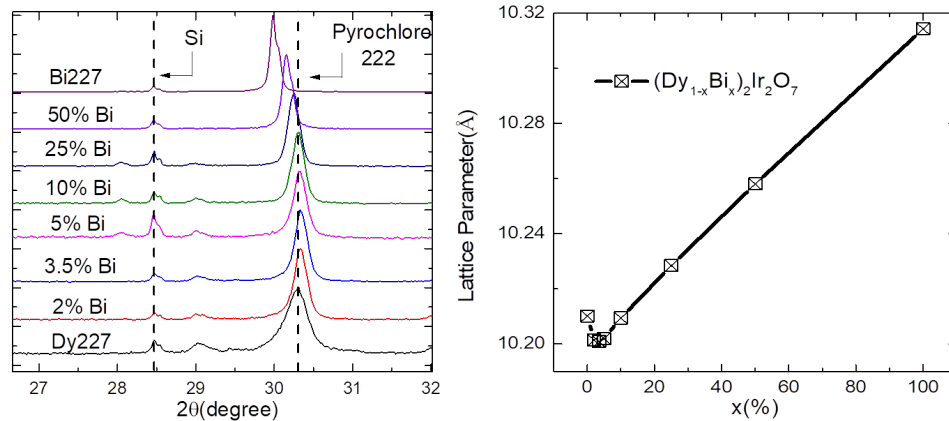


Figure 6.5: (a) Peak evolution across the $(\text{Dy}_{1-x}\text{Bi}_x)_2\text{Ir}_2\text{O}_7$ series (b) Evolution of lattice parameters extracted from unit cell.

X-ray diffraction experiments were carried out for the Gd-Bi series using the mail-in service at Argonne National Laboratory, as described earlier. The lattice parameters were obtained using the Rietveld refinement. The trend in the peak position and evolution of the lattice parameters is shown in Fig. 6.3. Representative Rietveld scans are shown in Fig. 6.4. For the $(\text{Dy}_{1-x}\text{Bi}_x)_2\text{Ir}_2\text{O}_7$ series, x-ray diffraction scans were done using the lab-based x-ray source with Si added as an internal standard, and the lattice parameters were extracted using the UNITCELL program. The peak position trend across the series and the lattice parameter evolution are shown in Fig. 6.5. Both the $(\text{Gd}_{1-x}\text{Bi}_x)_2\text{Ir}_2\text{O}_7$ and $(\text{Dy}_{1-x}\text{Bi}_x)_2\text{Ir}_2\text{O}_7$ show anomalous lattice contraction up to $x = 0.05$.

6.2 Physical properties

Next, we discuss the physical properties of these compositions. We study the changes in their electrical transport, magnetic susceptibility, and thermopower as a function of temperature and magnetic field across the whole series. Sm is a neighbour of Eu, and both these neighboring compounds share the AIAO ground state of the Ir-sublattice and have closely spaced (within ± 3 K of each other) transition temperatures. Hence while presenting the results for $\text{Sm}_{2-2x}\text{Bi}_{2x}\text{Ir}_2\text{O}_7$, we will often recall the analogous results for the $\text{Eu}_{2-2x}\text{Bi}_{2x}\text{Ir}_2\text{O}_7$ series.

6.2.1 Physical properties of the series $(\text{Sm}_{1-x}\text{Bi}_x)_2\text{Ir}_2\text{O}_7$

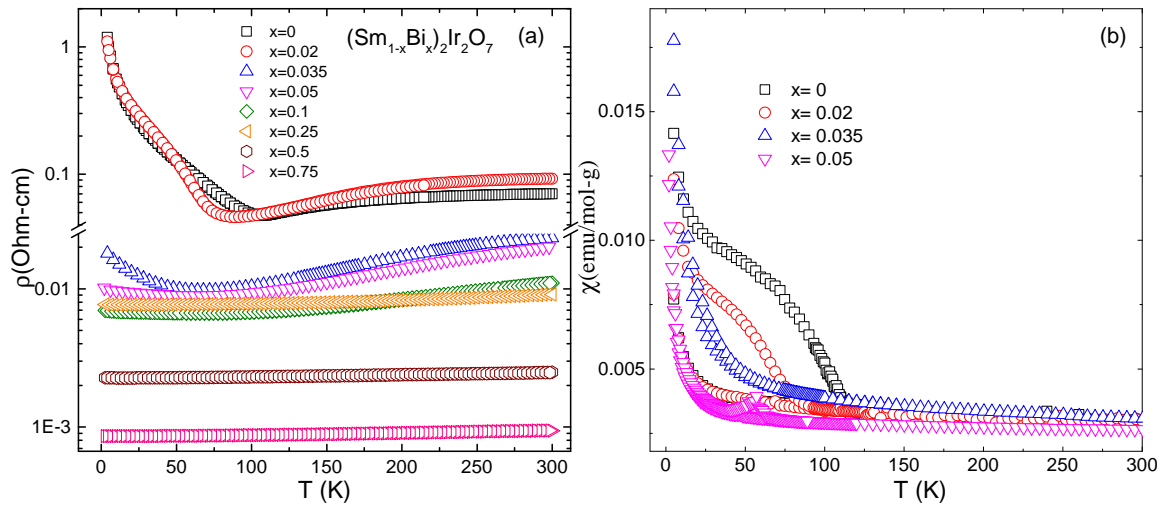


Figure 6.6: (a) The temperature variation of absolute resistivity for various x . The resistivity shows a sudden decrease in the magnitude for $x = 0.035$ which is apparent from the scaling on the y-axis. (b) The susceptibility (χ) for $x \leq 0.1$ is shown as a function of temperature. Thermomagnetic hysteresis is seen only for $x = 0, 0.02$ and 0.035 sample; the upper (lower) branch represents FC (ZFC) data. The kink in the $x = 0.05$ data around 50 K corresponds to the ordering of trapped oxygen.

$\text{Sm}_2\text{Ir}_2\text{O}_7$ (SIO), similar to EIO, shows a metal-to-insulator transition concomitant with AIAO antiferromagnetic ordering around 114 K which is in close agreement with the literature [47]. For Bi doping concentration of $x = 0.02$, the transition temperature decreases to nearly 90 K, which is a rather steep decrease compared to the change in the transition temperature in EIO for a similar doping concentration. For $x = 0.035$, the transition temperature drops further to $\sim 60\text{K}$; and for the compositions with higher

Bi-doping a metallic behaviour with weak upturn is observed down to the lowest measurement temperature of 2 K in our experiments (Fig. 6.6a).

The magnetic susceptibility data (Fig. 6.6b) echoes the transport behaviour. The bifurcation temperature in the field-cooled and zero-field-cooled data, which marks the onset of magnetic transition, coincides with the metal-insulator transition temperature obtained from the transport measurements. The susceptibility in the paramagnetic region could not be modelled using simple Curie-Weiss law. Such absence of Curie-Weiss behaviour is a common feature in trivalent Sm compounds which arises due to the multiplet-level structure of Sm^{3+} [44]. The susceptibility of SIO was observed to 3×10^{-3} emu/mol (1.5×10^{-3} emu/Sm) which is in reasonably good agreement with the free ion value of Sm^{3+} at 300 K (1.01×10^{-3} emu/mol) [124], given that Ir^{4+} itinerant moments also contribute in SIO.

A closer look at the low-temperature transport data reveals that both the insulating compositions, SIO and $x = 0.02$ show a $1/T^n$ dependence. For a Weyl semimetal, n is predicted to be unity by Hosur et. al. [106]. However, n turned out to be less than unity for SIO ($n = 0.8$) and further decreases for $x = 0.02$ ($n = 0.7$). In the case of EIO, dilute Bi substitution drove n to unity from $n < 1$, closer to the Weyl band crossing. Thus, upon Bi substitution in SIO, seems to take the system farther away from the Weyl band crossing.

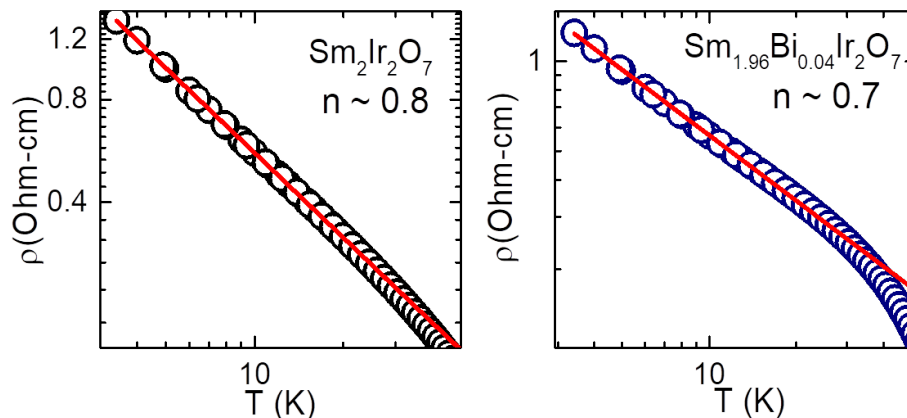


Figure 6.7: Low temperature fitting of ρ for $x = 0$ and 0.02 .

Next we discuss the changes in the thermopower (S). In the previous chapter, we saw that Bi substitution changes the sign of thermopower from positive to negative with increasing Bi doping. S for SIO (Fig. 6.7) is positive throughout the temperature range,

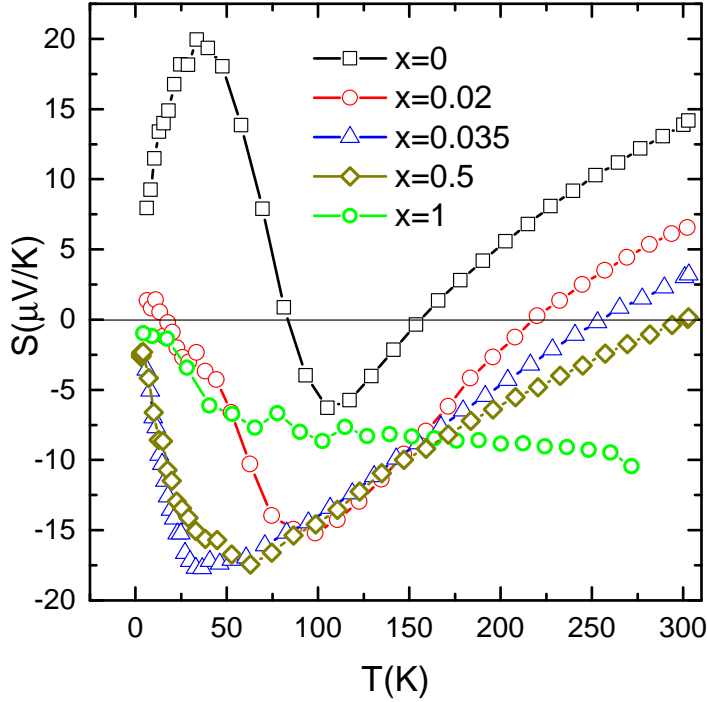


Figure 6.8: Thermopower plotted as a function of temperature for $x = 0, 0.02, 0.035, 0.05$ and 1 .

except in the narrow range $60 \leq T \leq 150$ K, in agreement with the literature [4]. It shows a dip at the metal-insulator transition and increases again as the temperature is lowered. However, this increase is terminated upon further cooling with a peak in S around 30 K, which is possibly due to the phonon drag. Upon further cooling S approaches zero as T goes to 0. For $x = 0.02$, we observe that the temperature range over which the sign turns to negative extends from around 230 K to 20 K with a prominent peak near $T = 80$ K, which coincides with the resistivity anomaly.

For $x = 0.035$, where, still an upturn is observed for the resistivity, the thermopower peak shifts to a lower temperature coinciding with the resistivity upturn. In the metallic region, for $x = 0.05$, the peak shifts to slightly higher temperature. Overall, the qualitative behaviour and the magnitude of S is comparable in all the three compositions, i.e., for $x = 0.02, 0.035$ and 0.05 in spite of the fact that their resistivities differ considerably. This suggests that the thermopower for these compositions does not scale with the electrical conductivity in a usual manner generally seen for the semiconducting samples ($\sigma \propto n$ and $S \propto n^{-2/3}$). A recent study on the thermopower of $\text{Nd}_{2-2x}\text{Ca}_{2x}\text{Ir}_2\text{O}_7$ series showed that such characteristics feature in the thermopower indicate the presence of

degenerate quadratic band touching [125].

6.2.2 Physical properties of the series $(\text{Gd}/\text{Dy}_{1-x}\text{Bi}_x)_2\text{Ir}_2\text{O}_7$

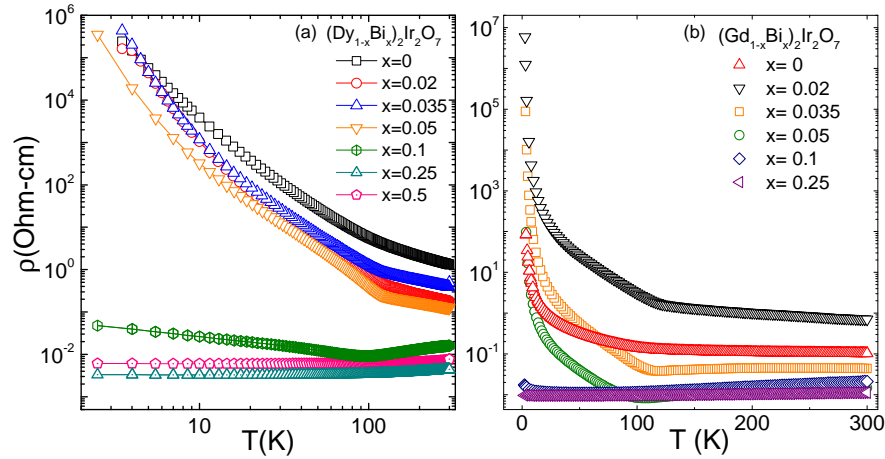


Figure 6.9: Transport plotted as a function of temperature for (a) $(\text{Dy}_{1-x}\text{Bi}_x)_2\text{Ir}_2\text{O}_7$ and (b) $(\text{Gd}_{1-x}\text{Bi}_x)_2\text{Ir}_2\text{O}_7$

The ground state of $\text{Dy}_2\text{Ir}_2\text{O}_7$ (DIO) is insulating, whereas $\text{Gd}_2\text{Ir}_2\text{O}_7$ (GIO) shows a small increase in the slope around 130 K (i.e., an insulator to insulator or a bad metal to insulator transition). ρ vs T for $(\text{Dy}_{1-x}\text{Bi}_x)_2\text{Ir}_2\text{O}_7$ and $(\text{Gd}_{1-x}\text{Bi}_x)_2\text{Ir}_2\text{O}_7$ is plotted in Fig. 6.9. In the range of the lattice expansion, up to $x = 0.05$, the resistivity behaviour continues to be insulating, however, a sharp increase in the slope of resistivity, akin to metal-insulator transition, is observed around 120 K for the Bi substituted compositions. The change in the slope is more stark for the $(\text{Gd}_{1-x}\text{Bi}_x)_2\text{Ir}_2\text{O}_7$ series compared to the $(\text{Dy}_{1-x}\text{Bi}_x)_2\text{Ir}_2\text{O}_7$ series. As the lattice contraction recovers for $x \geq 0.1$ for both the series, the resistivity drops by six to seven orders of magnitude compared to the insulating region for $(\text{Dy}_{1-x}\text{Bi}_x)_2\text{Ir}_2\text{O}_7$. For $(\text{Gd}_{1-x}\text{Bi}_x)_2\text{Ir}_2\text{O}_7$, the resistivity in the same regime drops by two orders of magnitude. The transition temperatures in the two series, however, shows different variations for the two series of solid solutions. For the $(\text{Dy}_{1-x}\text{Bi}_x)_2\text{Ir}_2\text{O}_7$, the transition temperature does not change much upon going from the highly insulating region for $0 \leq x \leq 0.05$ to a more conducting region for $x \geq 0.1$. On the other hand, in the $(\text{Gd}_{1-x}\text{Bi}_x)_2\text{Ir}_2\text{O}_7$ series the transition from insulating region ($x \leq 0.05$) to metallic ($x \geq 0.1$) region is accompanied by a drop in the transition temperature from 108 K ($x = 0.05$) to 50 K ($x = 0.1$).

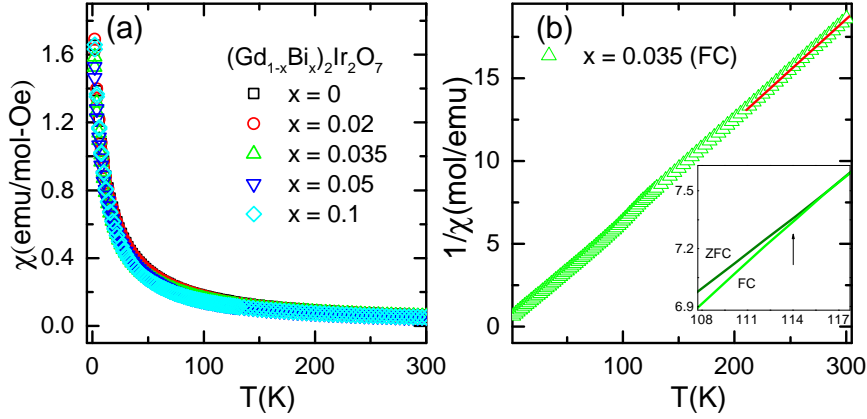


Figure 6.10: (a) χ vs. T plotted for the members of the series $(\text{Gd}_{1-x}\text{Bi}_x)_2\text{Ir}_2\text{O}_7$. (b) $1/\chi$ plotted vs T for $x = 0.035$; the red line shows the Curie-Weiss fit to the data in the range 200 - 300 K. The inset panel shows the bifurcation between ZFC and FC susceptibility marking the transition temperature.

Fig. 6.10 shows the magnetic susceptibility as a function of temperature for $(\text{Gd}_{1-x}\text{Bi}_x)_2\text{Ir}_2\text{O}_7$ series. Due to the very high moment of Gd ($\sim 7.9\mu_B$), the bifurcation between the zero-field-cooled (ZFC) and field-cooled (FC) susceptibility is very small at the transition temperature. Inset of Fig. 6.10(b) shows the $1/\chi$ plot vs. T where the transition can be seen for $x = 0.035$. The bifurcation between the ZFC and the FC was observed till $x = 0.05$. χ above the transition temperature could be fit using simple Curie-Weiss behaviour for all the compositions. The fitting was carried out in the temperature range of 200 K - 300 K. Representative plot showing the Curie-Weiss fit for $x = 0.035$ can be seen in Fig. 6.10(b). We obtained $\mu_{eff}/\text{f.u.}$ from the Curie constant. Assuming the theoretical value for the Gd moment to be $\sim 7.9\mu_B$, and the Landé- g factor to be 2, we calculated μ_{eff}/Ir using the following equation.

$$\mu_{eff}^2 = 2\mu_{Gd}^2 + 2\mu_{Ir}^2 \quad (6.1)$$

All the parameters are listed in Table 3. In pyrochlore iridates, Ir^{4+} has $5d^5$ electronic configuration. The combined effect of the octahedral crystal field and strong spin-orbit coupling leads to all the five electrons occupying the t_{2g} level which is further split into a completely filled $j_{eff} = 3/2$ quartet leaving one electron in the $j_{eff} = 1/2$ state. This gives an effective moment of $1.73\mu_B/\text{Ir}$ assuming g to be 2. However, using equation 6.1, we obtained rather large values for the Ir moments. Similar high values for the

Table 6.3: Parameters obtained from fitting of the magnetization data using Curie-Weiss expression $\chi = C/(T - \theta_P)$ for $(\text{Gd}_{1-x}\text{Bi}_x)_2\text{Ir}_2\text{O}_7$. μ_{eff}/Ir is calculated assuming Gd moments to be $7.9 \mu_B$ and the Landé-g factor for Ir to be 2. But the Gd ordering moment can range between $7.9 - 8.1 \mu_B$ and value of g_J for Ir can differ from 2 in the strong SOC limit, hence the μ_{eff}/Ir carries a considerable error bar.

$\text{Gd}_{2-2x}\text{Bi}_{2x}\text{Ir}_2\text{O}_7$	C (emu K mol ⁻¹)	$\mu_{eff}(\mu_B/\text{f.u.})$	$\mu_{eff}(\mu_B/\text{Ir})$
$x = 0$	0.0523	12.37	3.75
$x = 0.02$	0.0553	12.03	3.15
$x = 0.035$	0.06064	11.49	1.88
$x = 0.05$	0.06204	11.36	1.43
$x = 0.1$	0.0637	11.21	0.62

Ir moment were previously reported for $\text{Y}_2\text{Ir}_2\text{O}_7$ where only Ir moments contribute to the Curie-Weiss behaviour, which imparts more confidence in the extracted value for the effective moment of Ir [126]. In our case, the calculated Ir moment is less reliable for two reasons: i) the exact value of effective Gd moments is reported to vary between $7.9 - 8.1 \mu_B$ for various Gd compounds and ii) Landé-g factor can be different than 2 in the strong SOC limit. However, despite these uncertainties, it is evident that in $\text{Gd}_2\text{Ir}_2\text{O}_7$, the Ir moments are localised, and the effective moment per Ir is larger than the spin only value of $1.73\mu_B$, suggesting a highly anisotropic g-tensor with polycrystalline average differing considerably from the spin only value of $g = 2$.

As the conductivity increases going from $x = 0$ to $x = 0.1$, the effective Ir moment decreases. This suggests that for insulating compositions, Ir localised moment contributes to the total effective moment and as the compositions become more metallic, due to the itinerancy of Ir, the Ir moment decreases, which is also consistent with the fact that in $\text{Eu}_2\text{Ir}_2\text{O}_7$ the Ir moment is highly itinerant.

Fig. 6.11(a) plots S for $(\text{Dy}_{1-x}\text{Bi}_x)_2\text{Ir}_2\text{O}_7$ series where it can be seen that $x = 0.05$ has a positive thermopower over the whole temperature range, which becomes negative at low temperature $T \leq 175$ K for $x = 0.1$. Thus, in this doping range, the majority charge carriers start changing from holes to electrons.

Plot of S vs T for $(\text{Gd}_{1-x}\text{Bi}_x)_2\text{Ir}_2\text{O}_7$ series (Fig. 6.10(b)) shows that the majority charge carriers have already changed from holes to electron for $x = 0.05$ while still being in the insulating region. Upon going from $x = 0.05$ to $x = 0.1$, the thermopower increases in magnitude, and the temperature range over which S remains negative also

increases considerably.

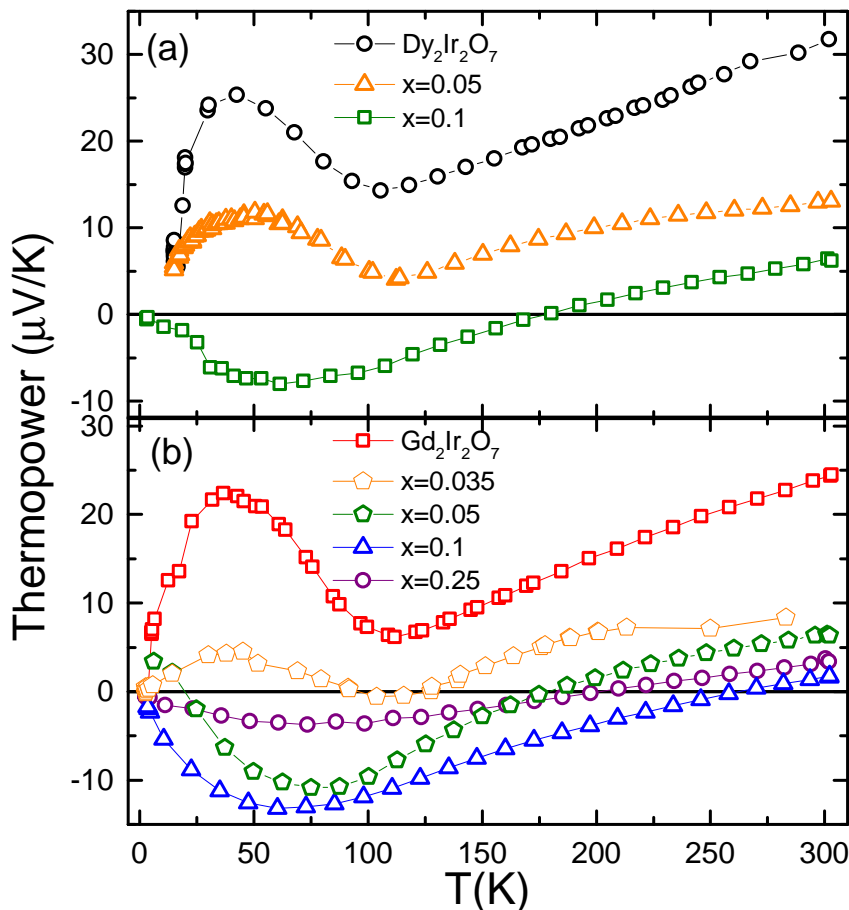


Figure 6.11: S plotted as a function of temperature for selected compositions in the series (a) $(\text{Dy}_{1-x}\text{Bi}_x)_2\text{Ir}_2\text{O}_7$ and (b) $(\text{Gd}_{1-x}\text{Bi}_x)_2\text{Ir}_2\text{O}_7$

6.3 Discussion and Summary

We will first discuss the anomalous lattice contraction. We observed that similar to Eu-Bi series, dilute Bi substitution also results in anomalous lattice contraction for the pyrochlore iridates $\text{A}_2\text{Ir}_2\text{O}_7$ ($\text{A} = \text{Sm}, \text{Gd}$ and Dy). The ionic radius of Bi is larger than the ionic radius of the rare-earths studied here. Hence, Bi substitution induces steric effect. However, Bi substitution is also accompanied by electronic effects where charge carriers are introduced, possibly due to the overlap between Bi 6p and Ir 5d orbitals. Hence the lattice contraction is a resultant of competition between the steric effect and the electronic effect. This is clearly manifested in the gigantic lattice contraction for Bi

substituted SIO where both SIO and BIO have equal lattice parameters and δ is nearly 658%.

The lattice contraction has interesting implications on the physical properties. The ordering temperature changes rather gradually for $A = \text{Dy}$ and similar as Eu-Bi series in the case of $A = \text{Gd}$. However, for $A = \text{Sm}$, significantly rapid suppression of the ordering temperature with Bi substitution is observed compared to the effect of Bi doping in EIO. In spite of the nearly same transition temperature for both EIO (120 K) and SIO (117 K), the rate of suppression of the ordering is very different for the two compositions. In the anomalous doping range, the rate of change of T_N is an order of magnitude higher ($\Delta T_N/T_N \leq 0.4$) compared to EIO ($\Delta T_N/T_N \leq 0.06$)

Now we will discuss the quantitative change in the ρ . For both DIO and GIO, the compositions become less insulating with increasing Bi substitution. However, the steep upturn in the resistivity at the transition temperature can be observed for all the compositions in the anomalous region. This behaviour collapses as the lattice constant recovers for $x = 0.1$. Though the change in the sign of the slope ($d\rho/dT$) is clearly discernable at $x = 0.1$, a significant drop in the magnitude of ρ to ≥ 0.1 Ohm-cm (at 2 K) is observed for both Dy-Bi and Gd-Bi series. A similar magnitude of ρ is also observed in the case of Eu-Bi series where the lattice contraction recovers. This underscores the point that beyond a certain carrier concentration, the steric effect dominates over the electronic effect. For Sm-Bi series, ρ continues to be around 0.09 Ohm-cm till $x = 0.25$ beyond which ($x = 0.05$) the magnitude of ρ drops to 0.01 Ohm-cm and the lattice constant start increasing.

DIO and GIO have positive thermopower indicating holes as majority charge carriers. According to our conjecture from chapter 4, Bi substitution in pyrochlore iridates tunes the Fermi energy from hole rich region to electron rich region while passing through the Weyl band crossing. This is nicely manifested in the thermopower measurements of Dy-Bi and Gd-Bi series. For the most insulating sample studied here, i.e. DIO, the majority charge carriers (concluded from the sign of thermopower) remain hole-like until $x = 0.05$ whereas for a relatively less insulating GIO, the thermopower sign change can be observed at just $x = 0.05$. The thermopower for undoped SIO itself changes sign in the intermediate temperature range ($60 \leq T \leq 150$ K) showing its proximity to the

Weyl band crossing (also reflected in the power law dependence at low temperature) and becomes negative over majority temperature range for $x = 0.02$.

We also studied magnetic susceptibility for both Sm-Bi and Gd-Bi series. The transition temperature is indicated by the bifurcation in the FC and ZFC susceptibility in both the cases. The paramagnetic susceptibility of the Gd-Bi series could be modelled using simple Curie-Weiss behaviour. The systematic decrease in the effective Ir moment with increasing conductivity suggests that Ir moment contribute to the overall moment even in the paramagnetic region and Ir itinerancy should be considered while discussing the paramagnetic susceptibility of pyrochlore iridates.

In summary, we investigated the structure and physical properties of $(A_{1-x}Bi_x)_2Ir_2O_7$ for $A = Dy, Gd$ and Sm . We established the electronic origin for the anomalous lattice contraction upon Bi-doping in the pyrochlore iridate family. The low-temperature ' ρ ' behaviour of the $(Sm_{1-x}Bi_x)_2Ir_2O_7$ samples (for $x = 0$, and 0.02) suggests that Bi-doping in $Sm_2Ir_2O_7$ pushes it away from the WSM ground state whereas, (as we saw in chapter 4), Bi-doping in EIO pushes it closer to the Weyl point.

Chapter 7

Summary and Outlook

In this thesis, our main aim was to realise novel electronic phases in pyrochlore iridate family. In particular, we focused on the Weyl semimetallic phase that was theoretically predicted almost a decade back. From the previous experimental works, it is known that the ground state of pyrochlore iridates ($A_2Ir_2O_7$) is sensitive to the unit cell parameter; hence chemical pressure could act as an excellent probe in tuning the relative interaction strength of Coulomb, spin-orbit and crystal field interactions to experimentally realize the Weyl semimetal ground state.

For this purpose, we chose the member $Eu_2Ir_2O_7$ (EIO) of the pyrochlore series. This choice is based on two important criteria: (i) EIO is located at the metal-to-insulator phase boundary, so the likelihood of finding the Weyl state, which, as shown by Krempa et al., appears over a very narrow window of the parameter space, are higher for this compound; and, (ii) Eu^{3+} is non-magnetic due to its $J = 0$ ground state, which means that intertwined magnetic and topological properties, i.e., the time reversal symmetry breaking leading to the WSM state, associated with the Ir 5d electrons can be probed directly without the huge magnetic background arising from the rare-earth moments. To tune the ground state of EIO, we decided to dope at the Eu site with another tri-positive (3+) ion so as to preserve the Ir^{4+} ($J = 1/2$) sublattice, which is crucial to the phenomenology of iridates. One of the possibilities before us was to use one of the lighter rare-earths (Sm, Nd or Pr) as the dopant; however, we did not consider this option simply to avoid additional complications arising due to magnetic nature of these ions. We, therefore, considered doping with Bi^{3+} since $Bi_2Ir_2O_7$ (BIO) has the requi-

site pyrochlore structure and is also metallic in nature. Also, its lattice parameter (a) is larger than that of $\text{Eu}_2\text{Ir}_2\text{O}_7$ (EIO), which means doping with Bi will shift the ground state of EIO in the desired (metallic) direction.

We synthesized a series $(\text{Eu}_{1-x}\text{Bi}_x)_2\text{Ir}_2\text{O}_7$ for $x = 0, 0.02, 0.035, 0.05, 0.1, 0.25, 0.5, 0.75$ and 1. For dilute Bi substitution, $x \leq 0.035$, we found a large anomalous lattice contraction. Since Bi^{3+} is larger in size compared to Eu^{3+} , we had expected a regular lattice expansion in the Eu-Bi solid-solution. However, on the contrary, we found an unusual contraction of the unit cell. The lattice contraction was confirmed using high-resolution synchrotron x-ray diffraction data at Elettra, Italy. Bi-doping also had a pronounced effect on physical properties. The ground state of EIO was found to be robust for compositions with $x \leq 0.035$ and is strongly suppressed for higher doping concentration ($x \geq 0.05$). In the anomalous region ($0 < x \leq 0.035$), we find that dilute Bi-doping tunes the ground state closer to the Weyl point, which is inferred from the behaviour of ρ vs. T , which is theoretically shown to follow a $1/T$ dependence as shown by Hosur et al. [106]. This was also supported by low-temperature thermopower which showed a change in the sign from positive to negative in the narrow doping range of $0.02 \leq x \leq 0.05$, and a concomitant reduction in the γ (i.e., coefficient of linear term in c_p) value. For $x = 0.1$, we observed a metallic behaviour and absence of any magnetic ordering down to 2 K. The absence of any ordering or freezing was further confirmed using μSR down to 20 mK. Also, the transport in this sample showed significant resemblance with PIO which is a proven Quadratic Band Touching (QBT) system. We thus conjectured that $x = 0.1$ realises a QBT ground state from which other non-trivial topological phases can be derived.

To understand the mechanism of the metal-insulator transition in the $(\text{Eu}_{1-x}\text{Bi}_x)_2\text{Ir}_2\text{O}_7$ series and to study any possible change in the valence state of any of the cations, we carried out HAXPES studies on these samples. We found that while all the cations maintain their formal valence state, there is a striking change in the peak shape of the core level spectra of Ir and Bi, traversing from insulating compositions to the metallic ones. The core-level spectra along with the valence band spectra indicated hybridisation between Bi 6p and Ir 5d orbitals as a possible mechanism for the emergence of metallic behaviour with increasing Bi doping.

We then extended Bi-doping to other members of the $\text{A}_2\text{Ir}_2\text{O}_7$ ($\text{A} = \text{Dy}, \text{Gd}, \text{Sm}$)

series. The most dramatic effect of Bi doping is observed for $A = \text{Sm}$; here the lattice parameter of $\text{Sm}_2\text{Ir}_2\text{O}_7$ (SIO) and BIO are closely matched but we found that all the intermediate compositions in the Sm-Bi solid solution had smaller lattice parameter than the end members, which clearly established the dominance of electronic effect over the steric effect. Lattice contraction was observed for other members of the series as well, similar to that of Eu. As the difference between the A-site ionic radius and Bi decreased, suppression of the insulating and magnetic ground state of the pyrochlore compounds occurred suddenly. In short, Bi suppressed the insulating ground state for $A = \text{Sm}$ just at $x = 0.035$, whereas a rather gradual decrease in the ordering temperature is observed for $A = \text{Dy}$. Nonetheless, Bi doping resulted in interesting changes in the physical properties for all the pyrochlore iridates.

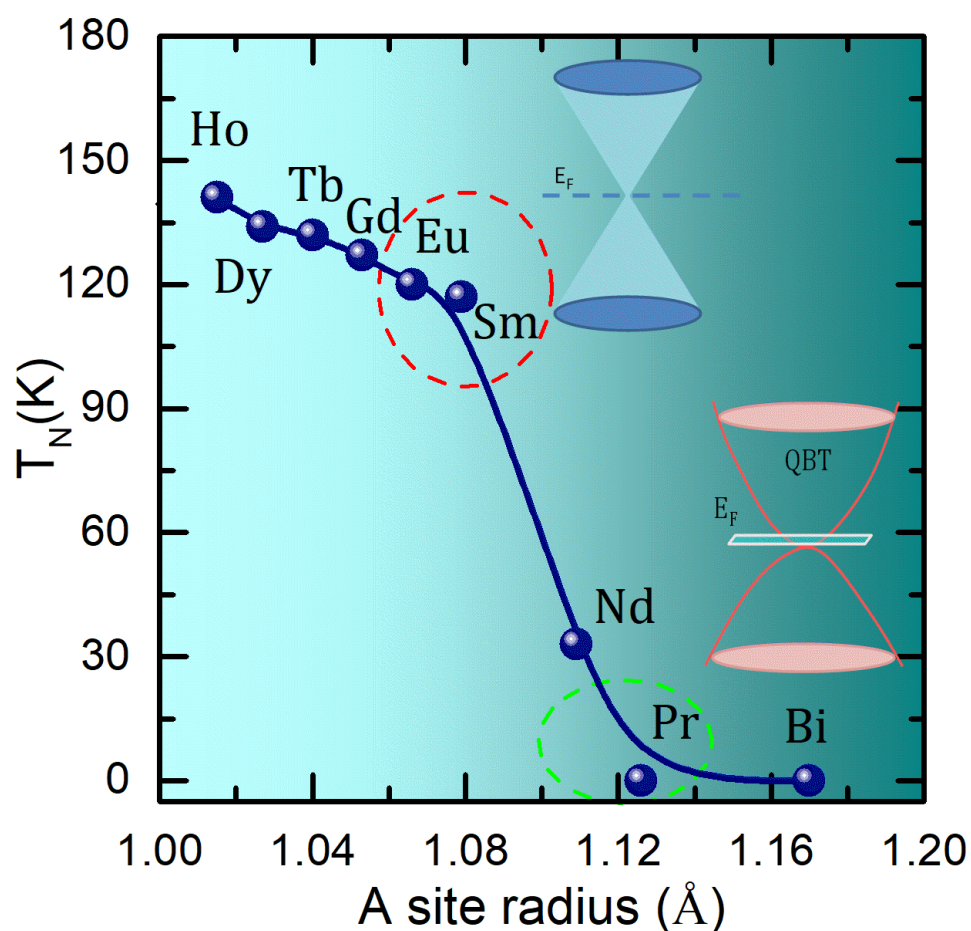


Figure 7.1: Phase diagram of the pyrochlore iridates.

We also addressed a discrepancy concerning the sign of the slope of ρ versus temperature plot in EIO above the metal-to-insulator transition, which is reported to be positive in some studies, negative in others, and a sign-changing one in other few. The sign-changing observation was previously thought to be a signature of a correlated “strange metal”. In our study, we showed that these varying behaviours, in effect, result from “stuffing” of Eu at the Ir site, due to minor changes in the structural parameters that were probed using a high-resolution synchrotron data. Since IrO_2 is volatile, we conjectured that the samples studied in previous reports had varying Eu/Ir ratio. We eventually proved that our conjecture is correct by varying Eu/Ir ratio in a controlled manner.

In future, single crystal growth of Bi-substituted pyrochlore iridates can open up new avenue for more detailed measurements, including ARPES, to study the Fermi arc states in the Weyl members. Also, magnetisation study of the metallic members of the Bi substituted pyrochlore iridates down to millikelvin temperature can be useful in exploring the itinerant spin dynamic. Bi doping in the metallic pyrochlore iridate member such as PIO, can also be an interesting avenue to understand the importance and effect of f-d interactions in these compounds.

To summarize, we investigated the effect of chemical pressure achieved by controlling the stoichiometry as well as doping on the structure and physical properties of pyrochlore iridates. We show that Bi-doping in pyrochlore iridates provides a unique platform, which, unlike Sr or Ca doping, does not create an $\text{Ir}^{4+} - \text{Ir}^{5+}$ charge disproportionation, and thus keep the Ir^{4+} sublattice intact, which is a key to obtaining various non-trivial topological phases. We reported a possible realization of Weyl semimetallic state as well as quadratic band touching upon Bi substitution in the pyrochlore iridate, thus proving Bi doping to be an interesting direction to realise novel ground states in the pyrochlore iridates. As shown in the phase diagram (Fig. 7.1), our study suggests that the probability of realizing a Weyl semimetallic ground state is the highest somewhere between $A = \text{Eu}$, and Sm whereas further increasing the A-site ionic radius towards Nd or Pr leads to a region where quadratic band touching emerges. Our findings are expected to motivate further research in exploring new quantum phases in the $U - \lambda$ phase space of $5d$ transition metal oxides.

Appendix A

Stuffing studies in pyrochlore stannate

$\text{Yb}_2\text{Sn}_2\text{O}_7$

A.1

Recently, pyrochlore compounds with Yb at the A site have garnered significant attention. In these pyrochlores, the crystal electric field (CEF) gives rise to a Kramers doublet ground state with easy XY planar anisotropy [127, 128]. In these XY pyrochlores, the anisotropic nearest neighbour exchange interaction between the A^{3+} ions, and the strong quantum spin fluctuations of the effective spin 1/2 moments, stabilizes a wealth of exotic ground states [128]. $\text{Yb}_2\text{Ti}_2\text{O}_7$ (YTO) is one such compound which has been widely studied [41, 58, 128, 129] in the past decade. In YTO, Ti^{4+} is non-magnetic, and hence the magnetism is driven solely by the Yb^{3+} which carries an effective 1/2 moment. For YTO, the local [111] Ising-like exchange interaction is considerably larger than the XY planar interaction [41], which helps in stabilising an unconventional first-order transition [130] that has been proposed to be a splayed-ferromagnet (SF) where the Yb^{3+} spins point along one of the global major axes with small canting [131]. This state is observed to be highly sensitive to low levels of quenched disorder that drastically impacts the formation of long-range magnetic order. Considerable research has been focused on quantifying the effect of off-stoichiometry on the ground state of YTO. However, the absence of conventional spin waves below T_C , irrespective of the stoichiometry, has resulted in various speculations concerning the true ground state for YTO [132, 133].

The interesting physics of YTO gives a natural motivation to study other Yb-based pyrochlores. In this regard $\text{Yb}_2\text{Sn}_2\text{O}_7$ (YSO) is an excellent candidate. Both YTO and YSO share the similarity of non-magnetic B site and ferromagnetic ground state with the absence of conventional spin waves [132] below T_C , which is 256 mK for YTO and 150 mK for YSO. The main difference between the two is in terms of their lattice parameters, which is 10.03 Å for YTO [57] and 10.306 Å for YSO [69]. However, in spite of this great similarity, the effect of off-stoichiometry on the ground state of YSO has never been explored to the best of our knowledge. In addition, the Yb-pyrochlores exhibit a rich phase diagram and their magnetic ground states are fragile and easily affected by perturbations, such as chemical pressure and off-stoichiometry [128]. Thus, it would be of great interest to study the effect of off-stoichiometry in YSO which may also prove helpful in gaining a better understanding of the ground state of YTO and other Yb based pyrochlores.

A.1.1 Synthesis and structural characterization

We synthesized $\sim 4\text{g}$ of five different compositions with the nominal stoichiometry as $\text{Yb}_{2-x}\text{Sn}_{2+x}\text{O}_7$ (for $x = -0.1, -0.04, 0, 0.04, 0.1$). All the compositions were synthesized using the standard solid-state synthesis route where the precursors Yb_2O_3 (Alfa Aesar, 99.9%) and SnO_2 (Sigma Aldrich, 99.9%) were mixed in appropriate ratio and synthesized at 1400°C for 96 hours with intermediate grinding and pelletizing.

To find out the effect of off-stoichiometry on the structural parameters, especially the O-position parameter, all the compositions were examined using the high-resolution neutron diffraction experiments at the neutron facility at Bhabha Atomic Research Center (BARC), Mumbai. However, the data consisted of artifacts due to time lag in one of the integrating detectors and hence could not yield reliable refinement (The refinement plot in Fig A. 3 shows the discrepancy in the fitting) . Thus, in this chapter we will compare the structural parameters extracted from the structural refinement of the long scans (~ 5 hrs) done on Bruker D8 powder x-ray diffractometer.

The Rietveld refinement plots for all the samples are shown in Fig A1-A2. The Rietveld refinement revealed that the Yb:Sn ratio agrees well with the nominal stoichiometry except for composition $x = 0.1$. For this sample, unreacted SnO_2 peaks are observed in the x-ray diffraction pattern, and the refinement of Yb:Sn ratio showed that only 2% of Sn has occupied the Yb site. For rest of the samples, the lattice parameter

Table A.1: Goodness of fit parameters for different values of x in $\text{Yb}_{2-x}\text{Sn}_{2+x}\text{O}_7$ samples, obtained using Rietveld refinement of powder X-ray diffraction data.

$\text{Yb}_{2-x}\text{Sn}_{2+x}\text{O}_7$	χ^2	R_p	R_{wp}	No. of phases refined	O(48f)
$x = 0$	4.3	8.6	7.1	1	0.33993
$x = 0.04$	5.1	9.3	8.1	1	0.33936
$x = -0.04$	4.9	8.9	7.3	1	0.33924
$x = 0.1$	4.7	9.3	8.1	2	0.33931
$x = -0.1$	5.1	10.1	9.6	1	0.33877

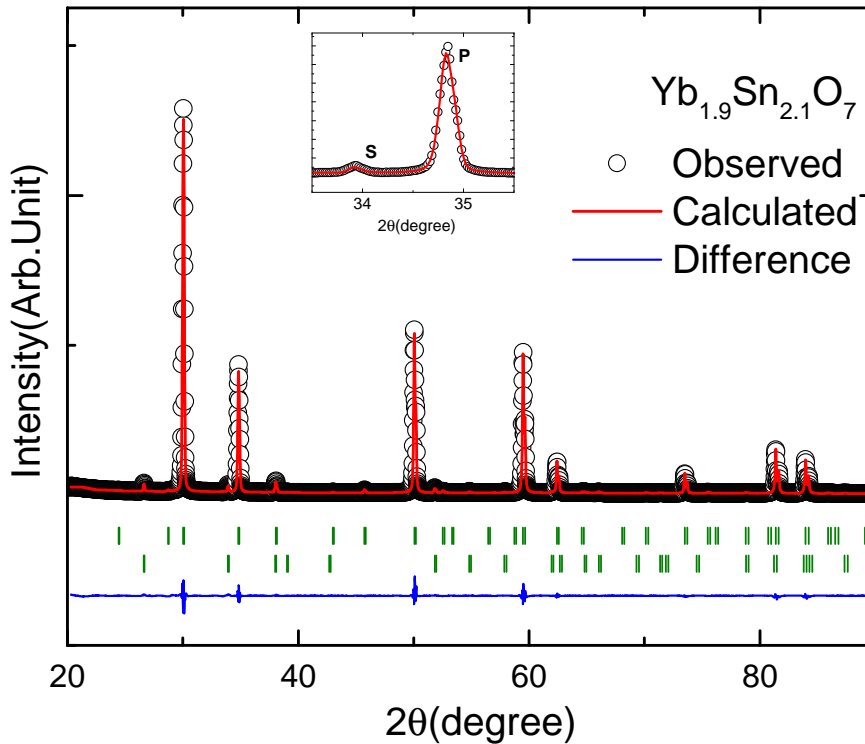


Figure A.1: Rietveld refinement of powder x-ray diffraction data of $\text{Yb}_{2-x}\text{Sn}_{2+x}\text{O}_7$ samples for $x = 0.1$. In this sample, due to the presence of SnO_2 peaks, a multi-phase refinement was carried out. Inset shows the fitting for a SnO_2 (S) as well as pyrochlore(P) peak.

trend followed a nearly linear behaviour with Yb:Sn ratio as shown in Fig A.4. As the ionic radius of Yb^{3+} (0.985 \AA) is greater than Sn^{4+} (0.69 \AA), stuffing Yb at the Sn site should result in an increase in the lattice parameter [71], whereas Sn occupying the Yb site would result in a smaller lattice parameter. However, in the case of $x = 0.1$, only a marginal stuffing of Sn at the Yb site is expected to create Yb vacancies, which can, in principle, result in an increase in the lattice parameter [69]. The lattice parameter of the stoichiometric sample is in good agreement with the previous literature [69]. The O-position parameter did not show any particular trend either with the Yb:Sn ratio or with the lattice parameter. The refined structural parameters and goodness of fit parameters are given in table 3.2.

A.1.2 Specific heat of $\text{Yb}_{2-x}\text{Sn}_{2+x}\text{O}_7$

The pyrochlore YSO is known to exhibit an anomaly in the specific heat data at its ordering temperature of $T_C = 0.15 \text{ K}$. However, around 2 K , a broad hump is also

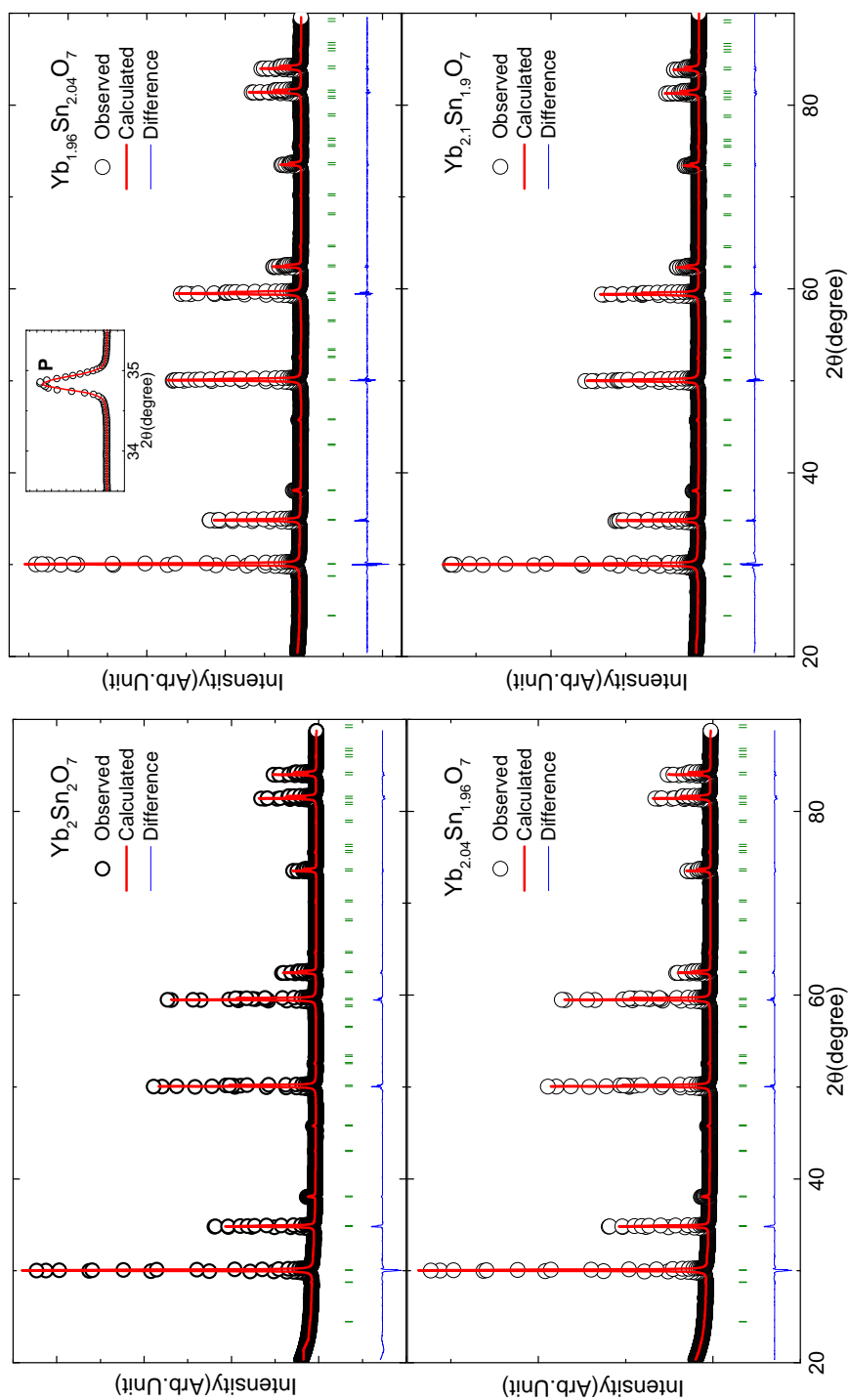


Figure A.2: Rietveld refinement of the powder x-ray diffraction data of $\text{Yb}_{2-x}\text{Sn}_{2+x}\text{O}_7$ samples for $x = 0, 0.04, -0.04, -0.1$. Inset panel for $y = 0.04$ shows absence of any SnO_2 impurity peak.

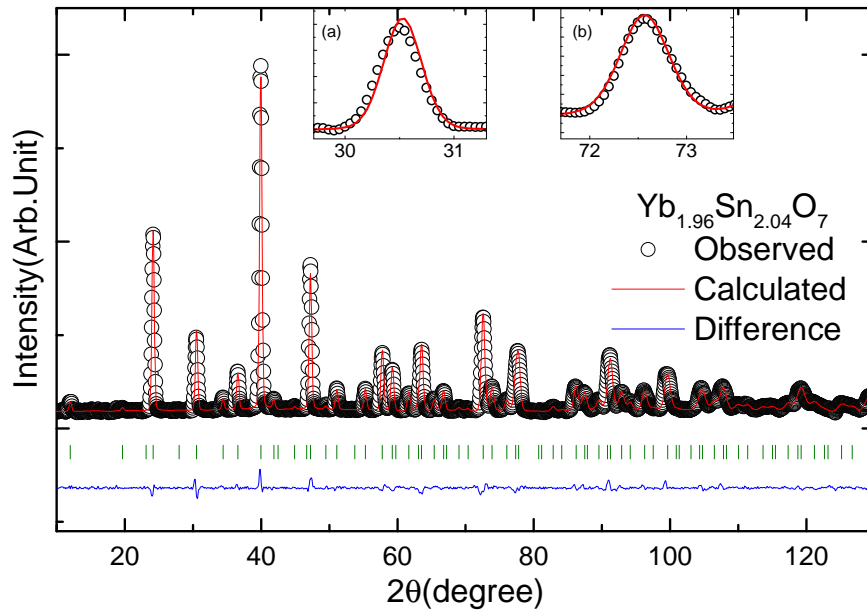


Figure A.3: Rietveld refinement of neutron diffraction data of $\text{Yb}_{1.96}\text{Sn}_{2.04}\text{O}_7$ sample. The inset panels highlight two different angular ranges. It can be seen that at smaller angle (inset a), the calculated profile is right shifted compared to the experimental data whereas at higher angles (inset b), exactly opposite trend was observed. This issue was a consequence of time lag while integrating the data from different detectors. The lattice parameters extracted by refining this data could not be trusted as lattice parameter value depended on the angular range selected for the refinement.

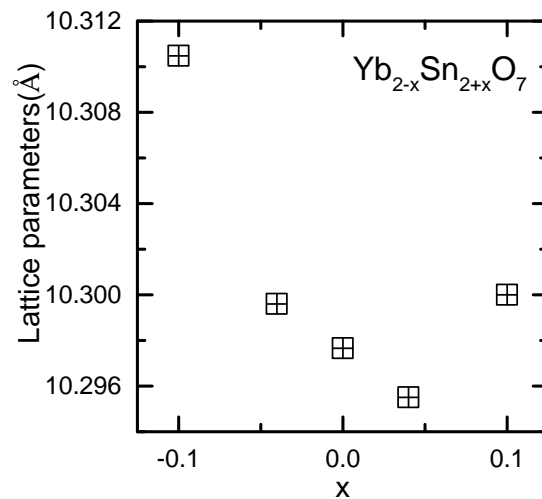


Figure A.4: Lattice parameters of $\text{Yb}_{2-x}\text{Sn}_{2+x}\text{O}_7$ samples plotted against x .

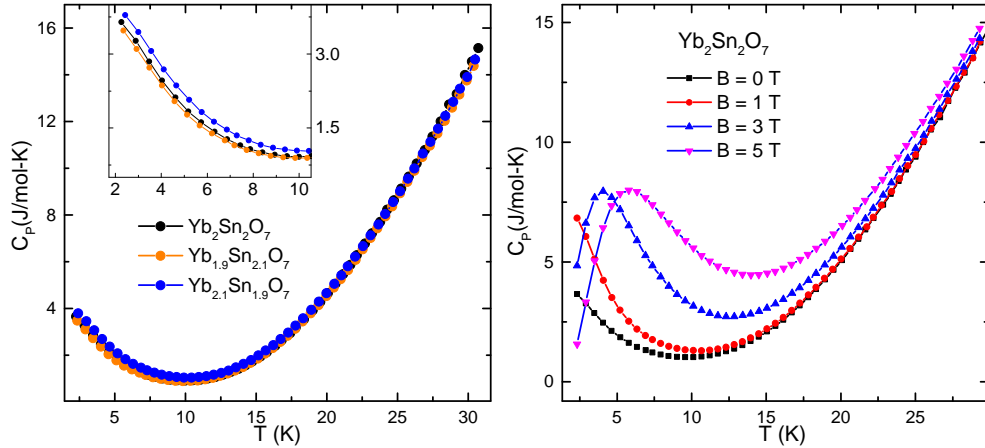


Figure A.5: Left Panel: Heat capacity of $\text{Yb}_{2-x}\text{Sn}_{2+x}\text{O}_7$ for $x = 0, -0.1, 0.1$. Right panel: Field dependence of heat capacity of $\text{Yb}_2\text{Sn}_2\text{O}_7$

reported which is believed to be of magnetic origin, and a universal feature of the Yb-pyrochlores [132]. This broad hump cannot originate from the Schottky anomaly as the crystal field excitation energy for the Yb-pyrochlore is around 600 K. From our measurement on stoichiometric YSO, we could observe the high-temperature tail of the 2 K anomaly. We observed that the molar specific heat showed marginal increment for Yb excess sample followed by the stoichiometric and Yb-deficit sample. We also measured the stoichiometric YSO composition in an applied magnetic field of $B = 0, 10, 30$ and 50 kOe. It was found that that with an increasing magnetic field, the 2 K anomaly shifts to higher temperatures; and what was an upturn in the zero-field turned into a well-defined peak centered around $T = 5$ K under an applied magnetic field of 50 kOe. This suggests a very high density of low energy magnetic excitations, consistent with a dynamic spin-ice state [134].

A.2 Summary

In the study of stuffed stannates, we reported the structural details and specific heat data for five YSO samples with stoichiometric composition as well as off-stoichiometry up to 5% on Yb and Sn sites alternatively. We observed that, while Yb can be stuffed at the Sn site, it is difficult to substitute Sn at the Yb site for concentrations higher than 2%. The low-temperature specific heat shows marginal change with Yb/Sn ratio indicating marginal if any, alteration of the ground state with off-stoichiometry. It would be inter-

esting to study these compositions down to their transition temperature to observe the changes if any.

Appendix B

Some additional measurements on the $(\text{Eu}_{1-x}\text{Bi}_x)_2\text{Ir}_2\text{O}_7$ series

In order to further probe the lattice anomaly observed in the series $(\text{Eu}_{1-x}\text{Bi}_x)_2\text{Ir}_2\text{O}_7$ for $0 < x \leq 0.035$, we performed several additional measurements. The results from these measurements are summarised in this appendix.

B.1 High-pressure x-ray diffraction measurements

In chapter 4, we had argued that the Weyl semi-metal (WSM) phase in $\text{Eu}_2\text{Ir}_2\text{O}_7$ may have some relation to the anomalous lattice contraction upon Bi doping. We performed high pressure x-ray diffraction on few selected samples (for $x = 0, 0.035, 0.1, 0.75$) in the series $(\text{Eu}_{1-x}\text{Bi}_x)_2\text{Ir}_2\text{O}_7$. The aim was to observe the response of physical pressure on the pure as well as Bi-doped compounds in order to delineate the effect of ionic size on the lattice volume with regard to the electronic doping effect and the influence of physical pressure on the lattice volume.

The measurements were carried at XPRESS beamline, Elettra synchrotron, Italy. All the measurements were done by placing the sample powders in a diamond anvil cell (DAC). A mixture of Ethanol and Methanol was used as a pressure transmitting medium. Diffractograms were collected with the incident beam energy at 25 keV ($\lambda = 0.4957 \text{ \AA}$). An image plate MAR 345 is used to collect the diffraction pattern. Conversion of 2D pattern to 1D diffraction pattern was done using Fit2D software.

Fig. B.1-B.4 shows the evolution of the x-ray diffraction patterns with increasing

pressure for $x = 0, 0.035, 0.1, 0.75$. For all the samples, the diffraction peaks shifted to higher two-theta values with increasing pressure due to volume contraction. The peaks also became broader with increasing pressure, a common effect observed due to strain-broadening in high-pressure xrd.

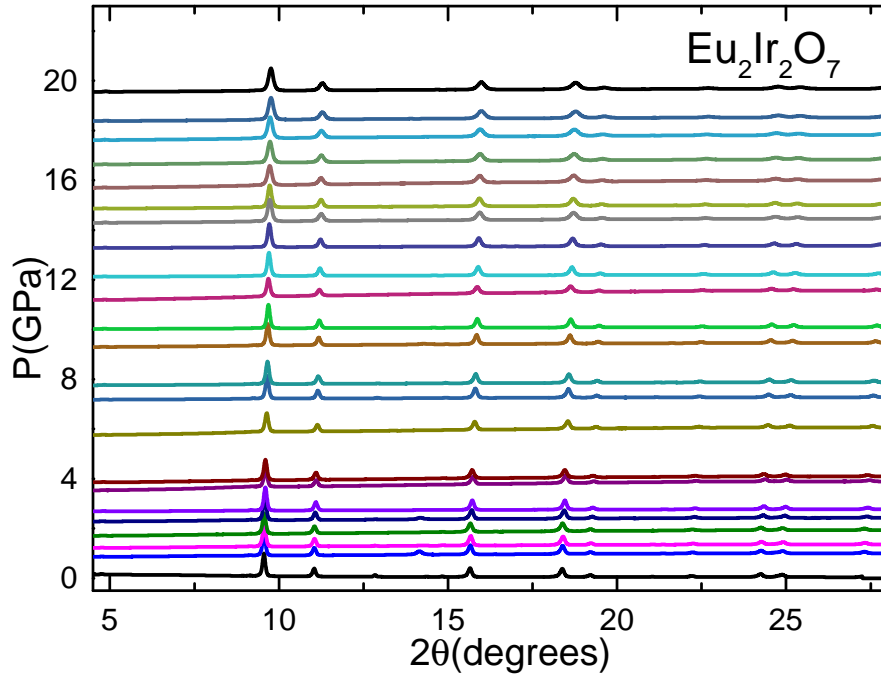


Figure B.1: Evolution of the x-ray diffraction pattern in the pressure range of 0-19 GPa for $x = 0$.

All the samples retained their cubic symmetry, as we observed neither new peak nor any peak splitting till the highest applied pressure for all the samples. We extracted the lattice parameters at different pressures by profile fitting the diffractograms in the Fullprof software. Fig. B.5 shows the change in lattice volume relative to the volume at ambient pressure for all the samples where it is evident that the volume reduces monotonically as a function of pressure. For the compositions with higher Bi substitution, i.e., $x = 0.1$ and 0.75 , there is a distinct change in the slope of a vs P plot around 10 GPa. However, no change in symmetry or peak splitting was observed in either of the two samples around 10 GPa. This feature can possibly originate from the pressure transmitting medium reaching its hydrostatic limit near 10 GPa. The relative change in the volume changes differs marginally for different samples. For $x = 0.035$ and 0.1 , a relatively higher volume contraction when compared to the undoped or $x = 0.75$ composition.

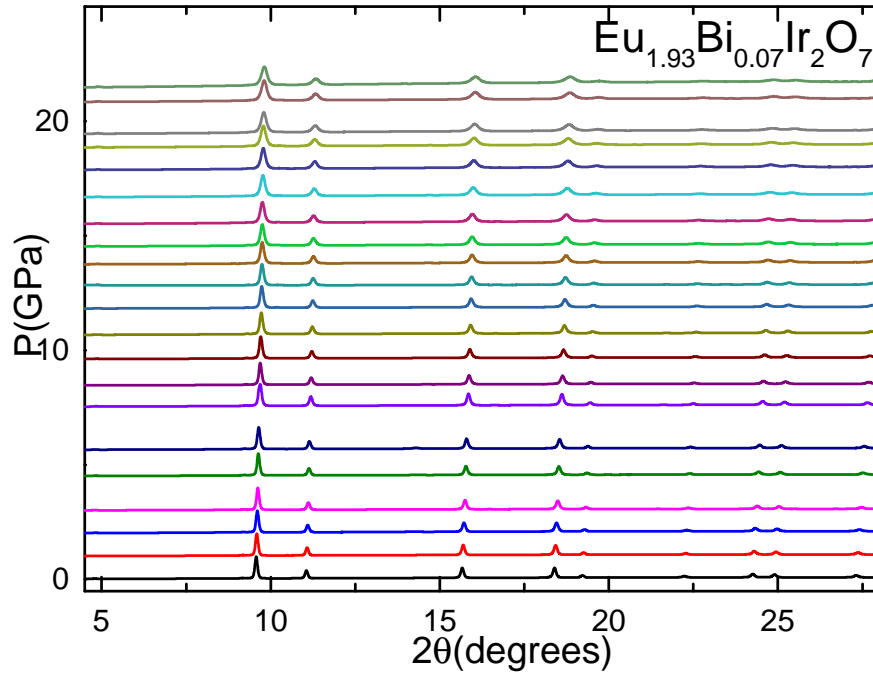


Figure B.2: Evolution of the x-ray diffraction pattern in the pressure range of 0-21 GPa for $x = 0.035$.

For the undoped and the $x = 0.035$ composition, the entire pressure range can be well fit by the Birch-Murnaghan equation, that describes the relation between hydrostatic pressure and volume contraction. The Birch-Murnaghan equation is given by:

$$P(V) = \frac{3B_0}{2} \left[\left(\frac{V_0}{V} \right)^{\frac{7}{3}} - \left(\frac{V_0}{V} \right)^{\frac{5}{3}} \right] \left\{ 1 + \frac{3}{4} (B_0' - 4) \left[\left(\frac{V_0}{V} \right)^{\frac{2}{3}} - 1 \right] \right\} \quad (\text{B.1})$$

where P is the pressure, V_0 is the lattice volume at ambient pressure, V is the deformed volume, B_0 is the bulk modulus at ambient pressure, and B_0' is the derivative of the bulk modulus with respect to pressure. The bulk modulus is obtained from fitting to the experimental data which is shown in fig. B.6. The bulk modulus and its derivative respectively were obtained as 156 GPa, 19 for $x = 0$ and 134 GPa, 23 for $x = 0.035$. The value of the bulk modulus for $x = 0$ is in good agreement with the value reported in the literature [62]. The increased value of the derivative of bulk modulus for the $x = 0.035$ composition compared to the undoped sample indicates its reduced

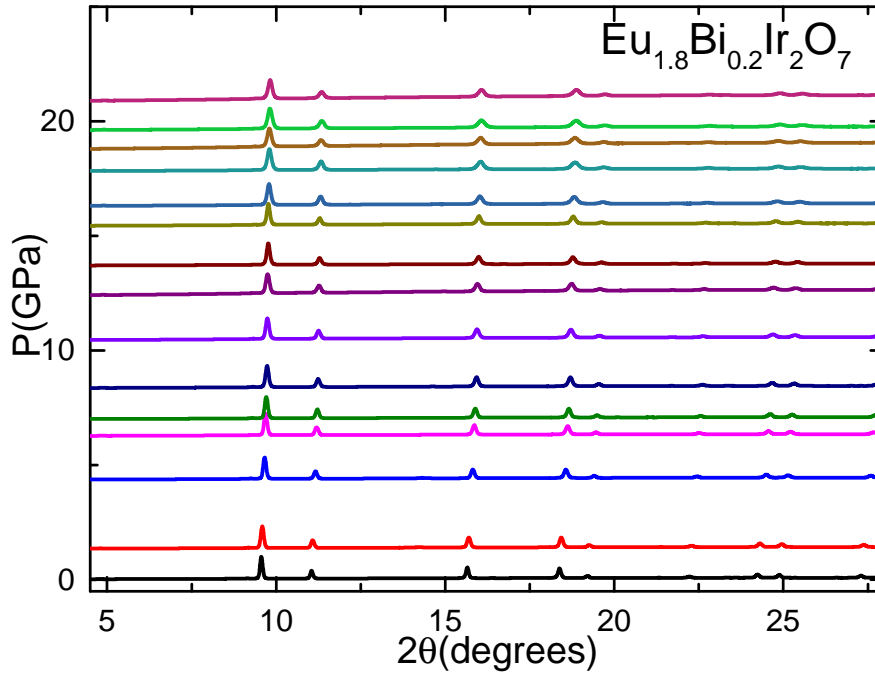


Figure B.3: Evolution of the x-ray diffraction pattern in the pressure range of 0-20 GPa for $x = 0.1$.

compressibility compared to the undoped sample.

In summary, we observed a regular lattice contraction under pressure for all the compositions, which suggests that the contraction upon Bi-doping is electronically driven corroborating the WSM ground state.

B.2 Low temperature x-ray diffraction

The structural anomaly observed at low Bi concentrations in the series $(\text{Eu}_{1-x}\text{Bi}_x)_2\text{Ir}_2\text{O}_7$ is also reflected in the physical properties such as resistivity and magnetization. The main objective of our investigation was to study the changes in the structural parameters as a function of temperature across the metal-insulator transition at 120 K for the series of composition $(\text{Eu}_{1-x}\text{Bi}_x)_2\text{Ir}_2\text{O}_7$ ($x=0, 0.02, 0.1$ and 1) using high-resolution x-ray diffraction. For comparison we also investigated $\text{Eu}_2\text{Sn}_2\text{O}_7$ and $\text{Sm}_2\text{Ir}_2\text{O}_7$.

We carried out x-ray diffraction experiments using high-energy photons at the beamline P02.1, Petra III, DESY. The experiments were carried out by the beam scientists Martin Cesnek and Jozef Bednarcik. The diffraction patterns were acquired in transmission mode with the beam wavelength of $\lambda = 0.020713$ nm. The experiments were

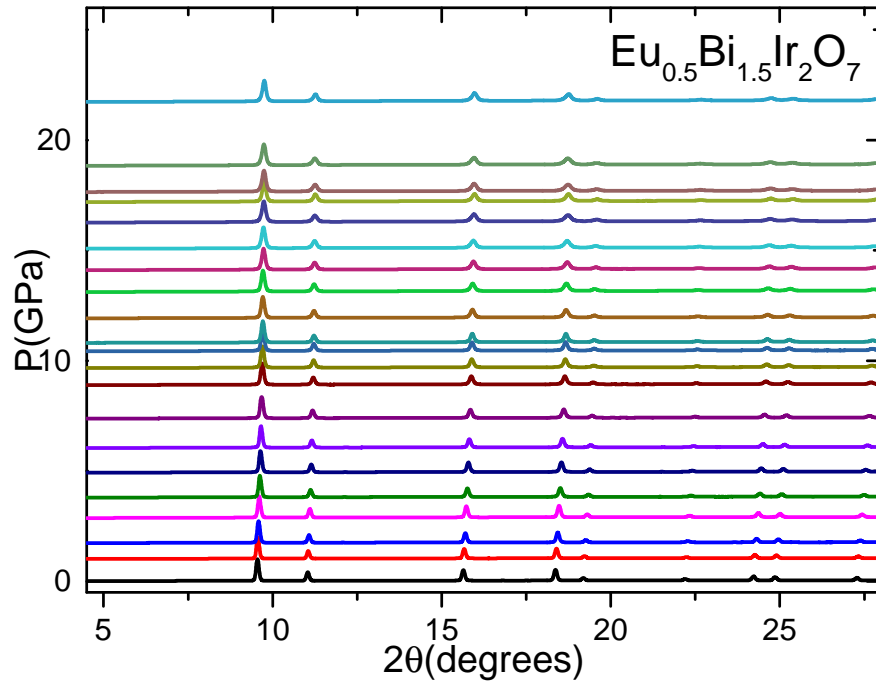


Figure B.4: Evolution of the x-ray diffraction pattern in the pressure range of 0-21 GPa for $x = 0.75$.

performed from room temperature down to 90 K at certain intervals.

The lattice parameters were extracted from the refinement of the low-temperature xrd data using Fullprof suite. The lattice parameters contracted in a regular manner for all the samples as can be seen from fig. B.7(a). Further, the lattice contraction of the same magnitude as that at the room-temperature was observed at 90 K.

Fig. B.8 shows the [844] peak for different temperatures for all the compositions studied here. Plotting the X-ray diffractograms as a function of temperature showed that the peak profile is highly asymmetric for Eu/Sm₂Ir₂O₇. Similarly, the 2% Bi substituted Eu₂Ir₂O₇ composition also showed an increasingly asymmetric peak profile with a lowering of temperature. The peak profile for Bi₂Ir₂O₇ and Eu₂Sn₂O₇, on the other hand, was found to be symmetric. This confirmed that the peak asymmetry in Eu/Sm is intrinsic to the samples. The peak asymmetry and FWHM were found to increase gradually with the lowering of temperature before it saturated close to the transition temperature. Also, this feature was found to be unique to the compositions with magnetic ordering and was not observed for samples where the ordering was suppressed or was absent.

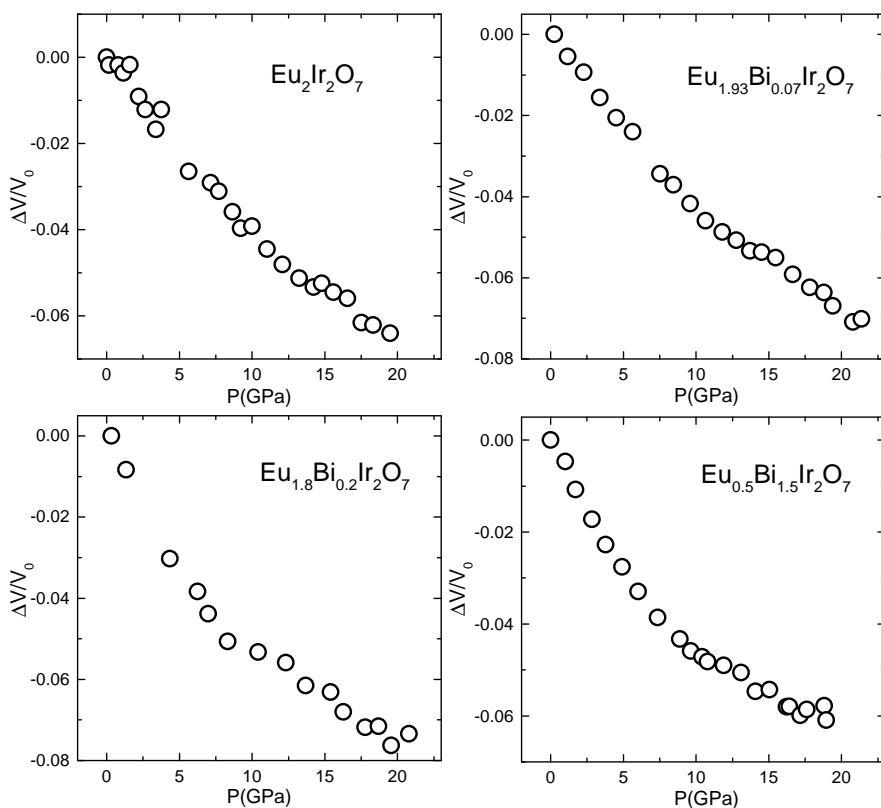


Figure B.5: The change in volume ΔV with respect to ambient pressure lattice volume V_0 plotted against the applied pressure for all the samples studied here.

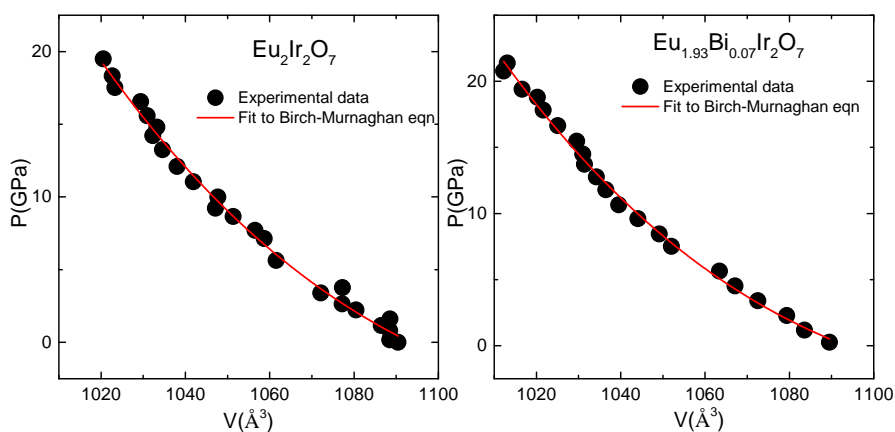


Figure B.6: Fitting of the Birch-Murnaghan equation to the lattice volume change plotted as a function of pressure.

The peaks became increasingly symmetric with increasing Bi concentration. The peaks exhibited symmetric nature when the metal-insulator transition was completely

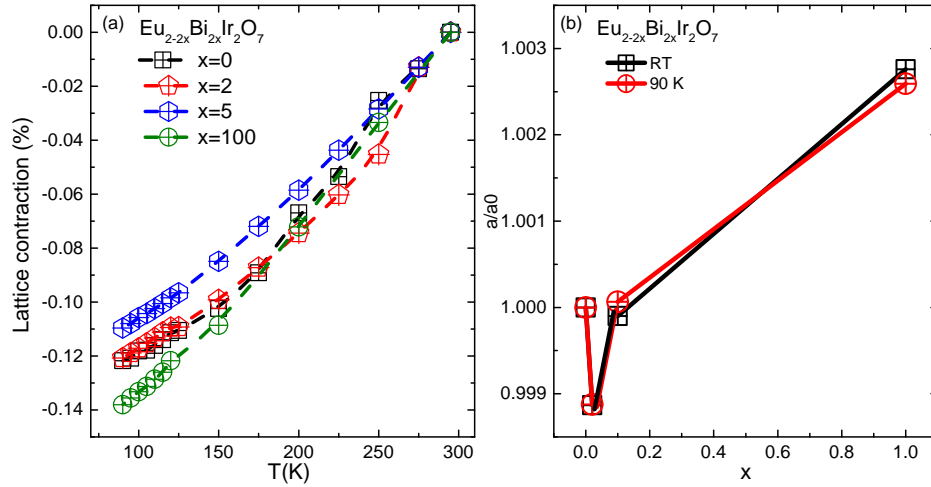


Figure B.7: (a) Evolution of lattice parameter with temperature for $x = 0, 0.02, 0.1$ and 1 in the series $(\text{Eu}_{1-x}\text{Bi}_x)_2\text{Ir}_2\text{O}_7$ (a_0 denotes the lattice constant at room temperature). (b) Comparison of lattice contraction at room temperature vs at 90 K.

suppressed at 10% Bi doping. However, we observed no anomalous shift in the x-ray peak or appearance of any new peak ruling out any major change in symmetry. Instead, our results hint at a subtle structural change that might be playing a role in the metal-insulator transition which takes place in $\text{Eu}/\text{Sm}_2\text{Ir}_2\text{O}_7$ around 120 K. Our observations stand in contrast with an earlier report of low-temperature xrd study using lab-based source on the pyrochlore iridates samples, where they failed to detect any change in the FWHM with lowering of temperature [60]. Though no structural transition is reported for pyrochlore iridates across the metal-insulator transition, a very recent polarised Raman-spectroscopy study [135] on $\text{Eu}_2\text{Ir}_2\text{O}_7$ reported line-shape anomalies for the Ir-O-Ir bending vibration at the magnetic transition temperature in addition to the appearance of a new peak below the transition temperature. These observations indicate strong electron-phonon and spin-phonon interactions, which are crucial for understanding the phase behavior of the pyrochlore iridates.

B.3 Summary

We performed x-ray diffraction measurements on compositions from the $(\text{Eu}_{1-x}\text{Bi}_x)_2\text{Ir}_2\text{O}_7$ series by i) applying external pressure and ii) by lowering the temperature below the magnetic transition. We observed that the application of external pressure did not bring any anomalous change in the lattice parameters. However, our low-temperature x-ray

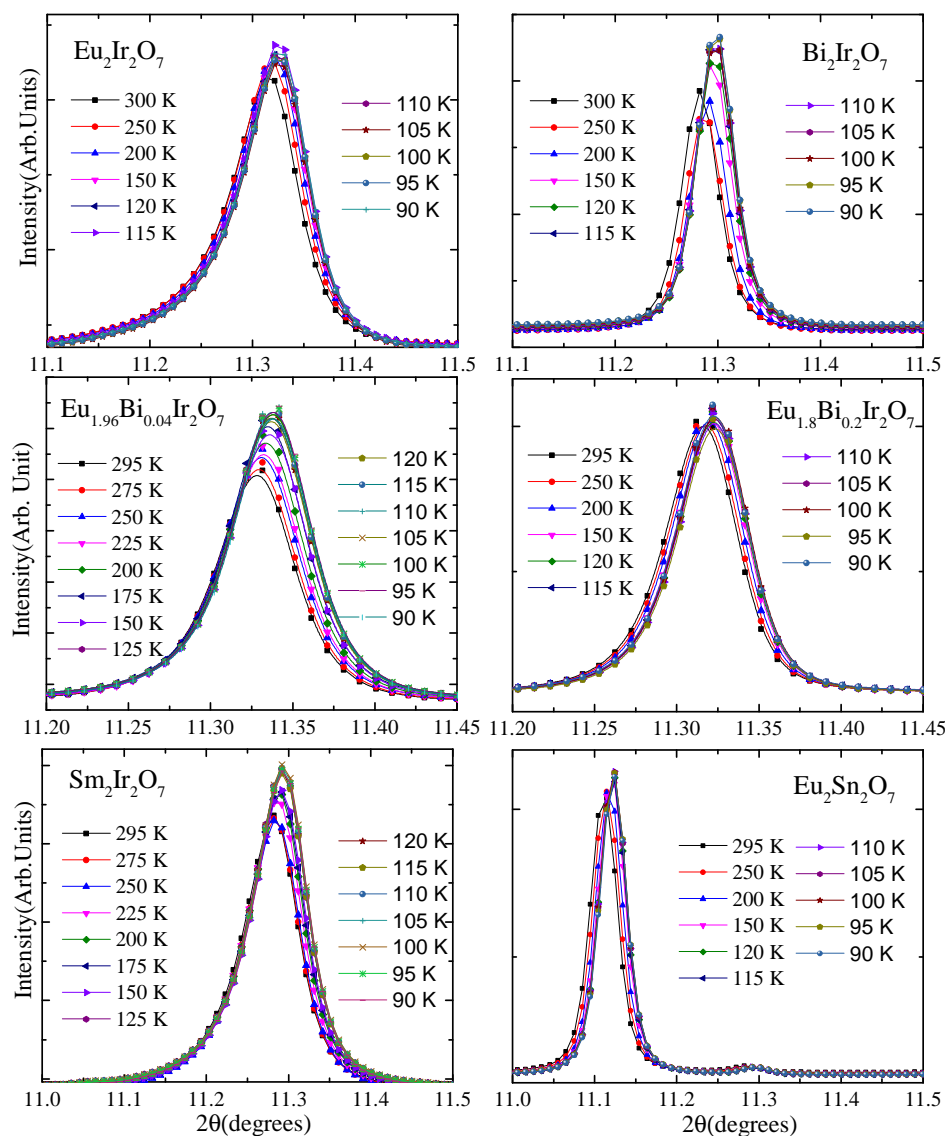


Figure B.8: 844 peak in the pyrochlore xrd pattern for different compositions showing the evolution of FWHM with lowering of the temperature. The samples with magnetic transition (left panel) show increase in the FWHM in addition to the peaks shifting to higher two theta values with lowering of temperature; whereas only right-shift of the peak position with decreasing the temperature can be observed for the non-magnetic samples (right panel).

diffraction experiments showed an increase in the FWHM with decreasing temperature for compositions with long-range magnetic ordering. Our observations indicate a strong electron-phonon coupling and underscore the importance of structural variations on the physical properties in pyrochlore iridates.

Bibliography

- [1] J. G. Rau, E. K.-H. Lee, and H.-Y. Kee, “Spin-orbit physics giving rise to novel phases in correlated systems: Iridates and related materials”, *Annual Review of Condensed Matter Physics* **7**(1), 195 (2016).
- [2] W. Witczak-Krempa, G. Chen, Y. B. Kim, and L. Balents, “Correlated quantum phenomena in the strong spin-orbit regime”, *Annual Review of Condensed Matter Physics* **5**(1), 57 (2014).
- [3] T. Ginley, Y. Wang, Z. Wang, and S. Law, “Dirac plasmons and beyond: the past, present, and future of plasmonics in 3d topological insulators”, *MRS Communications* **8**(3), 782 (2018).
- [4] K. Matsuhira, M. Wakeshima, Y. Hinatsu, and S. Takagi, “Metal-insulator transitions in pyrochlore oxides $\text{In}_2\text{Ir}_2\text{O}_7$ ”, *Journal of the Physical Society of Japan* **80**(9), 094701 (2011).
- [5] D. J. Thouless, M. Kohmoto, M. P. Nightingale, and M. den Nijs, “Quantized hall conductance in a two-dimensional periodic potential”, *Phys. Rev. Lett.* **49**, 405 (1982).
- [6] H. Zhang, C.-X. Liu, X.-L. Qi, X. Dai, Z. Fang, and Z. Shou-Cheng, “Topological insulators in bi_2se_3 , bi_2te_3 and sb_2te_3 with a single dirac cone on the surface”, *Nature Physics* **5**, 438 (2009).
- [7] C. N. R. Rao, “Transition metal oxides”, *Annual Review of Physical Chemistry* **40**(1), 291 (1989).

- [8] J. Hubbard, “Electron correlations in narrow energy bands”, *Proc. R. Soc. Lond. A* **276** (1963).
- [9] M. Imada, A. Fujimori, and Y. Tokura, “Metal-insulator transitions”, *Rev. Mod. Phys.* **70**, 1039 (1998).
- [10] G. Dresselhaus, “Spin-orbit coupling effects in zinc blende structures”, *Phys. Rev.* **100**, 580 (1955).
- [11] B. J. Kim, H. Jin, S. J. Moon, J.-Y. Kim, B.-G. Park, C. S. Leem, J. Yu, T. W. Noh, C. Kim, S.-J. Oh, J.-H. Park, V. Durairaj, G. Cao, and E. Rotenberg, “Novel $J_{\text{eff}} = 1/2$ mott state induced by relativistic spin-orbit coupling in Sr_2IrO_4 ”, *Phys. Rev. Lett.* **101**, 076402 (2008).
- [12] R. S. Perry, F. Baumberger, L. Balicas, N. Kikugawa, N. J. C. Ingle, A. Rost, J. F. Mercure, Y. Maeno, Z. X. Shen, and A. P. Mackenzie, “ Sr_2IrO_4 : a new, clean correlated electron metal”, *New Journal of Physics* **8**(9), 175 (2006).
- [13] K. v. Klitzing, G. Dorda, and M. Pepper, “New method for high-accuracy determination of the fine-structure constant based on quantized hall resistance”, *Phys. Rev. Lett.* **45**, 494 (1980).
- [14] S. Hyde, B. W. Ninham, S. Anderson, K. Larsson, T. Landh, Z. Blum, and S. Lidin. Chapter 1 - the mathematics of curvature. In *The Language of Shape*, pp. 1 – 42 (Elsevier Science B.V., Amsterdam, 1997).
- [15] S.-S. Chern and J. Simons, “Characteristic forms and geometric invariants”, *Annals of Mathematics* **99**(1), 48 (1974).
- [16] M. Born and V. Fock, “Beweis des adiabatsatzes”, *Zeitschrift für Physik* **51**(3), 165 (1928).
- [17] R. B. Laughlin, “Anomalous quantum hall effect: An incompressible quantum fluid with fractionally charged excitations”, *Phys. Rev. Lett.* **50**, 1395 (1983).
- [18] D. R. Hofstadter, “Energy levels and wave functions of bloch electrons in rational and irrational magnetic fields”, *Phys. Rev. B* **14**, 2239 (1976).

- [19] P. A. M. Dirac and R. H. Fowler, “The quantum theory of the electron”, *Proc. R. Soc. Lond. A* **117** (1928).
- [20] H. Weyl, “Elektron und gravitation. i”, *Zeitschrift für Physik* **56**(5), 330 (1929).
- [21] P. Fisher, B. Kayser, and K. S. McFarland, “Neutrino mass and oscillations”, *Annual Review of Nuclear and Particle Science* **49**(1), 481 (1999).
- [22] C. Herring, “Accidental degeneracy in the energy bands of crystals”, *Phys. Rev.* **52**, 365 (1937).
- [23] S. L. Adler, “Axial-vector vertex in spinor electrodynamics”, *Phys. Rev.* **177**, 2426 (1969).
- [24] J. S. Bell and R. Jackiw, “A pcac puzzle: $\pi^0 \rightarrow \gamma\gamma$ in the σ -model”, *Il Nuovo Cimento A (1965-1970)* **60**(1), 47 (1969).
- [25] H. Nielsen and M. Ninomiya, “The adler-bell-jackiw anomaly and weyl fermions in a crystal”, *Physics Letters B* **130**(6), 389 (1983).
- [26] X. Wan, A. M. Turner, A. Vishwanath, and S. Y. Savrasov, “Topological semimetal and fermi-arc surface states in the electronic structure of pyrochlore iridates”, *Phys. Rev. B* **83**, 205101 (2011).
- [27] M. Hirschberger, S. Kushwaha, Z. Wang, Q. Gibson, S. Liang, C. Belvin, B. Bernevig, R. Cava, and N. Ong, “The chiral anomaly and thermopower of Weyl fermions in the half-Heusler GdPtBi ”, *Nature Materials* **15**, 1161 (2016).
- [28] G. Xu, H. Weng, Z. Wang, X. Dai, and Z. Fang, “Chern semimetal and the quantized anomalous hall effect in HgCr_2Se_4 ”, *Phys. Rev. Lett.* **107**, 186806 (2011).
- [29] S. Murakami, “Phase transition between the quantum spin hall and insulator phases in 3d: emergence of a topological gapless phase”, *New Journal of Physics* **9**(9), 356 (2007).
- [30] G. B. Halász and L. Balents, “Time-reversal invariant realization of the weyl semimetal phase”, *Phys. Rev. B* **85**, 035103 (2012).

- [31] A. A. Burkov and L. Balents, “Weyl semimetal in a topological insulator multilayer”, *Phys. Rev. Lett.* **107**, 127205 (2011).
- [32] K.-Y. Yang, Y.-M. Lu, and Y. Ran, “Quantum hall effects in a weyl semimetal: Possible application in pyrochlore iridates”, *Phys. Rev. B* **84**, 075129 (2011).
- [33] B. Q. Lv, H. M. Weng, B. B. Fu, X. P. Wang, H. Miao, J. Ma, P. Richard, X. C. Huang, L. X. Zhao, G. F. Chen, Z. Fang, X. Dai, T. Qian, and H. Ding, “Experimental discovery of weyl semimetal taas”, *Phys. Rev. X* **5**, 031013 (2015).
- [34] M. Subramanian, G. Aravamudan, and G. S. Rao, “Oxide pyrochlores - a review”, *Progress in Solid State Chemistry* **15**(2), 55 (1983).
- [35] J. S. Gardner, M. J. P. Gingras, and J. E. Greedan, “Magnetic pyrochlore oxides”, *Rev. Mod. Phys.* **82**, 53 (2010).
- [36] S. T. Bramwell, M. J. Harris, B. C. den Hertog, M. J. P. Gingras, J. S. Gardner, D. F. McMorrow, A. R. Wildes, A. L. Cornelius, J. D. M. Champion, R. G. Melko, and T. Fennell, “Spin correlations in $\text{Ho}_2\text{Ti}_2\text{O}_7$: A dipolar spin ice system”, *Phys. Rev. Lett.* **87**, 047205 (2001).
- [37] W. F. Giauque and M. F. Ashley, “Molecular rotation in ice at 10°k. free energy of formation and entropy of water”, *Phys. Rev.* **43**, 81 (1933).
- [38] L. Pauling, “The structure and entropy of ice and of other crystals with some randomness of atomic arrangement”, *Journal of the American Chemical Society* **57**(12), 2680 (1935).
- [39] P. W. Anderson, “Ordering and antiferromagnetism in ferrites”, *Phys. Rev.* **102**, 1008 (1956).
- [40] D. J. P. Morris, D. A. Tennant, S. A. Grigera, B. Klemke, C. Castelnovo, R. Moessner, C. Czternasty, M. Meissner, K. C. Rule, J.-U. Hoffmann, K. Kiefer, S. Gerischer, D. Slobinsky, and R. S. Perry, “Dirac strings and magnetic monopoles in the spin ice $\text{Dy}_2\text{Ti}_2\text{O}_7$ ”, *Science* **326**(5951), 411 (2009).
- [41] K. A. Ross, L. Savary, B. D. Gaulin, and L. Balents, “Quantum excitations in quantum spin ice”, *Phys. Rev. X* **1**, 021002 (2011).

- [42] R. Bouchard and J. Gillson, “A new family of bismuth - precious metal pyrochlores”, *Materials Research Bulletin* **6**(8), 669 (1971).
- [43] N. Taira, M. Wakeshima, and Y. Hinatsu, “Magnetic properties of iridium pyrochlores $r_2\text{Ir}_2\text{O}_7$ ($r = \text{y, sm, eu and lu}$)”, *Journal of Physics: Condensed Matter* **13**(23), 5527 (2001).
- [44] D. Yanagishima and Y. Maeno, “Metal-nonmetal changeover in pyrochlore iridates”, *Journal of the Physical Society of Japan* **70**(10), 2880 (2001).
- [45] K. Matsuhira, M. Wakeshima, R. Nakanishi, T. Yamada, A. Nakamura, W. Kawano, S. Takagi, and Y. Hinatsu, “Metal-insulator transition in pyrochlore iridates $\text{In}_2\text{Ir}_2\text{O}_7$ ($\text{In} = \text{nd, sm, and eu}$)”, *Journal of the Physical Society of Japan* **76**(4), 043706 (2007).
- [46] S. Zhao, J. M. Mackie, D. E. MacLaughlin, O. O. Bernal, J. J. Ishikawa, Y. Ohta, and S. Nakatsuji, “Magnetic transition, long-range order, and moment fluctuations in the pyrochlore iridate $\text{eu}_2\text{Ir}_2\text{O}_7$ ”, *Phys. Rev. B* **83**, 180402 (2011).
- [47] C. Donnerer, M. C. Rahn, M. M. Sala, J. G. Vale, D. Pincini, J. Stremper, M. Krisch, D. Prabhakaran, A. T. Boothroyd, and D. F. McMorrow, “All-in/all-out magnetic order and propagating spin waves in $\text{sm}_2\text{Ir}_2\text{O}_7$ ”, *Phys. Rev. Lett.* **117**, 037201 (2016).
- [48] S. M. Disseler, “Direct evidence for the all-in/all-out magnetic structure in the pyrochlore iridates from muon spin relaxation”, *Phys. Rev. B* **89**, 140413 (2014).
- [49] S. Nakatsuji, Y. Machida, Y. Maeno, T. Tayama, T. Sakakibara, J. vanDuijn, L. Balicas, J. N. Millican, R. T. Macaluso, and J. Y. Chan, “Metallic spin-liquid behavior of the geometrically frustrated kondo lattice $\text{pr}_2\text{Ir}_2\text{O}_7$ ”, *Phys. Rev. Lett.* **96**, 087204 (2006).
- [50] P. J. Baker, J. S. Möller, F. L. Pratt, W. Hayes, S. J. Blundell, T. Lancaster, T. F. Qi, and G. Cao, “Weak magnetic transitions in pyrochlore $\text{bi}_2\text{Ir}_2\text{O}_7$ ”, *Phys. Rev. B* **87**, 180409 (2013).

- [51] W. Witczak-Krempa and Y. B. Kim, “Topological and magnetic phases of interacting electrons in the pyrochlore iridates”, *Phys. Rev. B* **85**, 045124 (2012).
- [52] W. Witczak-Krempa, A. Go, and Y. B. Kim, “Pyrochlore electrons under pressure, heat, and field: Shedding light on the iridates”, *Phys. Rev. B* **87**, 155101 (2013).
- [53] L. W. Bragg and H. W. Bragg, “The structure of some crystals as indicated by their diffraction of x-rays”, *Proc. R. Soc. Lond. A* **89** (1913).
- [54] H. M. Rietveld, “A profile refinement method for nuclear and magnetic structures”, *Journal of Applied Crystallography* **2**(2), 65 (1969).
- [55] A. Schenck, “Spin relaxation of polarized positive muons in paramagnetic solutions”, *Physics Letters A* **32**(1), 19 (1970).
- [56] K. Siegbahn and K. Edvarson, “ β -ray spectroscopy in the precision range of 1 : 10⁵”, *Nuclear Physics* **1**(8), 137 (1956).
- [57] K. Baroudi, B. D. Gaulin, S. H. Lapidus, J. Gaudet, and R. J. Cava, “Symmetry and light stuffing of Ho₂Ti₂O₇, Er₂Ti₂O₇, and Yb₂Ti₂O₇ characterized by synchrotron x-ray diffraction”, *Phys. Rev. B* **92**, 024110 (2015).
- [58] K. A. Ross, T. Proffen, H. A. Dabkowska, J. A. Quilliam, L. R. Yaraskavitch, J. B. Kycia, and B. D. Gaulin, “Lightly stuffed pyrochlore structure of single-crystalline yb₂ti₂o₇ grown by the optical floating zone technique”, *Phys. Rev. B* **86**, 174424 (2012).
- [59] P. Nachimuthu, S. Thevuthasan, M. H. Engelhard, W. J. Weber, D. K. Shuh, N. M. Hamdan, B. S. Mun, E. M. Adams, D. E. McCready, V. Shutthanandan, D. W. Lindle, G. Balakrishnan, D. M. Paul, E. M. Gullikson, R. C. C. Perera, J. Lian, L. M. Wang, and R. C. Ewing, “Probing cation antisite disorder in gd₂ti₂o₇ pyrochlore by site-specific near-edge x-ray-absorption fine structure and x-ray photoelectron spectroscopy”, *Phys. Rev. B* **70**, 100101 (2004).
- [60] H. Takatsu, K. Watanabe, K. Goto, and H. Kadowaki, “Comparative study of low-temperature x-ray diffraction experiments on R₂ir₂o₇ (r = Nd, eu, and pr)”,

- Phys. Rev. B* **90**, 235110 (2014). URL <https://link.aps.org/doi/10.1103/PhysRevB.90.235110>.
- [61] J. J. Ishikawa, E. C. T. O'Farrell, and S. Nakatsuji, "Continuous transition between antiferromagnetic insulator and paramagnetic metal in the pyrochlore iridate $\text{eu}_2\text{ir}_2\text{o}_7$ ", *Phys. Rev. B* **85**, 245109 (2012).
- [62] J. P. Clancy, H. Gretarsson, E. K. H. Lee, D. Tian, J. Kim, M. H. Upton, D. Casa, T. Gog, Z. Islam, B.-G. Jeon, K. H. Kim, S. Desgreniers, Y. B. Kim, S. J. Julian, and Y.-J. Kim, "X-ray scattering study of pyrochlore iridates: Crystal structure, electronic, and magnetic excitations", *Physical Review B* **94**(2) (2016).
- [63] F. F. Tafti, J. J. Ishikawa, A. McCollam, S. Nakatsuji, and S. R. Julian, "Pressure-tuned insulator to metal transition in $\text{eu}_2\text{ir}_2\text{o}_7$ ", *Phys. Rev. B* **85**, 205104 (2012).
- [64] L. Rebuffi, J. R. Plaisier, M. Abdellatif, A. Lausi, and P. Scardi, "Mcx: a synchrotron radiation beamline for x-ray diffraction line profile analysis", *Zeitschrift für anorganische und allgemeine Chemie* **640**(15), 3100 (2014).
- [65] E. H. P. Cordfunke and G. Meyer, "The system iridium - oxygen i. measurements on the volatile oxide of iridium", *Recueil des Travaux Chimiques des Pays-Bas* **81**(6), 495 (1962).
- [66] J. N. Millican, R. T. Macaluso, S. Nakatsuji, Y. Machida, Y. Maeno, and J. Y. Chan, "Crystal growth and structure of $\text{r}_2\text{ir}_2\text{o}_7$ (r=pr, eu) using molten kf", *Materials Research Bulletin* **42**(5), 928 (2007).
- [67] J. RodrÁguez-Carvajal, "Recent advances in magnetic structure determination by neutron powder diffraction", *Physica B: Condensed Matter* **192**(1), 55 (1993).
- [68] C. L. Chien and A. W. Sleight, "Mössbauer effect studies of europium pyrochlores", *Phys. Rev. B* **18**, 2031 (1978).
- [69] B. J. Kennedy, "Structural trends in pyrochlore-type oxides", *Physica B: Condensed Matter* **241**, 303 (1997).
- [70] G. Lau, B. Muegge, T. McQueen, E. Duncan, and R. Cava, "Stuffed rare earth pyrochlore solid solutions", *Journal of Solid State Chemistry* **179**(10), 3126 (2006).

- [71] R. D. Shannon, "Revised effective ionic radii and systematic studies of interatomic distances in halides and chalcogenides", *Acta Crystallographica Section A* **32**(5), 751 (1976).
- [72] J. VAN KRANENDONK and J. H. VAN VLECK, "Spin waves", *Rev. Mod. Phys.* **30**, 1 (1958).
- [73] K. Blacklock and H. W. White, "Specific heats of the pyrochlore compounds $\text{eu}_2\text{ir}_2\text{o}_7$ and $\text{lu}_2\text{ir}_2\text{o}_7$ ", *The Journal of Chemical Physics* **72**(3), 2191 (1980).
- [74] C. Kittel. *Introduction to Solid State Physics* (John Wiley & Sons, Inc., New York, 1986), 6th ed.
- [75] H. Sagayama, D. Uematsu, T. Arima, K. Sugimoto, J. J. Ishikawa, E. O'Farrell, and S. Nakatsuji, "Determination of long-range all-in-all-out ordering of ir^{4+} moments in a pyrochlore iridate $\text{eu}_2\text{ir}_2\text{o}_7$ by resonant x-ray diffraction", *Phys. Rev. B* **87**, 100403 (2013).
- [76] E. Lefrançois, V. Simonet, R. Ballou, E. Lhotel, A. Hadj-Azzem, S. Kodjikian, P. Lejay, P. Manuel, D. Khalyavin, and L. C. Chapon, "Anisotropy-tuned magnetic order in pyrochlore iridates", *Phys. Rev. Lett.* **114**, 247202 (2015).
- [77] K. Gatterer and H. P. Fritzer, "Magnetic susceptibility of the van vleck paramagnet $\text{cs}_5\text{eu}(\text{n}3)8$ ", *Journal of Physics: Condensed Matter* **4**(19), 4667 (1992).
- [78] M. J. Graf, S. M. Disseler, C. Dhital, T. Hogan, M. Bojko, A. Amato, H. Luetkens, C. Baines, D. Margineda, S. R. Giblin, M. Jura, and S. D. Wilson, "Magnetism and magnetic order in the pyrochlore iridates in the insulator-to-metal crossover region", *Journal of Physics: Conference Series* **551**(1), 012020 (2014).
- [79] D. K. C. MacDonald. In *Thermoelectricity: An interoduction to the principles* (Dover Publication, INC., 2006).
- [80] L. Minervini, R. W. Grimes, and K. E. Sickafus, "Disorder in pyrochlore oxides", *Journal of the American Ceramic Society* **83**(8), 1873 (2000).

- [81] J. González, “Competition between disorder and interaction effects in three-dimensional weyl semimetals”, *Phys. Rev. B* **96**, 081104 (2017).
- [82] F. Ishii, Y. P. Mizuta, T. Kato, T. Ozaki, H. Weng, and S. Onoda, “First-principles study on cubic pyrochlore iridates $\text{Y}_2\text{Ir}_2\text{O}_7$ and $\text{Pr}_2\text{Ir}_2\text{O}_7$ ”, *Journal of the Physical Society of Japan* **84**(7), 073703 (2015).
- [83] H. Zhang, K. Haule, and D. Vanderbilt, “Metal-insulator transition and topological properties of pyrochlore iridates”, *Phys. Rev. Lett.* **118**, 026404 (2017).
- [84] A. Apetrei, I. Mirebeau, I. Goncharenko, and W. A. Crichton, “Crystal structure under pressure of geometrically frustrated pyrochlores”, *Journal of Physics: Condensed Matter* **19**(37), 376208 (2007).
- [85] S. Saha, D. V. S. Muthu, C. Pascanut, N. Dragoe, R. Suryanarayanan, G. Dhalenne, A. Revcolevschi, S. Karmakar, S. M. Sharma, and A. K. Sood, “High-pressure raman and x-ray study of the spin-frustrated pyrochlore $\text{Gd}_2\text{Ti}_2\text{O}_7$ ”, *Phys. Rev. B* **74**, 064109 (2006).
- [86] M. Sakata, T. Kagayama, K. Shimizu, K. Matsuhira, S. Takagi, M. Wakeshima, and Y. Hinatsu, “Suppression of metal-insulator transition at high pressure and pressure-induced magnetic ordering in pyrochlore oxide $\text{Nd}_2\text{Ir}_2\text{O}_7$ ”, *Phys. Rev. B* **83**, 041102 (2011).
- [87] H. Guo, K. Matsuhira, I. Kawasaki, M. Wakeshima, Y. Hinatsu, I. Watanabe, and Z.-a. Xu, “Magnetic order in the pyrochlore iridate $\text{Nd}_2\text{Ir}_2\text{O}_7$ probed by muon spin relaxation”, *Phys. Rev. B* **88**, 060411 (2013).
- [88] E.-G. Moon, C. Xu, Y. B. Kim, and L. Balents, “Non-fermi-liquid and topological states with strong spin-orbit coupling”, *Phys. Rev. Lett.* **111**, 206401 (2013).
- [89] L. Savary, E.-G. Moon, and L. Balents, “New type of quantum criticality in the pyrochlore iridates”, *Phys. Rev. X* **4**, 041027 (2014).
- [90] B.-J. Yang, E. G. Moon, H. Isobe, and N. Nagaosa, “Quantum criticality of topological phase transitions in three-dimensional interacting electronic systems”, *Nature Physics* **10**, 774 (2014).

- [91] R. Wang, A. Go, and A. J. Millis, “Electron interactions, spin-orbit coupling, and intersite correlations in pyrochlore iridates”, *Phys. Rev. B* **95**, 045133 (2017).
- [92] T. Kondo, M. Nakayama, R. Chen, J. J. Ishikawa, E.-G. Moon, T. Yamamoto, Y. Ota, W. Malaeb, H. Kanai, Y. Nakashima, Y. Ishida, R. Yoshida, H. Yamamoto, M. Matsunami, S. Kimura, N. Inami, K. Ono, H. Kumigashira, S. Nakatsuji, L. Balents, and S. Shin, “Quadratic fermi node in a 3d strongly correlated semimetal”, *Nature Comm.* **6**, 10042 (2015).
- [93] A. B. Sushkov, J. B. Hofmann, G. S. Jenkins, J. Ishikawa, S. Nakatsuji, S. Das Sarma, and H. D. Drew, “Optical evidence for a weyl semimetal state in pyrochlore $\text{eu}_2\text{ir}_2\text{o}_7$ ”, *Phys. Rev. B* **92**, 241108 (2015).
- [94] D. Liang, H. Liu, N. Liu, L. Ling, Y. Han, L. Zhang, and C. Zhang, “Structural, magnetic and electrical properties in the pyrochlore oxide $\text{bi}_{2-x}\text{ca}_x\text{ir}_2\text{o}_{7-\delta}$ ”, *Ceramics International* **42**(3), 4562 (2016).
- [95] A. Banerjee, J. Sannigrahi, S. Giri, and S. Majumdar, “Observation of non-fermi liquid behavior in hole-doped $\text{eu}_2\text{ir}_2\text{o}_7$ ”, *Phys. Rev. B* **96**, 224426 (2017).
- [96] T. F. Qi, O. B. Korneta, X. Wan, L. E. DeLong, P. Schlottmann, and G. Cao, “Strong magnetic instability in correlated metallic $\text{bi}_2\text{ir}_2\text{o}_7$ ”, *Journal of Physics: Condensed Matter* **24**(34), 345601 (2012).
- [97] K. Sardar, S. C. Ball, J. D. Sharman, D. Thompsett, J. M. Fisher, R. A. Smith, P. K. Biswas, M. R. Lees, R. J. Kashtiban, J. Sloan, and R. I. Walton, “Bismuth iridium oxide oxygen evolution catalyst from hydrothermal synthesis”, *Chemistry of Materials* **24**(21), 4192 (2012).
- [98] G. Prando, O. Vakaliuk, S. Sanna, G. Lamura, T. Shiroka, P. Bonfà, P. Carretta, R. De Renzi, H.-H. Klauss, C. G. F. Blum, S. Wurmehl, C. Hess, and B. Büchner, “Role of in-plane and out-of-plane dilution in cefeaso: Charge doping versus disorder”, *Phys. Rev. B* **87**, 174519 (2013).
- [99] G. Prando, R. Dally, W. Schottenhamel, Z. Guguchia, S.-H. Baek, R. Aeschliemann, A. U. B. Wolter, S. D. Wilson, B. Büchner, and M. J. Graf, “Influence of

- hydrostatic pressure on the bulk magnetic properties of $\text{eu}_2\text{ir}_2\text{o}_7$ ", *Phys. Rev. B* **93**, 104422 (2016).
- [100] P. Telang, K. Mishra, A. K. Sood, and S. Singh, "Dilute stuffing in the pyrochlore iridate $\text{eu}_2\text{ir}_2\text{o}_7$ ", *Phys. Rev. B* **97**, 235118 (2018).
- [101] R. Kanno, Y. Takeda, T. Yamamoto, Y. Kawamoto, and O. Yamamoto, "Crystal structure and electrical properties of the pyrochlore ruthenate $\text{bi}_{2-x}\text{y}_x\text{ru}_2\text{o}_7$ ", *Journal of Solid State Chemistry* **102**(1), 106 (1993).
- [102] A. Janotti, B. Jalan, S. Stemmer, and C. G. V. de Walle, "Effects of doping on the lattice parameter of $\text{sr}_{1-x}\text{la}_x\text{o}_3$ ", *Applied Physics Letters* **100**(26), 262104 (2012).
- [103] T. Hogan, X. Wang, H. Chu, D. Hsieh, and S. D. Wilson, "Doping-driven structural distortion in the bilayer iridate $(\text{Sr}_{1-x}\text{La}_x)_3\text{ir}_2\text{o}_7$ ", *Phys. Rev. B* **95**, 174109 (2017).
- [104] X. Chen, T. Hogan, D. Walkup, W. Zhou, M. Pokharel, M. Yao, W. Tian, T. Z. Ward, Y. Zhao, D. Parshall, C. Opeil, J. W. Lynn, V. Madhavan, and S. D. Wilson, "Influence of electron doping on the ground state of $(\text{Sr}_{1-x}\text{La}_x)_2\text{irO}_4$ ", *Phys. Rev. B* **92**, 075125 (2015).
- [105] J. Bardeen and W. Shockley, "Deformation potentials and mobilities in non-polar crystals", *Phys. Rev.* **80**, 72 (1950).
- [106] P. Hosur, S. A. Parameswaran, and A. Vishwanath, "Charge transport in weyl semimetals", *Phys. Rev. Lett.* **108**, 046602 (2012).
- [107] B. Cheng, T. Ohtsuki, D. Chaudhuri, S. Nakatsuji, M. Lippmaa, and N. P. Armitage, "Dielectric anomalies and interactions in the three-dimensional quadratic band touching luttinger semimetal $\text{pr}_2\text{ir}_2\text{o}_7$ ", *Nature Comm.* **8**, 2097 (2017).
- [108] M. Udagawa, H. Ishizuka, and Y. Motome, "Non-kondo mechanism for resistivity minimum in spin ice conduction systems", *Phys. Rev. Lett.* **108**, 066406 (2012).
- [109] N. Fairley, "Casaxps processing software for xps spectra" (2009).

- [110] C. Caspers, M. Müller, A. X. Gray, A. M. Kaiser, A. Gloskovskii, C. S. Fadley, W. Drube, and C. M. Schneider, “Chemical stability of the magnetic oxide EuO directly on silicon observed by hard x-ray photoemission spectroscopy”, *Phys. Rev. B* **84**, 205217 (2011).
- [111] J. M. Kahn, C. G. Poll, F. E. Oropeza, J. M. Ablett, D. Céolin, J.-P. Rueff, S. Agrestini, Y. Utsumi, K. D. Tsuei, Y. F. Liao, F. Borgatti, G. Panaccione, A. Regoutz, R. G. Egdell, B. J. Morgan, D. O. Scanlon, and D. J. Payne, “Understanding the electronic structure of IrO_2 using hard-x-ray photoelectron spectroscopy and density-functional theory”, *Phys. Rev. Lett.* **112**, 117601 (2014).
- [112] W. Sun, J.-Y. Liu, X.-Q. Gong, W.-Q. Zaman, L.-M. Cao, and J. Yang, “Oer activity manipulated by IrO_6 coordination geometry: an insight from pyrochlore iridates”, *Scientific Reports* **6**, 38429 (2016).
- [113] P. A. Cox, R. G. Egdell, J. B. Goodenough, A. Hamnett, and C. C. Naish, “The metal-to-semiconductor transition in ternary ruthenium (IV) oxides: a study by electron spectroscopy”, *Journal of Physics C: Solid State Physics* **16**(32), 6221 (1983).
- [114] M. Campagna, G. K. Wertheim, H. R. Shanks, F. Zumsteg, and E. Banks, “Local character of many-body effects in x-ray photoemission from transition-metal compounds: Na_xWO_3 ”, *Phys. Rev. Lett.* **34**, 738 (1975).
- [115] N. Beatham, P. Cox, R. Egdell, and A. Orchard, “Core photoelectron spectra of narrow-band metallic materials”, *Chemical Physics Letters* **69**(3), 479 (1980).
- [116] V. Pfeifer, T. E. Jones, J. J. Velasco Velez, C. Massue, R. Arrigo, D. Teschner, F. Girgsdies, M. Scherzer, M. T. Greiner, J. Allan, M. Hashagen, G. Weinberg, S. Piccinin, M. Hävecker, A. Knop-Gericke, and R. Schlogl, “The electronic structure of iridium and its oxides”, *Surface and Interface Analysis* **48**(5), 261 (2016).
- [117] B.-J. Yang and Y. B. Kim, “Topological insulators and metal-insulator transition in the pyrochlore iridates”, *Phys. Rev. B* **82**, 085111 (2010).

- [118] K. H. Whitmire. *Bismuth: Inorganic Chemistry* (American Cancer Society, 2014).
- [119] E. A. Abdullah and T. K. Ban, “Synthesis and characterisation of penta-bismuth hepta-oxide nitrate, $\text{Bi}_5\text{O}_7\text{NO}_3$, as a new adsorbent for methyl orange removal from an aqueous solution”, *E-Journal of Chemistry* **9**, 2429 (2012).
- [120] W. Y. Hsu, R. V. Kasowski, T. Miller, and T. Chiang, “Band structure of metallic pyrochlore ruthenates $\text{Bi}_2\text{Ru}_2\text{O}_7$ and $\text{Pb}_2\text{Ru}_2\text{O}_6.5$ ”, *Applied Physics Letters* **52**(10), 792 (1988).
- [121] P. Day. *Emission and Scattering Techniques: Studies of Inorganic Molecules, Solids, and Surfaces*. Nato Science Series C: (Springer Netherlands, 2012).
- [122] J. Folmer and D. de Boer, “Xps core level line shapes in metallic compounds: A probe for the nature of the electrons at the fermi level”, *Solid State Communications* **38**(12), 1135 (1981).
- [123] J. Park, K. H. Kim, H.-J. Noh, S.-J. Oh, J.-H. Park, H.-J. Lin, and C.-T. Chen, “Photoemission and x-ray absorption spectroscopy studies on cubic pyrochlore ruthenates $\text{Bi}_{2-x}\text{Y}_x\text{Ru}_2\text{O}_7$ ”, *Phys. Rev. B* **69**, 165120 (2004).
- [124] H. Lal and N. Dar, “Low temperature magnetic susceptibility of $\text{Sm}_2(\text{WO}_4)_3$ ”, *Zeitschrift fuer Naturforschung Teil A* **30**, 1783.
- [125] R. Kaneko, M.-T. Huebsch, S. Sakai, R. Arita, H. Shinaoka, K. Ueda, Y. Tokura, and J. Fujioka, “Enhanced thermopower in the correlated semimetallic phase of hole-doped pyrochlore iridates”, *Phys. Rev. B* **99**, 161104 (2019).
- [126] H. Kumar, R. S. Dhaka, and A. K. Pramanik, “Evolution of structure, magnetism, and electronic transport in the doped pyrochlore iridate $\text{Y}_2\text{Ir}_{2-x}\text{Ru}_x\text{O}_7$ ”, *Phys. Rev. B* **95**, 054415 (2017).
- [127] A. Maisuradze, P. Dalmas de Réotier, A. Yaouanc, A. Forget, C. Baines, and P. J. C. King, “Anomalously slow spin dynamics and short-range correlations in the quantum spin ice systems $\text{Yb}_2\text{Ti}_2\text{O}_7$ and $\text{Yb}_2\text{Sn}_2\text{O}_7$ ”, *Phys. Rev. B* **92**, 094424 (2015).

- [128] A. M. Hallas, J. Gaudet, and B. D. Gaulin, “Experimental insights into ground-state selection of quantum xy pyrochlores”, *Annual Review of Condensed Matter Physics* **9**(1), 105 (2018).
- [129] K. E. Arpino, B. A. Trump, A. O. Scheie, T. M. McQueen, and S. M. Koohpayeh, “Impact of stoichiometry of $\text{yb}_2\text{ti}_2\text{o}_7$ on its physical properties”, *Phys. Rev. B* **95**, 094407 (2017).
- [130] J. A. Hodges, P. Bonville, A. Forget, A. Yaouanc, P. Dalmas de Réotier, G. André, M. Rams, K. Królas, C. Ritter, P. C. M. Gubbens, C. T. Kaiser, P. J. C. King, and C. Baines, “First-order transition in the spin dynamics of geometrically frustrated $\text{yb}_2\text{ti}_2\text{O}_7$ ”, *Phys. Rev. Lett.* **88**, 077204 (2002).
- [131] A. Yaouanc, P. Dalmas de Réotier, P. Bonville, J. A. Hodges, V. Glazkov, L. Keller, V. Sikolenko, M. Bartkowiak, A. Amato, C. Baines, P. J. C. King, P. C. M. Gubbens, and A. Forget, “Dynamical splayed ferromagnetic ground state in the quantum spin ice $\text{yb}_2\text{sn}_2\text{O}_7$ ”, *Phys. Rev. Lett.* **110**, 127207 (2013).
- [132] A. M. Hallas, J. Gaudet, N. P. Butch, M. Tachibana, R. S. Freitas, G. M. Luke, C. R. Wiebe, and B. D. Gaulin, “Universal dynamic magnetism in yb pyrochlores with disparate ground states”, *Phys. Rev. B* **93**, 100403 (2016).
- [133] R. M. D’Ortenzio, H. A. Dabkowska, S. R. Dunsiger, B. D. Gaulin, M. J. P. Gingras, T. Goko, J. B. Kycia, L. Liu, T. Medina, T. J. Munsie, D. Pomaranski, K. A. Ross, Y. J. Uemura, T. J. Williams, and G. M. Luke, “Unconventional magnetic ground state in $\text{yb}_2\text{ti}_2\text{O}_7$ ”, *Phys. Rev. B* **88**, 134428 (2013).
- [134] D. Prabhakaran, S. Wang, and A. Boothroyd, “Crystal growth of pyrochlore rare-earth stannates”, *Journal of Crystal Growth* **468**, 335 (2017). The 18th International Conference on Crystal Growth and Epitaxy (ICCGE-18).
- [135] K. Ueda, R. Kaneko, A. Subedi, M. Minola, B. J. Kim, J. Fujioka, Y. Tokura, and B. Keimer, “Phonon anomalies in pyrochlore iridates studied by raman spectroscopy”, *Phys. Rev. B* **100**, 115157 (2019).